

INVESTIGATION OF STRONGLY CORRELATED  
ELECTRON SYSTEMS WITH CELLULAR  
DYNAMICAL MEAN FIELD THEORY

BY MARCELLO CIVELLI

A dissertation submitted to the  
Graduate School—New Brunswick  
Rutgers, The State University of New Jersey  
in partial fulfillment of the requirements

for the degree of

Doctor of Philosophy  
Graduate Program in Physics

Written under the direction of

Prof. B. Gabriel Kotliar

and approved by

---

---

---

---

---

New Brunswick, New Jersey

May, 2006

## ABSTRACT OF THE DISSERTATION

# Investigation of Strongly Correlated Electron Systems with Cellular Dynamical Mean Field Theory

by Marcello Civelli

Dissertation Director: Prof. B. Gabriel Kotliar

In this thesis we study the strongly correlated electron physics in the framework of the longstanding H- $T_C$  superconductivity problem using a non-perturbative method, the Dynamical Mean Field Theory (DMFT), capable to go beyond standard perturbation theory techniques. DMFT is by construction a local theory which neglects spatial correlation. The latter is however shown in experiments to be a fundamental property of cuprate materials. In a first step, we approach the problem of the spatial correlation in the normal state of cuprate materials using a phenomenological Fermi-Liquid-Boltzmann model. We then introduce and develop in detail an extension to DMFT, the Cellular Dynamical Mean Field Theory (CDMFT), capable of considering short-ranged spatial correlation in a system and implemented it with the exact diagonalization algorithm. After testing CDMFT in an exact limiting case, we apply it to study the density-driven Mott metal-insulator transition in the two-dimensional Hubbard Model with particular attention to the anomalous properties of the normal state as the Mott insulator is approached. We finally study the superconducting state. We show that within CDMFT the one-band Hubbard Model supports a d-wave superconductive state, which strongly departs from the standard BCS theory. We conjecture a link between the instabilities found in the normal state and the onset of superconductivity.

## Acknowledgements

This thesis owns its birth to the ideas and long-term frontier research of Prof. Gabriel Kotliar. I am most grateful to him for providing the chance of studying very interesting and challenging problems. He has guided me through these graduate-school years teaching the way to do research and living with me either the moments of difficulties and of great exaltation.

I thank the people that worked with me in this project (in order of appearance): Andrea Perali, Srivenkateswara Sarma Kancharla, Massimo Capone, Olivier Parcollet, Tudor Stanescu. From them I learned a lot. In this work I also enjoyed the collaboration and the discussions with Bumsoo Kyung and André-Marie Trambly.

I am very grateful to the many people in the big Prof. Kotliar's "family" and to the many friends in graduate school. With them I shared a lot of things: offices, computers, lunch and dinner times, seminars, long nights (never mornings however), difficult and joyful moments (at the departments and outside). From them I got help, courage, advise and support.

I am grateful to the members of the committee, from whom I always had a great help: Prof. Eva Andrei, Prof. Paul Leath and Prof. Claude Lovelace. I own gratitude to many professors of the Physics and Astronomy Department, in particular to the three graduate directors and the professors of the Condensed Matter group, whose advise and suggestions have always been present. I enjoyed teaching with Prof. John Hughes, Prof. Gordon Thomson and Gabriel Alba. Special thanks to Kathy Di Meo, the first person I met in the Rutgers Physics Department, and to Francesca De Lucia.

I own the decision to pursue studies in physics to Alberto Parola "un fuoriclasse". He is my first teacher and a friend.

To my parents, who always supported me in any decision, all my gratitude. I thank

you the constant encouragement from all my family (in Italy and USA). Véronique, to her my love.

Finally I thank you all the friends and people that I had the luck to meet in Rutgers all over these years. Many of them have been like a family for me, that leaving Rutgers is like leaving home a second time.

## Dedication

To my grand-parents, Ai miei nonni, A mis abuelos.

# Table of Contents

<b>Abstract</b> . . . . .	ii
<b>Acknowledgements</b> . . . . .	iii
<b>Dedication</b> . . . . .	v
<b>Introduction</b> . . . . .	1
<b>1. High Temperature Superconductors</b> . . . . .	4
1.1. Structure and Phase Diagram . . . . .	4
1.1.1. $\text{La}_{2-x}\text{Sr}_x\text{CuO}_4$ . . . . .	5
1.1.2. Phase Diagram . . . . .	7
1.2. Multi-band Hamiltonian . . . . .	10
1.3. The Hubbard Model . . . . .	12
1.3.1. Weak Interaction Limit $U \ll t$ . . . . .	14
1.3.2. Hartree-Fock Approximation . . . . .	15
1.4. Heisenberg Hamiltonian . . . . .	21
1.4.1. AF Groundstate . . . . .	24
1.5. Is the Hubbard Model able to explain the key mechanisms of cuprates? . . . . .	30
<b>2. Non-Fermi-Liquid Normal State</b> . . . . .	32
2.1. Non Fermi-Liquid normal state region . . . . .	32
2.2. The Landau Fermi Liquid Theory . . . . .	34
2.2.1. The Non Interacting Fermion Gas . . . . .	34
2.2.2. The Quasiparticle Concept . . . . .	35
The Landau Fermi Liquid . . . . .	37
2.3. The Transport Boltzmann Equation . . . . .	38

2.3.1.	Frequency Dependent External Force . . . . .	41
2.4.	General Solution to the $N$ -Patch Model . . . . .	42
2.4.1.	The linearized Boltzmann Equation in the $N$ -Patch Model . . . . .	42
2.4.2.	$N$ -Patch solution to the BE . . . . .	43
2.4.3.	Invertibility and Inversion of the $\bar{\Gamma}$ Matrix . . . . .	44
2.4.4.	Transport Properties . . . . .	45
	Magnetic Field Dependence . . . . .	45
	Conductivity . . . . .	46
2.5.	The 5-Patch Model . . . . .	47
2.6.	Results . . . . .	51
2.6.1.	Forward scattering: a second order effect . . . . .	51
2.6.2.	Data Fitting Troubles with gaussian patches . . . . .	52
2.7.	The "panettone"-patch model . . . . .	56
<b>3.</b>	<b>Cellular Dynamical Mean Field Theory . . . . .</b>	<b>64</b>
3.1.	Dynamical Mean Field Theory DMFT . . . . .	65
3.2.	The Cluster Dynamical Mean Field Theory CDMFT . . . . .	69
3.3.	Exact Diagonalization Method . . . . .	72
3.3.1.	Truncation of the problem size . . . . .	72
3.3.2.	The ED-loop for CDMFT . . . . .	74
<b>4.</b>	<b>Implementation of CDMFT . . . . .</b>	<b>77</b>
4.1.	Benchmark on the 1D Hubbard Model . . . . .	77
4.1.1.	Improvement of CDMFT on DMFT . . . . .	77
4.1.2.	Implementation of CDMFT . . . . .	80
	Reducing the parametrization: double-bath-degeneracy in one di-	
	mension. . . . .	81
	Regular implementation of CDMFT . . . . .	81
	Fast implementation of CDMFT . . . . .	82
	A practical example of fast implementation . . . . .	84

4.1.3. Results with increasing bath-size . . . . .	88
4.2. Comparison between QMC and CDMFT . . . . .	91
4.3. Evaluation of Lattice Quantities . . . . .	94
4.3.1. Reconstruction of lattice-quantities and physical observables . . . . .	97
4.3.2. Lattice-quantities and local physics . . . . .	101
4.4. Cluster-size and cluster-lattice partitions dependencies . . . . .	103
4.5. Reduced bath-parametrization for the Exact Diagonalization procedure . . . . .	112
<b>5. Results in 2D . . . . .</b>	<b>118</b>
5.1. Strong Coupling $U/t=16$ . . . . .	118
5.1.1. Cluster quantities . . . . .	120
5.2. $\Sigma$ -scheme periodization: a conservative FL perspective . . . . .	125
5.3. Dependence of the Results on the periodizing-scheme . . . . .	130
5.4. The M-scheme perspective: an anomalous FL . . . . .	138
5.4.1. FS topology transition and Pseudogap regime . . . . .	139
<b>6. Superconductive Phase . . . . .</b>	<b>153</b>
6.1. CDMFT equations for a d-wave superconducting state . . . . .	154
6.2. An anomalous superconductive state . . . . .	155
6.2.1. Discrepancy between order parameter and anomalous gap . . . . .	157
6.2.2. Disappearance of the quasiparticle spectral weight at the MT . . . . .	158
6.2.3. Nature of the pairing . . . . .	159
6.2.4. The superconducting phase as "cure" for a ill normal state . . . . .	161
6.2.5. $k$ -dependent quantities . . . . .	163
<b>Conclusions . . . . .</b>	<b>170</b>
<b>Appendix A. The <math>tJ</math> Model . . . . .</b>	<b>173</b>
<b>Appendix B. The Lanczos Algorithm . . . . .</b>	<b>176</b>
B.1. The Lanczos idea . . . . .	176

B.2. The Lanczos algorithm in floating point arithmetic . . . . .	179
B.2.1. Selective reorthogonalization . . . . .	180
<b>Vita</b> . . . . .	185

## Introduction

In 1986 J. G. Bednorz e K. A. Muller announced the discovery of a superconductor material with the record high critical temperature of 30  $K$ . This was most unexpected, as this superconductive material was a cuprate ceramic, which is known to be a good insulator at room temperature. In the light of the well tested classical theory of superconductivity, the Bardeen-Cooper-Schrifferer (BCS) [7], it was not possible to explain the origin of the superconductivity in these materials. Even more mysterious was the fact that their critical temperature was an order of magnitude higher than that of the classical BCS superconductors.

These extraordinary results were successively re-confirmed by other experimental groups (Takagi et alteri [6]). Since then many high- $T_C$  superconductors have been discovered. (So far, the record critical temperature is from mercury-thallium-barium-calcium-copper-oxygen that becomes superconducting at 138 K [-135 C or -211 F]). Since 77 K is the boiling point of nitrogen, new technological applications are expected, such as superconducting quantum interference devices (SQUID), Josephson's effect based electronics and magnetic levitation of super-fast trains. This exciting technological scenario however looks still far in the future. Up to now the search for new materials has been an empirical procedure, since the key-mechanism the of high- $T_c$  superconductivity remains theoretically obscure. Many theories have been proposed, but none of them have given a definitive answer. On one hand, because of the complexity of the cuprates materials, it is very difficult to interpret the experimental results. Antiferromagnetism, disorder, phonons and strong anisotropy conspire together to hide the key ingredients. On the other hand, the theoretical tools to face the longstanding problem of strongly correlated systems, where standard perturbation theory cannot be applied, are still scarcely available. The theoretical model capable of explaining high- $T_c$  superconductivity may have been already identified, but we are not able to extract its

properties even approximately.

In this thesis we face the problem of high- $T_C$  superconducting materials from a theoretical point of view by studying the two-dimensional Hubbard Model on a simple square lattice. This model, proposed by J. Hubbard in 1964 [38], is universally considered the simplest minimal description of cuprate materials. In spite of this model's simplicity however, its properties have been well determined only in the one-dimensional limit, where an exact Bethe Ansatz (BA) solution exists (1968 [50]), and more recently in the infinite-dimensional limit (1989 [53]), where the exact solution has been determined by Dynamical Mean Field Theory (DMFT). However, no general consensus on its properties has been reached for finite dimensions (the realm of real materials), so it is not clear whether this model embodies the physics necessary to understand the high- $T_C$  superconducting mechanism.

In the first chapter of this thesis we introduce the high- $T_C$  superconducting materials and the two-dimensional Hubbard Model and review some of the results which have been obtained in the past using standard techniques. We show that the Hubbard Model is able to describe some of the physical properties of the cuprates materials, especially in the insulating state, and answers the fundamental question of the origin of the insulating (Mott) gap in half-filled-band systems. This is not however sufficient to understand the metallic and superconductive phases. To approach this problem we start from the infinite-dimensional-limit viewpoint and adopt an extension of the DMFT, the Cellular Dynamical Mean Field Theory (CDMFT, [44]), as an approximate tool to approach finite-dimensional systems. To support this approach, in chapter 2, we present a Boltzmann-Fermi-liquid study of the transport properties of the cuprate materials in the normal state. In this framework, we emphasize the importance of considering momentum-dependent scattering to describe the physics of these systems. DMFT, by construction, is not able to describe momentum-dependent (spatial-correlated) properties. It is therefore at its foundations a poor approximation for understanding cuprates. CDMFT, instead, is designed to introduce short-range spatial correlations into the system, allowing for the description of momentum-dependent quantities. A presentation of the building of CDMFT from DMFT is given in chapter 3. In this work the Lanczos

algorithm [48] is adopted to solve the associated quantum impurity problem (see also APPENDIX B). In chapter 4 we test CDMFT against the one dimensional exact Bethe-Ansatz solution, the worst case scenario for a mean field theory, and with previous Quantum Monte Carlo results. These tests provide a benchmark for the method. We then present details on the implementation of CDMFT and the schemes adopted to extract physical quantities in real and momentum space. In chapter 5 we apply CDMFT to the normal state of the two-dimensional Hubbard model, with attention to experimental results on cuprate materials and we study hole-doped as well as electron-doped cases. A complete description of the density-driven Mott metal-insulator transition is presented for the two-dimensional Hubbard Model. The creation of an anomalous Fermi-liquid state (pseudogap phase) is presented as a reliable possibility in the region which precludes a Mott transition. Finally in chapter 6 the superconducting state is studied. We find that the Hubbard Model in two dimensions and zero temperature supports a d-wave superconducting state, which clearly departs from the standard BCS theory. Its properties are described in light of the proximity to a parent antiferromagnetic Mott-insulator. A connection between the anomalous superconducting properties and the anomalies of the normal state are inferred.

## Chapter 1

### High Temperature Superconductors

#### 1.1 Structure and Phase Diagram

A characteristic feature of cuprate superconductors is a multilayered structure of  $\text{CuO}_2$  planes, separated by layers of other atoms (La, O, Ba,...). There are strong hints that the high- $T_c$  superconductivity is a two-dimensional phenomenon taking place within the  $\text{CuO}_2$  planes, while the intermediate layers are simply reservoirs for charges. Another fundamental property common to all these materials is an antiferromagnetic insulating state. The insulator is of the *Mott* kind, with the electronic band half-filled. Upon doping, the long-range antiferromagnetic order is destroyed, and the system becomes a paramagnetic metal which superconducts at temperatures below a critical value. Short-range antiferromagnetic correlations may, however, remain relevant and play a fundamental role in determining the superconductive mechanism.

Many high- $T_c$  superconducting materials have been synthesized: it is sufficient to vary the number of layers in the unit cell or the kind of intra-layer atoms to obtain an enormous variety. In the following table we report some of them along with their critical temperatures. For comparison, we also report the critical temperatures of the "classical" superconductors Nb, Pb and  $\text{Nb}_3\text{Ge}$ , which had the highest  $T_c$  before 1986.

Material	$T_c$ (K)
$HgBa_2Ca_2Cu_3O_{8+\delta}$	133
$Tl_2Ca_2Ba_2Cu_3O_{10}$	125
$YBa_2Cu_3O_7$	92
$Bi_2Sr_2CaCu_2O_8$	89
$La_{1.85}Sr_{0.15}CuO_4$	39
$Nd_{1.85}Ce_{0.15}CuO_4$	24
$Nb_3Ge$	23.2
Nb	9.25
Pb	7.20

Let's analyze in detail the structure of the most studied high- $T_c$  superconductor, the  $La_{2-x}Sr_xCuO_4$ , as shown in Fig 1.1 below.

### 1.1.1 $La_{2-x}Sr_xCuO_4$

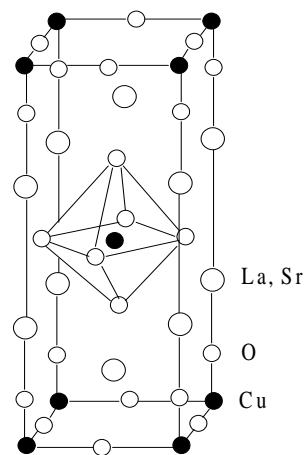


Figure 1.1: Structure of  $La_{2-x}Sr_xCuO_4$

This material, one of the first discovered, gives a good example of the properties common to all H-T<sub>c</sub> superconductors. Let us consider first the insulating state. La<sub>2</sub>CuO<sub>4</sub> has a structure body-centered-tetragonal (bct), well known from studies on K<sub>2</sub>NiF<sub>4</sub>, which is described in Fig.1.1. This structure can be seen as a pile of CuO<sub>2</sub> planes 6.6 Å apart and separated by two planes of LaO, which play the role of charge reservoirs for the CuO<sub>2</sub> planes, once doping has been added into the system. The Cu atoms in the CuO<sub>2</sub> planes are each of them surrounded by four coplanar O atoms, plus two other O atoms, denoted O<sub>z</sub>, in the upward and downward direction perpendicular to the CuO<sub>2</sub> planes. Each Cu atom is thus surrounded by an octahedron of oxygens; however the Cu-O<sub>z</sub> distance is roughly 2.4 Å, considerably greater than the distance Cu-O in the two-dimensional conducting planes, which is roughly 1.9 Å. The latter therefore are the dominant bonds, although the importance of the O<sub>z</sub> atoms in the superconductive mechanism is strongly debated. The electronic configurations are Cu:[Ar](3d)<sup>10</sup>(4s), O:[He](2s)<sup>2</sup>, La:[Xe](5d)(6s)<sup>2</sup> e Sr:[Kr](5s)<sup>2</sup>. To first approximation, it is possible to schematize the electronic structure with the oxygen in a O<sup>2-</sup> state, which completes its p shell, and the lanthanum in a La<sup>3+</sup> state, which has the more stable electronic configuration of Xe. In order to maintain electrical neutrality, the copper atoms must be in the Cu<sup>2+</sup> state, having lost an electron from the 4s level and one from the 3d level, where a hole is formed with a total spin of  $\frac{1}{2}$ . Upon doping, by substituting some percentage of La<sup>3+</sup> with Sr<sup>2+</sup>, fewer electrons remain for the oxygens in the CuO<sub>2</sub> planes. Therefore, in these planes more holes are formed. Either the oxygen completes again the p shell, getting a further electron from a Cu atom, where a hole is formed, or it remains in the state O<sup>-</sup>. The hole in this case localizes on the oxygen. We will see that the latter is the situation energetically favored. If the hole were localized on the Cu atom it would experience a strong Coulomb repulsion from the hole already present. Since the conduction band in these materials is very narrow, the effective mass of the carriers is very large, and thus their mobility greatly reduced and interactions between them are thereby amplified. The strong on-site coulomb repulsion at the Cu atoms is also the origin of the insulating state even when the electronic band is half-filled. The holes, which localize at the Cu atom in the insulating state, have the tendency to

freeze at their own site and thus do not find other hole-free Cu-sites to occupy. This is a classical case in which the free electron approximation fails completely. It is indeed the strong interaction between electrons which determines the macroscopic properties of the matter. With only a small percentage of doping ( $x \geq 0.04$ ), the system becomes metallic. The sign of the Hall coefficient shows that the electronic carriers are holes, as expected.

### 1.1.2 Phase Diagram

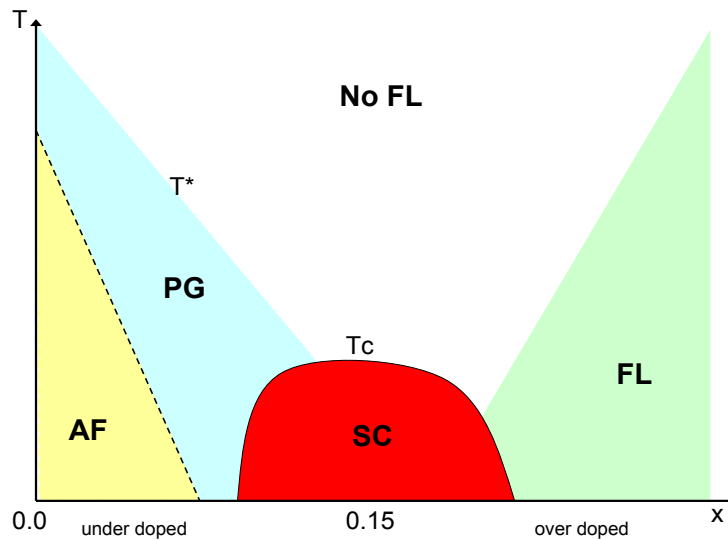


Figure 1.2: Schematic phase diagram of cuprate superconductors. The phases: Antiferromagnetic (AF), pseudogap (PG), superconductive (SC), Fermi-Liquid (FL) and Non-Fermi-Liquid (No FL).

The generic phase diagram of the cuprates shows a wide variety of behavior at different temperatures and levels of doping (Fig. 1.2). All the cuprate compounds investigated so far show similar characteristic changes in their thermodynamic and transport properties as the temperature or the number of holes per unit cell of  $\text{CuO}_2$  is varied. The number of holes per  $\text{CuO}_2$  unit,  $x$ , is a convenient parameter that can be used to compare the different cuprates. The physical properties of the cuprates change abruptly at the superconducting transition (and also at the antiferromagnetic transition). In the other regions of the phase diagram, however, the properties change

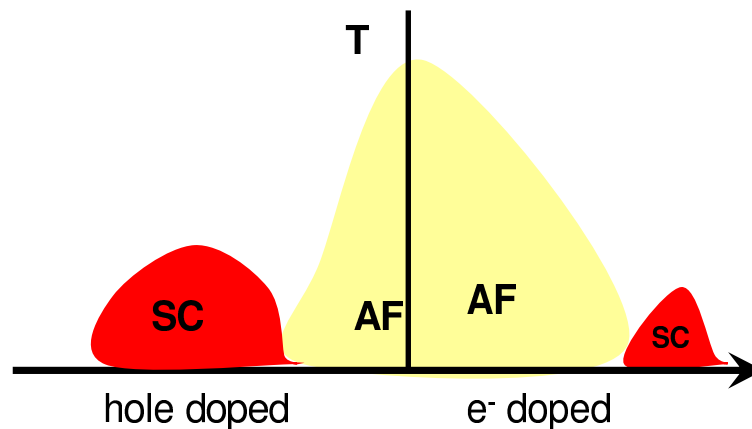


Figure 1.3: Schematic phase diagram of the hole-electron-doping asymmetry in cuprate superconductor materials. In the electron doped case (right hand side), the AF region spans a wider region of doping and the SC phase is strongly reduced with a much lower critical temperature.

gradually and there is a "cross-over" rather than a well defined phase transition. Understanding the phase diagram in Fig. 1.2 is tantamount to understanding the cuprates and their puzzling behaviors, including high-temperature superconductivity. We are interested in the thermodynamic, magnetic and transport properties of these materials, but it is a challenge to develop a microscopic theory that predicts all of these properties. The antiferromagnetic region (AF) is the best understood region in the phase diagram. At zero doping the cuprates are all insulators, that, below a few hundred Kelvin, are also antiferromagnets (i.e. the electron spins on neighbouring copper ions point in opposite directions). However, when the doping  $x$  is increased above a critical value ( about 5%, although this varies from compound to compound), the antiferromagnetic state disappears and we enter the so-called *pseudogap* (PG), or underdoped region, which will be discussed in chapter 5. This region is called "underdoped" because the level of doping is less than that which maximizes the superconducting transition temperature. Some of the most unusual behavior observed in the cuprates occurs in this region. The *Fermi-liquid* (FL) region of the phase diagram (at high doping) is also well understood. One of the central concepts in condensed-matter physics, introduced by Lev Landau, is

the "quasiparticle" concept. In a so-called Landau-Fermi liquid the properties of single free electrons are "renormalized" by interactions with other electrons to form "quasiparticles". The properties of the material can then be understood in terms of the weak residual interactions between the quasiparticles and their excitations. A key feature of the quasiparticle concept is that low-energy single-particle excitations have very narrow line-widths:  $\Delta\omega \simeq \omega^2$  where  $\omega$  is the energy of the excitation. When the quasiparticle approach is valid, there is a well defined boundary between particles and holes in both energy and momentum space at zero temperature. This boundary occurs at the Fermi energy and defines the "Fermi surface" in momentum space. However, the Landau quasiparticle model can only explain part of the phase diagram of the cuprates. We shall return on the concept of Fermi-liquid in the next chapter where we will attempt to approach the normal state properties of H- $T_C$  superconductors from a phenomenological point of view. We will consider the part of the phase diagram between the underdoped and Fermi-liquid regions, and above the area with the highest superconducting transition temperatures, which is called the *non-Fermi-liquid region*(No FL). The thermodynamic properties in this region are un-exceptional and, within experimental uncertainties, are similar to the behavior of a Fermi liquid. However, this region is characterized by simple but unusual power laws in all of its transport properties as a function of temperature. These transport properties include resistivity, optical conductivity, electronic Raman-scattering intensity, thermal conductivity, various nuclear relaxation rates, Hall conductivity and magnetoresistance. Because of these unusual transport properties this part of the phase diagram is called No FL region.

Another important property of these materials is the strong asymmetry in the phase diagram for hole-doped and electron-doped systems (Fig. 1.3). Compared with the hole-doped case, the electron-doped phase diagram displays a more stable AF state which extends to a wider region of doping (up to 15%) and a reduced SC state with a much lower critical temperature. We will investigate this asymmetry in the normal state (chapter 5), enlightening the physical mechanism underlying its formation, in conjunction to the proximity to the Mott metal-insulator transition and the set up of a d-wave superconductive state (chapter 6).

## 1.2 Multi-band Hamiltonian

In order to find a Hamiltonian that is able to describe the complex structure of high- $T_c$  cuprate materials, it is unavoidable that we make some simplifications. First we consider only the electrons in the two-dimensional  $\text{CuO}_2$  planes where the Cu-O bond is stronger so that a conduction band is formed. By ignoring the interaction between planes we neglect some effects that are present in real systems, such as the existence of a non-zero Néel critical temperature for the AF state, which quantum fluctuations would reduce to zero in a pure two-dimensional system. Nevertheless, we hope to be able to re-inject this feature in the system *a posteriori*, once the physics that rules the  $\text{CuO}_2$  two-dimensional electronic has been fully understood. However, in spite of this first necessary approximation the problem still remains extremely complex. There are nine electrons in the five  $d$  orbitals of the  $\text{Cu}^{2+}$  ions, while three  $p$  orbitals of the  $\text{O}^{2-}$  are occupied. So, in order to have a model from which we can extract important results it is necessary to introduce further simplifications. In the cuprates, every Cu atom is surrounded by oxygen ions: for example in the  $\text{La}_{2-x}\text{Sr}_x\text{CuO}_4$  there is a stretched octahedron around every  $\text{Cu}^{2+}$ . This structure breaks the rotational degeneracy in the  $d$  orbitals of an isolated copper atom: the  $d$  orbitals of the Cu and  $p$  orbitals of the O hybridize and split into separate levels (Fig. 1.4).

The state with the highest energy, where a hole remains, is of the  $d_{x^2-y^2}$  symmetry, hence a spin  $\frac{1}{2}$  localizes here. So, in the insulating state, there is a hole on each Cu ion of the  $\text{CuO}_2$  planes, and the system is well described by a model of localized spins with an AF groundstate. The orbitals at lower energy are all occupied and, to first approximation, can be disregarded in the model. But once doping is introduced into the system, electrons are removed from the  $\text{CuO}_2$  planes which is equivalent to adding holes in more energy levels of the scheme of Fig. 1.4. Where will the holes be added? A first guess might be to place another hole in the  $d_{x^2-y^2}$  level, but we must take into consideration the strong Coulomb repulsion between holes in the same orbital. So, we introduce a *multi-band* Hamiltonian in a hole notation, with the vacuum state defined in such a way that all the orbitals in Fig. 1.4 are electron-occupied.

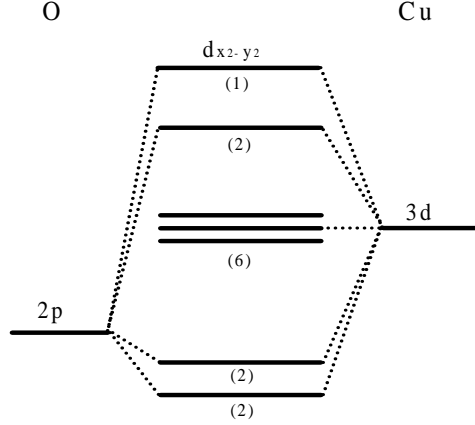


Figure 1.4: Hybridization of the  $Cu^{2+}$  and  $O^{2-}$  orbitals

$$\begin{aligned}
 H = & -t_{pd} \sum_{\langle ij \rangle} p_j^\dagger d_i + h.c. - t_{pp} \sum_{\langle jj' \rangle} p_j^\dagger p_{j'} + \varepsilon_d \sum_i n_i^d + \varepsilon_p \sum_j n_j^p + \\
 & + U_d \sum_i n_{i\uparrow}^d n_{i\downarrow}^d + U_p \sum_j n_{j\uparrow}^p n_{j\downarrow}^p + U_{dp} \sum_{\langle ij \rangle} n_i^d n_j^p
 \end{aligned}$$

where  $p_j$  is the fermionic operator which destroys a hole localized on the O of site  $j$ ,  $d_i$  is the fermionic operator which destroys the hole on the Cu of site  $i$ ,  $\langle ij \rangle$  refers to the nearest neighbor ions O in  $j$  and Cu in  $i$ . The parameter  $t_{pd}$  is the overlapping integral between the O and the Cu atoms. For completeness, we have also introduced the term  $t_{pp}$  for hopping between neighboring oxygens.  $U_d$  and  $U_p$  are positive constants which represent the Coulomb repulsion between two holes on the same orbital  $p$  or  $d$ .  $U_{pd}$  has a similar meaning for two holes occupying adjacent copper and oxygen ions. Generally distances longer than nearest neighbors should also be taken into account, but we assume here that the screening effect of the electrons cuts down the Coulomb repulsion beyond near neighbors. Finally, the  $\varepsilon_d$  and  $\varepsilon_p$  represent the different hole-occupation

energies of the orbitals O and Cu respectively. In the insulating half-filled-band case, there is a hole on each Cu ion which is energetically favored since  $\varepsilon_p - \varepsilon_d = \Delta > 0$ . When another hole is added to the unit cell, with  $U_d > \Delta$ , it prefers to occupy an oxygen orbital, because this is again energetically favored. This is in agreement with electron-energy-loss-spectroscopy (EELS) experiments [29]. Theoretical band structure calculations [39] have been used to fix the universally recognized numerical values of the parameters in  $H$ , as shown in the following table:

$U_d$	$U_p$	$U_{pd}$	$\varepsilon_p - \varepsilon_d$	$t_{pd}$	$t_{pp}$
10.5	4	1.2	3.6	1.3	0.65

Parameters of the multi-band Hamiltonian in eV

These data are consistent with the hypothesis presented above on the structure of the cuprate superconductors.

### 1.3 The Hubbard Model

The multi-band Hamiltonian presented in the previous section, though a plausible first-order-approximate description for cuprates, is still too complicated to perform calculations. We are therefore forced to introduce an even simpler Hamiltonian, which nevertheless is still able to describe the low energy properties of the system. Since the early days of H- $T_c$  superconductivity a simple model yet useful to describe the properties of the cuprates is the Hubbard Model, proposed by Hubbard in 1963 [38] to study the dynamics of the electrons in the transition metals. It is defined by this Hamiltonian:

$$H = -t \sum_{\langle ij \rangle, \sigma} (c_{i\sigma}^+ c_{j\sigma} + h.c.) + U \sum_i n_{i\uparrow} n_{i\downarrow}$$

where the fermionic operator  $c_{i\sigma}^+$  creates an electron with spin  $\sigma$  on site  $i$  of a square lattice,  $U$  is the on-site Coulomb repulsion, and  $t$  is the hopping amplitude. Cuprate

superconductors are better described by a structure with at least three main bands, as explained in the previous section, but the Hubbard model tries to simulate the presence of the gap  $\Delta = \varepsilon_p - \varepsilon_d$  through an effective value of the Coulomb repulsion  $U$ . In this way only two bands are involved, with the oxygen band being at lower energy (as schematically shown in the bottom panel of Fig. 1.5). This Hamiltonian however

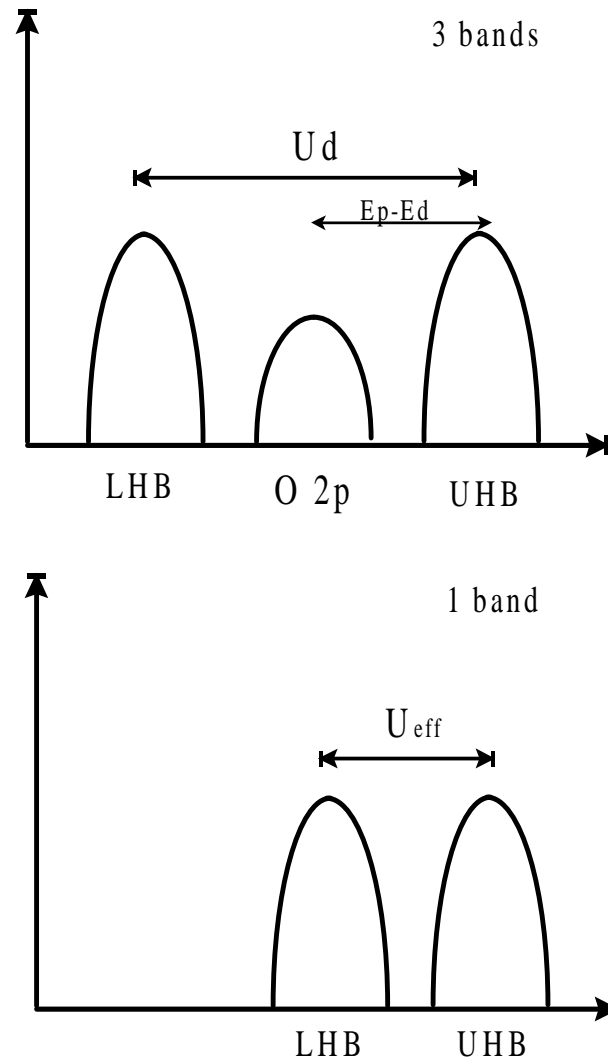


Figure 1.5: Effective band structure of the  $CuO_2$  planes.

does not consider the presence of the O, and the Coulomb interactions are reduced to on-site interactions only. There is not in fact a clear justifications *a priori* for the

choice of this model. However an *a posteriori* justification is that many of its properties qualitatively describe the cuprate superconductors in the normal state. Unfortunately there is not conclusive evidence concerning the superconductivity. This may be due to the limitations of the model, which misses some fundamental ingredients, or a failure of the techniques used to solve it. As in many cases when a theoretical model tries to explain a more complex reality, its introduction can be justified *a posteriori* only after its properties are completely understood.

### 1.3.1 Weak Interaction Limit $U \ll t$

To gain some understanding of the properties of the Hubbard Model we study the weak coupling limit  $U \ll t$ . Let us first consider the trivial  $U = 0$  case, which describes a simple non-interacting Fermi gas. Its ground state is given by:

$$|\Phi_0\rangle = \prod_{k < k_f, \sigma} c_{\mathbf{k}, \sigma}^+ |0\rangle$$

where  $|0\rangle$  is the vacuum state of the fermionic destruction operator  $c_{\mathbf{k}, \sigma}$ . The creation operator  $c_{\mathbf{k}, \sigma}^+$  is the Fourier transform of the site creation operator, namely

$$c_{\mathbf{k}, \sigma}^+ = \frac{1}{\sqrt{N}} \sum_i e^{i\mathbf{k}\mathbf{R}_i} c_{i, \sigma}^+ \quad (1.1)$$

where the quasimomentum  $k$  is given by periodic boundary conditions  $\mathbf{k} = \frac{2\pi}{\sqrt{Na}}(n_x n_y)$ ,  $N$  is the total number of sites in the system,  $a$  the lattice constant and  $\frac{\sqrt{N}}{2} + 1 \leq n_{x,y} \leq \frac{\sqrt{N}}{2}$ . We start from the Hamiltonian  $H_o$ :

$$H_o = -t \sum_{\langle ij \rangle, \sigma} (c_{i\sigma}^+ c_{j\sigma} + c_{j\sigma}^+ c_{i\sigma}),$$

which becomes:

$$H_o = -t \sum_{\mathbf{n}, i} \frac{1}{N} \sum_{\mathbf{k}, \mathbf{k}' \sigma} e^{i(\mathbf{k}-\mathbf{k}')\mathbf{R}_i} e^{i\mathbf{k}\mathbf{n}a} c_{\mathbf{k}\sigma}^+ c_{\mathbf{k}'\sigma}^+$$

where the sum  $\langle ij \rangle$  over nearest neighbors has become a sum over  $i$  and  $\mathbf{n}$  with  $\mathbf{R}_j = \mathbf{R}_i + a\mathbf{n}$ , where  $\mathbf{n}$  is the versor indicating the four possible directions in a two-dimensional

square lattice. Thus, we find:

$$H_o = -2t \sum_{\mathbf{k}, \sigma} \varepsilon_{\mathbf{k}} c_{\mathbf{k}\sigma}^{\dagger} c_{\mathbf{k}\sigma}$$

where the dispersion is given by  $\varepsilon_{\mathbf{k}} = -2t (\cos k_x a + \cos k_y a)$ .

The ground state is obtained by filling up the band to the Fermi level. As each single-particle state, labeled by the quasi-momentum vector  $\mathbf{k}$ , is spin-doubly degenerate, the total number of states for a system of  $N$  sites is  $2N$ . If (like in the case of the un-doped cuprates) there are also  $N$  electrons, one for each site, the band is half-filled and the Fermi level is given by:  $\cos(k_x a) + \cos(k_y a) = 0$ , i.e.  $|k_x| + |k_y| = \frac{\pi}{a}$ . According to single-band theory such system is a good metal. We have seen, however, that the un-doped cuprates superconductors materials are instead good insulators. This clearly shows the failure of standard band theory to describe such materials. It is therefore necessary to add an interaction  $U > t$  into the system. However, adding a small perturbation to a non-interacting electron Hamiltonian only re-normalizes the free electron gas, affecting only the energy levels  $\varepsilon_{\mathbf{k}}$  close to the Fermi energy. In order to radically change the physics of the system we must consider an interaction  $U$  strong enough to break the free-electron energy band and produce a new kind of fermionic gas.

### 1.3.2 Hartree-Fock Approximation

Let us now apply to the un-perturbed Hamiltonian  $H_0$  a mean-field Hartree-Fock interaction term  $H_1$ :  $H_{HF} = H_0 + H_1$  with

$$H_1 = U \sum_i (\langle n_{i\uparrow} \rangle n_{i\downarrow} + n_{i\uparrow} \langle n_{i\downarrow} \rangle)$$

where  $\langle n_{i\uparrow} \rangle$  is the ground-state expectation value of the density operator  $n_{i\uparrow}$ , which has to be determined self-consistently from  $H_{HF}$ . We can in fact write  $n_{i\sigma} = \langle n_{i\sigma} \rangle + \Theta$  to good approximation if  $\langle \Theta^2 \rangle \ll \langle n_{i\sigma} \rangle^2$ . Since  $(n_{i\uparrow} - \langle n_{i\uparrow} \rangle)(n_{i\downarrow} - \langle n_{i\downarrow} \rangle) \sim \Theta^2$ , we have to first order in perturbation theory:

$$n_{i\uparrow} n_{i\downarrow} \cong \langle n_{i\uparrow} \rangle n_{i\downarrow} + n_{i\uparrow} \langle n_{i\downarrow} \rangle - \langle n_{i\uparrow} \rangle \langle n_{i\downarrow} \rangle.$$

In  $H_1$  we have omitted the last term which is a constant. We once again consider the case of the half-filled band ( $\rho=1$ ) materials. For this case we anticipate antiferromagnetic (AF) properties to be relevant. So, to describe them we divide the lattice into two equivalent sub-lattices, each describing the two different spin orientations in a symmetry-broken AF state. In Fig. 1.6a we indicate the AF ground-state, with the

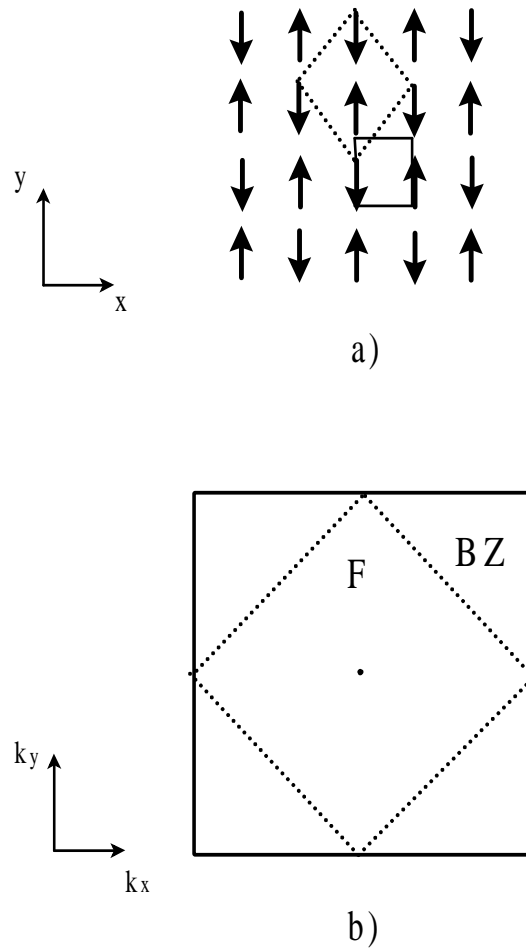


Figure 1.6: Unitary cell and BZ in an AF lattice.

spins polarized along opposite  $z$ -directions on the two different sublattices. In this representation the unit cell (dashed line in *a*), is twice the unit cell of the original lattice.

Hence the Brillouin Zone (BZ) in the reciprocal space  $\mathbf{F}$  (bottom drawing) is half of the original BZ, reflecting the periodicity of the AF state. The unit vectors in the reciprocal lattice change to:

$$\begin{cases} \frac{2\pi}{a}(1, 0) \\ \frac{2\pi}{a}(0, 1) \end{cases} \rightarrow \begin{cases} \frac{\pi}{a}(1, 1) \\ \frac{\pi}{a}(1, -1) \end{cases}$$

If  $\mathbf{R}_j = (ra, sa)$  is the vector localizing site  $j$  in the lattice, we parameterize:

$$\begin{cases} \langle n_{j\uparrow} \rangle = \frac{1}{2} + (-1)^{r+s} m \\ \langle n_{j\downarrow} \rangle = \frac{1}{2} - (-1)^{r+s} m \end{cases} \quad (1.2)$$

where,  $m = \frac{(-1)^{r+s}}{2} (\langle n_{j\uparrow} \rangle - \langle n_{j\downarrow} \rangle)$  is the on-site magnetization to be self-consistently determined. Notice that if  $m = 0$   $\langle n_{j\uparrow} \rangle = \langle n_{j\downarrow} \rangle = \frac{1}{2}$  and the system is paramagnetic. In the opposite limit  $\langle n_j \rangle = \langle n_{j\uparrow} \rangle + \langle n_{j\downarrow} \rangle = \langle n_{j\uparrow} \rangle = 1$  if  $r+s$  is even, and  $\langle n_j \rangle = \langle n_{j\downarrow} \rangle = -1$  if  $r+s$  is odd, and the system is in a perfect AF state. The Hartree-Fock Hamiltonian becomes:

$$H_{HF}^{SF} = -t \sum_{\langle ij, \sigma \rangle} (c_{i\sigma}^+ c_{j\sigma} + h.c.) + \sum_{i, \sigma} \frac{U}{2} (1 - m\sigma e^{i\mathbf{q}\mathbf{R}_i}) c_{i\sigma}^+ c_{i\sigma}$$

where  $\sigma = +(-)1$  for  $\uparrow$  ( $\downarrow$ ) spins, and  $\mathbf{q} = \frac{\pi}{a}(1, 1)$ .  $e^{i\mathbf{q}\mathbf{R}_j} = \pm 1$  according to which of the two sub-lattices  $j$  belongs. We disregard the constant term  $\sum_i \frac{U}{2} n_i = \frac{U}{2} N$ , since the number of particles is conserved, and obtain:

$$H_{HF}^{AF} = \sum_{\mathbf{k}, \sigma} \varepsilon_{\mathbf{k}} c_{\mathbf{k}\sigma}^+ c_{\mathbf{k}\sigma} - mU \sum_{\mathbf{k}\sigma} \sigma c_{\mathbf{k}+\mathbf{q}\sigma}^+ c_{\mathbf{k}\sigma} \quad (1.3)$$

Notice that, owing to the periodicity of the lattice [58]:

$$\varepsilon_{\mathbf{k}+2\mathbf{q}} = \varepsilon_{\mathbf{k}}$$

$$\varepsilon_{\mathbf{k}+\mathbf{q}} = -\varepsilon_{\mathbf{k}}$$

$$c_{\mathbf{k}+2\mathbf{q}} = c_{\mathbf{k}}$$

The Hamiltonian 1.3 can be diagonalized using a Bogoliubov transformation. The time evolution of the electron destruction operators  $c_{\mathbf{k}\uparrow}$  and  $c_{\mathbf{k}\downarrow}$  in Heisenberg notation is given by:

$$i\hbar \dot{c}_{\mathbf{k}\sigma} = [c_{\mathbf{k}\sigma}, H_{HF}]. \quad (1.4)$$

Thus, using eq. 1.3, we have:

$$i\hbar \begin{pmatrix} \dot{c}_{\mathbf{k}\sigma} \\ \dot{c}_{\mathbf{k}+\mathbf{q}\sigma} \end{pmatrix} = \begin{pmatrix} \varepsilon_{\mathbf{k}} & -\sigma\Delta \\ -\sigma\Delta & -\varepsilon_{\mathbf{k}} \end{pmatrix} \begin{pmatrix} c_{\mathbf{k}\sigma} \\ c_{\mathbf{k}+\mathbf{q}\sigma} \end{pmatrix}$$

where  $\Delta = mU$ . For convenience, let  $\mathbf{M}$  be the time-evolution matrix. The transformation  $\mathbf{S}(\sigma, \mathbf{k})$  which diagonalizes  $H_{HF}$  also diagonalizes  $\mathbf{M}$ , so that:

$$\mathbf{S}^{-1}\mathbf{M}\mathbf{S} = \mathbf{D} = \begin{pmatrix} E_{\mathbf{k}}^1 & 0 \\ 0 & E_{\mathbf{k}}^2 \end{pmatrix}.$$

This is the diagonal matrix with the eigenvalues:

$$\begin{pmatrix} \alpha_{\mathbf{k}+\mathbf{q}\sigma} \\ \alpha_{\mathbf{k}\sigma} \end{pmatrix} = \mathbf{S}^{-1} \begin{pmatrix} c_{\mathbf{k}\sigma} \\ c_{\mathbf{k}+\mathbf{q}\sigma} \end{pmatrix}. \quad (1.5)$$

The new quasiparticles thus evolve in time simply as:

$$i\hbar \begin{pmatrix} \dot{\alpha}_{\mathbf{k}+\mathbf{q}\sigma} \\ \dot{\alpha}_{\mathbf{k}\sigma} \end{pmatrix} = \begin{pmatrix} E_{\mathbf{k}}^1 & 0 \\ 0 & E_{\mathbf{k}}^2 \end{pmatrix} \begin{pmatrix} \alpha_{\mathbf{k}\sigma} \\ \alpha_{\mathbf{k}+\mathbf{q}\sigma} \end{pmatrix}.$$

and the Hamiltonian can be written:  $H_{HF} = \sum_{\mathbf{k}\sigma} (E_{\mathbf{k}}^1 \alpha_{\mathbf{k}+\mathbf{q}\sigma}^+ \alpha_{\mathbf{k}+\mathbf{q}\sigma} + E_{\mathbf{k}}^2 \alpha_{\mathbf{k}\sigma}^+ \alpha_{\mathbf{k}\sigma})$  as required by 1.4. The eigenvalues  $E_{\mathbf{k}}^{1(2)}$  are determined by resolving the determinant for  $\mathbf{M}$ . We obtain  $E_{\mathbf{k}}^{1(2)} = \pm E_{\mathbf{k}} = \pm \sqrt{\varepsilon_{\mathbf{k}}^2 + \Delta^2}$ . The transformation  $\mathbf{S}$  has however to be chosen in order to preserve the canonical commutation relations, so that:  $\alpha_{\mathbf{k}\sigma}^+$  and  $\alpha_{\mathbf{k}\sigma}$  are real fermionic-quasiparticle construction and destruction operators. The matrix  $\mathbf{S}$  is the eigenvector matrix of  $\mathbf{M}$ :

$$\begin{pmatrix} u_{\mathbf{k}} & \sigma v_{\mathbf{k}} \\ -\sigma v_{\mathbf{k}} & u_{\mathbf{k}} \end{pmatrix}$$

with the constraint

$$\Delta v_{\mathbf{k}} = (E_{\mathbf{k}} - \varepsilon_{\mathbf{k}})u_{\mathbf{k}}. \quad (1.6)$$

If we assume  $u_{\mathbf{k}}$  and  $v_{\mathbf{k}}$  real, using (1.5) we find [58]:

$$\{c_{\mathbf{k}\sigma}, c_{\mathbf{k}'\sigma}^+\} = (u_{\mathbf{k}}^2 + v_{\mathbf{k}}^2)\delta_{\mathbf{k}\mathbf{k}'} + u_{\mathbf{k}}v_{\mathbf{k}'}\delta_{\mathbf{k}'\mathbf{k}+\mathbf{q}} + v_{\mathbf{k}}u_{\mathbf{k}'}\delta_{\mathbf{k}\mathbf{k}'+\mathbf{q}} \equiv \delta_{\mathbf{k}\mathbf{k}'}$$

which requires that

$$u_{\mathbf{k}}^2 + v_{\mathbf{k}}^2 = 1 \quad (1.7)$$

and that the labels  $\mathbf{k}$  and  $\mathbf{k}' + \mathbf{q}$  are never equal, for all couple  $(\mathbf{k}, \mathbf{k}')$ , in such a way that  $\delta_{\mathbf{k}\mathbf{k}'+\mathbf{q}} = \delta_{\mathbf{k}+\mathbf{q}\mathbf{k}'} = 0$ . This is in fact always true if we constrain the sum of the quasi-momenta  $\mathbf{k}$  to the reduced BZ  $F$  defined by the AF lattice. Moreover, since the Hamiltonian is diagonal with respect to  $\alpha_{\mathbf{k}}^+ \alpha_{\mathbf{k}}$  and  $\alpha_{\mathbf{k}+\mathbf{q}}^+ \alpha_{\mathbf{k}+\mathbf{q}}$ , where  $\mathbf{q}$  is a primitive vector of the reciprocal lattice, all the possible states are covered even if the sum is restricted to  $F$  only. Equations (1.6) and (1.7) determine in this way the transformation  $\mathbf{S}$ . Finally we obtain:

$$H_{HF} = \sum_{\mathbf{k} \in F, \sigma} E_{\mathbf{k}} (\alpha_{\mathbf{k}+\mathbf{q}\sigma}^+ \alpha_{\mathbf{k}+\mathbf{q}\sigma} - \alpha_{\mathbf{k}\sigma}^+ \alpha_{\mathbf{k}\sigma}).$$

In summary, the effect of the interaction  $U$  with respect to the unperturbed case  $U=0$  is to split the band in two sub-bands of energies:  $-E_{\mathbf{k}}$  and  $+E_{\mathbf{k}}$  for  $\mathbf{k} \in F$ , the reduced BZ. Being the latter half of the original BZ, the states in each sub-band are also half of the original unperturbed one. In the half-filled case ( $\rho = 1$ ), the lower band is filled, and the first accessible states are in the upper band, which is separated by a gap of  $2\Delta$ . The Hubbard model proves therefore able to explain the insulating properties of the half-filled state of the cuprate materials. These are the result of the strong on-site interactions between particles of opposite spin, which is described in the model by the  $U$  parameter. Systems with these properties are called *Mott insulators*.

In order to implement self-consistency in the method we have to determine the magnetization  $m$ , requesting that the parameterized form of  $\langle n_{i\sigma} \rangle$  assumed in 1.2 is equal to that derived from the calculated  $H_{HF}$ . Writing for example  $n_{j\uparrow}$  as a function of the quasiparticle operators which diagonalize the Hamiltonian, we find [58]

$$m = \frac{1}{N} \sum_{\mathbf{k} \in F} 2u_{\mathbf{k}}v_{\mathbf{k}}$$

and using the expressions for  $u_{\mathbf{k}}$  and  $v_{\mathbf{k}}$  (1.6) (1.7), we obtain a *gap equation*:

$$\frac{U}{N} \sum_{\mathbf{k} \in F} \frac{1}{E_{\mathbf{k}}} = 1$$

which in the continuous limit becomes

$$\frac{Ua^2}{(2\pi)^2} \int_F \frac{1}{\sqrt{\varepsilon_{\mathbf{k}}^2 + \Delta^2}} d^2k = 1$$

Changing variables  $\frac{a^2 d^2 k}{(2\pi)^2} \rightarrow \rho(\varepsilon) d\varepsilon$ , where  $\rho(\varepsilon)$  is the density of states  $\varepsilon_{\mathbf{k}}$  and taking into account that for  $\mathbf{k} \in F$ ,  $\varepsilon \in (-4t, 0)$ , we find that the gap equation becomes :

$$U \int_0^{4t} \rho(\varepsilon) \frac{1}{\sqrt{\varepsilon^2 + \Delta^2}} d\varepsilon = 1.$$

For the case of weak interaction  $U \ll t$ , we expect a solution close to the unperturbed case: being  $\Delta = mU$ ,  $\Delta \rightarrow 0$ . The integrand is dominated by a term in the neighborhood of  $\varepsilon = 0$ , where it can be shown  $\rho(\varepsilon) \rightarrow \infty$ . Hence expanding the integrand near  $\varepsilon = 0$  [58], we find:

$$\Delta = 16t e^{-2\pi\sqrt{t/U}}.$$

For  $U \rightarrow 0$  therefore the system exponentially converges to the free case, with the gap  $\Delta$  going to zero and the magnetization given by  $m = \Delta/U$ . But this convergence is less quick than in a system with a regular density of states at the Fermi level  $\varepsilon = 0$ , for which we would find an exponential of  $-t/U$  rather than that of  $-\sqrt{t/U}$ . AF instabilities show therefore to be favored in the half-filled Hubbard Model.

In the opposite limit  $U \gg t$  instead we have  $\Delta \gg t$ , which dominates the denominator in the integrand of the gap equation. Thus we find approximately:

$$\frac{U}{\Delta} \int_0^{4t} \rho(\varepsilon) d\varepsilon = 1 \quad \text{and since} \quad \int_{-4t}^{4t} \rho(\varepsilon) d\varepsilon = 1$$

$\Delta = U/2$ . The gap between the lower and upper bands tends to  $U$ , in agreement with the intuitive idea that single particle excitations are due to the double occupation of the same sites. The magnetization becomes  $m = \Delta/U = 1/2$ , which corresponds to a classical AF. This was in fact the landscape on which we have built the Hartree-Fock construction.

Let's now add doping into the system, with  $\delta$  holes for each site. We expect a phase transition into a metallic phase taking place. We can re-write the relations 1.2:

$$\begin{cases} \langle n_{j\uparrow} \rangle = \frac{1-\delta}{2} + (-1)^{r+s} m \\ \langle n_{j\downarrow} \rangle = \frac{1-\delta}{2} - (-1)^{r+s} m \end{cases}$$

and the gap equation becomes

$$\frac{U}{N} \sum_{\mathbf{k} \in K} \frac{1}{E_{\mathbf{k}}} = 1$$

where  $K \subset F$  is the new region of the phase space occupied by electrons that now do not fill completely the lower band. Taking, as above the continuous limit:

$$U \int_{\varpi_0}^{\varepsilon_0} \rho(\varepsilon) \frac{1}{\sqrt{\varepsilon^2 + \Delta^2}} d\varepsilon = 1$$

where  $\varpi_0$  is the bottom energy of the lower Hubbard band and the Fermi energy  $\varepsilon_0$  of the non-interacting system is defined as

$$\int_{\varpi_0}^{\varepsilon_0} \rho(\varepsilon) d\varepsilon = \frac{1 - \delta}{2}.$$

As  $\varepsilon_0 < \varepsilon_F = 0$ , is negative, the integrand is no longer singular in the neighborhood of  $\varepsilon_F = 0$ , and remains finite for  $\Delta = 0$ , where it assumes its maximum value. There exists therefore a finite  $U_c$  which satisfies the gap equation condition and for  $U < U_c$  there is no solution. Hence, for decreasing  $U$ , there is a metal-insulator transition, corresponding to the AF-paramagnet transition.

In conclusion, a mean-field Hartree-Fock approach to the Hubbard model is able to qualitatively describe the behavior of the H- $T_c$  superconductors in their insulating and normal metallic states. This explains a posteriori the introduction of this model, which embodies the essential properties of these materials. Whether the model can explain the rich phase diagram of H- $T_c$  superconductors or can reproduce a H- $T_c$  superconductive mechanism remains an open question.

## 1.4 Heisenberg Hamiltonian

The Hartree-Fock results of the previous section suggest that the ground-state of the Hubbard Model is close to a classical AF state. The on-site magnetization assumes alternatively a value which tends to  $\pm \frac{1}{2}$ , and each electron can be thought to be occupying a single site with a double occupation forbidden. In this section we want to reverse this point of view from the Hartree-Fock treatment starting instead from the strong interacting limit. Let's assume  $U \gg t$ , and let us consider the interaction part of the Hamiltonian as the un-perturbed portion:  $H_0 = U \sum_{\langle ij \rangle} n_{i\uparrow} n_{j\downarrow}$ . The kinetic term  $H_1 = U \sum_{\langle ij \rangle} (c_{j\sigma}^\dagger c_{i\sigma} + h.c.)$ , now becomes the perturbation. Since a doubly occupied site is very expensive in terms of energy (with a cost of order  $U$ ), we constrain the

treatment to the subspace  $\Xi$ , generated by the eigenvectors  $\{\varphi_0\}$  of  $H_0$  corresponding to the eigenvalue  $E = 0$ , where double occupation is forbidden. In the half-filled case, the groundstate of  $H_0$ ,  $|\Phi_0\rangle$  is given by assigning a single electron to each site so that  $H_0|\Phi_0\rangle = 0$  and  $|\Phi_0\rangle \in \Xi$ . Because of the spin degeneracy there are  $2^N$  such states, where  $N$  is the total number of sites in the system. An excited state is created by doubly occupying a site. In this case  $H_0|\Phi_1\rangle = U|\Phi_1\rangle$ , and in general,  $|\Phi_n\rangle$  corresponds to  $n$  doubly occupied sites,  $H_0|\Phi_n\rangle = nU|\Phi_n\rangle$ . The energy-gap between the groundstate and the first excited state is  $U$ , and in the limit  $U \rightarrow \infty$  double occupation is forbidden. We can therefore assume that, for sufficiently  $U$ , confining the system to the subspace  $\Xi$  would be a good approximation. Adding the kinetic perturbation removes the  $2^N$  degeneracy and creates an energy-band that is narrow compared to the energy-scale  $U$  of the charge excitation.

We now apply perturbation theory to find an effective Hamiltonian in the subspace  $\Xi$ . Let's consider  $H = H_0 + \lambda H_1$ , with the small parameter  $\lambda$  introduced for convenience, and  $|\Psi\rangle$  the generic eigenstate of  $H$ . We can write  $|\Psi\rangle = |\Psi_0\rangle + \lambda|\Psi_1\rangle$ , where  $|\Psi_0\rangle \in \Xi$ , assuming without loss of generality that  $|\Psi_1\rangle \perp |\Psi_0\rangle$ . From the eigenvalue equation  $H|\Psi\rangle = E|\Psi\rangle$  we obtain:

$$\begin{cases} H_0|\Psi_0\rangle = 0 & (i) \\ \lambda H_1|\Psi_0\rangle + \lambda H_0|\Psi_1\rangle = \lambda E_1|\Psi_0\rangle & (ii) \\ \lambda^2 H_1|\Psi_1\rangle = \lambda^2 E_2|\Psi_0\rangle & (iii) \end{cases}$$

where we have expanded the eigenvalue in powers of  $\lambda$ ,  $E = E_0 + \lambda E_1 + \lambda^2 E_2$ , where  $E_0 = 0$ . Formula (i) is just the eigenvalue equation of the un-perturbed Hamiltonian. Multiplying both sides of (ii) by  $\langle\Psi_0|$  we obtain  $E_1 = \langle\Psi_0|H_1|\Psi_0\rangle + \langle\Psi_0|H_0|\Psi_1\rangle = 0$ , since the two terms in the second side of the equation are both zero, because  $H_1|\Psi_0\rangle \perp |\Psi_0\rangle$  (its effect is to move an  $e^-$  to the next neighbor site which however is already occupied) and  $H_0|\Psi_0\rangle \in \Xi$  is  $\perp |\Psi_1\rangle$ . Multiplying (iii) by  $\langle\Psi_0|$  we obtain  $E_2 = \langle\Psi_0|H_1|\Psi_1\rangle$ . In order to evaluate  $\langle\Psi_0|H_1|\Psi_1\rangle$ , we multiply (ii) by  $\langle\Psi_0|H_1$  to

obtain  $\langle \Psi_0 | H_1 | \Psi_1 \rangle = -U^{-1} \langle \Psi_0 | H_1^2 | \Psi_0 \rangle$ , so that finally:

$$\langle \Psi_0 | -\frac{1}{U} H_1^2 | \Psi_0 \rangle = E_2.$$

This equation is equivalent to the initial eigenvalue equation to first order in perturbation theory and shows that the first correction to the un-perturbed energy in the subspace  $\Xi$  is  $E_2$ . The effective Hamiltonian is therefore given by:

$$H_{eff} = -\frac{1}{U} H_1^2. \quad (1.8)$$

The appearance of  $H_1^2$  means that forbidding double occupation restricts the system to virtual electron-jumps to neighboring sites. This Hamiltonian can be written in this more representative form:

$$H_1^2 = t^2 \sum_{klj, \sigma\sigma'} c_{k\sigma}^+ c_{l\sigma'} c_{i\sigma}^+ c_{j\sigma}$$

and since the only jumps permitted are virtual, the only non-zero terms in the sum are the ones for which  $k = j$  and  $l = i$ , so that:

$$H_{eff} = -\frac{1}{U} \sum_{kl, \sigma\sigma'} c_{k\sigma}^+ c_{l\sigma'} c_{l\sigma}^+ c_{k\sigma}.$$

We can now use spin-operators, defined as:

$$c_{\sigma}^+ c_{\sigma} \rightarrow \frac{1}{2} + \sigma S^z$$

$$c_{\sigma}^+ c_{-\sigma} \rightarrow S^x + i\sigma S^y$$

where  $\sigma = \pm 1$  for spin  $\uparrow$  or  $\downarrow$ , and satisfying the usual angular momentum commutation relations  $[S^x, S^y] = iS^z$ . If we keep only next-neighbors in the sum:

$$H_{eff} = \frac{4t^2}{U} \sum_{\langle ij \rangle} (\mathbf{S}_i \mathbf{S}_j - \frac{1}{4})$$

The effective Hamiltonian which describes the behavior of the Hubbard Hamiltonian in the limit of strong interaction  $U \rightarrow \infty$  is naturally the Heisenberg Hamiltonian with coupling constant  $J = 4t^2/U > 0$ .

### 1.4.1 AF Groundstate

What can we say about the groundstate? From the Hartree-Fock treatment a natural guess would be to consider a classical AF state where the spins are alternatively  $S^z = \pm \frac{1}{2}$ , parting the lattice into two ferromagnetic sublattices  $A$  and  $B$ :

$$|\Phi_0\rangle = \prod_{i \in A} \prod_{j \in B} |\uparrow\rangle_i |\downarrow\rangle_j.$$

If the spins were classical vectors, the energy of this state would be  $E_0 = -JNg/8$ , where  $g$  is the number of next-neighbors.  $|\Phi_0\rangle$  however is not even an eigenstate of Hamiltonian, as can easily be checked by applying it to  $H_{eff}$  (the kinetic  $S_i^+ S_j^-$  term in fact destroys the perfect AF arrangement in  $|\Phi_0\rangle$ ). However, it is easily verified ([5] pg. 704) that the real value of  $E_0$  in the Heisenberg Hamiltonian with spin  $S$  is bounded as follows:

$$-S(S+1)\frac{g}{2}NJ \leq E_0 \leq -S^2 \frac{g}{2}NJ.$$

Notice that in the classical limit  $S \rightarrow \infty$ , the ratio of the two boundaries tends to 1 and we recover the classical AF solution. In the present case, however, the value of  $S$  is small and a precise determination of  $E_0$  is not possible. For example in the exactly solvable one dimensional case [8],  $E_0 = -2NJ(\ln 2 - 1/4) = -0.886NJ$ , and  $-0.5NJ \geq E_0 \geq -1.5NJ$ : far from a precise estimate of the exact value. Eventually, if we could turn off quantum mechanics we would recover the classical limit. Let's imagine therefore to perform an ideal experiment in which  $S \rightarrow \infty$  keeping  $JS^2$  finite while  $\mathbf{S}/S \rightarrow 1$ . In this way  $1/S$  plays the role of Planck's constant  $\hbar$ . As soon as we allow  $1/S$  to grow from zero, two radical happenings may take place in the system: i) either the AF symmetry survives until a finite value of  $1/S$ , ii) or AF is immediately destroyed. The latter is in fact what happens in the one dimensional case, while it is likely that the first case is applicable in higher dimensions. The correct way to realize such an ideal experiment is to introduce bosonic operators in place of the spins through a Holstein-Primakoff transformation:

$$S^+ = (2S)^{\frac{1}{2}} \sqrt{1 - a^+ a / 2S} a$$

$$S^- = (2S)^{\frac{1}{2}} a^+ \sqrt{1 - a^+ a / 2S}$$

$$S^z = S - a^+ a$$

This transformation is exact except for the fact that the Fock's space of the boson operators has infinite dimension, contrary to the finite dimension of the spin's space. Its advantage is straightforward, the bosonic operators obey to appropriate commutation relations. Straightforward is also the disadvantage: the transformation is not linear and it is necessary to expand in series the square root in every practical calculation. This introduces non-quadratic terms in the boson operators and also non-physical states which do not correspond to any spin state. In order to justify the expansion of the square root the ratio  $a^+ a / 2S$  has to be small in a relevant portion of the Hilbert space. We can then expand in powers of  $1/S$ . If we keep only the leading term we find in fact the classical AF Néel state with alternatively  $\langle S^z \rangle = \pm S$  in the two sublattices  $A$  and  $B$ . The leading term does not have quantum fluctuations. We start to see the quantum effects when we consider the next term in the expansion. The Hamiltonian is in this case quadratic in the boson operators and can be diagonalized with a standard Bogoliubov's transformation. The result contains two normal modes for every quasimomentum  $\mathbf{k}$  in the BZ, which correspond to waves of the vector  $\mathbf{S}$ . These are the so called *spin waves* (SW). The SW spectrum is gapless, as prescribed by Goldstone's theorem. The expectation value of  $S^z$  is given by:

$$S - \langle S^z \rangle = \text{const.} \int_0^\Lambda \frac{k^{d-1}}{k} dk.$$

$\Lambda$  is a micro-wave cut-off, of the order of the inverse lattice constant. In one dimension,  $d = 1$ , the integral is diverging: the deviation of the spin from its maximum value is infinite because of quantum fluctuations. So the  $k \rightarrow 0$  SW destroy the AF long range order, and the groundstate is a non-degenerate singlet. There is no spontaneous symmetry breaking with non-zero order parameter. We can suppose that if already the first order term in the expansion is enough to kill the long range order, terms of

following order will act in the same direction, and the groundstate in one dimension has no AF order. In bigger dimensions the integral is convergent. For the two dimensional case:

$$\langle S^z \rangle = S - 0.197 + o(1/S).$$

At this point we may wonder whether the  $1/S$  series is convergent. It is difficult to answer, but we can start hypothesizing that for  $d \geq 2$  quantum fluctuations are not enough to completely destroy the Néel AF state. It is likely that the  $1/S$  expansion is in fact only asymptotic. We can however consider some numerical results, which show that the AF order is preserved in the groundstate at zero temperature, not only for  $J \rightarrow 0$  but also for finite values of  $J = U/t$ . As an example we report a numerical study [32], Fig. 1.7, made in a square lattice of 16 sites for  $J = U/t = 4$ . Using Lanczos technique, the spin-spin correlation function

$$C(r) = \frac{1}{4} \langle (n_{i\uparrow} - n_{i\downarrow})(n_{i\uparrow} - n_{i\downarrow}) \rangle$$

has been calculated, where the expectation value has been taken on the groundstate of the Hubbard Model (in the notation  $i = (i_x, i_y)$ ). The point labelled A corresponds to the site (2,0) in the lattice while B to the site (2,2). The hints to a AF long range are evident. The SW theory is able to predict characteristic quantities of the system, and their values can be confronted with for example Quantum Monte Carlo (QMC) calculations. Useful quantities are for example the SW speed  $c$ :

$$c = \frac{2S\sqrt{2}ja}{\hbar} Z_c(S)$$

where the re-normalization factor  $Z_c$  is

$$Z_c = 1 + 0.158/2S + O(1/2S)^2,$$

the magnetic susceptibility in the direction perpendicular to the magnetization (in units  $g\mu_B/\hbar = 1$ ):

$$\chi_{\perp} = \frac{\hbar^2}{8Ja^2} Z_{\chi},$$

where the re-normalization factor is  $Z_{\chi} = 1 - 0.552/2S + O(1/2s)^2$ , or the on-site magnetization  $\langle S^z \rangle$  itself. A comparison of the re-normalization constants with QMC

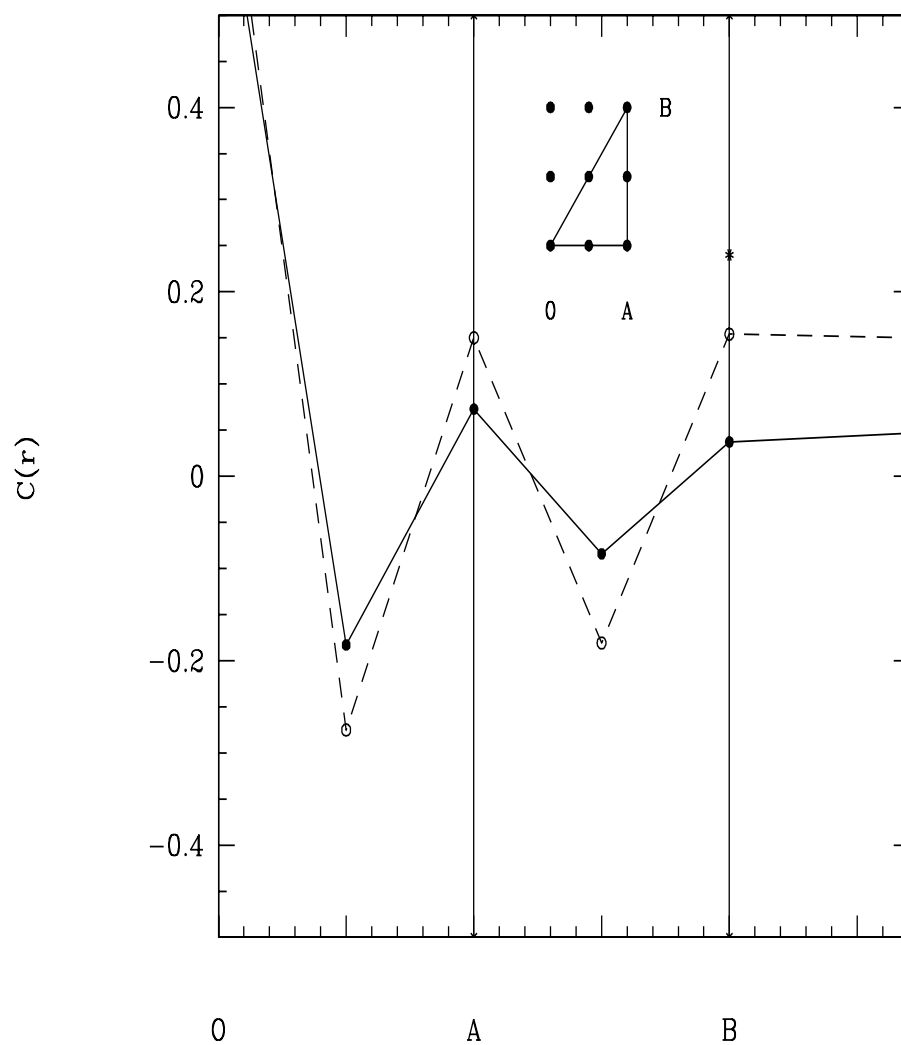


Figure 1.7: Spin-spin correlation function  $C(r)$ . The solid line represents the half-filled system, the dashed line a two-hole-doped system. L

results for  $S = 1/2$  [63]:

	<i>SW</i>	<i>MC</i>
$Z_c =$	1.158	$1.18 \pm 0.02$
$Z_\chi =$	0.448	$0.52 \pm 0.03$
$\langle S^z \rangle =$	0.303	$0.302 \pm 0.007$

appears indeed to be satisfactory and supports the SW theory and its conclusions on a AF groundstate. The SW theory can be also developed for temperatures higher than zero, and its predictions confronted directly with experimental results. We find then the H- $T_C$  superconductors' properties (like  $La_2CuO_4$ ) can be well explained on a Néel's ground state assumption. This gives full legitimation to the model that has been proposed.

As an example we report in Fig. 1.8 the correlation length of the spin-spin correlation function  $\xi$  as a function of the temperature [28], obtained from neutron scattering experiments. If the correlation between the spins take place in the  $CuO_2$  planes, we expect the dynamical form factor  $S(\mathbf{q}_\parallel)$  independent from the momentum exchanged perpendicularly to these planes. The static form factor is therefore given:

$$S(\mathbf{q}_\parallel) = \int_{-\infty}^{+\infty} S(\mathbf{q}_\parallel, \omega) d\omega.$$

The correlation length  $\xi$  is given by fitting  $S(\mathbf{q}_\parallel)$  with a lorentzian form:

$$S(\mathbf{q}_\parallel) \sim \frac{1}{\mathbf{q}_\parallel^2 + (1/\xi)^2}.$$

The dotted line is the SW-theory prediction for  $S = 1/2$ : the agreement is in fact satisfactory.

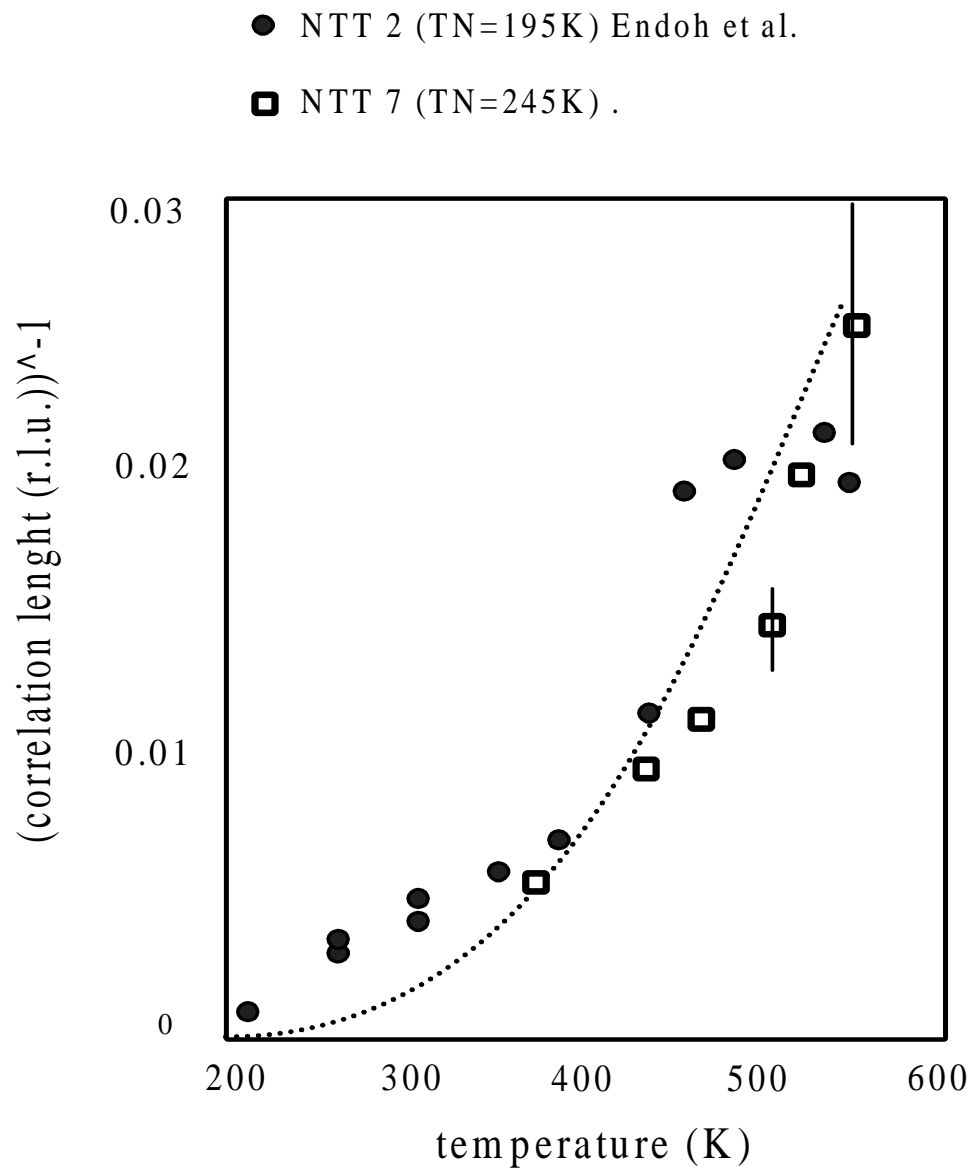


Figure 1.8: Correlation length as a function of temperature

## 1.5 Is the Hubbard Model able to explain the key mechanisms of cuprates?

We end this introductory chapter with a question that is the starting point of the thesis investigation. The answer has been the focus of one of the most enduring open problems in condensed matter physics. This problem is very difficult because we lack tools capable of extracting information from the model. The standard techniques we used in the previous sections (perturbation theory in two opposite limits) were able to provide some first insights in the insulating phase of these materials, and they showed the capacity of the Hubbard Model in explaining at least these properties. However, to answer the question of whether the simple Hubbard Model, derived as extreme simplification of a much more complex reality, is capable to account for the richness of the phase diagram presented in section 1.1 is a more difficult challenge. Many different instabilities appear to compete: Mott metal-insulator transition, antiferromagnetism, pseudogap, anomalous normal state, anomalous superconductivity. Simple perturbation theory does not suffice anymore and non-perturbative approaches are required.

In this project we tackle the problem in the frame-work of Dynamical Mean Field Theory (DMFT) [53]. This is a local non-perturbative method which fully takes into account the quantum-dynamics of the system. DMFT has in recent years proved successful in describing the longstanding problem of the Mott metal-insulator transition of Hubbard-like systems [35]. For construction, however, it is a purely local theory which becomes exact only in the limit of infinite dimension. The thesis develops as follows:

- We will see that in order to describe real finite-size systems, local correlation must be taken into account. This will be presented in chapter 2 with a phenomenological Boltzmann-Laundau-Fermi-Liquid approach to the cuprate properties in the normal No FL state.
- We will then start from a microscopic approach in chapter 3 introducing an extension of DMFT, the Cellular DMFT (CDMFT) [44], capable of taking into account short-range spatial correlations, allowing the study of the finite dimensional Hubbard problem. We will then be able to confront its properties with the real system

ones.

- We will benchmark CDMFT with known results and develop an implementation of the method in chapter 4 using the Lanczos algorithm [48] to solve the associated Anderson Impurity Model. Attention will be given to the right method of extracting the momentum dependent quantities which are the observables measured in real systems.
- In chapter 5 we will apply CDMFT to study the normal state properties of the 2-dimensional Hubbard Model, which promises to be a metallic phase with anomalous properties, as shown in the phase diagram of section 1.1.
- In chapter 6 we study the superconductive phase, connecting its anomalous properties with those of the normal state.

## Chapter 2

### Non-Fermi-Liquid Normal State

#### A Macroscopic approach

#### 2.1 Non Fermi-Liquid normal state region

As sketched in the phase diagram picture of Fig. 1.2, in the underdoped regime a pseudogap appears in the excitation spectrum of the metallic state above the superconductive critical temperature  $T_c$  and below a doping dependent crossover temperature  $T^*$  (PG region in Fig. 1.2). At optimal doping the  $T^*$  almost coincides with  $T_c$ , and the PG region if present is very small. The normal state of cuprates at optimal doping however still strongly deviates from the regular FL behavior observed in simple metals. This can be experimentally measured in the normal state transport properties. Typical examples are:

- At optimal doping, the in-plane DC-resistivity is linear in temperature from  $T_c$  to very high temperatures  $\rho(T) \sim T$ , [33][67]
- The thermoelectric power is linear  $TEP \sim -T$ , [52]
- The cotangent of the Hall angle displays a  $T^\gamma$ -dependence  $\cot\theta_H \sim T^\gamma$ , with  $1.6 < \gamma < 2$  [13], [18], [42] and [4]
- the magnetoresistance has approximately a  $T^\alpha$ -dependence  $MR \sim T^{-\alpha}$ , with  $\alpha \simeq 4$  [4]
- The thermal Hall conductivity has approximately a  $T^\beta$ -dependence  $THC \sim T^{-\beta}$ , with  $\beta \simeq 1.2$  [70]

The non FL anomalies of these materials are also evident in angle resolved photoemission experiments (ARPES) [15],[11]. For example in Fig. 2.1 it is shown the planar

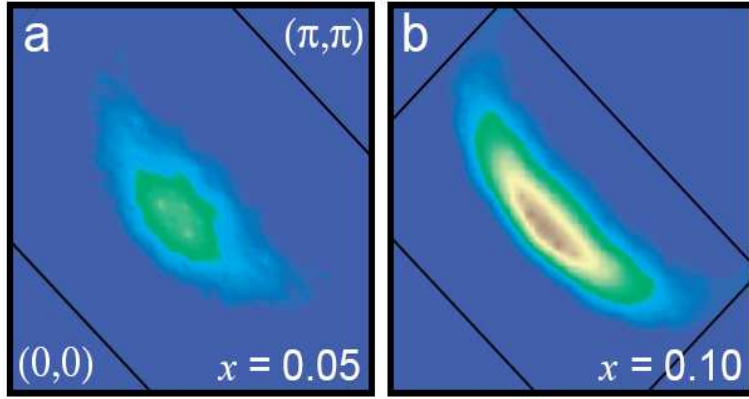


Figure 2.1: Angle Resolved Photo-Emission Spectra  $A(k, \omega = 0^+) = -\frac{1}{\pi} \text{Im}G(k, \omega = 0^+)$  in the first quadrant of the Brillouin Zone for the normal state of a hole-doped cuprate superconductor material close to the Mott metal-insulator transition. Doping is labeled  $x$ . (data taken from [27])

spectral function  $A(k, \omega \rightarrow 0) = -\frac{1}{\pi} \text{Im}G(k, 0^+)$  in a doped cuprate superconductor [27] in the first quadrant of the two dimensional  $(k_x, k_y)$ -plane in the Brillouin zone. The color scale spans from blue to bright red for the highest spectral weight. Close to optimal doping (right-hand panel at 10% doping) we observe that the spectral weight remains in the region close to the point  $(\pi/2, \pi/2)$  of momentum space and almost completely disappears around  $(0, \pi)$   $(\pi, 0)$ , indicating that in the last regions the quasiparticles have disappeared and the Fermi Surface (FS) has broken up. An arc remains instead close to the  $(\pi/2, \pi/2)$  region. If we then look at  $A(k, \omega)$  vs  $\omega$  in the specific direction  $(0, 0) \rightarrow (\pi, \pi)$  of the  $k$ -space (Fig. 5.24), we observe around  $(\pi/2, \pi/2)$  a quasiparticle peak (the line-width is of the order of 0.05-0.1 eV at  $T = 100\text{K}$  [26]) and a wave-vector dispersion of this peak together with the temperature dependence can be followed. On the contrary, in the regions around  $(0, \pi)$   $(\pi, 0)$  the spectral function is very broad (the line-width is of the order of 0.2-0.3 eV at  $T = 100\text{K}$  [26]) and a quasiparticle cannot easily be distinguished. These features are typical of incoherent (localized) states where a very strong scattering mechanism is dominant. The ratio of the Fermi velocities in the two regions is  $v_F(\pi/2, \pi/2)/v_F(0, \pi) \simeq 3$ . The quasiparticle states around the nodal points  $(\pi/2, \pi/2)$  look therefore coherent (delocalized states) and the scattering mechanism is weaker and more conventional.

All these experimental observations motivate the introduction of phenomenological semi-classical methods to describe the non-FL normal state properties of cuprates. In this chapter we will present a Boltzmann theory approach due to Perali, Sindel and Kotliar [57]. In their study they introduced a strongly momentum dependent scattering rate, dividing the FS in *hot* regions (around  $(0, \pi)$   $(\pi, 0)$ ), where the scattering between quasiparticles is strong and the Fermi velocity low, and *cold* regions (around  $(\pi/2, \pi/2)$ ), where the scattering is weak and the Fermi velocity large. Attributing Fermi-like scattering properties to the cold region (a temperature  $T^2$  dependence of the scattering rate) and insulating ones to the hot region ( $T$ -independent scattering rate), we can attempt (relying on few reasonable assumptions) to capture some of the anomalous normal-state transport properties in the framework of a Boltzmann Theory. We start introducing in the next section the general formulation of the semi-classical transport Boltzmann theory for fermion gas. We will then present the *multi-patch model* parametrization of the scattering matrix of the Boltzmann equation introduced in [57], where a practical *2-patch* model was studied in detail. We generalize this method to a *5-patch* model and present possible conjectures that better explain the observed experimental results on transport quantities.

## 2.2 The Landau Fermi Liquid Theory

### 2.2.1 The Non Interacting Fermion Gas

A Fermi gas of noninteracting particles, at equilibrium at some temperature  $T$ , is described by the Fermi distribution function, which expresses the probability to find a particle in a state of energy  $\epsilon = p^2/2m$ :

$$f(\epsilon) = \frac{1}{1 + \exp[(\epsilon - \mu)/kT]} \quad (2.1)$$

where  $\mu$  is the chemical potential and  $k$  is the Boltzmann's constant. For most practical purposes in studying real fermionic systems, it is enough to consider the degenerate case  $T \rightarrow 0$ , for which  $f(\epsilon)$  reduces to the Fermi-Dirac step function, which jumps from 1 to zero when  $\epsilon$  crosses the positive chemical potential  $\mu$ . If the system has  $N$  particles, the ground state is obtained by filling the  $N$  states of less energy, so that in correspondence

with  $\epsilon = \mu$ , a *Fermi Surface* is formed: all the states inside this surface are filled, while those outside are empty. The chemical potential is the energy needed to add a particle to the system:

$$\mu = E_0(N + 1) - E_0(N) = \frac{\partial E_0}{\partial N}, \quad (2.2)$$

where the  $E_0$  is the total energy:

$$E_0 = \sum_{\epsilon < \mu} \epsilon f(\epsilon). \quad (2.3)$$

Excitations in the system are created by "exciting" a certain numbers of particles across the Fermi Surface. In this way we also create an equal number of *holes* in the space enclosed by the Fermi Surface. For a non interacting system, the excitation energy  $E$  of an excited state can be expressed with respect to the energy  $E_0$  of the ground state:

$$E - E_0 = \sum_{\epsilon} \epsilon \delta f(\epsilon), \quad (2.4)$$

where  $\delta f(\epsilon)$  is the departure from equilibrium of the distribution function, and it is +1 if a particle is created in the state  $\epsilon$ , or -1 if instead a particle is destroyed (or equivalently a hole is created).

Sometimes it is more convenient to consider the chemical potential  $\mu$  conserved in the system, instead of the total number of particles  $N$ . In such cases the relevant quantity is the Free Energy:  $F = E - \mu N$  at zero temperature. In this case the Free Energy of an excited system is:

$$F - F_0 = \sum_{\epsilon} (\epsilon - \mu) \delta f(\epsilon). \quad (2.5)$$

### 2.2.2 The Quasiparticle Concept

Let us now consider the case of an interacting Fermi Liquid. We can imagine generating such a system starting from an eigenstate of the ideal noninteracting gas and slowly turning on the interaction between particles. Under such an adiabatic procedure, the ideal eigenstate would progressively transform into certain eigenstate of the real interacting system. *This is an assumption* : there is no a priori justification to why in this way all the eigenstates of the real system can be generated. The case of a superconductor is in fact an evident example for which this assumption is false. We will consider in

the following only Fermi liquids for which this adiabatic procedure is applicable. This kind of Fermi liquids are called *Normal Fermi Liquids*.

To consider what happens in the real system when an excitation is created, let us first add a particle with a certain momentum  $\mathbf{p}$  in the ideal system, and then turn adiabatically on the interaction between the particles, until the real excited state is reached. If the interaction is turned on slowly enough, we can assume the gas remains in equilibrium. But this time, because of interaction, the particle's motion affects also the motion of its neighbor particles, dragging them around. In field theory language we say that the particle is now *dressed*, while in the non-interacting case it was bare. The dressed particle is considered as an independent entity, which is called *quasiparticle*. The excited state created in this way corresponds to the real ground state plus the added quasiparticle. If we wish to create elementary excitations, we can imagine again to start from the ideal non interacting case, moving a particle into a state outside the Fermi surface and leaving a hole in a state inside the Fermi surface, and then turning on the adiabatic procedure until we reach the real state. In this way we establish a one to one correspondence between ideal gas and real liquid.

What are the main limitations to the quasiparticle concept? The limitations concern the finite lifetime of the excited states and the idea of the adiabatic procedure, which requires an infinitely long duration. Due to the particles interaction, the excited states have, in fact, a lifetime that is shorter, the further the excited particles are far from the Fermi Surface. This is due to the uncertainty principle. It is not possible to generate an excited state whose life is longer than the time required to accomplish the adiabatic procedure. On the other hand, one cannot be too fast in turning on the interaction, otherwise the procedure would cease to be adiabatic. Accordingly, the quasiparticle idea is well defined in the limit of quasiparticle excitations that are very close to the Fermi Surface, for which the lifetime is sufficiently long to consider the state stable (typically the ground state, where the particles are all on the Fermi surface, or for example in the zero temperature limit...).

## The Landau Fermi Liquid

We wish now to consider how the energy of a real excited state changes with respect to its ground state. To this purpose, under the FL viewpoint, we can move quasiparticles from states inside to states outside the FS, as we would do for the noninteracting Fermi gas. So, as in the latter case (2.4), we can think that the main contribution to the change in energy comes from the change in the occupation of the energy levels. The free energy  $F$ , which, as pointed out in the previous section, is the quantity of real interest in studying physical systems, can be written in the form (2.5). However, the apparently first-order expansion of (2.5) is indeed a second order one. Most of the properties we would like to study, in fact, involve a thin region of states  $\delta$  around the FS, where the value of  $\delta f_p$  is appreciably different from zero. For such region the difference  $\epsilon_p - \mu$  is also of order  $\delta$ , so  $F - F_0$  is in fact of order  $\delta^2$ . To be consistent, we have to take into account also the interaction between quasiparticles, and allow for a second order expansion of the free energy:

$$F - F_0 = \sum_p (\epsilon - \mu) \delta f_p + \frac{1}{2} \sum_{p,p'} f_{pp'} \delta f_p \delta f_{p'} + O(\delta f^3). \quad (2.6)$$

This expression is the main assumption in the phenomenological theory of Landau (1956). The new coefficient  $f_{pp'}$  describes the interaction between quasiparticles, and it represents the interaction energy of the excited particles  $p$  and  $p'$ . It is invariant under permutation of  $p$  and  $p'$ , and it is supposed continuous when crossing the FS. It is convenient to introduce the single particle free energy in the following way:

$$\tilde{\epsilon}_p - \mu = (\epsilon_p - \mu) + \sum_{p'} f_{pp'} \delta f_{p'}, \quad (2.7)$$

The quantity  $\tilde{\epsilon}_p$  becomes crucial in taking into account the effect on particle  $p$  coming from the interactions with all the other surrounding particles. It is mathematically convenient also to introduce the distribution function:

$$\bar{f}_p^0 = f^0(\tilde{\epsilon} - \mu) \quad (2.8)$$

where  $f^0$  is the usual Fermi-Dirac step function. Defining

$$\delta \bar{f}_p = f_p - \bar{f}_p^0 \quad (2.9)$$

the departure from equilibrium  $\delta f_p$  is given by

$$\delta f_p = \delta \bar{f}_p + \frac{\partial f_p^0(\epsilon - \mu)}{\partial \epsilon_p} (\tilde{\epsilon}_p - \epsilon_p) \quad (2.10)$$

or, using equation above (2.7),

$$\delta f_p = \delta \bar{f}_p + \frac{\partial f_p^0(\epsilon - \mu)}{\partial \epsilon_p} \sum_{p'} f_{pp'} \delta f_{p'}.$$

### 2.3 The Transport Boltzmann Equation

In order to study the transport properties of the Normal Fermi Liquid, Landau considered the quasiparticles as independent entities with velocity given by  $\nabla_p \tilde{\epsilon}$  and subjected to the force  $-\nabla_r \tilde{\epsilon}$ . Let us suppose for the moment that there are no external forces acting on the system. We can set up a kinematic equation, which expresses the variation in time of the distribution function ( $df_p/dt$ ) due to quasiparticle collisions:

$$\frac{\partial f_p}{\partial t} + \nabla_r f_p \cdot \nabla_p \tilde{\epsilon}_p - \nabla_p f_p \cdot \nabla_r \tilde{\epsilon}_p = C_p. \quad (2.11)$$

$C_p$  is the collision integral, which gives the balance in the particles entering and going out of an element of phase space  $d^3p$  centered around  $p$ . If only binary collisions

$$p + q \rightarrow p' + q'$$

are considered relevant,  $C_p$  is equal to:

$$- \sum_{q, p', q'} \delta^4(p, q, p', q') |T(p, q, p', q')|^2 [f_p f_q (1 - f_{p'}) (1 - f_{q'}) - (1 - f_p) (1 - f_q) f_{p'} f_{q'}],$$

where  $T(p, q, p', q')$  is the transition matrix element between the initial state  $|p, q\rangle$  of the two particles before the collision, and the final state  $\langle p', q' |$  of the two particles coming out of the collision:

$$T(p, q, p', q') = \langle p', q' | T(E) | p, q \rangle$$

$$T(E) = V + V(E - H_0 + i\epsilon)^{-1} V + \dots$$

with  $H_0$  the unperturbed Hamiltonian,  $V$  the potential, and  $\epsilon \rightarrow 0^+$ .

$$\delta^4(p, q, p', q') \equiv \delta^3(p' + q' - p - q) \delta(\tilde{\epsilon}_{p'} + \tilde{\epsilon}_{q'} - \tilde{\epsilon}_p - \tilde{\epsilon}_q)$$

expresses the conservation of energy and momentum in the collision.

Only excited quasiparticles close to the FS can contribute to the flow in the phase space according to Landau's theory. Only the departure from the equilibrium distribution  $f_p^0$  in fact enters in the description of all transport quantities. Let us write  $f_p = f_p^0 + g_p$ , where  $g_p$  represents the departure from the equilibrium distribution. Plugging this expression in (2.11) and retaining only the first order terms in  $g_p$ , we have:

$$\frac{\partial g_p}{\partial t} + \nabla_r g_p \cdot v_p - \nabla_p f_p^0 \cdot \sum_{p'} f_{pp'} \nabla_r g_{p'} = C_p, \quad (2.12)$$

where we have taken into account the relation (2.7), and that:

$$\frac{\partial f_p^0}{\partial t} + \nabla_r f_p^0 \cdot \nabla_p \tilde{\epsilon}_p - \nabla_p f_p^0 \cdot \nabla_r \epsilon_p - \nabla_p g_p \cdot \nabla_r \epsilon_p = 0$$

as the equilibrium distribution function  $f_p^0$  and the particle's energy  $\epsilon$  do not depend on  $t$  and  $r$  in the non interacting system. The first two terms in the expression (2.12) represent the flow of totally independent quasiparticles. The last term comes from the interaction between the quasiparticles, and it represents the flow of the ground state quasiparticles dragged by interaction. If we use the notation in (2.10) to describe the departure from equilibrium, and we retain only the linear terms in  $g_p$ , this expression takes an easier form:

$$\frac{\partial g_p}{\partial t} + \nabla_r \bar{g}_p \cdot v_p = C_p. \quad (2.13)$$

The meaning of  $\bar{g}_p$  is now more transparent: it describes a diffusion term, and so the *local* departure from equilibrium.

We wish now to linearize the collision integral  $C_p$ . It is more convenient to start with the notation introduced in (2.8) and (2.9), and write the distribution function as  $f_{p_j} = \bar{f}_{p_j}^0 + \bar{g}_{p_j}$ . Keeping again only the linear terms,  $C_p$  is equal to:

$$- \sum_{q,p',q'} \delta(p, q, p', q')^4 |T(p, q, p', q')|^2 [\bar{f}_p^0 \bar{f}_q^0 (1 - \bar{f}_{p'}^0)(1 - \bar{f}_{q'}^0) - (1 - \bar{f}_p^0)(1 - \bar{f}_q^0) \bar{f}_{p'}^0 \bar{f}_{q'}^0]$$

plus the sum of the four terms

$$- \delta' \sum_{q,p',q'} \delta(p, q, p', q')^4 |T(p, q, p', q')|^2 [\bar{f}_j^0 (1 - \bar{f}_k^0)(1 - \bar{f}_l^0) + \bar{f}_k^0 \bar{f}_l^0 (1 - \bar{f}_j^0)] \bar{g}_i \quad (2.14)$$

that we can obtain starting with the set of indexes  $(i, j, k, l) = (p, q, p', q')$  and exchanging in the three remaining ways the position of two indexes in each couple simultaneously. The coefficient  $\delta'$  is  $+1$  if  $i = p$  or  $q$ ,  $-1$  if  $i = p'$  or  $q'$ . Under the binary collision point of view, the first case corresponds to the  $i$  particle undergoing the collision, the second to the  $i$  particle coming out from the collision.

It is straightforward to check that the choice of the Fermi distribution at equilibrium  $\bar{f}_{p_j}^0$  cancel the first term (2.14), because of the conservation of energy in the binary collision  $\tilde{\epsilon}_p + \tilde{\epsilon}_q = \tilde{\epsilon}_{p'} + \tilde{\epsilon}_{q'}$  implied by the  $\delta^4$  factor. Neither spatial rotations, reflections, nor time reversals change the physics of the binary collision. The  $T$  matrix is in fact invariant under all such transformations, moreover the  $\delta(p, q, p', q')^4$  factor appearing in the integrand is invariant. We can in this way show that two of the 4 terms cancel out and the final expression for  $C_p$  can be written:

$$C_p = \sum_{p'} [C_{pp'} \bar{g}_{p'} - C_{pp'} \bar{g}_p], \quad (2.15)$$

where  $C_{pp'}$  is the scattering matrix element defined as:

$$C_{pp'} = \sum_{q, q'} \delta(p, q, p', q')^4 |T(p, q, p', q')|^2 [\bar{f}_q^0 (1 - \bar{f}_{p'}^0)(1 - \bar{f}_q^0) + \bar{f}_{p'}^0 \bar{f}_q^0 (1 - \bar{f}_q^0)]. \quad (2.16)$$

It expresses the probability that a particle with momentum  $p$  scatters into the momentum  $p'$  after the collision, and vice versa.

To complete the transport equation we have only to add an external force to the system:

$$F_p \cdot \nabla_p f_p.$$

Usually  $g_p$  is proportional to the external applied force  $F_p$ , a typical example is an electric field force  $F(r) = -e E(r)$ . As we are interested only in the first order terms we can replace  $f_p$  by the equilibrium distribution function  $f_p^0$ . However, if we consider, for example, a magnetic field force  $F_B(r) = -e v_p \times B(r)$ , this is clearly orthogonal to  $\nabla_p f_p^0 = \partial f_p^0 / \partial \tilde{\epsilon}_p \cdot v_p$ , and it does not give any contribution. So we have to consider as first non-zero term  $F_B \cdot \nabla_p \bar{g}_p$ . We thus obtain at the end the Linearized Boltzmann Transport Equation (BE):

$$\frac{\partial g_p}{\partial t} + \nabla_r \bar{g}_p \cdot v_p + F_p \cdot v_p \frac{\partial f_p^0}{\partial \tilde{\epsilon}_p} - (e v_p \times B) \frac{\partial \bar{g}_p}{\partial p} = C_p, \quad (2.17)$$

with the collision integral  $C_p$  given by (2.15). From this equation we can derive all the transport properties of a Fermi Liquid.

### 2.3.1 Frequency Dependent External Force

We wish now to consider the case in which the external force is time dependent, so let us write

$$F = F_0 e^{-i\omega t}.$$

Let us plug it in (2.17) and, in the limit of small  $\omega$ , let us seek for the the linear response solution  $g_p(t) = g_p \exp(i\omega t)$ . We obtain:

$$i\omega g_p - F_0 \cdot v_p \frac{\partial f_p^0}{\partial \epsilon_p} = C_p,$$

where for simplicity we suppose an uniform medium for which  $\nabla_r g_p = 0$ . Remembering we can write (2.15)

$$C_p = \sum_q [C_{pq} \bar{g}_q - C_{qp} \bar{g}_p],$$

and defining the relaxation time  $\tau_p$

$$1/\tau_p = \sum_q C_{pq}, \quad (2.18)$$

we can write:

$$i\omega g_p + \frac{1}{\tau_p} \bar{g}_p - \sum_q C_{pq} \bar{g}_q = F_0 \cdot v_p \frac{\partial f_p^0}{\partial \epsilon_p}.$$

In order to calculate the transport property we need to solve this equation in  $\bar{g}_p$  [14].

We can use relation (2.10) to obtain

$$[i\omega + \frac{1}{\tau_p}] \bar{g}_p - \sum_q C_{pq} \bar{g}_q + i\omega \left( \frac{\partial f_p^0}{\partial \epsilon_p} \right) \sum_q f_{pq} g_q = F_0 \cdot v_p \frac{\partial f_p^0}{\partial \epsilon_p}. \quad (2.19)$$

We stress here that if we wish to recover the solutions for the transport quantities in the time dependent case by simply applying the substitution  $1/\tau_p \rightarrow 1/\tau_p + i\omega$  to the solutions of the time independent case, as is commonly done, we would neglect the third term in the left-hand side of equation (2.19).

## 2.4 General Solution to the $N$ -Patch Model

### 2.4.1 The linearized Boltzmann Equation in the $N$ -Patch Model

We briefly review the solution to the  $N$ -Patch Model proposed by Perali, Sindel and Kotliar in [57]. Starting from Boltzmann's equation (2.19), in the case of zero magnetic field  $B = 0$ , and for the steady case, we have

$$g_k/\tau_k - \sum_{k'} C_{k,k'} g_{k'} = [ev_k \vec{E} - \epsilon_k v_k \nabla T/T] (-\partial_{\epsilon_k} f_k^0)$$

where  $g_k$  is the departure from the equilibrium distribution function  $f_k^0$ ,  $C_{k,k'}$  is the scattering matrix element,  $\tau_k$  is the relaxation time for the state  $k$  defined as  $1/\tau_k \equiv \sum_{k'} C_{k,k'}$ . In order to include a non trivial momentum dependence of the scattering process and the division of the Brillouin Zone (BZ) in *hot* and *cold* regions, as discussed in the introduction to this chapter, one possibility is to expand the scattering matrix  $C_{k,k'}$  via a set of functions  $\phi_j(k)$ , which weight differently the various regions of the BZ

$$C_{k,k'} = \sum_{\alpha,\beta}^N \phi_\alpha(k) c_{\alpha\beta} \phi_\beta(k'). \quad (2.20)$$

$\phi_j(k)$  localizes a precise area in the momentum space, the  $j$ th *patch*, which we want to have scattering properties different from the other regions.  $N$  is the total number of patches in which the BZ is divided.  $c_{\alpha\beta}$  is the scattering amplitude between patches  $\alpha$ th and  $\beta$ th, and it is a symmetric, temperature dependent  $N \times N$  matrix. In this way, the Boltzmann's equation takes a form which allows an exact analytical solution.

In fact, we can write

$$g_k = \tau_k \sum_{\alpha,\beta} c_{\alpha\beta} \phi_\alpha(k) \sum_{k'} \phi_\beta(k') g_{k'} + \tau_k [ev_k \vec{E} - \epsilon_k v_k \nabla T/T] (-\partial_{\epsilon_k} f_k^0) \quad (2.21)$$

that, for convenience, we rewrite in a more compact notation:

$$g_k = \tau_k \underline{\phi}_k \cdot \bar{c} \cdot \sum_{k'} \underline{\phi}_{k'} g_{k'} + \vec{\Theta}_k \cdot \vec{v}_k \quad (2.22)$$

where  $\underline{\phi}_k$  is the  $N$  dimensional vector  $(\phi_1(k), \dots, \phi_N(k))$ , the  $N \times N$  matrix  $(\bar{c})_{\alpha\beta} = c_{\alpha\beta}$  and

$$\vec{\Theta}_k = \tau_k [ev_k \vec{E} - \epsilon_k v_k \nabla T/T] (-\partial_{\epsilon_k} f_k^0).$$

If in the quasimomentum space we define the vector

$$(\vec{g})_k = g_k$$

the matrix

$$\Pi_{kk'} = \tau_k \underline{\phi}_k \cdot \bar{c} \cdot \underline{\phi}_{k'}$$

and the antisymmetric vector

$$(\vec{u})_k = \vec{\Theta}_k \cdot \vec{v}_k$$

The BE is a simple linear equation:

$$\vec{g} = \Pi \cdot \vec{g} + \vec{u},$$

or, defined  $\chi = \vec{1} - \Pi$

$$\chi \cdot \vec{g} = \vec{u}. \tag{2.23}$$

To seek for the solution to the BE we have then to invert the matrix  $\chi$

$$\vec{g} = \chi^{-1} \cdot \vec{u}. \tag{2.24}$$

However, before performing this operation, we should first recognize that  $\chi$  is not invertible in a strictly mathematical sense. It has in fact the form

$$\chi_{kk'} = \delta_{kk'} - \tau_k C_{kk'}$$

and, bearing in mind  $1/\tau_k \equiv \sum_{k'} C_{k,k'}$ , it is straightforward to observe that the sum over the columns labeled  $k'$  is identically zero for all  $k$ , i.e. means that the column vectors are not linearly independent. We will show later that there is a superfluous unphysical solution, corresponding to  $\vec{g}$  containing a constant term, which ought be disregarded. In the solution we are going to present we shall assume to act in the physical subspace of the total Hilbert space where the unphysical solutions have been cut away, so that  $\chi$  becomes invertible.

### 2.4.2 $N$ -Patch solution to the BE

Let's consider in (2.22) the  $k$ -independent vector in the  $N$  dimensional space

$$\underline{b} = \sum_k \underline{\phi}_{k'} g_{k'},$$

so that

$$g_k = \tau_k \underline{\phi}_k \cdot \bar{\mathbf{c}} \cdot \underline{\mathbf{b}} + \bar{\Theta}_k \cdot \vec{v}_k. \quad (2.25)$$

Multiplying both side of the above equation for the vector  $\underline{\phi}_k$ , and then summing all over  $k$ , we obtain an equation for  $\underline{\mathbf{b}}$ :

$$\bar{\Gamma} \cdot \underline{\mathbf{b}} = \sum_k \underline{\phi}_k (\bar{\Theta}_k \cdot \vec{v}_k)$$

where we introduce the  $N \times N$  matrix

$$\bar{\Gamma} = [\bar{\mathbf{1}} - \sum_k \underline{\phi}_k \tau_k (\underline{\phi}_k \cdot \bar{\mathbf{c}} \cdot \dots)]. \quad (2.26)$$

As  $\bar{\Gamma}$  acts on a  $N$  dimensional space, it is more easily inverted than the  $\chi$  matrix, which is instead acting on the quasimomentum space. So the vector

$$\underline{\mathbf{b}} = \sum_k \bar{\Gamma}^{-1} \underline{\phi}_k (\bar{\Theta}_k \cdot \vec{v}_k),$$

and it can be plugged in eq. (2.25), giving the solution

$$g_k = \sum_{k'} \left[ \delta_{kk'} + \tau_k (\underline{\phi}_k \cdot \bar{\mathbf{c}} \cdot \bar{\Gamma}^{-1} \underline{\phi}_{k'}) \right] (\bar{\Theta}_{k'} \cdot \vec{v}_{k'}),$$

i.e.

$$\vec{\mathbf{g}} = \chi^{-1} \cdot \vec{\mathbf{u}},$$

so that we finally obtain  $\chi^{-1}$

$$\chi_{kk'}^{-1} = \delta_{kk'} + \tau_k (\underline{\phi}_k \cdot \bar{\mathbf{c}} \cdot \bar{\Gamma}^{-1} \underline{\phi}_{k'}). \quad (2.27)$$

### 2.4.3 Invertibility and Inversion of the $\bar{\Gamma}$ Matrix

As  $\chi$  is not invertible, from eq. (2.27) it follows that  $\bar{\Gamma}$  is not invertible. We show in fact that there is at least a vector,  $\underline{\mathbf{b}}^0$ , different from  $\underline{\mathbf{0}}$ , which  $\in \text{Ker}(\bar{\Gamma})$ , and  $\bar{\Gamma} \cdot \underline{\mathbf{b}}^0 = 0$ .

Taken

$$\underline{\mathbf{b}}^0 = \sum_k \underline{\phi}_k,$$

we have

$$\bar{\Gamma} \cdot \underline{\mathbf{b}}^0 = [\bar{\mathbf{1}} - \sum_k \underline{\phi}_k \tau_k (\underline{\phi}_k \cdot \bar{\mathbf{c}} \cdot \dots)] \cdot \left( \sum_k \underline{\phi}_k \right) =$$

$$\sum_{k'} \underline{\phi}_{k'} - \sum_{kk'} \tau_k \underline{\phi}_k (\underline{\phi}_k \cdot \bar{c} \cdot \underline{\phi}_{k'})$$

which is evidently zero from the definition (2.18),  $\tau_k = 1/(\sum_{k'} \underline{\phi}_k \cdot \bar{c} \cdot \underline{\phi}_{k'})$ . As already pointed out,  $\underline{b}^0$  corresponds to the "zero harmonic" solution  $\vec{g}_0 =$  containing a constant term. From eq. (2.25):

$$g_k^0 = \tau_k (\underline{\phi}_k \cdot \bar{c} \cdot \underline{b}^0) + \vec{\Theta}_k \cdot \vec{v}_k = 1 + \vec{\Theta}_k \cdot \vec{v}_k.$$

This solution is not acceptable, because it does not conserve the number of particles  $n$  in the system. It is required that  $\sum f_k = \sum f_k^0 + g_k = n$ , a condition evidently not satisfied by  $g_k^0$ . Moreover, because  $\sum f_k^0 = n$  in the equilibrium condition, we also observe that for every physically acceptable solution  $g_k$ , it has to be

$$\sum g_k = 0. \quad (2.28)$$

So, in order to invert  $\bar{\Gamma}$ , we have first to exclude from the total Hilbert space the  $\text{Ker}(\bar{\Gamma})$ . This was done through the Singular Value Decomposition technique (SVD) which allows one to separate the total Hilbert space into all the eigenspaces corresponding to the eigenvalues of  $\bar{\Gamma}$ , isolating the ones which have zero eigenvalues. We could check that  $\dim[\text{Ker}(\bar{\Gamma})]$  is in fact 1, corresponding to the eigenvector  $\underline{b}^0$ , invert  $\bar{\Gamma}$  in the physical subspace, and then we finally checked that the condition Eq. (2.28) is satisfied in the solution found.

## 2.4.4 Transport Properties

### Magnetic Field Dependence

In order to study the magneto-transport properties in the system, a magnetic field is added in the BE. Eq. (2.23) and (2.24) become:

$$\Xi \cdot \vec{g} = \vec{u}. \quad (2.29)$$

$$\vec{g} = \Xi^{-1} \cdot \vec{u}. \quad (2.30)$$

with

$$\Xi = [1 + \frac{e}{\hbar c} (\vec{v}_k \times B) \cdot \nabla_k] \delta_{kk'} - \tau_k C_{kk'}.$$

Following [57], we consider weak magnetic fields, so that the term containing  $B$  in the equation above can be considered as a small perturbation.  $\Xi$  is split in two parts,  $\Xi = \chi + \Omega_B$ , so that the magnetic field dependence remains in  $(\Omega_B)_{k,k'} = [\frac{e}{\hbar c}(\vec{v}_k \times B) \cdot \nabla_k] \delta_{kk'}$ .  $\chi$  is the previously considered zero magnetic field matrix.  $\Xi$  can be then perturbatively expanded in powers of  $B$ , and its inverse takes the form:

$$\Xi^{-1} = \chi^{-1} - \chi^{-1} \cdot \Omega_B \cdot \chi^{-1} + \chi^{-1} \cdot \Omega_B \cdot \chi^{-1} \cdot \Omega_B \cdot \chi^{-1} + O(B^3). \quad (2.31)$$

According to the quantity we want to calculate, we will consider different terms of this expansion.

### Conductivity

We shall mainly consider the electrical conductivity  $\sigma$  in the absence of a temperature gradient. Upon the application of an electrical field  $\vec{E}$ , the electrical current  $\vec{J} = e \sum_k \vec{v}_k g_k$  is  $\vec{J} = \bar{\sigma} \vec{E}$ , with the conductivity tensor  $\bar{\sigma}$  given by:

$$\sigma^{\mu\nu} = 2e^2 \sum_{k,k'} v_k^\mu \Xi^{-1} v_{k'}^\nu (-\partial_{k'} f_{k'}^0).$$

Considering the solution of  $\chi$  (2.27) and truncating to first order in the expansion (2.31), we get the direct conductivity  $\sigma_{xx}$

$$\sigma_{xx} = 2e^2 \sum_k \tau_k (v_k^x)^2 + 2e^2 \sum_{ijl} c_{ij} \bar{\Gamma}^{-1} \left[ \sum_k v_k^x \tau_k \phi_i(k) \right] \left[ \sum_{k'} v_{k'}^x \tau_{k'} \phi_l(k') (-\partial_{k'} f_{k'}^0) \right] \quad (2.32)$$

Notice how the first term in the right-hand side of this expression coincides with the one used in [57]. In fact, because of the topological symmetry in the BZ of the two-patch model used in [57], the second term in  $\bar{\Gamma}^{-1}$  is cancelled.

For the Hall conductivity  $\sigma_{xy}$ , we must consider instead the second order in the expansion (2.31), as the first gives identically zero. It is:

$$\sigma_{xy} = -2e^2 \sum_{k,k'} k, k' v_k^x \tau_k \Upsilon_{k,k'} v_{k'}^y \tau_{k'} (-\partial_{k'} f_{k'}^0)$$

where the matrix  $\Upsilon$  is

$$\Upsilon_{k,k'} = (\delta_{k,k'} + \tau_{k'} \mu_{k,k'}) \vec{F}_{k'} \cdot \nabla_{k'} + \sum_l (\delta_{k,l} + \tau_l \mu_{k,l}) \vec{F}_l \cdot \nabla_l (\tau_l \mu_{l,k'}),$$

with  $\vec{F}_k = \frac{e}{\hbar c}(\vec{v}_k \times \vec{B})$  and where we have defined  $\mu_{k,k'} = (\underline{\phi}(k) \cdot \vec{c} \cdot \bar{\Gamma}^{-1} \underline{\phi}(k'))$ . Developing this expression, we can also elucidate the dependence of  $\sigma_{xy}$  on the  $\bar{\Gamma}^{-1}$  matrix:

$$\sigma_{xy} = -2e^2 (X_1 + X_2 + X_3 + X_4) \quad (2.33)$$

where

$$\begin{aligned} X_1 &= \sum_k v_k^x \tau_k \vec{F}_k \cdot \nabla_k (v_k^y \tau_k) (-\partial_k f_k^0) \\ X_2 &= \sum_{ijl} c_{ij} \bar{\Gamma}_{jl}^{-1} \left[ \sum_k v_k^x \tau_k \phi_i(k) \right] \left[ \sum_{k'} \tau_{k'} \phi_l(k') \vec{F}_{k'} \cdot \nabla_{k'} (v_{k'}^y \tau_{k'}) (-\partial_{k'} f_{k'}^0) \right] \\ X_3 &= \sum_{ijl} c_{ij} \bar{\Gamma}_{jl}^{-1} \left[ \sum_k v_k^x \tau_k \vec{F}_k \cdot \nabla_k (\tau_k \phi_i(k)) \right] \left[ \sum_{k'} v_{k'}^x \tau_{k'} \phi_i(k') (-\partial_{k'} f_{k'}^0) \right] \\ X_4 &= \sum_{ijm} \sum_{pqr} c_{ij} c_{pq} \bar{\Gamma}_{jm}^{-1} \bar{\Gamma}_{qr}^{-1} \left[ \sum_k v_k^x \tau_k \phi_i(k) \right] \\ &\quad \left[ \sum_{k'} v_{k'}^x \tau_{k'} \phi_i(k') (-\partial_{k'} f_{k'}^0) \right] \left[ \sum_l \phi_m(l) \tau_l \vec{F}_l \cdot \nabla_l (\tau_l \phi_p(l)) \right]. \end{aligned}$$

Again, the  $\bar{\Gamma}^{-1}$  dependent terms  $X_2$ ,  $X_3$ ,  $X_4$  are identically zero if we consider the two-patch model in [57].

In order to have a direct comparison with experimental results [42] [4], it will be useful to consider the cotangent of the Hall angle, defined as the ratio between the direct conductivity and the Hall conductivity:

$$\cot \theta_H = \frac{\sigma_{xx}}{\sigma_{xy}}. \quad (2.34)$$

For this quantity, from [42] [4], we expect a behavior  $\cot \theta_H \propto T^\alpha$ , with  $\alpha \simeq 2$  close and beyond optimal doping.

## 2.5 The 5-Patch Model

In order to extend the results of [57], we now introduce a more general patch-division of the BZ, which could allow for example to take into account the forward scattering terms. This could verify the conjectures of [68] on the different temperature power-law dependence of the parallel and transverse conductivity. The property is experimentally observed in the linear temperature-dependence of the resistivity and the  $T^\gamma$ -dependence of the cotangent of the Hall angle. The weakness in all such models, which

try to describe the transport properties of cuprates using the assumption of a strong momentum-dependent scattering rate, is the very different power-law dependence of these two quantities. In a regular FL the linear  $T$ -dependence in the resistivity completely determines the  $T$ -dependence of the transverse conductivity too, which therefore follows the same law. So let us describe the *cold* regions as "disks" centered in the 4 points  $\vec{k}_j$ , with  $j = 1, 2, 3, 4$  (Fig. 2.2)

$$\vec{k}_j = (k_x, k_y) = (\pm \frac{\pi}{2}, \pm \frac{\pi}{2}),$$

and, for the patch functions, we first chose a convenient gaussian form:

$$\phi_j(\vec{k}) = A^2 e^{-2p(\vec{k}-\vec{k}_j)/\Delta k^2}, \quad (2.35)$$

where  $p(\vec{k} - \vec{k}_j)$  is a function having the periodicity of the Bravais lattice. We chose:

$$p(\vec{k} - \vec{k}_j) = 2[2 - \cos(k_x - k_{jx}) - \cos(k_y - k_{jy})],$$

so that in the limit  $\vec{k} \rightarrow \vec{k}_j$ ,  $p(\vec{k} - \vec{k}_j) \sim (\vec{k} - \vec{k}_j)^2$ , and the pure gaussian form of  $\phi_j$  is restored.  $\Delta k$  measures the width of the cold patch function. For  $\vec{k} - \vec{k}_j \gg \Delta k$ ,  $\phi_j$  falls to zero much faster than a simple gaussian. The normalization constant  $A$  has to be determined in such a way that the sum of all the patch functions (including the *hot* patch function  $\phi_0$ ) in all the points  $k$  of the BZ is 1. We define the hot patch function:

$$\phi_0(\vec{k}) = 1 - \sum_{j=1}^4 \phi_j(\vec{k})$$

and require that  $\phi_0$  totally disappears in the centers of the cold regions, where we wish a complete Fermi liquid behavior (and where the maximum of the sum of the 4 cold patch functions is). We obtain in this way the constraint that gives the constant  $A$ :

$$A^2 = \left( \sum_{j=1}^4 e^{-2p(\frac{\pi}{2}, \frac{\pi}{2})/\Delta k^2} \right)^{-1}. \quad (2.36)$$

We now consider the scattering matrix  $\bar{c}$ . As already pointed out, it has to be symmetric and with all the elements positive. Actually, the off-diagonal elements describe the scattering amplitude between two electrons coming from different patches, the diagonal elements, instead, describe the scattering inside the same patch. Because of the

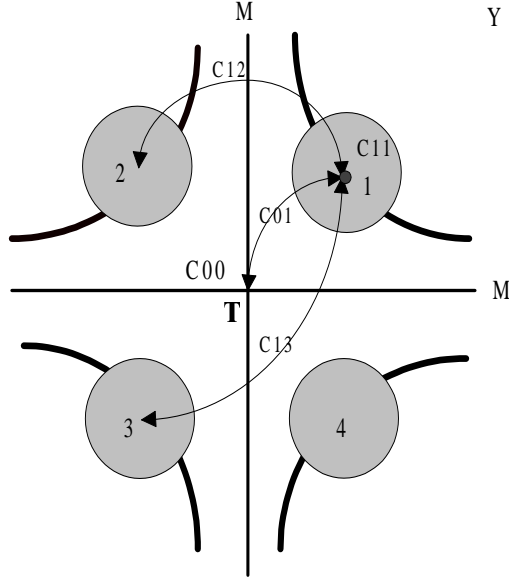


Figure 2.2: 5-Patch division of the BZ

symmetry of the patches on the reciprocal lattice (see Fig. 2.2), it is:

$$\begin{aligned}
 c_{00} &\neq c_{11} = c_{22} = c_{33} = c_{44} \\
 c_{12} &= c_{23} = c_{34} = c_{41} \\
 c_{01} &= c_{02} = c_{03} = c_{04} \\
 c_{13} &= c_{24}
 \end{aligned} \tag{2.37}$$

At first approximation, we also choose for the diagonal scattering amplitudes between cold patches:

$$c_{13} = c_{12}.$$

The main difference with the two patches model considered in [57] is the introduction of different amplitudes for the *in*-cold patch scattering and *between* cold patches scattering:

$$c_{11} \neq c_{12} \tag{2.38}$$

This should allow us to characterize differently the small angles scattering in the cold region and in this way to introduce also the effect of the forward scattering on the transport properties. On the contrary, if  $c_{11}$  were equal to  $c_{12}$ , it is straightforward to

verify that the solution to the Boltzmann equation coincides, except for the choice of the patch functions, to the one used in [57]. In fact, taken the Boltzmann equation (2.23)

$$(\vec{\Gamma} - \Pi) \cdot \vec{g} = \vec{u},$$

let's consider the solution in [57]

$$(\vec{g})_k \propto \vec{\Theta}_k \cdot \vec{v}_k.$$

If  $c_{11} = c_{12}$  it is straightforward to verify that

$$\Pi \cdot \vec{g} = 0,$$

because of the even symmetry of the cold region on the BZ and the odd symmetry of the solution proportional to  $v_k$ . Therefore also in our case  $\vec{g}$  satisfies the Boltzmann equation.

The temperature dependence of the scattering matrix  $\bar{c}$  is similar to the one chosen in [57]:

$$c_{00} = b ; c_{11} = a_0 + a_1 T^2 ; c_{12} = a_1 T^2 ; c_{01} = cT \quad (2.39)$$

In the cold region the scattering rate is low, and a Fermi Liquid behavior with a  $T^2$ -dependence is a reasonable assumption. On the other hand, in the hot region, where the scattering rate is high, the temperature independence is suggested by ARPES experiments. The coupling between hot and cold region is the key assumption in [57]: the inter-patch scattering is considered to be linear in the temperature, and this is important to obtain a linear temperature dependence in the resistivity. As mentioned above, the new assumption introduced here is the difference in the *in-cold* and *between-cold* patches scattering, through the temperature independent constant  $a_0$ . Under a physical point of view, it is introduced with the aim to represent the forward scattering in the cold region, which is mainly temperature independent and involves only small angles. Its effect is therefore confined inside each single cold patch only.

## 2.6 Results

### 2.6.1 Forward scattering: a second order effect

As mentioned in the previous section, in order to consider the possible effect of the forward scattering due to impurity in the cold region, we have introduced different scattering amplitudes for the *in-cold* patch scattering  $c_{11}$  and the *between-cold* patches scattering  $c_{12}$ , choosing an  $a_0 \neq 0$ . The condition (2.38) was in fact necessary to obtain the  $\bar{\Gamma}^{-1}$  dependent terms in the expressions for the conductivity (2.32),(2.33), which otherwise would be identically zero as in the 2-patch model. In the following we show the results on the resistivity  $\rho_{xx}$  (Fig. 2.3) and on the hall conductivity  $\sigma_{xy}$  (Fig. 2.4). To simulate a small angle impurity scattering, we chose a quite narrow *cold patch*, with  $\Delta k = 2\pi/5$  (formula 2.35).

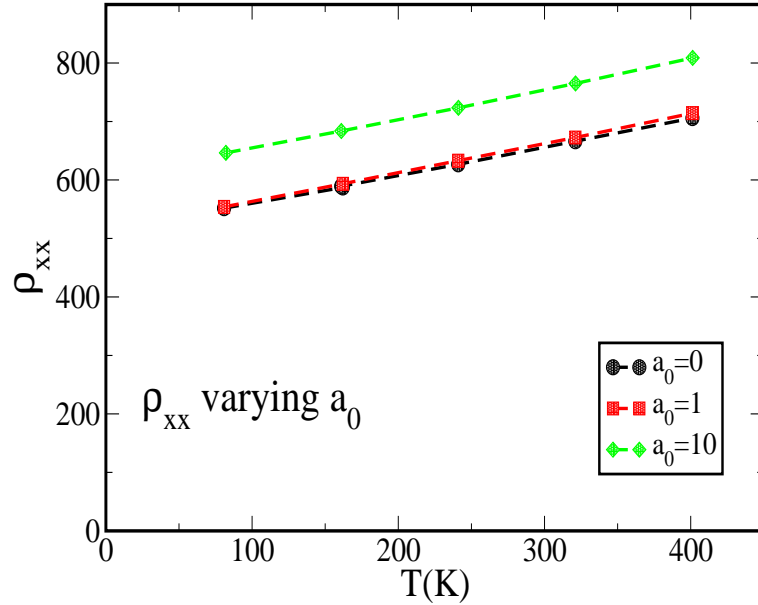


Figure 2.3:  $\rho_{xx}$  as a function of  $T$  varying  $a_0$ ,  $\Delta k = 2\pi/5$ ,  $a_1 = 50$ ,  $b = 1$ ,  $c = 7$

We will show in this section that the forward scattering is indeed a second order perturbation effect which cannot explain the different  $T$ -dependence of the in-plane parallel and transverse conductivity. In both graphs, we display three possible values of  $a_0 = 0, 1$  and  $10$ . The introduction of the small forward scattering effect is likely better

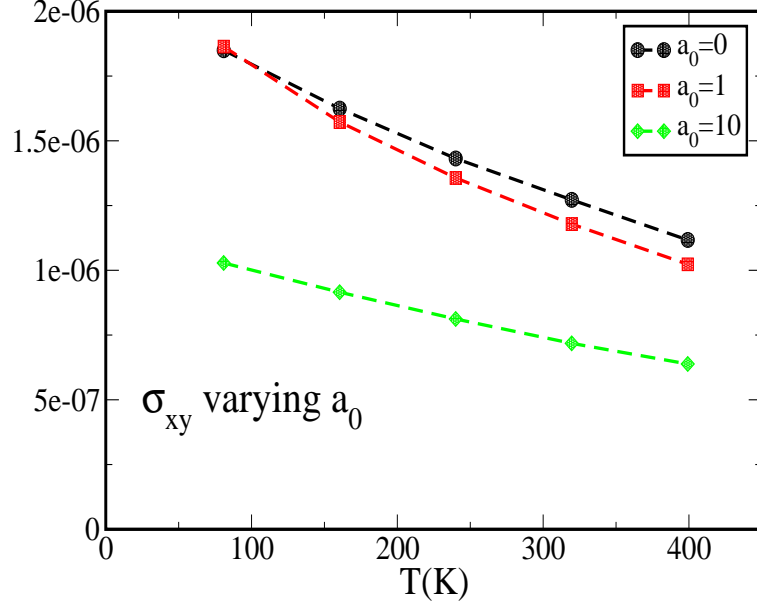


Figure 2.4:  $\sigma_{xy}$  as a function of T varying  $a_0$ ,  $\Delta k = 2\pi/5$ ,  $a_1 = 50$ ,  $b = 1$ ,  $c = 7$

simulated passing from  $a_0 = 0$  to  $a_0 = 1$ . But in this case only a small change appears in either  $\rho_{xx}$  and  $\sigma_{xy}$ . So the impurity forward scattering should have only a small influence on the conductivity. On the other hand, a big variation from  $a_0 = 0$  (for example the displayed  $a_0 = 10$ ) causes a vertical translation either for  $\rho_{xx}$  and  $\sigma_{xy}$ . In Fig. 2.5 we show the four contributions to  $\sigma_{xy}$   $X_i$ ,  $i = 1, \dots, 4$  of eq. (14). The  $\bar{\Gamma}^{-1}$  dependent corrections  $X_2$  and  $X_3$  are two and one order of magnitude smaller than the leading term  $X_1$  (the only present when  $a_0 = 0$ ), while the  $(\bar{\Gamma}^{-1})^2$  dependent correction  $X_4$  is even four orders of magnitude smaller. This already shows that, although the forward scattering term does indeed contribute to the bending of the cotangent of the Hall angle as a function of temperature, the effect is a second order one and it cannot account for the experimentally observed temperature-exponent of the cotg of the Hall angle, which is close to 2.

### 2.6.2 Data Fitting Troubles with gaussian patches

Difficulties in finding different exponents in the  $\rho_{xx}$  and the  $\cot(\theta_H)$  are also encountered in the 5-patch model study if we attempt a fit of the experimental results, as

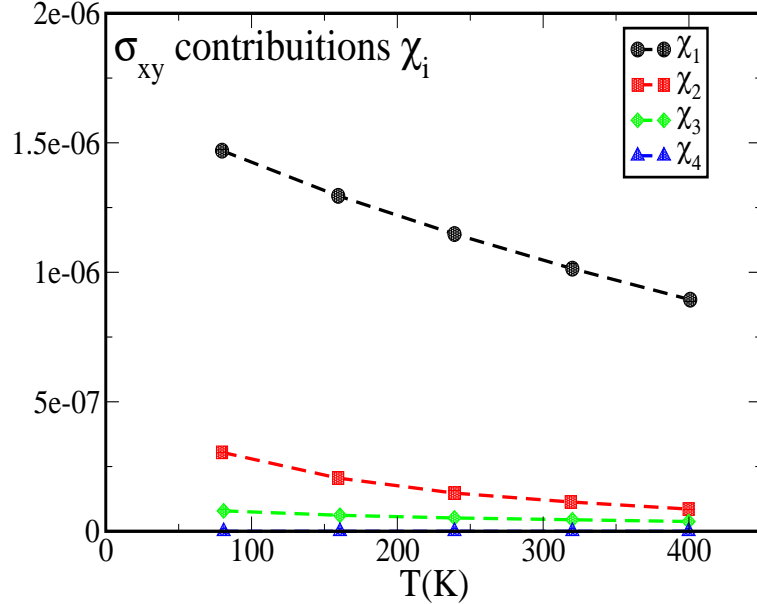


Figure 2.5: Contributions to  $\sigma_{xy}$ ,  $a_0$ ,  $\Delta k = 2\pi/5$ ,  $a_1 = 50$ ,  $b = 1$ ,  $c = 7$

systematically done in [57]. As first step, we could analyze the behavior of the resistivity  $\rho_{xx}$  and the Hall angle  $\cot(\theta_H)$ . We chose starting parameter values close to the ones used in [57]. The resistivity is inversely increasing with the size of the cold region (Fig. 2.7), i.e. it is inversely proportional to the doping, as observed for the 2-patch model [57], and in agreement with the experimental observation [4], [42]. It shows also the expected linear behavior (Fig. 2.6 and 2.7). Deviation from linearity is, in fact, observed for very large size of the cold patch, when the system becomes a FL: fitting with the law  $\rho_{xx} = A + BT^\alpha$  for the case shown in the graph  $\Delta k = \pi/0.7$ ,  $\alpha$  turns out to be 2. The  $\cot(\theta_H)$  behavior is shown in Fig. 2.8. Like  $\rho_{xx}$ , it is decreasing with increasing doping, i.e. with increasing cold patch size. This agrees with the experimental data [4][42]. However, strong differences are seen in our result. First of all, according to [4][42],  $\cot(\theta_H)$  should be smaller than  $\rho_{xx}$  (almost half) for the same set of parameters, but in our case it is exactly the opposite, with a  $\cot(\theta_H)$  that is almost twice  $\rho_{xx}$ , no matter the set of parameters chosen. Second,  $\cot(\theta_H)$  should show a  $T^\alpha$  behavior, with  $\alpha$  going from 2 for the underdoped region to 1.5 in the overdoped ( $\alpha \simeq 1.7$  for optimal doping). So in a  $\cot(\theta_H)$  vs.  $T^2$  plot, we should observe straight lines (i.e.  $\cot(\theta_H) \sim T^2$ ) that get smaller and smaller in absolute value

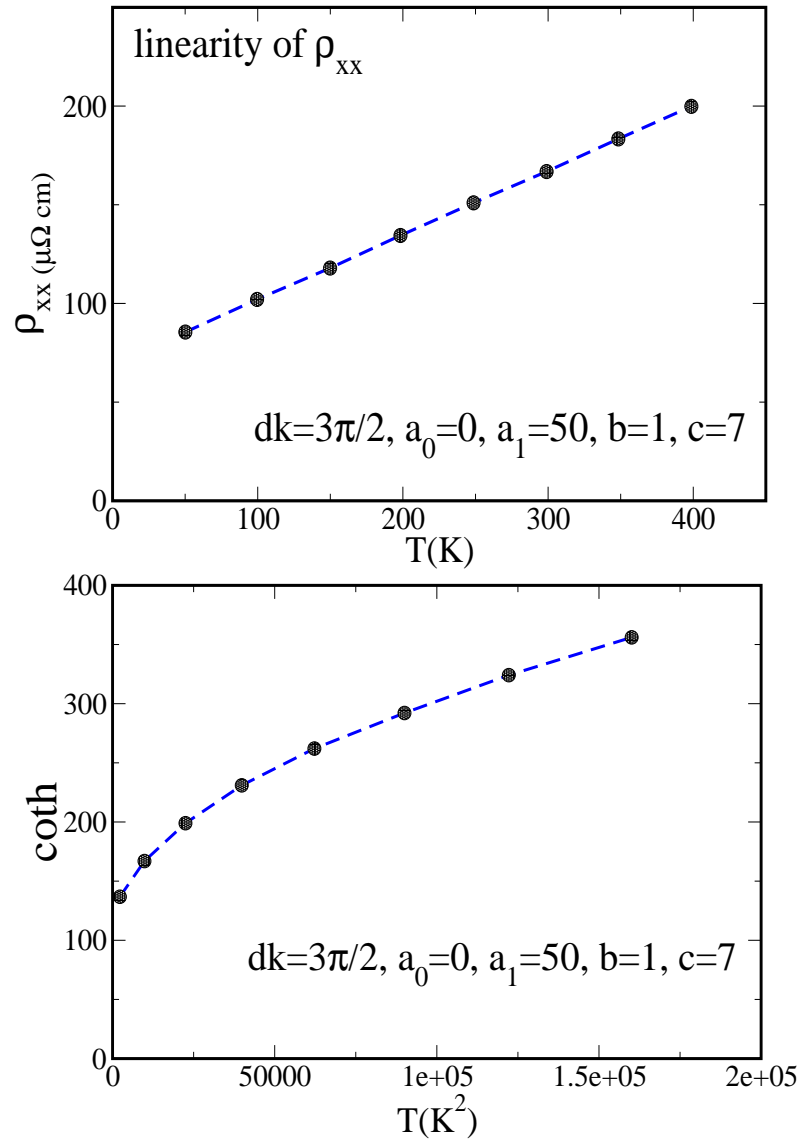


Figure 2.6:  $\rho_{xx}$  and  $\text{coth}$  vs.  $T$   $\Delta k = \pi/1.5$ ,  $a_0 = 0$ ,  $a_1 = 50$ ,  $b = 1$ ,  $c = 7$

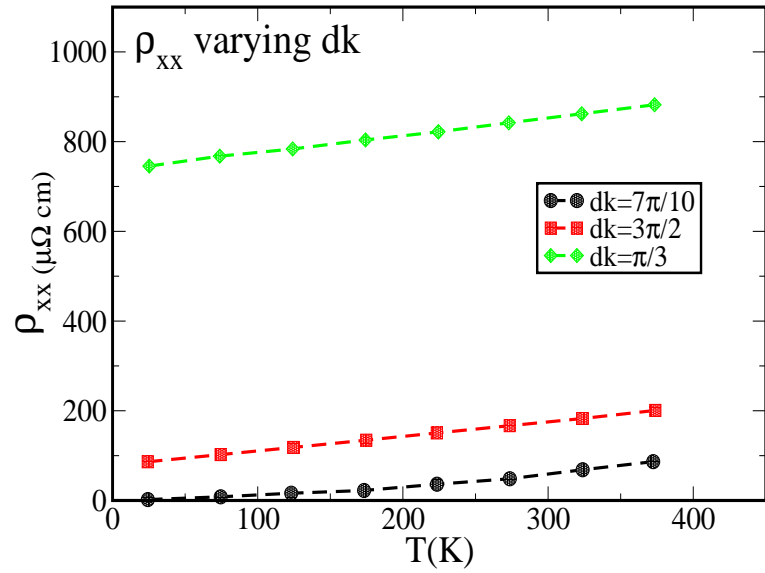


Figure 2.7:  $\rho_{xx}$  and  $\cot\theta$  vs.  $T$   $\Delta k = \pi/1.5$ ,  $a_0 = 0$ ,  $a_1 = 50$ ,  $b = 1$ ,  $c = 7$

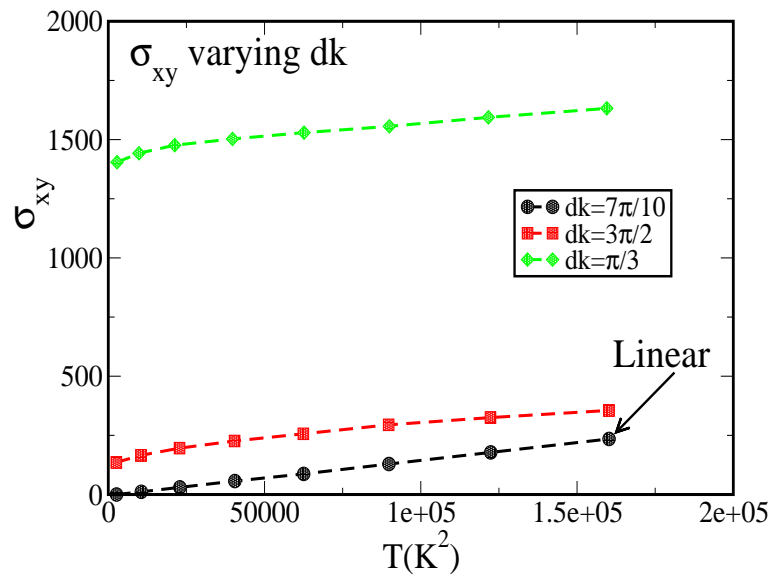


Figure 2.8:  $\cot\theta$  vs.  $T^2$  varying doping, i.e.  $\Delta k$

and start to curve ([4][42]) with increasing doping, as  $\alpha$  becomes smaller than 2. In fact in Fig. 2.8 we observe exactly the opposite behavior, with straight lines that curve when the doping is increased. The  $\cot(\theta_H)$  seem to have a opposite behavior from the one expected given experimental results and, as expected from the observations of the previous section, its power-law behavior follows closely the one of the resistivity.

## 2.7 The "panettone"-patch model

The results derived in the previous sections show some problems in the developing of a 5-patch model using gaussian patch-functions:

1. The introduction of a  $T$ -independent forward scattering, made possible the a 5-patch structure, appears as a second order perturbation effect which does not substantially modify the  $\gamma$  exponent in the  $\cot \theta_H$ .
2. the values we can obtain for the resistivity and the Hall conductivity do not match what is expected given experimental observation of cuprate systems. The  $\cot \theta_H$  is in fact always bigger than the plane resistivity  $\rho_{xx}$ .
3. while it is possible to obtain a linear in temperature resistivity  $\rho_{xx}$ , the  $\cot \theta_H$  displays a  $T^\gamma$ -dependence with an exponent  $1 < \gamma < 1.5$ . Albeit  $\gamma > 1$ , its dependence from the model parameters tightly follows the resistivity behavior like in a regular FL.

Accordingly, the fundamental question that remains is how does one obtain two independent temperature exponents for the resistivity  $\rho_{xx}$  and for the  $\cot \theta_H$ ? In particular  $\cot \theta_H \simeq T^\gamma$  with  $\gamma \leq 2$ . The results presented here for the 5-patch model with gaussian patch-function seem even to worsen the results of the 2-patch, where a different patch was used [57]. In the latter case point (1) above was essentially solved and a  $\gamma > 1.5$  was found. It was in fact possible to obtain a lower Hall conductivity  $\sigma_{xy}$  (and therefore a lower  $\cot \theta_H$ ) by introducing a steep interlacing region trough hyperbolic patch-functions (see left hand side Fig. 2.9):

$$\phi(k) = \prod_{i=1}^4 \phi_i(k) \tag{2.40}$$

$$\phi_i(k) = \frac{1}{2} \left[ 1 + (-1)^i \tanh \left( \frac{k_y - m_i k_x - t_i}{w} \right) \right] \quad (2.41)$$

where  $m_i = m_1$  for  $i = 1, 4$ ,  $m_i = m_2$  for  $i = 2, 3$ ,  $t_i = t_1$  for  $i = 3$ ,  $t_i = t_2$  for  $i = 4$  and  $t_i$  is zero for  $i = 1, 2$ . For more details refer to the work in [57]. This creates a cold region like the one shadowed in Fig. 2.9. The hot patch  $\psi_k$  is defined has:  $\psi_k =$

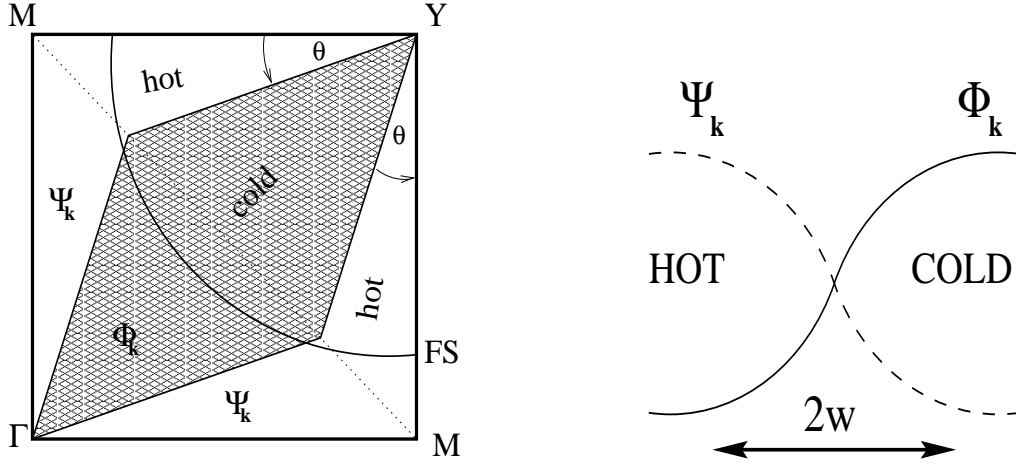


Figure 2.9: Left hand side: Patch used in [57] in the first quadrant of the BZ. Right hand side: intermediate region of overlapping hot/cold patch.

$1 - \phi_k$  Introducing smoothly varying patch-functions is necessary (ref. [57]) to avoid un-physical  $\mathbf{k}$ -derivative-diverging terms in the leading order of the magnetoresistance. The smooth change between hot and cold regions (measured by a width parameter  $w$ ) is, in this case, described by hyperbolic functions (shown at the right hand side of Fig. 2.9). This however looks to be important also in matching the right quantitative order of the resistivity  $\rho_{xx}$  and the  $\cot \theta_H$ , as expressed in the point (2) above. The shape of the patch enters in fact in the parametrization of the collision integral  $C_{kk'}$  (formula 2.20), which determines the collision integral (2.15) (or equivalently the lifetime  $\tau_k$  (2.18) of the quasiparticles). In turn, this quantity completely determines the flow of quasiparticles in the phase-space as determined by the BE (2.17). It is therefore important not only to well parametrize the cold patch (with a Fermi-like  $T^2$ -dependence of the scattering amplitude) and the hot patch (where the scattering amplitude is assumed temperature-independent), but also the intermediate region, which have to vary smoothly but fast enough. Hyperbolic-like tail seems to work better than a gaussian tail, in spite they

select a similar region of the  $k$ -space. We display a schematic diagram of the scattering matrix  $C_{kk'}$  on the FS in Fig. 2.10. Quasiparticle are present only on small stripe of width  $\sim k_B T$  around the FS (the only active states in a Fermi liquid close to accessible quasiparticle states), therefore only in that region the effect of  $C_{kk'}$  is important in determining the solution to the BE. In the top panel we fix  $k = k_F$ ,  $k \in$  the cold region and we vary  $k'$  on the FS in the first quadrant of the BZ, measuring its position through the angle  $\theta$  with respect to the  $x$ -axis. This describes a particle originally in the cold region undergoing a collision and ending in the state  $k'$ . In the bottom panel  $k = k_F$  but  $k \in$  the hot region. As we said, in order to fit the right values of  $\rho_{xx}$  and  $\cot \theta_H$ , in this diagrams the tail of the cold/hot intermediate region has to be steep, at least more than in a gaussian function. This is the reason why the choice of gaussian patches, albeit practical, does not work efficiently.

We can restore the quality of results found in [57] by introducing a 5-patch structure with a more steep tanh-like varying *cold*-patch:

$$\phi_i(k) = \frac{1}{2} [1 - \tanh(w^{-1}(r_{\mathbf{k}} - r_o))] \quad i = 1...4 \quad (2.42)$$

where  $r_{\mathbf{k}}$  measures the distance from the center of the patch  $(c_x, c_y) = (\pm \frac{\pi}{2}, \pm \frac{\pi}{2})$ , in the four center-quadrant of the Brillouin Zone:

$$r_{\mathbf{k}} = \sqrt{(k_x - c_x)^2 + (k_y - c_y)^2} \quad (2.43)$$

and  $w$  is again the width parameter of the cold/hot smoothing region. This is akin to substituting the gaussian patches introduced in the previous section by "panettone"-like shaped patches (see Fig.2.11). The qualitative change with respect to the topological division in hot/cold patches used in [57] (Fig. 2.9) is minimal, being the parts of the  $k$ -space effectively involved in the calculation of transport quantities small stripes around the Fermi surface  $-(\partial f_{\mathbf{k}}/\partial \mathbf{k})$ .

Here, however, we wish to add a further hypothesis: *we introduce a temperature dependent "panettone", which presently finds solely a "mathematical" justification in the way it is able to reproduce the experimentally observed data.* We therefore naively

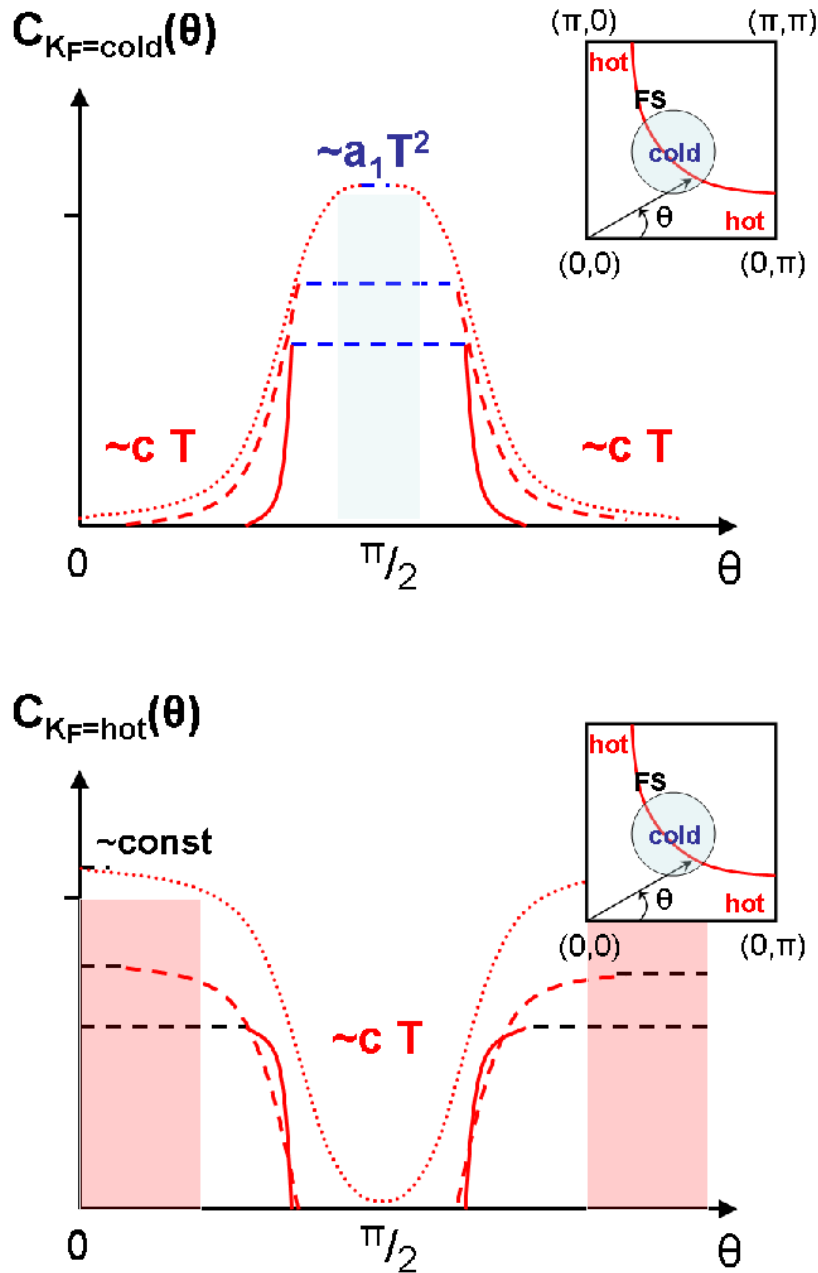


Figure 2.10: Scattering matrix  $C_{kk'}$  (formula 2.20) parametrized with a 5-patch model. In the top panel we display  $k \in \text{cold-patch}$  and  $k'$  varying on the FS (measured with the angle  $\theta$  from the  $x$ -axis). In the bottom panel we display  $k \in \text{hot-patch}$  and  $k'$  varying on the FS (measured with the angle  $\theta$  from the  $x$ -axis). We elucidate the temperature  $T$ -dependence in the different regions. Notice that in the 5-patch "panettone" model a temperature Fermi-function-like dependent (three different temperature are shown in the picture) patch is introduced in the smoothly varying intermediate cold/hot region (according to formulas 2.42 and 2.44), besides the phenomenological linear- $T$  dependence of the scattering amplitude  $c_{\alpha\beta}$  used in the 2-patch model.

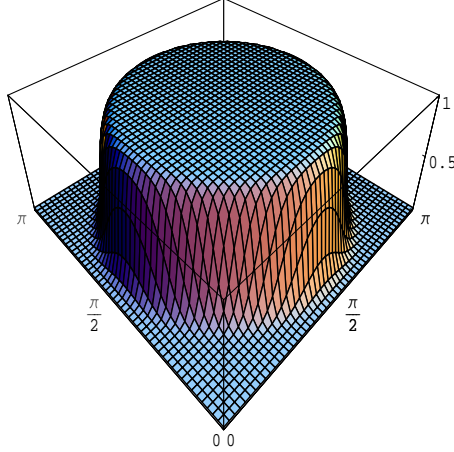


Figure 2.11: "Panettone"-patch in the first-quadrant of the BZ.

assume that the parameter determining the spreading of hot/cold intermediate region  $w$  behaves like an effective temperature:

$$w(T) = w_o T \quad (2.44)$$

We just indicate some observations:

- the size of the cold patch has been heuristically linked to the doping in the system [57]. The cold patch behaves in this sense as a pocket of fermionic particles (whose size and smoothness is dependent on the temperature).
- According to what observed above, the edge of a cold patch would be like a fermionic FS. This is right the shape we guessed for the panettone-patch edge, which decays at his border as fast as a Fermi function (which is another way to write tanh). Such behavior in the intermediate hot/cold region is important not only to avoid a ill defined MR, but also to match quantitatively the order of magnitude of  $\cot \theta_H$  as compare to the resistivity  $\rho_{xx}$ .

The smaller the temperature  $T$ , the steeper the edge of the panettone-patch, as with the edges of a Fermi distribution function.  $w_o$  enters like a Boltzmann's constant, and we treat it as a fitting parameter. We can now re-do the same fitting procedure on experimental data, as in [57]. We do not aim for a systematic comparison, nor look for the complete explanation of the transport properties of cuprate materials. We want

$r_o$ (2.42)	$\vec{c}$ (2.43)	$w_o$ (2.44)	$a_0$	$b$	$c$
0.5	(1.15,1.15)	16	70	0.4	2.8

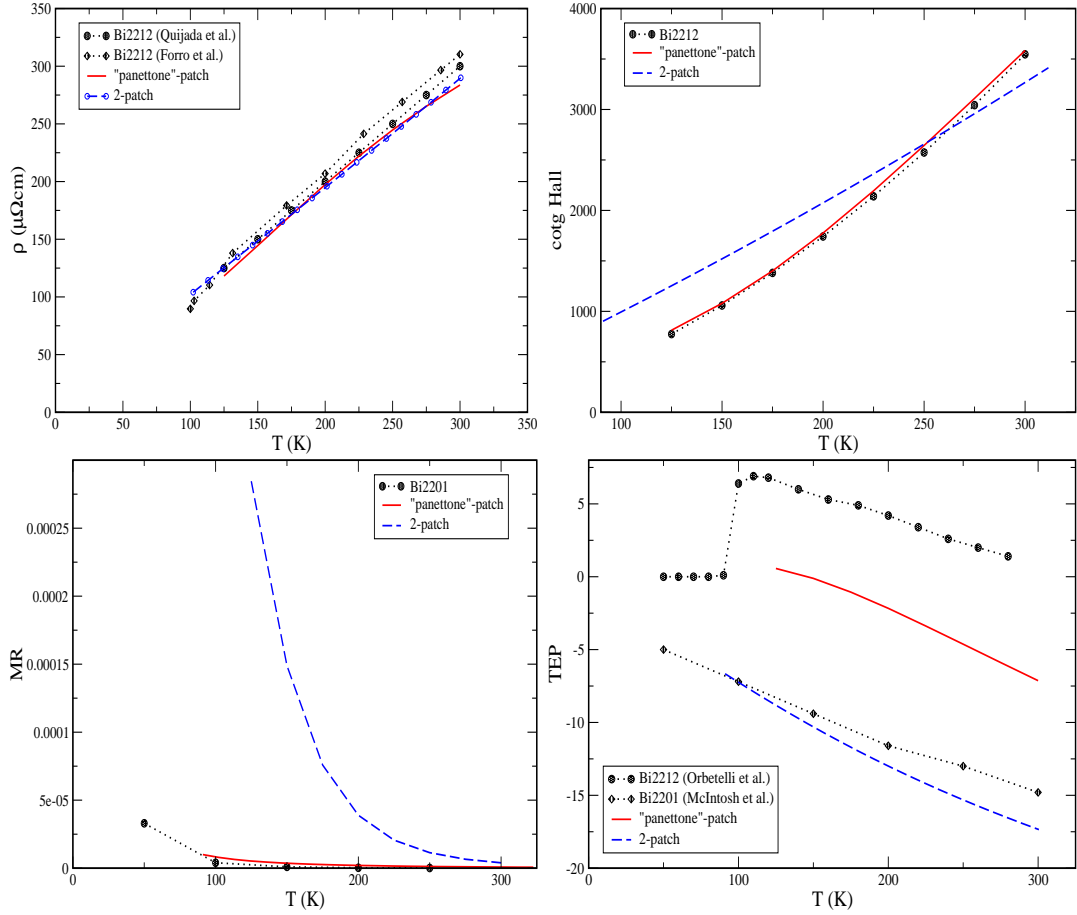


Figure 2.12: Top left: the experimental linear dependence in temperature in the resistivity  $\rho_{xx}$  of Bi2212 [59][33] is confronted with the 2-patch model of [57] and the "panettone"-patch. Top right: The improvement of the "panettone"-patch on the 2-patch model in describing the  $T^\gamma$ -dependence of the  $\text{coth } \theta_H$  is evident. Bottom left: with the same fitting parameters used to fit  $\rho_{xx}$  and  $\text{coth } \theta_H$ , the "panettone"-patch magneto-resistance MR is confronted with the experimental results on of Bi2201 and the 2-patch model. Bottom right: the experimental termo-electric power TEP of Bi2212 [54] and of Bi2201 [52] are confronted with the "panettone"-patch model and the 2-patch model.

only to verify if the introduction of this particular  $T$ -dependent panrettone-patch, and therefore of a different scattering matrix  $C_{kk'}$  (formula 2.20), may improve the 2-patch model of [57]. In particular, we want to see if it is possible to obtain a  $T$ -linear resistivity and, at the same time, a pronounced curved  $\cot \theta_H$  –the main problem in the 2-patch model.

The result is shown in 2.12. The resistivity  $\rho_{xx}$  and the  $\cot \theta_H$  vs temperature are shown in the upper panels. As in [57], these 2 quantities have been chosen to fit the parameters. We expect that the terms  $\nabla_k \phi_k$ , which introduce new  $T$ -dependent contributions, enter in the  $\rho$  expression as second order terms (formula 2.32), while they should be more relevant in determining the behaviour of  $\cot \theta_H$ , because the first order terms are in this case zero. This is explicitly seen in formula (2.33), where the terms  $\nabla_k \phi_k$  appear in  $\nabla_k \phi_k$ . And in fact we succeed in obtaining a result which reproduces incredibly well the  $T^{1.7}$  curvature (red-dotted line) as compared to the 2-patch model (blue-dashed line) and follows very well experimental data, while the resistivity keeps a good linearity. Having fit the parameters with these two quantities, let's have a look to what happens to other quantities, like for example the magneto-resistance (MR) and the thermo-electric power (TEP) in the lower panels. We observe that the MR shows a noticeable improvement too with the panettone-patch (again red line) compared to the 2-patch model (blue-dashed line), either quantitatively and qualitatively, being better portrayed the  $\alpha \simeq -4$  exponent of the MR  $\sim T^{-\alpha}$  law. The TEP gives a quantitative result comparable to [57] and between experimental values. Notice the correspondence with the TEP  $\sim -T$  law. How much constant lattice contribution to the thermal transport quantities may be relevant is still an open debate. The *ad hoc* modifications introduced seem therefore to generate the correct qualitative behaviour for the transport properties of these materials. The hypothesis was however introduced to fit experimental observations and cannot be justified at this phenomenological level: they can only be taken as steps in the right direction. To make steps forward it is necessary to start our study from a microscopic theory capable of deriving the cuprate properties, e.g. the Hubbard model presented in the previous chapter, which explains at least some of the fundamental properties of cuprate material in the insulating state. For

this, a method for performing reliable calculations on strongly correlated many-body systems is most required.

## Chapter 3

### Cellular Dynamical Mean Field Theory

In the previous chapter we studied the normal state (NS) properties of cuprate superconductors at optimal doping using a macroscopic phenomenological Boltzmann theory. Given a few *ad hoc* assumptions regarding the anisotropic scattering properties of these systems on experimental observation, we constructed and extended the  $N$ -patch solution to the Boltzmann transport equation found in [57] and determined the temperature-dependence of transport quantities. Both the qualitative and quantitative agreement with experimental data was surprisingly satisfactory, in spite of the simplicity of the Boltzmann quasiparticle approach enriched by an anisotropic scattering rate and parametrized by a only  $N = 2 - 5$  -patch model. However, to get insight into the mechanism that arises in anomalous properties from a simple FL already in its NS (as in going from high doping to the Mott insulating state of cuprate systems), and to justify the hypothesis introduced in the phenomenological Boltzmann approach, we need a microscopic theory able to support and explain the strong scattering anisotropy starting from a model Hamiltonian, like the aforesaid Hubbard Model. For this a method able to contend with strongly correlated many body electron system is required. In recent years a great success was achieved through the use of Dynamical Mean Field Theory (DMFT) [35]. This method reduces the full lattice many-body problem to a local impurity embedded in a self-consistent effective bath of free electrons, which mimics the effect of the full lattice on the local site. While in this way spatial correlations are disregarded, time-dependent correlations are fully taken into account by the dynamical bath. A self consistency condition links the effective impurity model to the original lattice problem. DMFT already proved its power giving the first unified scenario of the Mott transition, where the high and low energy physics has to be treated on equal

footing through a dynamical approach [35]. Despite DMFT being an exact theory only in the limit of infinite dimension, it has proved an excellent approximation to deal with real finite dimensional systems. Combined with electronic structure method it was able for example to explain transition metal oxides physics [45]. The assumption of locality however, being the foundation on which the mean field theory rests, may be too restrictive if applied to systems where local correlations are fundamental in determining their properties. This is the case for cuprate systems: if strong momentum dependent properties are relevant, as seems to be the case, they arise from non-local spatial correlations. Moreover with a pure local theory we cannot describe broken-symmetry-states where some spatial arrangement of the order parameter is required, like for instance AF of  $d$ -wave SC. In this chapter we review and develop an extension to DMFT which is able to partially cure its spatial limitations, the Cellular Dynamical Mean Field Theory (CDMFT). We replace the site-impurity by a cluster of impurities embedded in a self-consistent bath. Short-ranged spatial correlation are in this way treated exactly inside the cluster, and a first momentum-dependence of the properties of the system is recovered. In the next chapter we will benchmark CDMFT with the exactly solvable one dimensional case, which is the worst case for a mean field approach, and we will discuss its possible implementation according to the shape and size of the cluster. In chapters 5 and 6 we will apply it to the experimentally relevant two dimensional case. A key-technique used in our procedure the Exact Diagonalization (ED) algorithm used to solve the impurity problem. ED allows access to zero temperature physics and real frequency information, as well as a wide range of model-parameters, as compared to other high temperature methods (like for example Quantum Monte Carlo (QMC) ).

### 3.1 Dynamical Mean Field Theory DMFT

We briefly review Dynamical Mean Field Theory, as to discuss more clearly in the next section the innovations of *Cluster* Dynamical Mean Field Theory. For a full reference on this method and a complete bibliography of technical implementations and results we refer to [35]. Here we wish to convey the simple ideas underlying DMFT. Accordingly, let us consider a general Hubbard problem on a lattice of dimension  $d$ , described by the

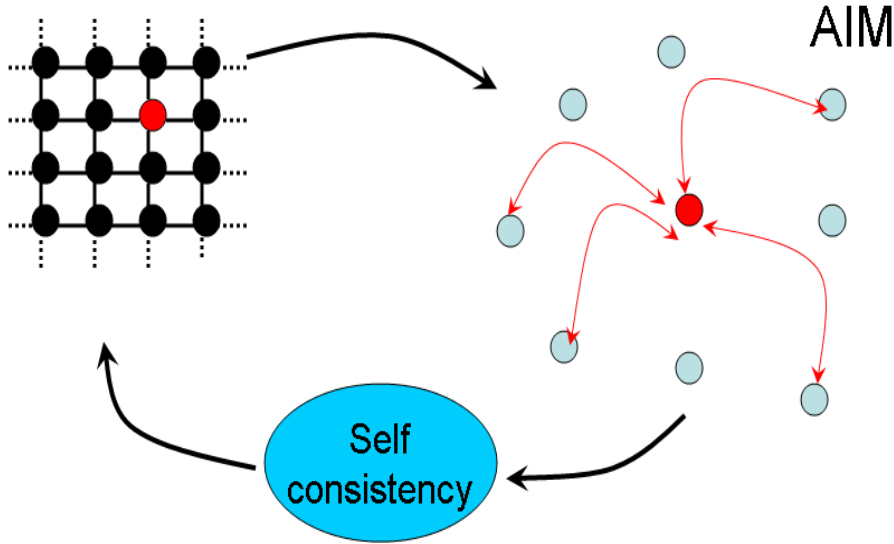


Figure 3.1: DMFT loop

Hamiltonian:

$$H = - \sum_{i,j,\sigma} t_{ij} (c_{i\sigma}^\dagger c_{j\sigma} + h.c.) + U \sum_i n_{i\uparrow} n_{i\downarrow} - \mu \sum_i n_i \quad (3.1)$$

where we indicate with  $c_{j\sigma}$  the destruction operator of a fermion with spin  $\sigma = \pm\frac{1}{2}$  on site  $j$  of the  $d$  dimensional lattice. The first term in the Eq. 3.1 describes a kinetic term where a particle can jump from site  $i$  to site  $j$  and viceversa with a probability measured by the orbital overlapping integral parameter  $t$ . The second term acts when two fermions of opposite spin occupy the same lattice orbital  $i$ , and expresses mutual Coulomb repulsion of intensity  $U$ . The two terms compete to determine the physics of the system: the first would like to move electrons in order to lower the energy, the second instead strongly un-favors the double occupancy. As we explained in the first chapter, in spite of the simplicity of this model it is extremely hard to extract reliable information at finite dimension. Only in one dimension there exists the exact *Bethe Ansatz* solution [50]. Now let's see how DMFT approaches the Hubbard problem to give a solution, which becomes exact in the opposite limit of  $d = \infty$ ). A schematic diagram is shown in Fig. 3.1:

1. We do not attempt a solution of the full lattice problem and focus instead on a single site (marked in red on the left-hand side of Fig. (3.1)).

2. We then simulate the effect of all the other sites in the lattice by an effective bath of free fermions (right hand side of Fig. 3.1). Differently from a normal static mean field theory, the effective impurity model (Anderson impurity model AIM) is able to mimic dynamical processes wherein particles jumping out of a site and returning to it after some time.
3. the effective-bath construction has to be completed by imposing a self-consistency condition which links the local Green's function of the effective AIM to the one of the original lattice Hubbard model.

In mathematical language, this is well explained by the "cavity construction" (see for example [35]).

$$\frac{1}{Z_{ef}} e^{-S_{eff}[c_{o\sigma}^\dagger, c_{o\sigma}]} \equiv \frac{1}{Z} \int \prod_{(i,j,\sigma) \neq (o,o)} Dc_{i\sigma}^\dagger Dc_{j\sigma} e^{-S} \quad (3.2)$$

Given the imaginary-time the action  $S[c^\dagger, c]$ , we construct an effective action  $S_{ef}[c_o^\dagger, c_o]$  integrating out all the sites  $(i, j) \neq o = (i_o, j_o)$ , where  $o$  is the site chosen as impurity (Eq. 3.2).  $S_{ef}[c_o^\dagger, c_o]$  can be written in the quadratic form:

$$S_{ef} = \int_0^\beta d\tau \sum_\sigma c_{o\sigma}^\dagger(\tau) \mathcal{G}_\sigma^{-1}(\tau) c_{o\sigma} + U \int_0^\beta d\tau n_{o\uparrow}(\tau) n_{o\downarrow}(\tau) \quad (3.3)$$

where  $\mathcal{G}_o(\tau)$  plays the role of an effective Weiss field. It expresses the probability of destroying a particle on the impurity site  $o$  at time  $\tau = 0$  and recreating it on the same impurity site  $o$  after an imaginary time  $\tau$  elapsed. The primary difference with a static mean field is that now  $\mathcal{G}_o(\tau)$  is a time-dependent Green's function which fully takes into account the local temporal dynamics despite the truncation of spatial degrees of freedom. It represents the bare Green's function of the effective action, but it should not be confused with the bare Green's function of the original lattice model. Having the effective action at hand  $S_{ef}$ , we can now calculate the local Green's function of the effective impurity model (in a following section we will go over this point in more detail):

$$G_{imp}(\tau) = -T_\tau \langle c_o^\dagger(\tau) c_o \rangle_{S_{ef}} \quad (3.4)$$

and through Dyson's equation:

$$\Sigma_{\mu\nu}(i\omega_n) = \mathcal{G}_\sigma^{-1}(i\omega) - G_\sigma^{imp-1}(i\omega) \quad (3.5)$$

which allows to extract the local self-energy  $\Sigma$ , evaluate the original lattice local Green's function:

$$G(k, i\omega) = \frac{1}{i\omega + \mu - \varepsilon_k - \Sigma} \quad (3.6)$$

and obtain once again the local Green's function summing all over the BZ:

$$G_{loc}(i\omega) = \sum_k \frac{1}{i\omega + \mu - \varepsilon_k - \Sigma} \quad (3.7)$$

Here we have expressed the green's function on the Matsubara axis

$G(i\omega) = \frac{1}{2} \int_0^\beta e^{i\omega\tau} G(\tau)$ . The self-consistency conditions requires the two local Green's functions (3.4) and (3.7) to be the same:

$$G_{imp} \equiv G_{loc} \quad (3.8)$$

or equivalently

$$\Sigma(i\omega) = \mathcal{G}_\sigma^{-1}(i\omega_n) - G_\sigma^{loc-1}(i\omega, \Sigma) \quad (3.9)$$

Behind equations 3.3 and 3.7 lies the foundational assumption of DMFT. It is clear that we assume

$$\Sigma(i\omega) \neq \Sigma(\mathbf{k}, i\omega) \quad (3.10)$$

the self-energy is a purely local quantity. This is also the assumption required for the gaussian form of  $S_{ef}$  in Eq. 3.3 to be exact and it is true in the limit  $\mathbf{d} \rightarrow \infty$ , where the DMFT solution is exact. One can get an idea of this through the cavity construction.

Writing the quantum action:

$$S = S_o + \Delta S + S^o$$

where  $S^o$  contains the lattice sites except site  $o$ ,  $S_o$  only site  $o$ ,  $\Delta S$  contains terms connecting site  $o$  with the rest of lattice

$$S_o = \int_0^\beta d\tau \sum_\sigma c_{o\sigma}^\dagger(\tau) (\partial_\tau - \mu) c_{o\sigma} + U \int_0^\beta d\tau n_{o\uparrow}(\tau) n_{o\downarrow}(\tau)$$

$$\Delta S = - \int_0^\beta d\tau \sum_{i\sigma} c_{o\sigma}^\dagger(\tau) c_{i\sigma} + c_{i\sigma}^\dagger(\tau) c_{o\sigma}$$

We have

$$\frac{1}{Z_{ef}} e^{-S_{eff}[c_{o\mu\sigma}^\dagger, c_{o\nu\sigma}]} \sim \int \prod_{(i,j,\sigma) \neq (o,o)} Dc_{i\sigma}^\dagger Dc_{j\sigma} e^{-\Delta S} e^{S^o}$$

i.e. the expectation value  $\langle e^{-\Delta S} \rangle_{S^o}$  calculated in the system with a "cavity" in place of site  $o$ . The effective action can therefore be written:

$$S_{ef} \sim \sum_{n=1}^{\infty} \sum_{i_1 \dots i_n} t^{2n} \int c_{i_1}^\dagger(\tau_{i_1}) \dots c_{i_n}^\dagger(\tau_{i_n}) G_{i_1 \dots j_n}^o(\tau_{i_1} \dots \tau_{i_n}, \tau_{j_1} \dots \tau_{j_n}) c_{j_1}(\tau_{j_1}) \dots c_{j_n}(\tau_{j_n})$$

Now in growing the dimension of the system, conservation of energy implies that the hopping terms scale like  $t_{ij} \sim \sqrt{1/d^{|i-j|}}$  (the space traveled by the particle grows like a random walk), so that in the  $d \rightarrow \infty$  limit only the nearest neighbor  $n = 1$  term survives. This implies a local self-energy (Eq. 3.5).

### 3.2 The Cluster Dynamical Mean Field Theory CDMFT

While DMFT has proved remarkably successful in describing problems whose physics is mainly local [35], having provided for example the first unified scenario of the Mott metal-insulator transition, it is not very suitable when the hypothesis of pure locality (Eq. 3.10) does not describe the physical properties of the system well. A natural extension of DMFT, able to introduce short range spatial correlation, is the Cluster Dynamical Mean Field Theory (CDMFT). The idea is very simple and preserves the spirit of the DMFT. Instead of considering a single site as impurity, we consider a cluster of sites and, as in DMFT, we construct an effective action by integrating out all the other degrees of freedom on the lattice (see Fig. 3.2):

$$\frac{1}{Z_{ef}} e^{-S_{eff}[c_{\mu\sigma}^\dagger, c_{\nu\sigma}]} \equiv \frac{1}{Z} \int \prod_{(i,j,\sigma) \neq (\mu,\nu)} Dc_{i\sigma}^\dagger Dc_{j\sigma} e^{-S}$$

where with  $(\mu, \nu)$  we indicate the coordinates inside the cluster-impurity. We obtain cluster-impurity problem embedded in a bath of free fermions, which again we write in a quadratic form:

$$S_{ef} = \int_0^\beta d\tau \sum_{\mu\nu\sigma} c_{\mu\sigma}^\dagger(\tau) \mathcal{G}_{\mu\nu\sigma}^{-1}(\tau) c_{\nu\sigma} + U \int_0^\beta d\tau \sum_{\mu} n_{\mu\uparrow}(\tau) n_{\mu\downarrow}(\tau)$$

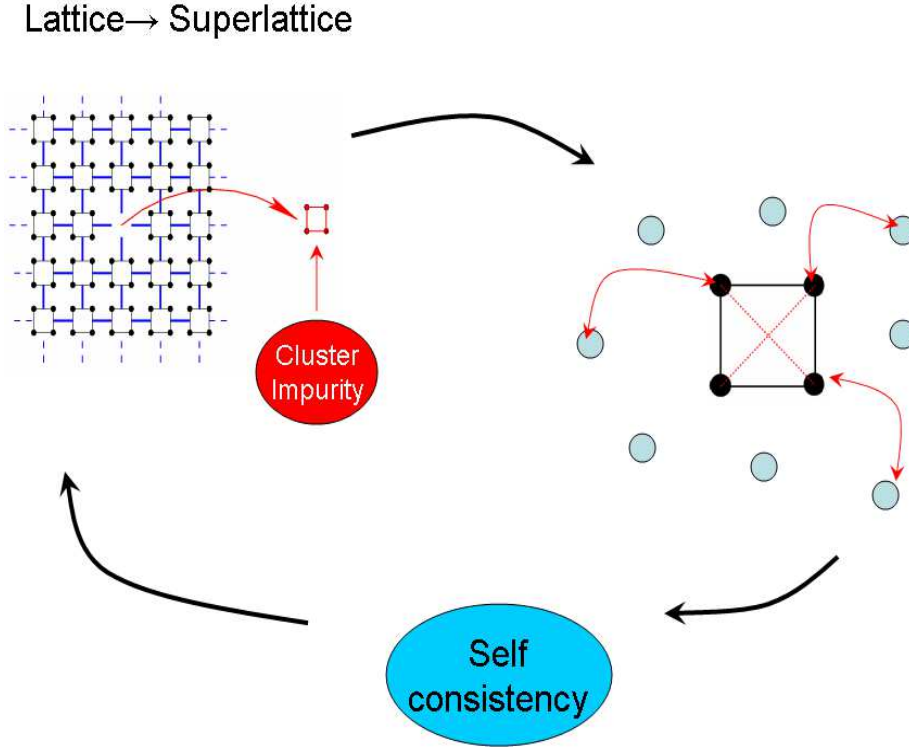


Figure 3.2: CDMFT loop

The difference with respect to DMFT is that now the Weiss field  $\mathcal{G}_{\mu\nu\sigma}(\tau)$  is a  $N \times N$  matrix expressing all the possible site-relations inside an impurity cluster of  $N^2$  sites. At this point we once again impose the self-consistency conditions requiring that the local cluster Green's functions is equal to the cluster Green's functions of the original model. "Local" this time means "inside the cluster", so that again we have  $N \times N$  Green's function relations:

$$G_{\mu\nu\sigma}(\tau) = -T_\tau \langle c_{\mu\sigma}^\dagger(\tau) c_{\nu\sigma} \rangle_{S_{ef}} \quad (3.11)$$

But how do we evaluate the lattice Greens's function having now not only the local self-energy  $\Sigma$  but a set of cluster-self-energies  $\Sigma_{\mu\nu}$ ? Here lies the central idea in CDMFT. We apply the same concept of DMFT to the cluster-impurity, considered as a site of a "super-lattice" whose sites are in their turn cluster of sites of the original lattice (top left hand-side of Fig.3.2). We construct a super-lattice Green's function assuming the cluster-self energy  $\Sigma_{\mu\nu}$  local as in DMFT (but this time the term local covers a range

of the size of the cluster-impurity):

$$\hat{G}(K, \omega) = \frac{1}{(\omega + \mu) \hat{\mathbf{1}} + \hat{t}_K - \hat{\Sigma}} \quad (3.12)$$

The Fourier space of the superlattice  $K$  is defined in a Brillouin Zone (RBZ), reduced by the partition of the original lattice into  $N$ -site-clusters. Here the  $N \times N$  relations inside the cluster-impurity are expressed in a matrix notation,  $\hat{\mathbf{1}}$  is the  $N \times N$  identity matrix,  $\hat{t}_K$  the intra-cluster hopping matrix, and it expresses the band-dispersion in the superlattice, like  $\varepsilon_k$  was the band dispersion in the momentum space of the original lattice in DMFT (expression 3.7). As usual, the local cluster-Green's function is the sum in the RBZ of the super-lattice Green's function:

$$\hat{G}_{loc}(\omega_n) = \sum_K \hat{G}(K, \omega) = \int_{RBZ} \frac{1}{(\omega_n + \mu) \mathbf{1} - \hat{t}_K - \hat{\Sigma}(\omega_n)} \frac{dK^d}{(2\pi)^d/N_c} \quad (3.13)$$

and then we obtain a set of closed equations imposing this local cluster-Green's function  $\hat{G}_{loc}$  equal to the one obtained from the effective quantum action:

$$\hat{G} \equiv \hat{G}_{loc} \quad (3.14)$$

or equivalently

$$\Sigma_{\mu\nu}(\omega) = \mathcal{G}_{\mu\nu}^{-1}(\omega_n) - G_{\mu\nu\sigma}^{loc-1}(\omega, \hat{\Sigma}) \quad (3.15)$$

CDMFT allows for consideration of the correlation between particles up to a distance of the order of the cluster-size. The advantage is clear, as we can now cope with problems whose relevant physical properties are not purely local. These are typically encountered in real finite size systems. Taking the limit  $d \rightarrow \infty$  would be in this case not very efficient, as  $\Sigma_{ij} \rightarrow 0$  for every  $i \neq j$ , i.e. CDMFT  $\rightarrow$  DMFT. But in using CDMFT on finite size systems, it is also clear that the gaussian representation of the effective action  $S_{ef}$  is no longer exact, unlike DMFT, and we are using an approximation. The quality of the approximation is dependent on the cluster-size as compared to how much local is the physics of the problem specifically considered. We will make clear examples and applications in the following chapter.

### 3.3 Exact Diagonalization Method

We now face the problem of solving the effective associated impurity problem. Fortunately, as the Anderson impurity problem has been studied for over 35 years, there exist various methods well-established in literature, either analytical (perturbation theory methods, projective methods [34]) and numerical (Quantum Monte Carlo [40] and Exact Diagonalization [10][60][62]). In this work we use the Exact Diagonalization (ED) method on small (up to 12 sites) cluster. The advantage of ED is the high precision in determining the zero-temperature groundstate-properties and the access to real frequency information, as well as the ability to treat the large- $U$  regime, which is hardly accessible by Quantum Monte Carlo (QMC).

#### 3.3.1 Truncation of the problem size

In practical implementations the quadratic effective action  $S_{ef}$  is derived from an Anderson Impurity Hamiltonian  $\mathcal{H}_{AI}$ . In CDMFT the site-impurity is replaced by a cluster-impurity:

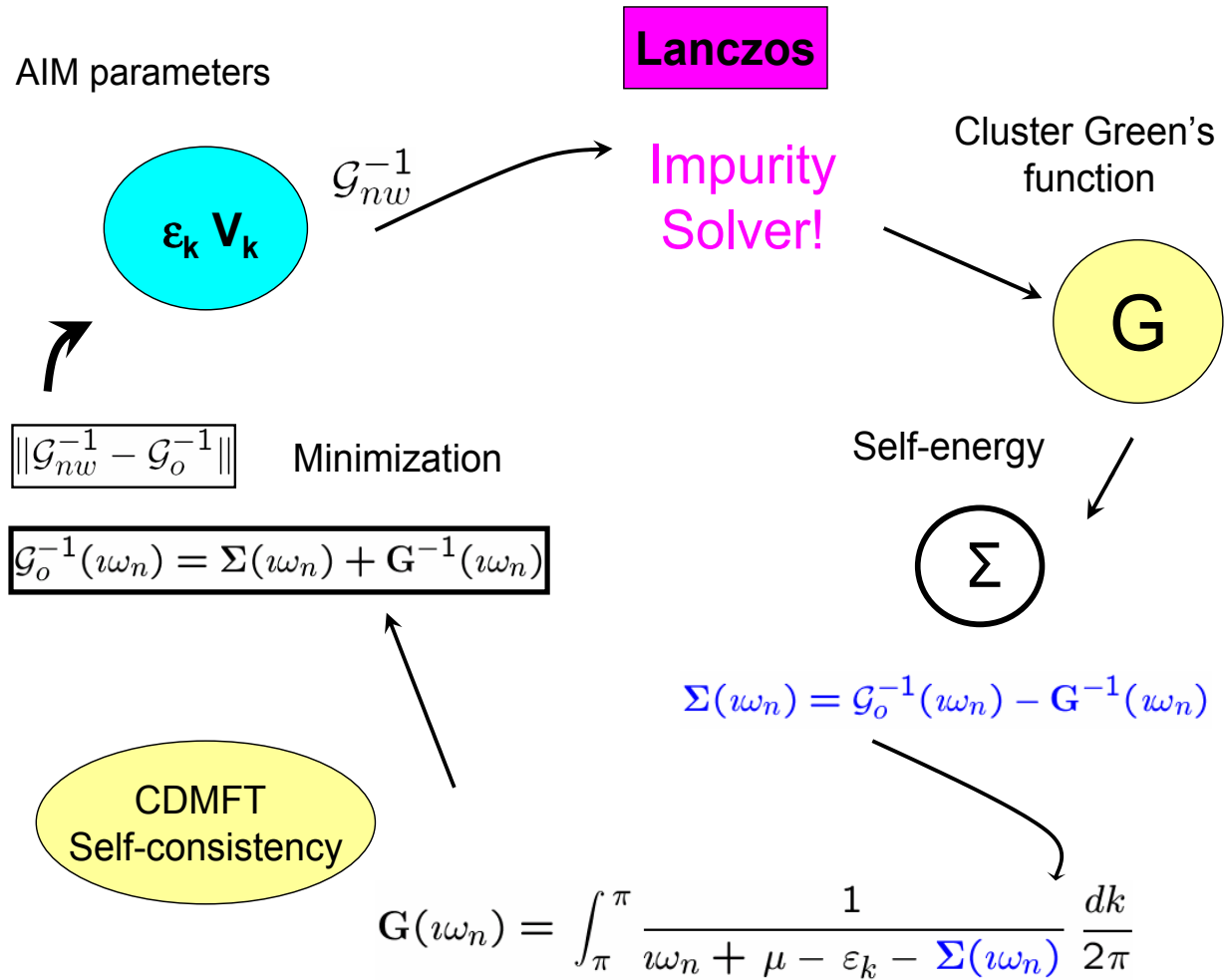
$$\mathcal{H}_{AI} = \sum_{\mu\nu} \sum_{\sigma}^{n_c} E_{\mu\nu\sigma} c_{\mu\sigma}^{\dagger} c_{\nu\sigma} + U \sum_{\mu}^{n_c} c_{\mu\uparrow}^{\dagger} c_{\mu\uparrow} c_{\mu\downarrow}^{\dagger} c_{\mu\downarrow} \quad (3.16)$$

$$\sum_k \sum_{\sigma}^{n_b} \varepsilon_{k\sigma} a_{k\sigma}^{\dagger} a_{k\sigma} + \sum_k \sum_{\mu\sigma}^{n_b} V_{k\mu\sigma} a_{k\sigma}^{\dagger} c_{\mu\sigma} + V_{k\mu\sigma}^* c_{\mu\sigma}^{\dagger} a_{k\sigma} \quad (3.17)$$

$$(3.18)$$

Here we have introduced the fermionic operators  $c_{\mu\sigma}$  which destroy an electron with spin  $\sigma$  on site  $\mu$  of the cluster-impurity, and  $a_{k\sigma}$  which destroys an electron on site  $k$  of the free electron bath. The matrix  $E_{\mu\nu\sigma}$  contains the original model hopping parameters (for example for the Hamiltonian 3.1 it the chemical potential  $\mu$  on the diagonals and the hopping parameter  $-t$  in nearest neighbor sites  $|\mu - \nu| = 1$ ). The Hamiltonian describes the cluster-impurity (labels  $\mu, \nu$ ) embedded in a self-consistent free electron bath with dispersion  $\varepsilon_k$  which is hybridized through the hopping parameters  $V_{k\mu\sigma}$ . The  $(\varepsilon_k, V_{k\mu\sigma})$  are the variables to be determined by the self-consistency condition. The primary simplification of the ED-method lies in considering a finite-site ( $n_s$ ) AIM, where the bath is truncated to a finite number of orbitals  $n_b$  (in practice the total number of

Figure 3.3: ED loop



sites handled is  $n_s \simeq 12$ ). The problem can be thereby solved using standard *Lanczos* algorithms (see APPENDIX B for more detail). We stress here that a truncation in the effective Anderson impurity problem does not imply a truncation in the original lattice problem, which fully retains its thermodynamical limit. The free-electron bath determines the cluster-impurity Weiss field,

$$\mathcal{G}_o^{\mu\nu}(\imath\omega_n)^{-1} = \imath\omega_n \delta_{\mu\nu} + E_{\mu\nu} - \sum_k^{\infty} \frac{V_{\mu k}^* V_{k\nu}}{\imath\omega_n - \varepsilon_k}$$

which within this procedure is therefore truncated in a finite-pole expansion:

$$\mathcal{G}_{ob}^{\mu\nu}(\imath\omega_n)^{-1} = \imath\omega_n \delta_{\mu\nu} + E_{\mu\nu} - \sum_k^{n_b} \frac{V_{\mu k}^* V_{k\nu}}{\imath\omega_n - \varepsilon_k} \quad (3.19)$$

The AIM is then solved self-consistently, using the Dyson's equation 3.15.

### 3.3.2 The ED-loop for CDMFT

The ED-loop consists of the following steps (see Fig. 3.3):

1. The truncated impurity problem is solved with a *Lanczos* procedure, which accurately determines the ground state  $|gs\rangle$  of the associated AI Hamiltonian  $\mathcal{H}_{AI}$ . This is done in the usual way, i.e. by picking a random wave-function  $|\varphi\rangle$  in an appropriate subspace of the full Hilbert space, according to the symmetries of  $\mathcal{H}_{AI}(\varepsilon_k, V_k)$ , and diagonalizing  $\mathcal{H}_{AI}$  in a linear hull of  $|\varphi\rangle, \mathcal{H}_{AI}|\varphi\rangle, \dots, \mathcal{H}_{AI}^n|\varphi\rangle$ . The local zero-temperature cluster-impurity Green's  $G_{\mu\nu}$  is obtained choosing as initial vector  $|\varphi\rangle = c^\dagger|gs\rangle$  and implementing a second Lanczos procedure, which takes advantage of the continued-fraction representation of a Green's function describing the "particle" ( $\omega > 0$ ) and "hole" excitations [35]:

$$G_{\mu\nu}(\omega) = G_{\mu\nu}^>(\omega) + G_{\mu\nu}^<(\omega)$$

with

$$G_{\mu\nu}^>(\omega) = \frac{\langle gs | c_{\mu\nu} c_{\mu\nu}^\dagger | gs \rangle}{\omega - a_0^> - \frac{b_1^>{}^2}{\omega - a_1^> - \frac{b_2^>{}^2}{\omega - a_2^> - \dots}}}$$

$$G_{\mu\nu}^<(\omega) = \frac{\langle gs | c_{\mu\nu}^\dagger c_{\mu\nu} | gs \rangle}{\omega - a_0^< - \frac{b_1^{<2}}{\omega - a_1^< - \frac{b_2^{<2}}{\omega - a_2^< - \dots}}}$$

The  $a$  and  $b$  parameters entering this expression are directly determined in the diagonalization procedure of  $\mathcal{H}_{AI}$ . We notice that the same equations can be used to extract the Green's function on the real axis as well as on the Matsubara axis by simply using analytical continuation  $\omega_n \rightarrow \omega + i\delta$ , where  $\delta$  is a small number giving a spreading around the real-axis pole. This is an advantage over other techniques, in the QMC, for example, the analytic continuation procedure is non-trivial.

- Using the self-consistency condition 3.9 to extract first  $\Sigma$ , we can close the DMFT equations determining the local cluster-Green's function:

$$\hat{G}(\omega, \hat{\Sigma}) = \sum_{k \in RBZ} \frac{1}{\hat{\mathbf{I}}(\omega + \mu) + \hat{t}_k - \hat{\Sigma}}$$

- We then use again the self consistency condition 3.9 to determine a new Weiss function:

$$\mathcal{G}_{o_{new}}^{\mu\nu}(\omega)^{-1} = \Sigma_{\mu\nu}(\omega) + G_{\mu\nu}(\omega)^{-1}$$

- The final step, which determines the new bath parameters  $\varepsilon_k$  and  $V_k$  in the  $\mathcal{H}_{AI}$ , is the more subtle one. In the CDMFT-Lanczos-procedure the problem consists of finding the best set of  $\varepsilon_k$  and  $V_k$  determining the new finite-pole expansion of the Weiss function  $\mathcal{G}_{o_{nb}}^{\mu\nu}(\omega)$ , which better describes the new  $\mathcal{G}_{o_{new}}^{\mu\nu}(\omega)$  coming from the CDMFT-self-consistency. This is equivalent to projecting  $\mathcal{G}_{o_{new}}^{\mu\nu}(\omega)$  onto a space of functions  $\{\mathcal{G}_{o_{nb}}^{\mu\nu}\}$  built from a finite set of orbitals  $n_b$ . For this there is not one unique procedure, and different methods have been proposed (for a review [35]). In this work we follow the method developed in the context of single site ED-DMFT by Caffarel and Krauth [10], which defines a distance-function  $f = \|\mathcal{G}_{o_{nb}}^{\mu\nu}(\omega_n)^{-1} - \mathcal{G}_{o_{new}}^{\mu\nu}(\omega_n)^{-1}\|$  and a *minimization* procedure to determine the set of bath-parameters which minimize this distance. We notice that:

- the definition of  $f$  is arbitrary, being difficult to define a unique criterion of distance between two functions. We will follow physical intuition in defining a  $f$ , verifying *a posteriori* the results. We will adopt in this work mainly two distancefunctions  $f$ :

$$f = \sum_n^{n_{\max}} \frac{1}{|\omega_n|} \left| \mathcal{G}_{onb}^{\mu\nu}(\omega_n)^{-1} - \mathcal{G}_{onew}^{\mu\nu}(\omega_n)^{-1} \right| \quad (3.20)$$

$$f = \sum_n^{n_{off}} \left| \mathcal{G}_{onb}^{\mu\nu}(\omega_n)^{-1} - \mathcal{G}_{onew}^{\mu\nu}(\omega_n)^{-1} \right| \quad (3.21)$$

The distance  $f$  is defined on the Matsubara axis where the functions have no pole and are smoothly behaved. In definition 3.20  $n_{\max}$  is an upper energy-cutoff which includes the typical maximum scale of the problem (in a Hubbard problem, for example, some factor of the on-site interaction  $U$ ). The  $\frac{1}{|\omega_n|}$  is chosen with the task to weight more the low-energy scale, which is important in capturing the low-energy physics of the Mott metal-insulator transition. The success of this choice in describing the MT is showed in a one-dimensional study of the Hubbard Model (next chapter and [12]). In definition 3.21,  $n_{off}$  is a low energy cut-off of the order of the bandwidth  $\sim t$ . This definition is more suitable to describe the low energy physics of the doped systems not very close to the MT, where the transfer of spectral weight from the low-energy peak to the Hubbard Bands is still a negligible effect.

- Introducing the distance  $f$  on the Matsubara axis requires defining a fictitious temperature, which determines a low energy cutoff. This temperature acts like a virtual temperature in the system: despite the Green's function being evaluated on the ground state of the associated AIM, the self-consistency is implemented at a virtual temperature  $1/\beta$  determined by the grid of points it selects on the Matsubara axis. In the following chapter we will show examples on how this effects the results in connection with QMC-impurity-problem studies at high temperature.

## Chapter 4

### Implementation of CDMFT

#### 4.1 Benchmark on the 1D Hubbard Model

In order to elucidate some of aspects of the ED-CDMFT procedure we present in this section a comparison with the exact Bethe Ansatz (BA) solution for the one dimensional Hubbard Model [50]. This is the worst case scenario for a mean field theory: the doped system is a Luttinger Liquid which presents a non-analytic behavior in the low frequency part of the Green's functions . Nevertheless we can study the metal-insulator transition focusing the attention on thermodynamical quantities, such as for example the density in the system or the charge compressibility. We first present the result leaving for the following subsections practical examples on the CDMFT implementation.

##### 4.1.1 Improvement of CDMFT on DMFT

In Fig. 4.1, we display a plot of the density of the system  $n$  as a function of the chemical potential  $\mu$  for the Hubbard Model with only two sites in the cluster  $N_c = 2$  and  $N_b = 8$  sites in the bath. Two case are shown: the weakly interacting  $U = t$  (upper panel) and the intermediate  $U = 4.0t$  (lower panel). We compare the result of CDMFT with the single-site DMFT and benchmark it with the exact Bethe Ansatz (BA). For  $U = t$  we observe that both CDMFT and DMFT are able to well portray the exact density. All the CDMFT-circles and the DMFT-crosses lay on the continuous BA-curve, up to the half-filled state at density  $n = 1$ . We will see later (Fig. 4.2), however, that, contrary to CDMFT, DMFT is giving a wrong insulating state even if the density is correctly described. The differences between CDMFT and DMFT are seen sharply in the intermediate coupling case  $U = 4t$ , where the value of interaction is equal to the bandwidth, and the interacting and kinetic parts of the Hubbard Hamiltonian are in

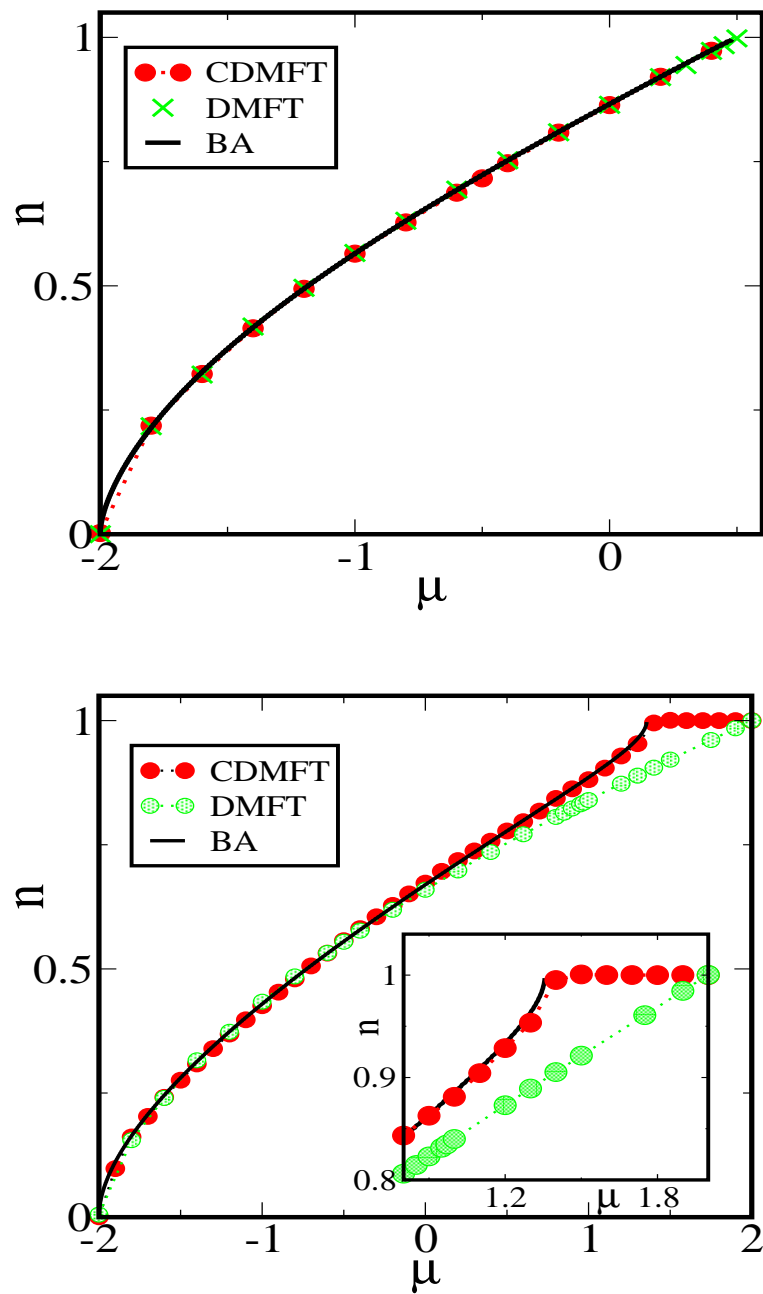


Figure 4.1: Density  $n$  vs. chemical potential  $\mu$  in the 1D Hubbard Model. The CDMFT method is compared with the single-site DMFT and the exact Bethe Ansatz (BA) result. Upper panel:  $U/t = 1.0$ ,  $N_c = 2$ ,  $N_b = 8$ . Lower panel:  $U/t = 4.0$ ,  $N_c = 2$ ,  $N_b = 8$ . The inverse virtual temperature is  $\beta = 300$ .

competition. At high doping (up to  $n \sim 0.75$ ) CDMFT and DMFT once again perform equally well in describing the correct density of the system. The situation is clearly different near the half-filled insulating state. The insulating phase, in fact, persists around the particle-hole symmetric point  $\mu = U/2$ , where the  $n$  vs.  $\mu$  curve shows a plateau of values, until sharply going into the metal phase at some critical  $\mu$ . The charge compressibility is at this point divergent, as is shown by the continuous black BA line. This behavior is difficult to capture in a mean field approach. Single-site DMFT (green dotted line) fails in fact in describing the MT. Cluster-DMFT instead, with only two sites  $N_c = 2$  in the impurity-cluster, is able to follow very successfully the BA line (as evidenced in the inset), following then the half-filled insulating solution at constant density  $n = 1.0$ .

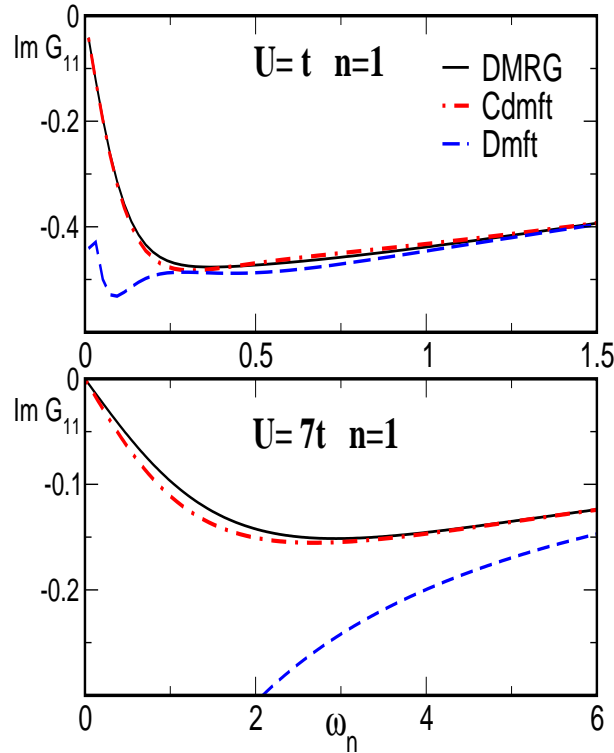


Figure 4.2: Imaginary part of the local cluster Green's function at half-filling. The CDMFT result is compared with the previous single-site DMFT. DMRG calculation, provided in [9], is used as bench-mark. The upper panel shows the weakly interacting case  $U/t = 1$ , the lower panel the strongly interacting  $U/t = 7$ .  $N_c = 2$ ,  $N_b = 8$  and  $\beta = 300$ .

These considerations are also supported by the analysis of dynamical quantities. As in Ref. [9], we consider the imaginary part of the on-site Green's function  $G_{11}$  on the Matsubara axis, which is plotted for  $U/t = 1, 7$  and for  $n = 1$  (Fig. 4.2). We display CDMFT and single-site DMFT, again for  $N_c = 2$  and  $N_b = 8$ , compared with the results of Density-Matrix Renormalization Group (DMRG), a numerical approach which is known to provide essentially exact results for one-dimensional systems (for more details on our calculation of dynamical properties with DMRG, see Ref. [9]). The agreement of CDMFT with the virtually exact DMRG results is extremely good for  $U/t = 1$ . Interestingly, the single-site DMFT completely fails in the description of dynamical properties even if the  $n-\mu$  curve shown in Fig. 4.1 is close to the exact solution. In the strong coupling case  $U/t = 7$ , CDMFT closely follows the DMRG result while single-site DMFT totally fails.

This examples show:

1. how important it is to consider short-ranged local interaction in finite dimensional systems to describe the peculiarity of the the MT.
2. the importance of correctly weighting the low energy scale as compared with the high energy scale of the Hubbard bands. This result has been obtained in fact using the low-energy weighted distance introduced in the previous section which gives importance to the low energy physics at the critical point of the transition.

But how precise is the result and how much depends on the number of sites used to solve the associated AIM?

#### 4.1.2 Implementation of CDMFT

We answer the question at the end of the previous subsection by explicitly showing how to implement the Lanczos-CDMFT in an efficient way. We offer a clever way of exploiting symmetries (particularly in one dimension) in order to reduce the number of the degrees of freedom in the bath-parametrization and, in addition, a fast way to select the ground-state of the associated Anderson impurity problem by first freezing the particle number and choosing then the right particle-sector.

### Reducing the parametrization: double-bath-degeneracy in one dimension.

We discuss here a peculiarity of the topology of the 1D CDMFT-implementation, which allows a reduction of the number of free parameters used (a similar parametrization for the 2D case is introduced at the end of this chapter). In 1D we can in fact consider the full bath as divided into two sub-baths (for example in the case  $N_b=8$ , we have 2 baths with  $N_b=4$ ). Pictorially, one sub-bath is placed at the left and the other on the right of the  $N_c=2$  cluster-dimer (Fig. 4.3). The electrons in the left site of the cluster can only jump to the left bath, while electrons in the right site can only jump to the right. We also require for there to be a trivial mirror-symmetry, imposing the bath energy  $\varepsilon$  and the  $V$ s to be the same on the left and on the right. The number of effectively used  $\varepsilon$  is reduced of  $\frac{1}{2}$ , and the number of  $V$ s of  $\frac{1}{4}$ . This reduction in the number of bath parameters derived from symmetry considerations in the one dimensional chain has its roots in the CDMFT-self-consistency condition (formula 3.8), which in 1D imposes that the nearest neighbor term of the hybridizing function  $\Delta_{12}$  (from formula 3.19)

$$\Delta_{\mu\nu}(i\omega_n) = \sum_k^{n_b} \frac{V_{\mu k}^* V_{k\nu}}{i\omega_n - \varepsilon_k} \quad (4.1)$$

is identically zero ([66]). This can be seen by explicitly calculating  $\Delta_{12}$  for the one-dimensional case in formula 3.8. In other words, under the viewpoint of the cluster-AIM, a particle can for example jump from the right site of the 2-site-cluster impurity onto the right free-interacting bath. There, it undergoes many dynamical processes before jumping back into the cluster-impurity. However, because of the 1D-topology of the chain, the particle in the right bath is forbidden to enter directly into the left-side bath or the left site in the cluster-impurity. In this way the nearest neighbor hybridizing field  $\Delta_{12}$  is zero, i.e. the nearest neighbor hopping, is not renormalized by the bath.

### Regular implementation of CDMFT

The CDMFT-solution depends on the initial guess of the AI bath parameters  $\varepsilon_k$  and  $V_k$ . In the ED method in particular, given the truncation of the bath to a finite number of orbitals  $N_b$ , the self-consistency condition formula 3.8 is only approximately fulfilled, being the degree of precision given by the fitting distance  $f$  between the continuous

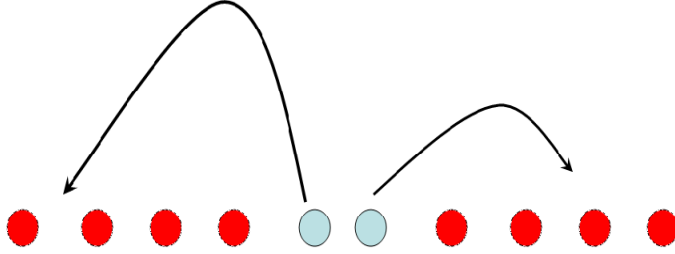


Figure 4.3: 2-site cluster-impurity in 1D. The particular topology of this case splits the free-particle bath in two degenerate sub-baths each one coupled to the correspondent site of the cluster-impurity.

and the discrete Weiss fields  $\Delta_{\mu\nu}$  (see section 3.4.1). It is in fact this minimization procedure, ultimately dependent on the definition of distance function  $f$ , that at each ED iteration determines the new AI bath parameters  $\varepsilon_k$  and  $V_k$  to be fed back into the impurity solver. The lowest-energy solution is then picked as the ground state, searching into all the particle sectors  $(n_{\uparrow}, n_{\downarrow})$  of the associate AIM. It is not clear *a priori* in which particle sector of the AIM the solution has to be looked for. It depends on the Hamiltonian parameters  $U/t$  and  $\mu/t$ , as well as on the starting guess of the AI bath parameters  $\varepsilon_k$  and  $V_k$ . Given a starting guess, however, the algorithm moves into the region around the  $(\varepsilon_k, V_k)$ -starting-point, searching for the best compromise between fulfillment of the self-consistency condition (minimum in the distance-function  $f$ ) and determination of the ground state.

### Fast implementation of CDMFT

In order to clarify how the algorithm works in balancing between the self-consistency constrain and the determination of AIM-groundstate, we present in the following a procedure which allows on one hand a faster determination of the AIM-groundstate, on the other the resolution of converging problems that can arise in frequent changes between particle-sectors at each DMFT-iterational step. The latter situation may take place if the ground-state energies of two different particle-sectors of the AIM are very close. This can make it difficult to determine a convergent DMFT-solution, as the algorithm gets trapped in a resonant loop between the two different (yet close) solutions

$U/t=4.0$   $N_c=2$   $N_b=6$

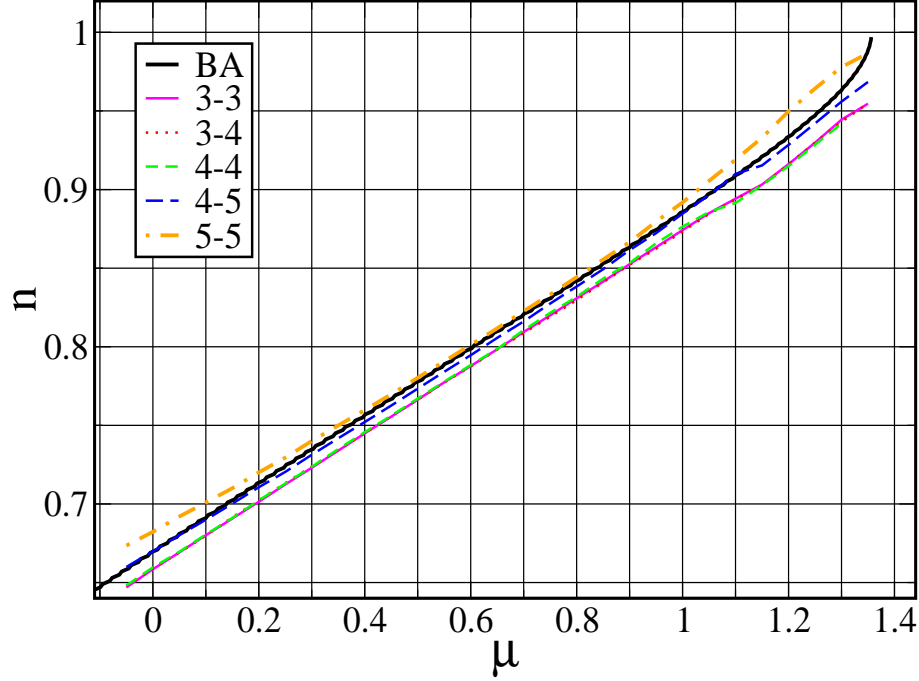


Figure 4.4: Density vs. chemical potential,  $n$  vs.  $\mu$  in the 1D Hubbard Model. Solutions are obtained starting from the same seed and fixing the number of particle-sector in the AIM. Sector span from  $(n_{\uparrow}, n_{\downarrow}) = 3 - 3$  to  $5 - 5$ . The black continuous line is the BA solution.

in the two different particle-sectors. We therefore

1. constrain the particle-sector  $(n_{\uparrow}, n_{\downarrow})$ , and there seek the CDMFT-solution. Naturally more tasks can be attempted in parallel for each particle sector: notably this saves computational time in the determination of the impurity solver ground-state.
2. then check each particle sector to ensure that the solution determined is a real ground-state of the AIM by allowing a loop on all the other  $(n_{\uparrow}, n_{\downarrow})$  sectors: if the bath [ i.e. the AI parameters  $(\varepsilon_k, V_{\mu k})$  ] do not change the solution is accepted, otherwise it is disregarded.

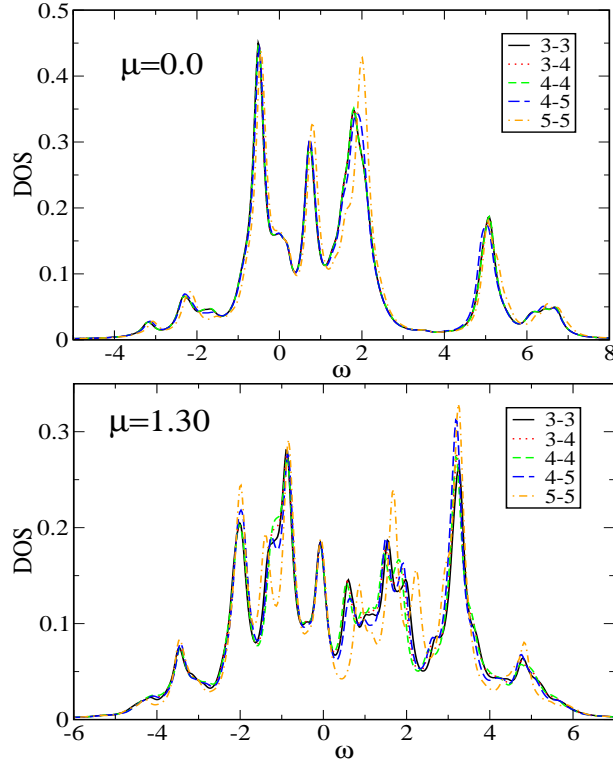


Figure 4.5: Local DOS in two points,  $\mu = 0.0$  and  $\mu = 1.30$ , of the  $n$  vs.  $\mu$  curve displayed in Fig. 4.4. The curves shown are for different particle-sectors, nevertheless the physics described is the same.

### A practical example of fast implementation

We show now the advantages and equivalence of this fast implementation with respect to the regular implementation. In Fig. 4.4 we freeze the particle sectors  $(n_{\uparrow}, n_{\downarrow})$  of the associated AIM and seek for the solution in each of them separately. In the case displayed  $U/t = 4.0$ , the chain used is  $N_s = 8$  sites long with  $N_c = 2$  sites in the impurity-cluster and  $N_b = 6$  sites in the bath. We start with the same bath-parameter guess  $(\varepsilon_k, V_{\mu k})$  and span the sectors from  $(n_{\uparrow}, n_{\downarrow}) = (3, 3)$  to  $(5, 5)$ , a reasonable occupation for the densities expected in the range of chemical potential displayed. Starting from the same seed we let the solution develop in each particle sector. As evidenced from Fig. 4.4, we obtain different curves which at their best mimic the BA exact curve (continuous black line). Because of the constrained  $(n_{\uparrow}, n_{\downarrow})$ , the algorithm does its best to adjust the bath parameters  $\varepsilon_k$  and  $V_k$  in order to best fulfill self-consistency (looking

for a minimum in  $f$ ). So, in each fixed particle sector, the paths in the parameter space taken to the solution are all different, as well as the final sets of  $\varepsilon_k$  and  $V_k$ . Nevertheless the curves are reasonably close, the difference being of the order of 1%. In fact from particle sector  $(n_\uparrow, n_\downarrow) = (3, 3)$  to  $(4, 4)$  the solutions are practically the same, more different are the ones in sector  $(4, 5)$  and  $(5, 5)$ . Notice that the  $(4, 5)$ -sector solution is the one that better reproduces the BA curve, except very close to the MT point; this however cannot be considered as a criterion to set the solution as the "best" one in the CDMFT procedure. We show now that, in spite of the apparent quantitative difference in the densities of the solutions in different sectors (which we remark is nevertheless quite small, of the order of 5% in the worst case), the physics described is the same. In Fig. 4.5 we display the local density of states  $\text{DOS} = -\frac{1}{\pi} G_{11}(\omega)$  in two points of the  $n$  vs.  $\mu$  diagram, one in the far doping region ( $\mu = -0.10$  and  $n = 0.68$ , upper panel of Fig. 4.5) and close to the MT point ( $\mu = 1.3$  and  $n = 0.96$ , lower panel of Fig. 4.5). It is once again evident that the solution from sectors  $(3, 3)$  to  $(4, 4)$  are for all practical purpose the same, despite the ground-state of the AIM is evaluated in different particle sectors. The differences with sectors  $(4, 5)$  and  $(5, 5)$  are tiny even quantitatively in the far doped case (upper panel), larger close to the MT (lower panel), overall they describe the same solution. This is most comforting: even if we constrain the impurity solver (in this case the particle sector), CDMFT works to achieve the same physical results in the limits imposed by the constrain. But among the many possible solutions in different sectors, which one do we pick? As said above, we choose the solution in the sector that is a real ground-state for the associated AIM, i.e. the solution which does not change once the fixed- $(n_\uparrow, n_\downarrow)$ -constrain is relaxed. In this case the winning sector is  $(n_\uparrow, n_\downarrow) = (4, 4)$ .

We show that this fast procedure is in fact equivalent to the regular procedure, taking advantage once again of the example we used above. In Fig. 4.6 we start from the set of solutions determined in Fig. 4.4 by constraining the particle-sector, and we use them as starting seed to implement a new calculation with free number of particles in the impurity solver. All the solutions end on the same curve, independent of the sector we started from. In order to have a better understanding on how the result

$$U/t=4.0 \quad N_c=2 \quad N_b=6$$

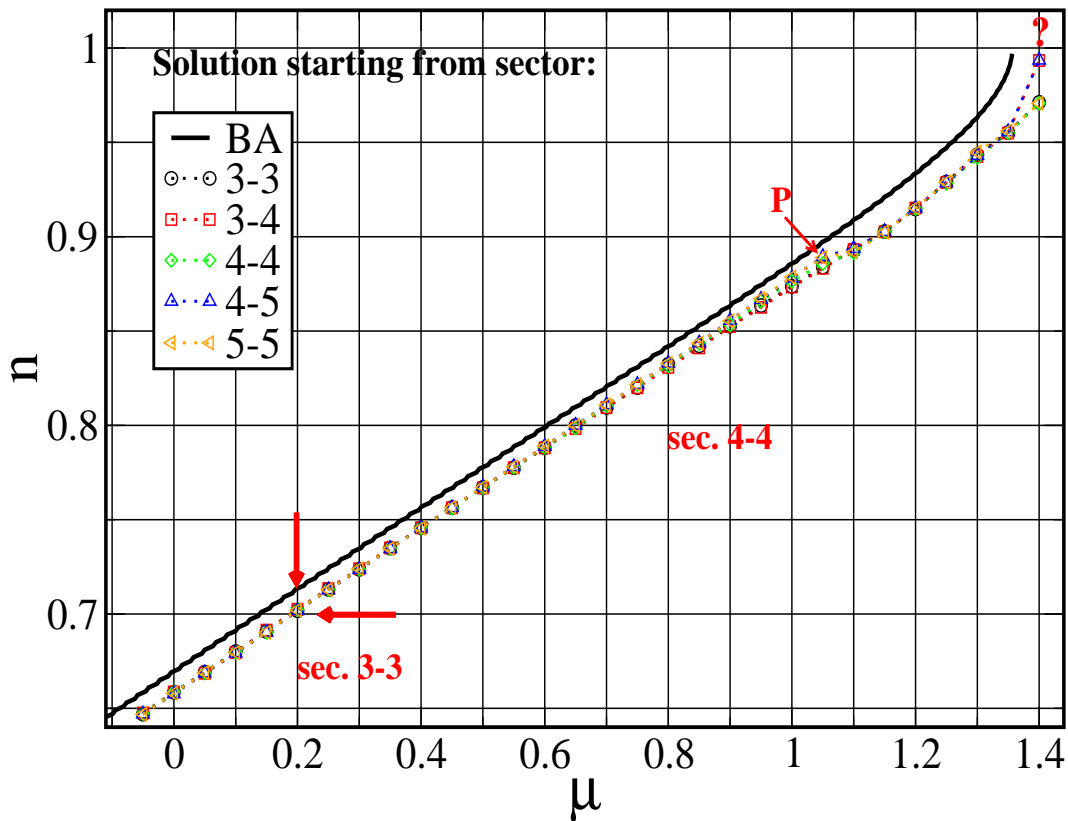


Figure 4.6: We show the result  $n$  vs.  $\mu$  obtained starting in each particle sector from the previously determined solution (ref. Fig. 4.4) at fix number of particles in the AIM and freeing the particle sectors. All the runs end onto the same solution.

develops, let us take a closer look to the curves of Fig. 4.6. First of all, we observe that in all the cases the solutions found share the same particle-sector  $(n_{\uparrow}, n_{\downarrow})$ , and that the solutions are the same in the limit of computational precision. An estimate of the latter is given close to the point  $P$  indicated in Fig. 4.6, where the solutions differ the most. We stress that this tiny difference does not correspond to a different physical solution. It indicates that, according to the particle-sector we started from, in some cases the solution chosen acquires a bigger distance function  $f$  or a higher G.S.E., contrary to the common intuition that these two quantities should be as small or negative as possible. Secondly, we notice that all the solutions start from far doping in the sector  $(n_{\uparrow}, n_{\downarrow}) = (3, 3)$  and at some point (around  $\mu = 0.20$  and  $n = 0.70$ ) they

switch to the sector  $(n_{\uparrow}, n_{\downarrow}) = (4, 4)$  (two perpendicular arrows in Fig. 4.4). This is natural: according to the actual filling of the system which is monotonically increasing with the chemical potential  $\mu$ , the associated AIM tends to increase its particle density too. The point corresponding to  $\mu = 0.20$  is highly degenerate, being the G.S.E of the sectors  $(n_{\uparrow}, n_{\downarrow}) = (3, 3), (3, 4), (4, 4)$  very close, in the limit of a continuous line of  $n$  vs.  $\mu$  equal. This signals the passage from sector  $(n_{\uparrow}, n_{\downarrow}) = (3, 3)$  to  $(4, 4)$ . The set of curves remains in the latter sector until they reach the MT point in correspondence of  $\mu = 1.4$ . Here it is not possible to reach a converged solution very easily (question mark in Fig. 4.4). The solutions oscillates between two densities  $n = 0.97$  and  $n = 0.99$  corresponding to sectors  $(n_{\uparrow}, n_{\downarrow}) = (4, 5)$  and  $(n_{\uparrow}, n_{\downarrow}) = (5, 5)$ . Evidently the solution attempts a switch of particle sector, this time from  $(n_{\uparrow}, n_{\downarrow}) = (4, 5)$  to  $(n_{\uparrow}, n_{\downarrow}) = (5, 5)$ , demonstrating in this way the diverging compressibility of the 1D result. However the steep change in the density for a small change in the chemical potential requires a slow move from point to point on the  $n$  vs  $\mu$  line close to the MT-region, in order to direct the solution to convergence (as it was done on Fig. 4.1). Another efficient way to determine this point is to use a finite-temperature Lanczos-calculation (see APPENDIX B). We can start introducing a temperature in the system (a virtual  $\beta^{-1}$  was already introduced in the zero-temperature-Lanczos-procedure to determine a grid of points on the Matsubara axis) whose magnitude has the same order of the difference in energy between the ground-states in sector  $(4, 5)$  and  $(5, 5)$ . A  $\beta = 64$  (in energy units of  $t$ ) satisfies the condition in this case. In principle we can consider many excited states, either ground-states of different particle sectors and excited states within the same sector, according to the cut-off determined by the scale of  $\beta^{-1}$ . The resulting density is a value between the two oscillating  $n = 0.97$  and  $n = 0.9$  displayed in Fig. 4.6, resulting from the mixing of states weighted by the Boltzmann's factors  $e^{-\beta(E-E_0)}$ . As the temperature is increasingly lowered, the state which has the minimum in energy (in sector  $(5, 5)$  in this case) dominates the mixing and the solutions approaches more and more this state.

### 4.1.3 Results with increasing bath-size

We wish now to study the effect of increasing bath size on the CDMFT solution. We therefore consider the  $N_b = 6$  solution determined in the previous section as starting point to build the solution with a bigger bath. We do not consider here a  $N_b = 7$ -bath

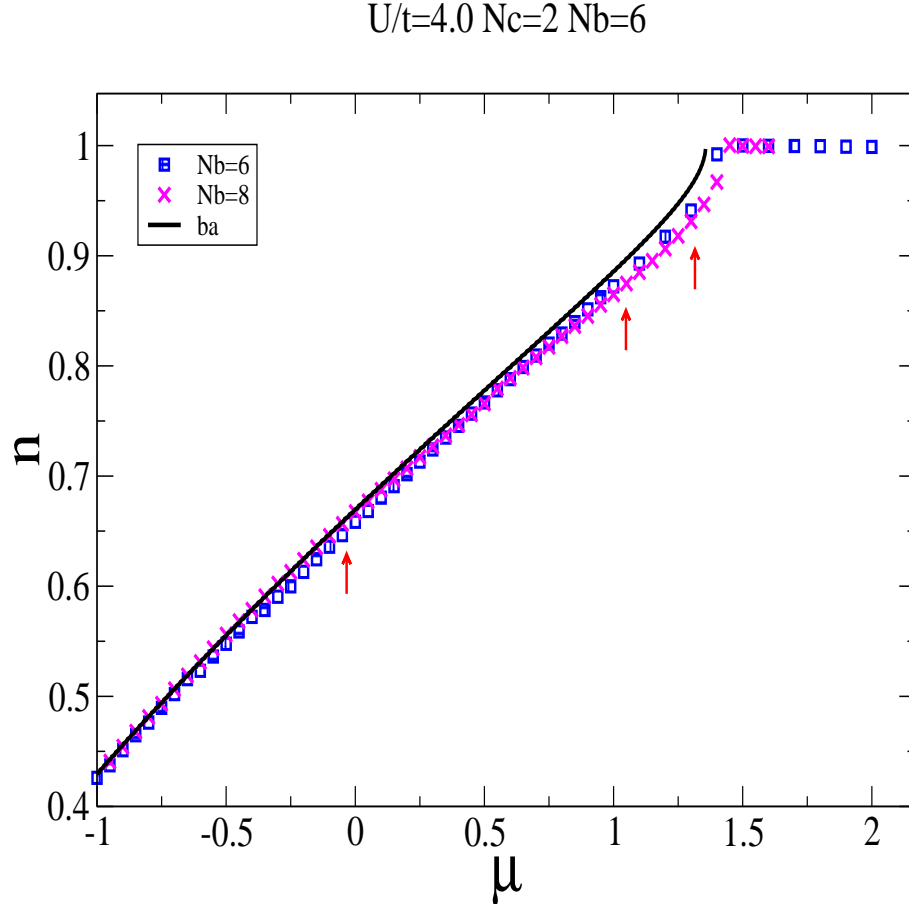


Figure 4.7:  $n$  vs.  $\mu$  curve obtained with  $N_b = 8$  (magenta crosses) from the  $N_b = 6$  (blue squares) of Fig. 4.4. The black continuous line is the BA solution.

sites case. Because of the breaking in the right-left double-chain symmetry (Fig.4.3), this kind of system is frustrated and yields worst result than  $N_b = 6$ . We therefore study a  $N_b = 8$  system, i.e. we add a site in the right and left-hand bath. A systematic way to proceed is to guess a value for the added pole  $\varepsilon_X$  and choose the hybridizing parameters  $V_{kX}$  an order of magnitude smaller than the ones determined with the  $N_b = 6$  solution, so that in the first iterational loop the result will not change too much

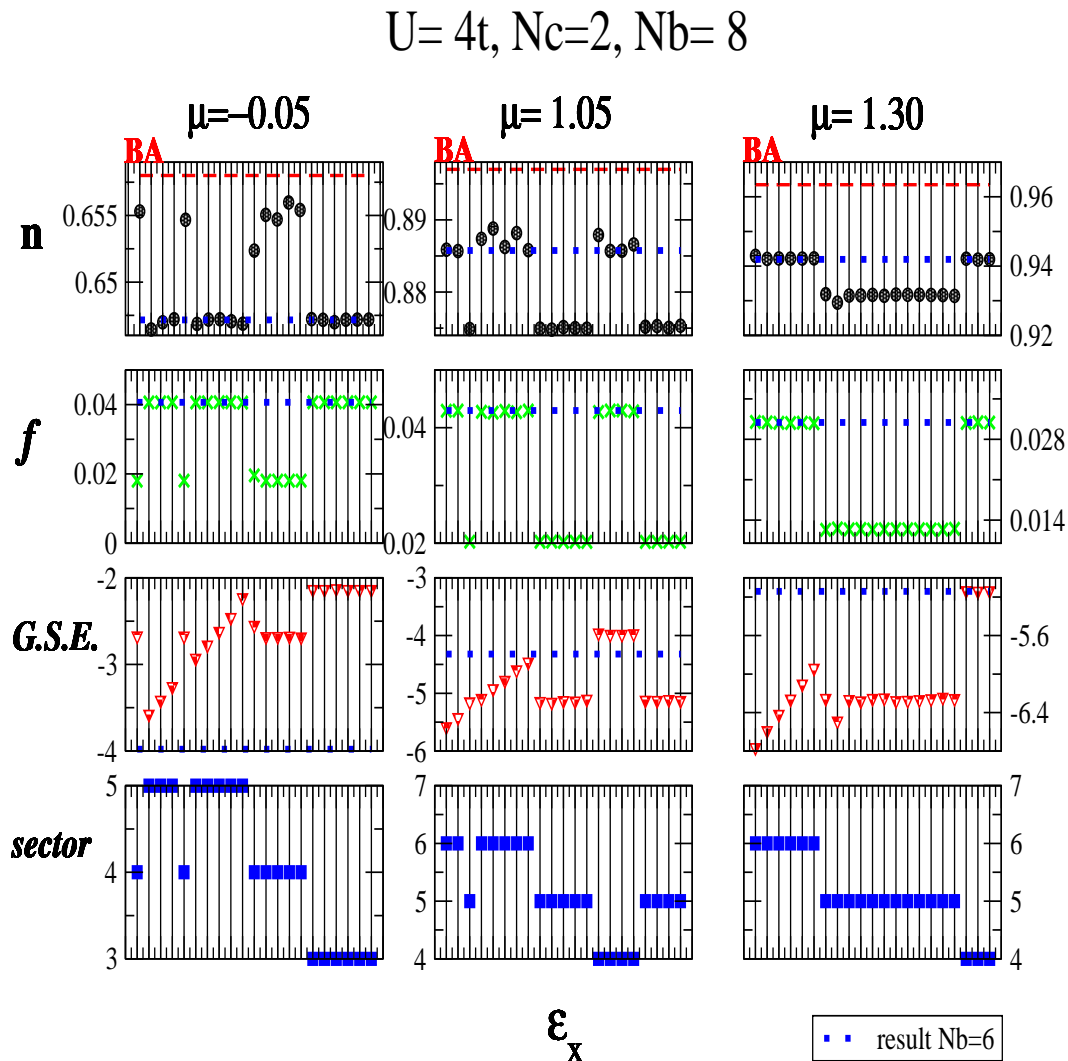


Figure 4.8: Three points of the  $N_b = 8$  solution (red arrows of Fig. 4.7), corresponding to  $\mu = -0.05$ ,  $\mu = 1.05$  and  $\mu = 1.30$  (each different column) are here analyzed in detail for many possible starting guesses grown from the  $N_b = 6$  result (labeled  $\epsilon_x \in [-0.4, 0.4]$  is the value of the bath-energy added to the  $N_b = 6$  solution). From the top to bottom we display: the density  $n$  (black dots) compared to the  $N_b = 6$  density (blue dotted line) and the BA density (dashed red line), the distance function  $f$  (green crosses, blue dots are always the  $N_b = 6$  result), the ground state energy of the AIM and, in the last row, the particle-sector of the AIM in which the solution was found. Notice that the  $N_b = 8$  solutions which lie on the blue dotted line do not improve the  $N_b = 6$  result, rather they reproduce it with a higher computational effort.

from the  $N_b = 6$  case. If the CDMFT condition favors a bath-energy in correspondence of the guessed  $\varepsilon_X$ , the  $V_{kX}$  starts growing and a new solution that better satisfies the CDMFT-condition develops. In this case we expect the distant-function  $f$ , which measures the precision in the self-consistency condition 3.8, to decrease from its  $N_b = 6$  value. In Fig. 4.8 we show the result of this procedure for three selected points: a far doping case at chemical potential  $\mu = -0.05$  and BA density  $n = 0.658$  (first column in Fig. 4.8), and close to the MT region  $\mu = 1.05$  and BA density  $n = 0.898$  (second column in Fig. 4.8) and  $\mu = 1.30$  and BA density  $n = 0.964$  (third column in Fig. 4.8). These three points are also indicated by the arrows in Fig. 4.7. We sample the added-pole  $\varepsilon_x$  in the range of values  $[-0.4, 0.4]$  which includes all the bath-energy levels  $\varepsilon$  for the  $N_b = 6$  solutions (but we also checked for values out of this range, not finding relevant modifications for the discussion that follows). The graph Fig.4.8 displays four rows, the vertical grid lines elongating in each column mark the same solution for a starting  $\varepsilon_x$ . The graphs in the first row from the top display the density  $n$  for each solution. The dashed red line is the BA value. The dotted blue line is the value of the  $N_b = 6$  result. In the second row we show the distance function  $f$  (again compared with the  $N_b = 6$  value). The third row displays the ground-state energy G.S.E. of the associated AIM. In the last row it is shown the particle sector where the solution was found.

First we observe that in all cases some solutions give the same result as in the  $N_b = 6$  case used as starting seed. These are the points that overlap with the dotted blue lines representing the value of the  $N_b = 6$  solution. This is true for the density as well as for the distance function  $f$  for all the three cases displayed. This set of solutions does not improve the  $N_b = 6$  result, rather it reproduces it but with a higher computational effort. Therefore these solutions are not to be considered good  $N_b = 8$  results and should be disregarded. Another set of solutions does change the  $N_b = 6$  result, lowering the distance function  $f$ , as evidenced in the second row (the set of green crosses which departs from the blue-dotted line) and showing a move toward the large size-limit solution. In the high-doped case  $\mu = -0.05$  (first column) this set of solutions corresponds not only to a smaller  $f$  (and so to a better satisfaction of the

self-consistency condition) but also to a net improvement in the density with respect to the BA value. The other two solutions close to the MT  $\mu = 1.05$  and  $\mu = 1.30$  (second and third column respectively) do not correspond to an improvement in the calculated density. The change is however small (less than 1%), and it is relevant that the divergent compressibility, a peculiar and difficult to capture feature of the MT in 1D, is well portrayed. So in the high doping region we observe a systematic improvement of the density of the system with increasing bath-size as compared to the exact BA value. At small doping, close to the MT, though this improvement is not observed, the self-consistency condition is better satisfied and the difficult character of the MT is well described (Fig. 4.7). There is no evident connection with the G.S.E. of the associated AIM, as evidenced in the third row of Fig. 4.8.

## 4.2 Comparison between QMC and CDMFT

We want to stress here the differences as compared with the previous high temperature Quantum Montecarlo study (QMC) of O. Parcollet, G. Biroli and G. Kotliar [56]. In their work they considered a strongly frustrated two-dimensional Hubbard Model at half-filling varying the on-site repulsion  $U$ . The cluster-impurity used was a  $2 \times 2$  square of 4 sites strongly anisotropic in the diagonal direction of the square. In their result they found that the imaginary part of the on-site cluster self-energy  $\text{Im}\Sigma_{11}$  was going to zero for  $\omega \rightarrow 0$ , while the diagonal cluster self-energy  $\text{Im}\Sigma_{13}$  was growing for small  $\omega$  close to the MT. This was the key-effect giving rise to the phenomenon of hot/cold spot modulation in  $k$ -space spectral properties. It was argued however that if  $\text{Im}\Sigma_{11} \rightarrow 0$  for  $\omega \rightarrow 0$ , so  $\text{Im}\Sigma_{13}$  had to do in order to preserve causality (i.e the cluster matrix  $\Sigma_{\mu\nu}$  has to be definite positive), an intrinsic property of the CDMFT method. This effect could not be observed in the Montecarlo study, which could not reach the required low energy scale because of the well known sign problem. The ED-CDMFT method is alternative and complementary to the QMC-CDMFT. It allows reaching a lower temperature range and higher values of the local interaction  $U$ . In Fig. 4.9 and 4.10 we show a comparison between ED and QMC results for the two dimensional Hubbard Model  $U/t = 8.0$ ,  $t' = 0.0$  in the metal phase at density  $n = 0.90$  (left panel of Fig. 4.9 and Fig. 4.10)

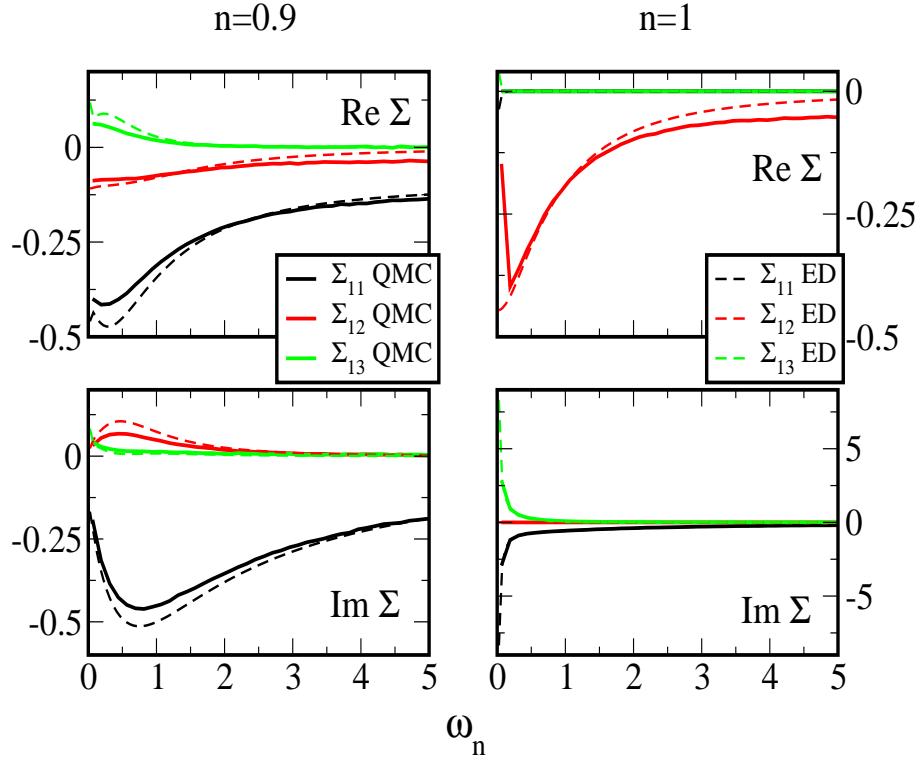


Figure 4.9: Confront between ED (dashed lines) and QMC (continuous lines),  $U/t=8.0$   $t'=0$ . QMC results are taken from [55], where energy units on the axis are half-bandwidth  $D = 4t$ . The cluster self-energies are shown for a doped system ( $n = 0.90$ ) on the left-hand side, and in the insulating half-filled system ( $n = 1.0$ ) on the right-hand side. In the latter case the particle-hole symmetry produces zero real parts in  $\Sigma_{11}$  and  $\Sigma_{13}$  (top right hand side panel). The inverse QMC temperature is  $\beta = 12.5$  (in the  $t = 1$  energy units used in this thesis), the virtual temperature of the ED solution is  $\beta = 32$ .

and at half-filling ( $n = 1.0$ , right panel Fig. 4.9). Here the cluster-impurity is a 4 site  $2 \times 2$  isotropic plaquette, which we will consider later in further two dimensional studies in the following chapter (displayed in Fig. 5.1). The inverse temperature of the QMC result is  $\beta = 12.5$  (in  $t = 1.0$  units), the inverse virtual temperature of the ED varies from  $\beta = 32$  to  $\beta = 200$ . Fig. 4.9 shows the real and imaginary part of the cluster Green's function while Fig. 4.10 the imaginary part of the cluster on-site self-energy  $\Sigma_{11}$  and diagonal  $\Sigma_{13}$  on the Matsubara axis, where the QMC result is guaranteed to converge quadratically to the exact result [with an error  $O(\Delta\tau^2)$ ] and ED does not have the "artificial spreading" of the poles required in the analytical continuation on

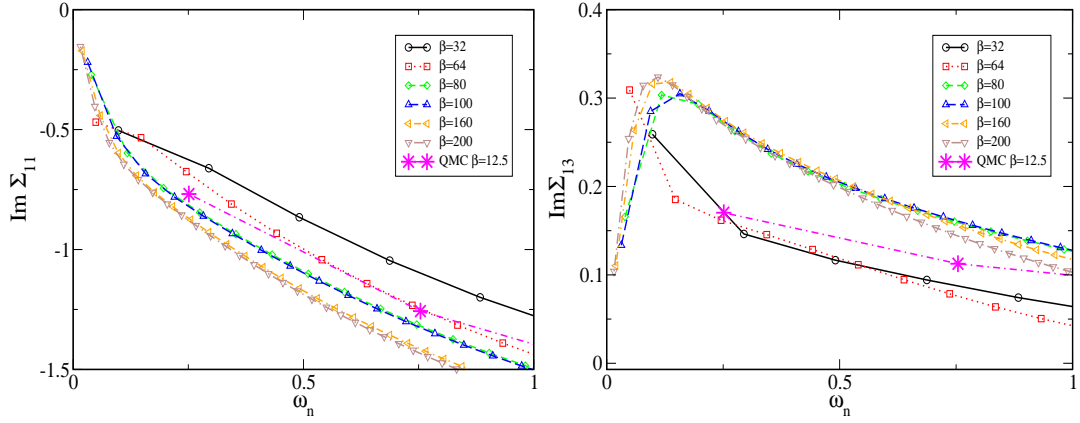


Figure 4.10: Imaginary parts of the on-site cluster self-energy  $\Sigma_{11}$  and the next nearest-neighbor  $\Sigma_{13}$  for increasing values of the virtual temperature  $\beta$  in the 2D Hubbard Model.  $U = 8.0t$ , the chemical potential of the system is fixed at  $\mu = 1.8$  and the density  $n = 0.9$ . QMC results are displayed as magenta stars with  $\beta = 12.5$ . The energy unit is set here  $t = 1.0$ .

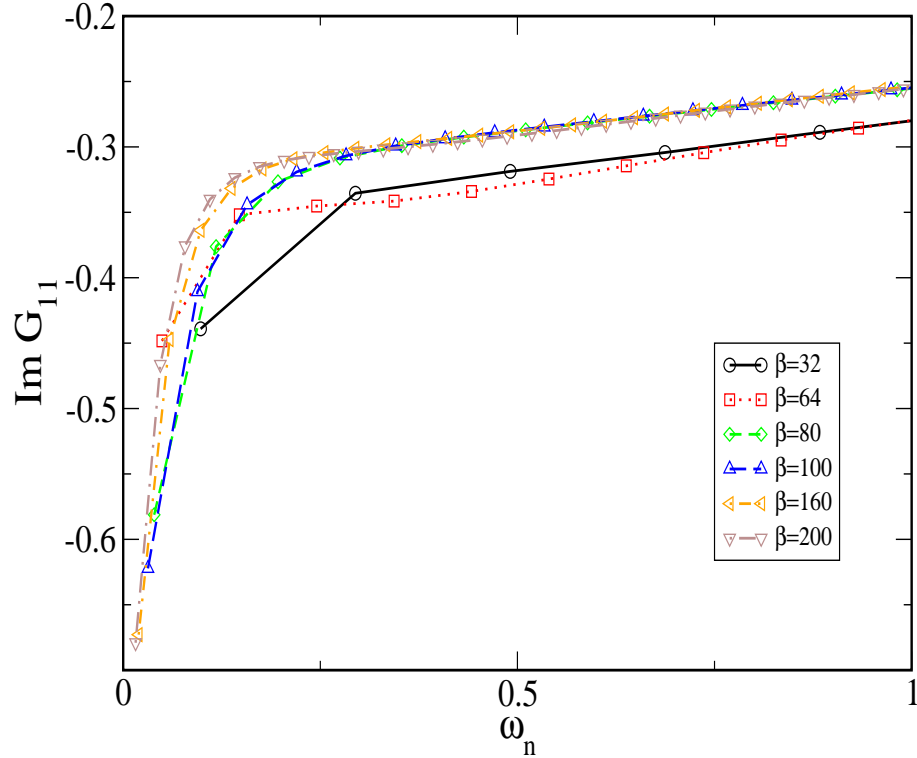


Figure 4.11: Imaginary part of the on-site Green's function  $G_{11}(\omega_n)$  for increasing values of the virtual temperature  $\beta$  in the 2D Hubbard Model.  $U = 8.0t$ , the chemical potential of the system is fixed at  $\mu = 1.8$ ,  $n = 0.90$ . QMC results are displayed as magenta stars with  $\beta = 12.5$ . The energy unit is  $t = 1.0$ .

the real axis. If we confront the highest-temperature (lowest  $\beta$ ) ED-run with the QMC result the agreement is remarkably good in spite of the much lower virtual temperature of ED. This provides a bridge connecting high and low temperature physics and gives credibility to both methods.

In figures 4.10 and 4.11 we also show an example on how the virtual temperature defined on the Matsubara axis enters into the ED-calculation with respect to the real temperature used in QMC. The virtual temperature simulates the effect of a real temperature in the system, even if the state considered in the solution of the associated Anderson impurity problem is the ground-state only. For low  $\beta$  (high virtual temperature), the curves behave similarly to the QMC results (pink stars in 4.10), and change quickly with increasing  $\beta$ , until collapsing onto the same curve for  $\beta$  high enough ( $\simeq 100$ ). We may therefore consider (at least for  $U=8.0$ ) this value of beta like a limiting case in order to obtain genuine  $T=0$  calculations.

### 4.3 Evaluation of Lattice Quantities

Once a converged solution has been determined, the final step in the CDMFT procedure is to extract physically interpretable lattice quantities. In the spirit of dealing with problems whose dominant physics is "local", (like for example Hubbard-like problems), the intuitive idea lies in using the cluster quantities like effective Fourier coefficients in a truncated Fourier expansion of the momentum-dependent quantities. The most natural way of determining these effective Fourier coefficients from the original lattice problem is by averaging the correspondent super-lattice quantities. Given an impurity-cluster configuration in fact (for example a 2-site dimer in a one dimensional chain or a 2X2 plaquette in a two dimensional lattice), there are more than one possible super-lattice-partitions of the full lattice into such clusters, corresponding to the many different symmetry operations  $S$  (translation, rotation...) with whom one possible super-lattice-partition can be mapped into another. Given a physically local quantity  $W(r)$ , that we assume going quickly to zero for  $r >$  the cluster size, and its corresponding super-lattice quantity  $W^S(r)$  calculated in the CDMDT-scheme within the cluster, for a given

lattice-partition  $S$  of the lattice into cluster-impurities, we evaluate:

$$W(r) \simeq \frac{1}{N_s} \sum_S W^S(r) \quad (4.2)$$

$N_s$  is the number of possible ways the the full lattice can be parted, once a cluster-impurity configuration is chosen. We stress that Eq.(4.2) represents a super-lattice

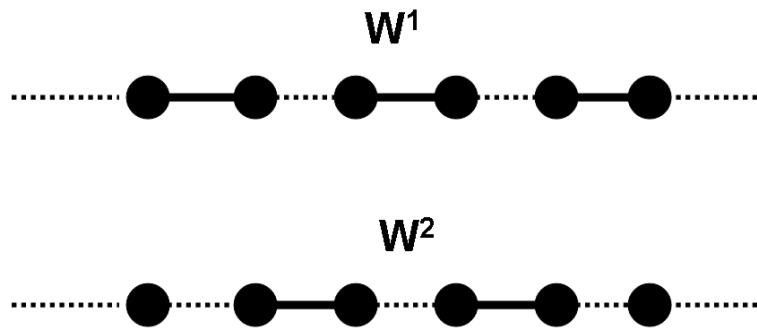


Figure 4.12: Possible partition in dimers for a 1D chain.

average, not a cluster average. Contributions  $W^S(r)$ , which connect two points belonging to different clusters are systematically zero. For example in Fig. 4.12 we present the simplest example with a 1D chain parted in  $N_c = 2$ -dimer clusters. There are two possible partitions ( $S = 2$ ) of the 1D chain into dimers (drawn as continuous links). Therefore we have two possible values for the link-quantity  $W^S$  (connecting two neighbor sites),  $W^1$  and  $W^2 = 0$ , i.e. :

$$W = (W^1 + W^2)/2 = W^1/2 \equiv W^c/2$$

where we indicate with  $W^c$  the in-cluster-value of  $W$  evaluated for a fixed partition of the lattice ( $S = 1$  in the present case). Notice that typically for a square lattice the number of possible partitions of the full lattice into clusters is  $N_s = N_c$ , the number of

cluster-sites. The momentum-dependent quantity is then evaluated:

$$W(k, \omega) = \sum_r e^{ikr} W(r) = \frac{1}{N_c} \sum_{\mu, \nu=1}^{N_c^{1/2}} e^{ik\mu} W^c(|\mu - \nu|) e^{-ik\nu} \quad (4.3)$$

What is the right "local" quantity to periodize ? There is no a trivial answer to this question. We present in this study three possibilities:

1. The  $\Sigma$ -scheme, where the cluster self-energy  $\Sigma_{\mu\nu}$  is periodized [25]:

$$\Sigma(k, \omega) = \frac{1}{N_c} \sum_{\mu, \nu=1}^{N_c} e^{ik\mu} \Sigma(|\mu - \nu|) e^{-ik\nu} \quad (4.4)$$

2. The  $M$ -scheme where the cluster-cumulant  $M_{\mu\nu}$  is periodized [64]:

$$M(k, \omega) = \frac{1}{N_c} \sum_{\mu, \nu=1}^{N_c} e^{ik\mu} M(|\mu - \nu|) e^{-ik\nu} \quad (4.5)$$

3. The  $G$ -scheme where the Green's function on the super-lattice (a cluster  $N_c \times N_c$  matrix) is periodized [61]:

$$G(k, \omega) = \frac{1}{N_c} \sum_{\mu, \nu=1}^{N_c} e^{ik\mu} \left[ \hat{\mathbf{1}} \omega + \hat{t}_k - \hat{\Sigma} \right]_{\mu\nu}^{-1} e^{-ik\nu} \quad (4.6)$$

Notice that the cluster-cumulant arising from the expansion of the free energy around the atomic limit is related to the cluster-self-energy (arising from the usual weak-coupling expansion of the free-energy) by the expression:

$$\mathbf{M}(\omega) = [(\omega + \mu)\mathbf{1} - \mathbf{\Sigma}(\omega)]^{-1} \quad (4.7)$$

and that the super-lattice Green's function entering in the  $G$ -scheme is the same used in the CDMFT self-consistency condition (3.7). These three methods are *a priori* equally justified. We will in the following confront them, first in the one dimensional case, where we can take advantage from the comparison with the exact solution, then in the two dimensional case, stressing the physical consequences and implications of the different methods.

### 4.3.1 Reconstruction of lattice-quantities and physical observables

The problem of extracting momentum-dependent quantities is of fundamental importance in identifying the right system observables that are not generically the cluster ones. A DMFT approach is based on the assumption that the important physics of the system is local, thus the local quantities determined in the cluster-impurity are a good representation of the translational-invariant lattice ones. This is generally true for a "pure local quantity", as for example the on-site density of the system, which can be well determined directly from the cluster-impurity density. With a small size-cluster however (which is the only solvable case in practical applications with ED), the boundary-sites are renormalized by the surrounding bath, and the "non-pure local quantities" related to these kind of sites (as for example, the Kinetic Energy) are also renormalized inside the cluster. In the following section we will study this effect in the bench-marking one dimensional case enlightening the dependence of cluster-quantities from the cluster-size. In this section we show, however, that in order to rightly evaluate physical quantities, it is important to establish the correct link between CDMFT-cluster quantities and lattice observables. The three methods presented in the previous section are three different ways to achieve this goal. We present here an example applying again 2-site-cluster CDMFT on the one-dimensional Hubbard Model, where the exact BA solution can be used as a benchmark. As we said above, the number of possible ways a one-dimensional chain can be parted into 2-sites dimers is  $N_s = 2$ . So, if  $W_r$  is a local quantity that we assume small for  $r \geq 2$  (for example the self-energy or the cumulant..) calculated within the cluster (the  $W^S$  in formula 4.2), according to formula (4.3) of the previous section:

$$W(k, \omega) = W_0(\omega) + W_1(\omega) \cos(k) \quad (4.8)$$

A truncated Fourier expansion of  $W(k, \omega)$

$$W(k, \omega) = W_0^{latt}(\omega) + 2 W_1^{latt}(\omega) \cos(k) \quad (4.9)$$

implies that the next-nearest neighbor cluster-coefficient

$$W_1(\omega) = W_1^{latt}(\omega)/2 \quad (4.10)$$

is renormalized by a geometrical factor 2 with respect to its lattice correspondent, as

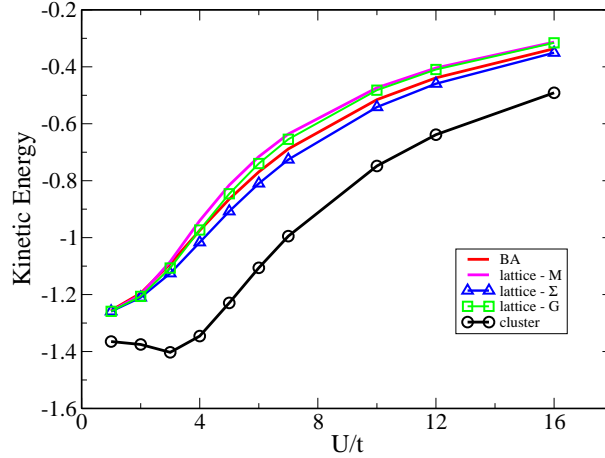


Figure 4.13: Kinetic energy of the half-filled one-dimensional Hubbard Model as a function of the on-site interaction  $U$  at zero temperature. Results from the three periodization schemes  $\Sigma$  (blue triangles),  $M$  (magenta line) and  $G$  (green squares) and from the cluster Green's function (circles) are confronted with the exact BA solution (red line).

expected from the discussion in formula 4.2. To understand how this reflects on the determination of non-pure local quantities, we can further calculate the kinetic energy from the cluster and from the lattice. The former is the energy integral of the nearest-neighbor cluster Green's function  $G_{12}(\omega)$  evaluated directly from the ground-state of the AIM. The latter is evaluated by first periodizing the self energy or the cumulant or the super-lattice Green's function with the  $\Sigma$ -scheme, the  $M$ -scheme or the  $G$ -scheme respectively (as explained above), in order to obtain the full lattice Green's function  $G^{lat}(k, \omega)$ .  $G_{12}^{lat}(\omega)$  is then evaluated as second Fourier coefficient, and its energy integral again gives the kinetic energy. These two values can be confronted with the known BA result. This is shown in Fig. 4.13, where the kinetic energy is plotted as a function of the on-site interaction  $U$ . The values of the kinetic energy given by the cluster Green's function are significantly different from the exact BA result, while the values obtained from the lattice Green's functions extracted with the three different schemes are close to the BA line. This shows clearly that the quantity which to be physically interpreted is the lattice and not the cluster Green's function. We also notice that the lines calculated

with the  $M$ -scheme (magenta line) and the  $G$ -scheme (green squares) are remarkably close, especially in the strong coupling regime, and both underestimate the BA value, while the line from the  $\Sigma$ -scheme (blue triangles) overestimates it. In Fig. 4.15 we show the difference between the BA kinetic energy (black line) and the cluster one (circles) renormalized by a factor  $1/\sqrt{2}$ :  $\Delta E_{Kin} = K_{BA} - K_{clu}/\sqrt{2}$  as a function of  $U$ . Notice that for a value of the on-site interaction greater than the bandwidth  $U > 4t$ , this difference is very close to zero, indicating that that the kinetic energy calculated from the cluster is underestimated by the factor  $\sqrt{2}$ . This has a geometrical origin and depends on the cluster size and the dimensionality of the problem. On the left side of Fig. (4.15) we also plot the difference between the BA kinetic energy and an averaged kinetic energy from the  $\Sigma$  and  $M$  methods  $\Delta E_{kin} = K_{BA} - (K_{\Sigma} - K_M)/2$  (squares), which appears to be a reasonably good estimate of the true value. Let us now turn

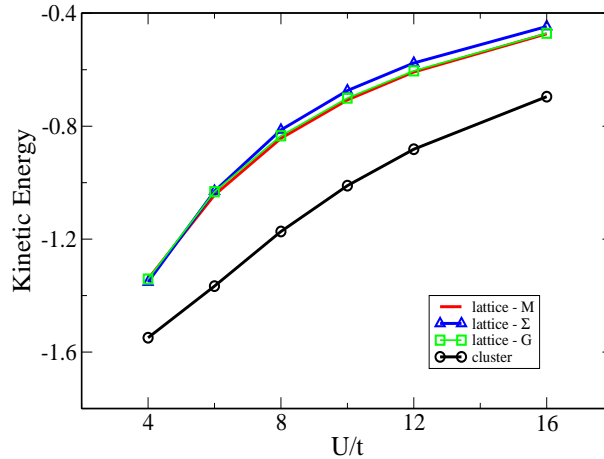


Figure 4.14: Kinetic energy of the half-filled two-dimensional Hubbard Model as a function of the on-site interaction  $U$  at zero temperature. Results from the three periodizing schemes  $\Sigma$  (blue triangles),  $M$  (magenta line) and  $G$  (green squares) are confronted with the ones from the cluster Green's function (circles) which are clearly different .

to the two-dimensional case, where we studied a  $2X2$  cluster-impurity. For this case lattice quantities  $W(k)$ , which could be the self-energy  $\Sigma_k(\omega)$  in the  $\Sigma$ -method or the cumulant  $M_k(\omega)$  in the  $M$ -method, can be explicitly evaluated using formulas 4.4 and 4.5 and exploiting the symmetry of the square-lattice:

$$W(k, \omega) = W_0^{latt}(\omega) + 2W_1^{latt}(\omega) (\cos k_x + \cos k_y) + W_2^{latt}(\omega) \cos k_x \cos k_y \quad (4.11)$$

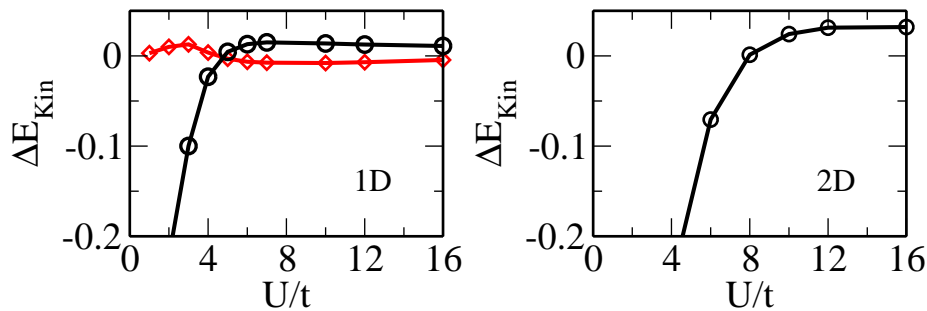


Figure 4.15: On the left-hand side we display (black line with circles)  $\Delta E_{Kin} = K_{BA} - K_{clu}/\sqrt{2}$  as a function of the interaction  $U$  for the 1D Hubbard Model. Notice the factor  $\sqrt{2}$  which reflects the geometry of the  $N_c = 2$ -site cluster. We also show the difference between the BA solution and an average of the results from the  $\Sigma$  and  $M$ -schemes  $\Delta E_{kin} = K_{BA} - (K_{\Sigma} - K_M)/2$  (red line with squares). In the right-hand graph we display  $\Delta E_{Kin} = K_{BA} - K_{clu}/\sqrt{2}$  for the two-dimensional case. The difference gets close to zero again for  $U > 4t$ , the bandwidth of the model in 2D.

For the  $G$ -method we once again refer to formula 4.6. The expression for the self-energy  $\Sigma_k(\omega)$  is:

$$\Sigma_{\text{latt}}(k, \omega) = \Sigma_{11} + \Sigma_{12} (\cos kx + \cos ky) + \Sigma_{13} \cos kx \cos ky \quad (4.12)$$

and for the cumulant:

$$M_{\text{latt}}(k, \omega) = M_{11} + M_{12} (\cos kx + \cos ky) + M_{13} \cos kx \cos ky \quad (4.13)$$

In Fig. 4.14 we show the kinetic energy for the half-filled Hubbard Model at zero temperature obtained by calculating the lattice Green's function  $G_k(\omega)$  using the 3 different periodizing methods. The qualitative picture is strikingly similar to the 1D case. Although a benchmark exact solution is missing in 2D, the difference between the results coming from the lattice Green's functions calculated with the three periodizing schemes and the one coming directly from the cluster Green's function supports the same conclusions as in the 1D case. This time we plot in Fig. 4.15 the difference between the averaged kinetic energy from the  $M$  and  $\Sigma$  schemes and the kinetic energy from the cluster, the latter renormalized by the factor  $1/\sqrt{2}$ :  $\Delta E_{Kin} = K_{BA} - K_{clu}/\sqrt{2}$ . Once again, for a local interaction greater than the bandwidth  $U > 8t$ , the difference tends to zero, showing a dimensional-geometrical dependence as in 1D. This discussion

shows the importance of extracting the lattice quantities, which have physical meaning, from the impurity-cluster results. For this it is necessary to fully understand the differences between the periodizing schemes proposed, and, in turn, understand which of the schemes represents the best procedure to obtain the correct physical interpretation.

### 4.3.2 Lattice-quantities and local physics

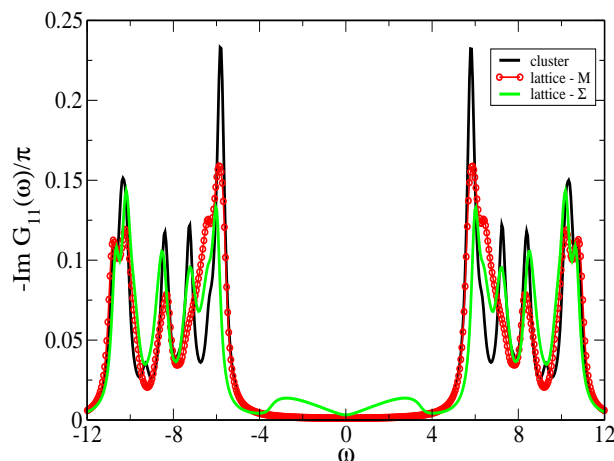


Figure 4.16: Density of states as a function of frequency for the half-filled 2D Hubbard Model with  $U = 16t$  at zero temperature (ED-CDMFT). The black line represents the local density of states for the cluster, the red circle where obtained by periodizing the cumulant, the green line by periodizing the self-energy.

Are the three periodization schemes equivalent? We recall that a cluster DMFT procedure is based on the assumption that the physically relevant quantities are local, we therefore expect that a good periodization scheme preserves them. If we, for example, extract the lattice Green's function  $G(\mathbf{k}, \omega)$  using the  $\Sigma$ ,  $M$  or  $G$ -schemes, we expect that the local Green's function  $G_{loc}(\mathbf{k}, \omega)$  (the only "purely local" quantity in the small cluster we will consider in practice) obtained evaluating the energy-integral of the lattice Green's function all over the BZ  $G_{loc}(\mathbf{k}, \omega) = \sum_{\mathbf{k}} G(\mathbf{k}, \omega)$  well describes the local cluster Green's function obtained directly from the AIM. This is a tautology by construction in the  $G$ -scheme, but it is not trivially true for the  $\Sigma$  and  $M$ -schemes. In Fig. 4.16 we present the DOS  $(-1/\pi) \text{Im}G_{loc}(\omega)$  of the two-dimensional Hubbard Model for  $U/t = 16$  at half-filling calculated within the cluster with ED-CDMFT (black

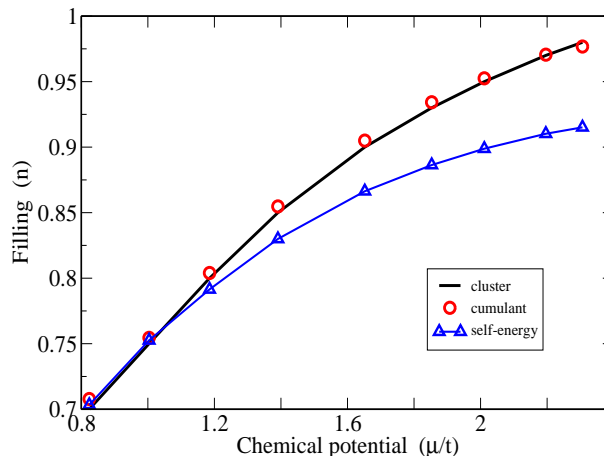


Figure 4.17: Density as a function of  $\mu$  for the 2D Hubbard Model with  $U = 8t$  calculated with NCA solver at a temperature  $T = 0.1t$ . The black line is the filling calculated directly from the cluster, the filling calculated from the periodized Green's function are the circles for the  $M$ -scheme and the triangles for the  $\Sigma$ -scheme.

line), confronted with the results obtained from the lattice Green's function through the  $\Sigma$  (green line) and  $M$ -schemes (red line with circles). We observe right away that the  $M$ -scheme well portrays the original DOS, preserving in particular the Mott gap (in this case quite large due to the choice of a high on-site interaction  $U$ ). On the contrary, the  $\Sigma$ -scheme creates states inside the Mott gap. These states are obviously un-physical, and they signal a failure of the  $\Sigma$ -scheme to describe the insulating state of the Hubbard Model. It is expected that the  $M$ -scheme, based on cumulants arising from the atomic limit of the original Hamiltonian, describes better the Mott-insulating state with respect the  $\Sigma$ -scheme, which is instead arising from the weak coupling perturbative expansion of the original problem. Cumulants are better quantities than the self-energy in describing a localized insulating state. We expect the  $\Sigma$ -scheme to better work in the metal phase, where electrons are itinerant and the Fermi Liquid picture is valid. In Fig. 4.17 we show the filling of the system calculated from the DOS as a function of the chemical potential  $\mu$  in the doped state of the Hubbard Model in 2D for  $U/t = 8.0$ . Again the black line is the filling calculated from the impurity-cluster, confronted with the  $\Sigma$  (blue triangles) and the  $M$  schemes (red circles). The two schemes rapidly approach the cluster-density at high doping, close to the M-I transition the

$\Sigma$ -scheme creates spurious states in the gap of the DOS, and it gives lower values of the density. The  $M$ -scheme, instead, follows the cluster-line, until reaching the insulator, appearing to be more appropriate for describing lattice quantities in correspondence of the MT transition. The failure of the  $\Sigma$ -scheme at the MT region is also the reason also for the failure of the Periodizing CDMFT (PCDMFT) method introduced in [56] and compared with CDMFT in [12]. In this method, the lattice translational invariance of the system is restored inside the DMFT loop itself by evaluating the lattice self-energy with a  $\Sigma$ -scheme. An alternative to the PCDMFT based on the periodization of the cumulant, the explicit cavity construction (ECC)-DMFT, proposed by T. Stanescu and G. Kotliar [64], cures the defects of PCDMFT.

#### 4.4 Cluster-size and cluster-lattice partitions dependencies

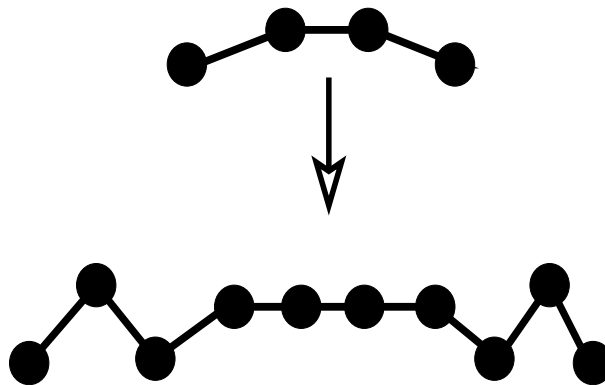


Figure 4.18: 1D chain-density profile as increasing the number of cluster-sites  $N_c$ .

CDMFT breaks the translational invariance of the system as soon as a cluster shape and size have been chosen. The translational invariance is restored only at the end, once the solution has been determined by imposing the CDMFT self-consistency condition on the cluster-impurity, and lattice quantities are extracted through one of the periodizing schemes presented above. It is therefore important to understand the extend to which the physical results are dependent on the choice of the cluster and on the way lattice is parted by these clusters. We start addressing the issue of the dependence of the result on the number of sites in the cluster  $N_c$ , and we start to consider the 1D case

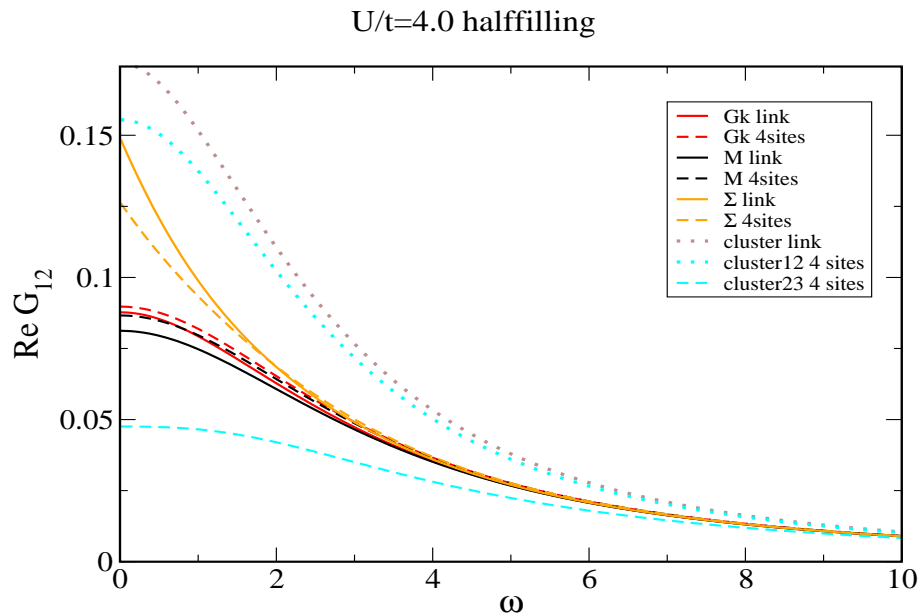


Figure 4.19: Real part of the nearest neighbor propagator  $G_{12}(\omega)$  for a 1D case at half-filling calculated with the different schemes and for increasing cluster size  $N_c = 2$  to  $N_c = 4$ . Also  $G_{12}$  calculated directly within the cluster on the ground-state of the AIM is displayed. The energy integral is equal to the kinetic energy.

as we did in previous sections. Even in this case, however, it is difficult to study in a systematic way the dependence of static quantities, e.g. the density versus the chemical potential, using ED. In the Lanczos for example the total number of sites  $Ns$  is limited by computer power, and increasing the number of sites in the cluster  $Nc$  reduces the number of sites available for the bath  $Nb$ . For example, looking only at the density of the system  $n$  for fixed chemical potential  $\mu$  we notice that a  $Nc = 4$  and  $Nb = 8$  run reproduces the same values of a  $Nc = 2$  and  $Nb = 8$  run. In a  $Nc = 4$  and  $Nb = 8$  chain, the result is indeed an un-homogeneous system, with the 2 central sites having different densities than the external ones (see upper Fig.4.18). If we look at the values of the hybridizing hoppings  $V_{\mu k}$ , which connect the sites of the chain with the bath, we notice that the central ones are systematically sent to zero, i.e. the central chain chemical potential and hopping are not renormalized by the bath. Nevertheless, if confronted with the true BA value, the density of the 2 central sites is not the best approximation: the best result is obtained averaging over the cluster sites. We may think that the

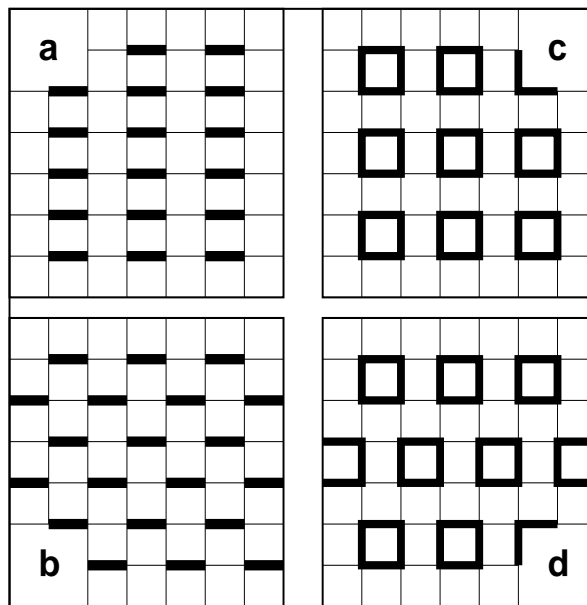


Figure 4.20: Possible choices for a CDMFT super-lattice starting from a two-dimensional square lattice and a two-site unit cell (a, b), or a four-site unit cell (plaquette) (c, d). In the auxiliary super-lattice problem the hopping is the same on all the links while the non-local irreducible cumulants or the self-energies are equal to the cluster values for the links marked with thick lines and zero otherwise.

boundary effect of the bath not only affects the most external sites but propagates inside the cluster, and that only with a larger cluster than the one we consider with ED ( $Nc = 4$ ) it is possible to reach the bulk limit of the density (a qualitative picture is shown in the lower line of Fig.4.18, we refer for a more systematic study to [25], and for a similar picture obtained on larger cluster with QMC-CDMFT [47], in particular Fig. 6). In spite the local (density) quantity does not seem to improve with a the  $Nc = 4$  cluster size in growing from  $Nc = 2$  to  $Nc = 4$ , a real improvement in the nearest neighbor quantities takes place, as shown in Fig. 4.19. Here we display the real part of the nearest neighbor Green's function as a function of the frequency (the integral of this function is the lattice kinetic energy of the Hubbard Model). This run has been obtained for strong coupling  $U/t = 8$  at half-filling. The lattice Green's functions have been obtained with the different periodizing schemes the  $G$ -method (red line), the cumulant  $M$ -method (black line) and the  $\Sigma$ -method (orange line). A comparison is displayed with the link cluster ( $Nc = 2$ ) and the 4-sites ( $Nc = 4$ ),  $Nb = 8$  in both

cases. The nearest neighbor Green's function derived directly from the cluster is also displayed for the link (brown dotted line) and for the 4-sites (light blue lines), labelled the latter  $G_{12}$  and  $G_{23}$  in a 4 sites cluster 1-2-3-4. We can observe first of that the cluster Greens' functions 1-2 and 2-3 are strongly in-homogeneous, far from the bulk limit. The averages for any scheme, however, are already better and lie between the 2 cluster value. Also we see that all 3 periodizing methods move toward a common curve for increasing cluster size  $Nc$ . As expected the  $M$ -method and the  $G$ -method are very close with respect to the  $\Sigma$ -method, and look to reach very quickly the same curve. Also they display a similar qualitative behaviour in the shape of the curve with respect to the  $\Sigma$ -method, indicating they describe the same physics. So even if the results for  $Nc = 4$  are still far from the their bulk values, the average represent a good approximation which converges for increasing  $Nc$  (as shown in Fig. 4.19 by the small change in the average-curve of  $\text{Re}G_{12}$  in going from  $Nc = 2$  to  $Nc = 4$  in all the periodizing schemes).

We now investigate how the solutions may be affected by the partition into cluster of the original lattice. In fact, given a cluster-impurity there are many possible ways the clusters can be arranged on the lattice (see for example panels (a), (b) and (c), (d) of Fig. 4.20 for a two-dimensional square lattice). A clear understanding of this feature may be helpful determine the minimal dimension of the impurity-cluster that has to be considered in order to properly describe the local physics. Reasonably, if the cluster is chosen big enough the solution should be weakly dependent on its shape and on the way the lattice is parted. We investigate this issue with some practical example in the two-dimensional square lattice of Fig. 4.20, where we use two different cluster sizes: a two-site link with two different partitions of the lattice (panels (a) and (b)), and a 2X2 plaquette, which also results in two possible different partitions of the lattice (panels (c) and (d)). The CDMFT results for the local spectral functions in the two link-geometries (a) and (b) are represented in Fig. (4.21) by the blue line (for super-lattice "a") and the black line (for super-lattice "b"). We can clearly see that the two results are qualitatively different, especially in the regions near the Mott gap edges. A possible way to decide which of the two is closer to the real solution is to confront them with ECC-DMFT [64], an improvement of PCDMFT based on the periodization

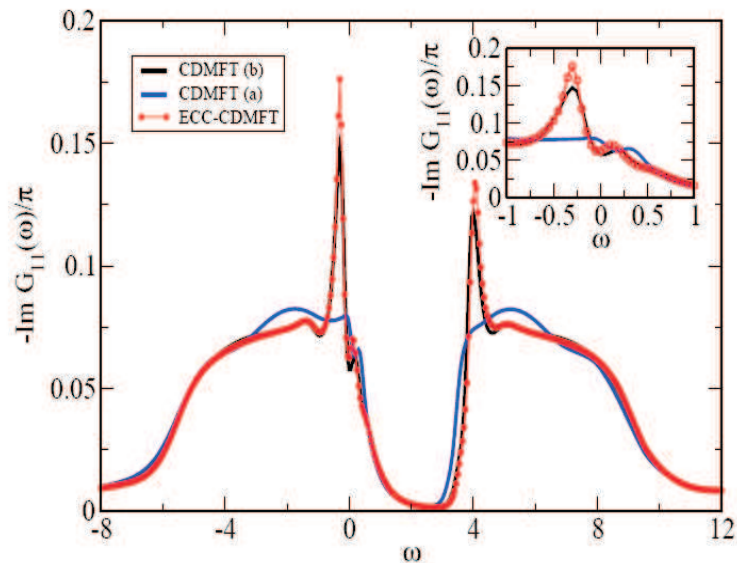


Figure 4.21: Comparison between the on-site spectral functions for the 2D Hubbard model obtained using: 1) CDMFT on a super-lattice of type “a” (blue curve); 2) CDMFT on a super-lattice of type “b” (black curve); 3) ECC-DMFT on a link (red circles), which preserves translational invariance by construction. The calculations were done for a model with a hopping matrix element  $t$  and on-site interaction  $U=8t$  at a temperature  $T=0.15t$  and filling  $n=0.95$  using NCA for the impurity solver. A detail of the low-energy behavior is shown in the inset.

of the cumulant instead of the self-energy, which is independent of the geometry of the super-lattice due to its built-in translational invariance. The corresponding values for the local spectral function are also shown in Fig. (4.21) (red line with circles). The solid agreement between the ECC-DMFT result and the black curve (super-lattice “b”) strongly suggests that the partition (4.20b) is the best choice for this case. The qualitative difference between the solution based on the super-lattice (4.20a) and (4.20b) indicates that in CDMFT the physics of a two-dimensional Hubbard model may not well captured by a two-site cluster approximation. This problem should in principle be cured by increasing the cluster size. In Fig. (4.20 - c,d) we show two possible super-lattices having a plaquette as the unit cell. The corresponding spectral functions are represented in Fig. (4.22) by two almost identical curves (the red line and the blue circles correspond to the super-lattices (4.20c) and (4.20d), respectively). This

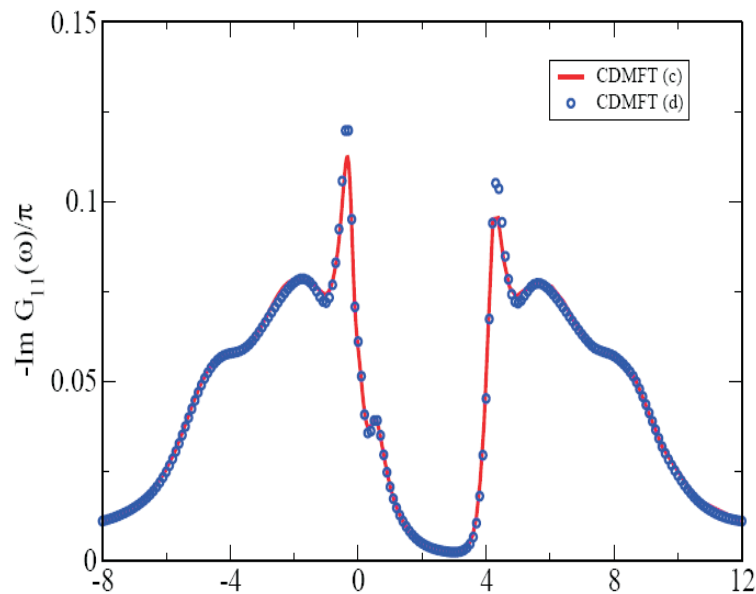


Figure 4.22: Comparison between the on-site spectral functions for the 2D Hubbard model obtained using CDMFT on a super-lattice of type “c” (red curve) and CDMFT on a super-lattice of type “d” (blue circles). The parameters for this calculation are  $U=8t$ ,  $T=0.15t$ ,  $n=0.95$  and we used an NCA impurity solver.

example shows that the implementation of a CDMFT-type approach depends on the partition of the super-lattice. If different geometries give different results, the ambiguity can be possibly eliminated by increasing the cluster size (in the case where this is not possible due to technical limitations, a possible way to discriminate is to use the ECC-DMFT scheme for the same cluster size [64]). Finally, but most importantly, the fact that a plaquette-cluster in the 2D Hubbard Model is independent of the choice of the super-lattice, suggests that a four-site cluster approximation is able to capture the basic physics of the model.

In Figs 4.23 we show how the DOS calculated with the  $\Sigma$  and  $M$ -schemes evolves with increasing cluster size  $N_c$  from the link configuration (4.20b) to the plaquette configuration 4.20d). The on-site interaction is  $U/t = 8.0$  and the system is at 5% doping. The impurity problem has been solved again with NCA, at a temperature  $T = 0.1t$ . For comparison the DOS directly calculated from the impurity-cluster is also displayed. It is clear how the  $M$ -scheme and the latter DOS are always closer in

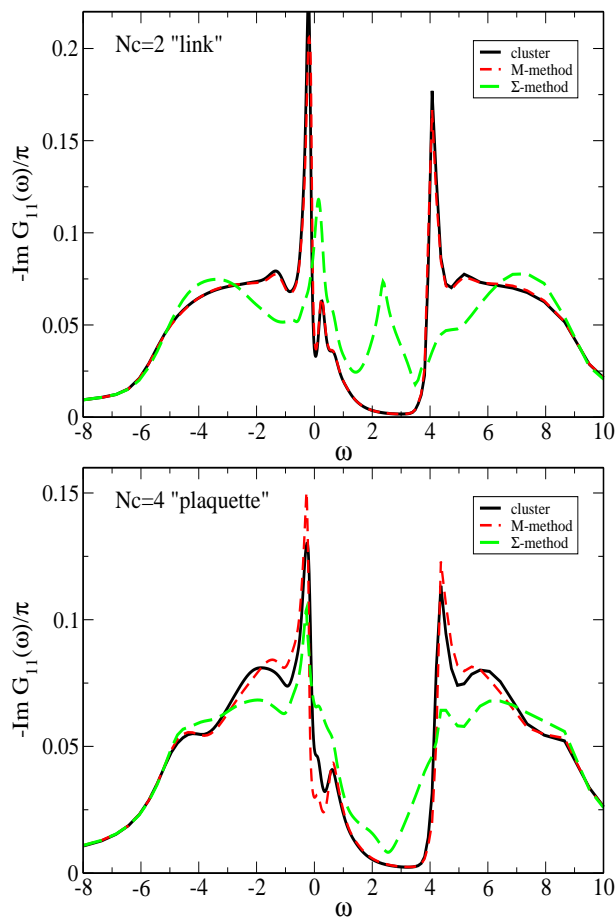


Figure 4.23: The local DOS is compared between the  $\Sigma$  and  $M$ -schemes. The cluster DOS (black line) is also displayed. The on-site interaction in the system is  $U/t = 8.0$ , the doping is at 5%. The impurity problem has been solved by NCA at a temperature  $T = 0.1t$  (courtesy of T. Stanescu and C. Haule). Notice the Hubbard bands structure is preserved in all cases. The left hand picture is a two-site link arrange as in configuration 4.20b), the right hand picture is for a 2X2 plaquette arranged according to partition 4.20d).

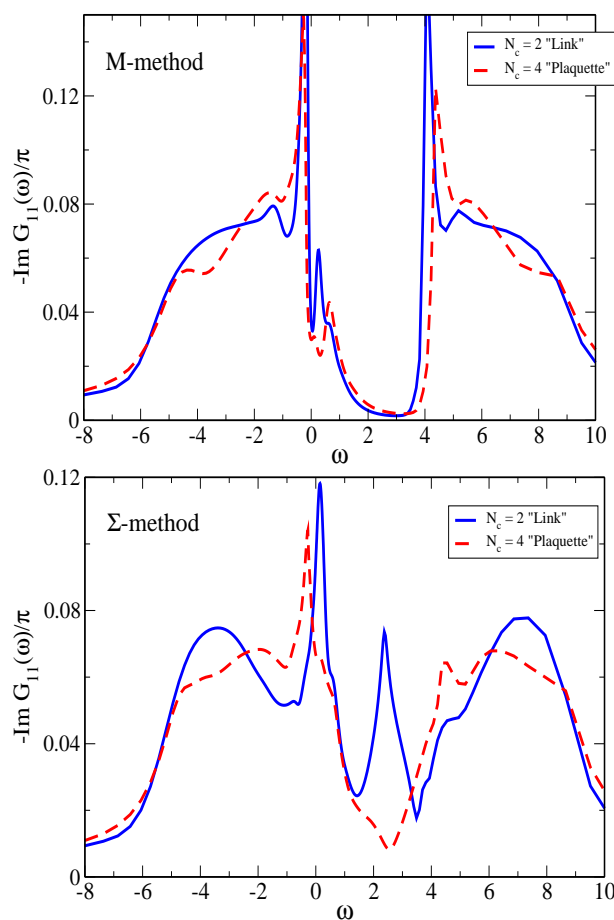


Figure 4.24: Same as in Fig. 4.23, but the evolution of the DOS from the two-site link to the four-site plaquette is evidenced for the  $M$ -scheme (left-hand side) and the  $\Sigma$ -scheme (right-hand side). Notice the more detailed feature at the Fermi level  $\omega = 0$  of the plaquette calculation in comparison with the link. For the  $\Sigma$ -scheme (right-hand side) less states occupy the Mott gap part of the spectrum.

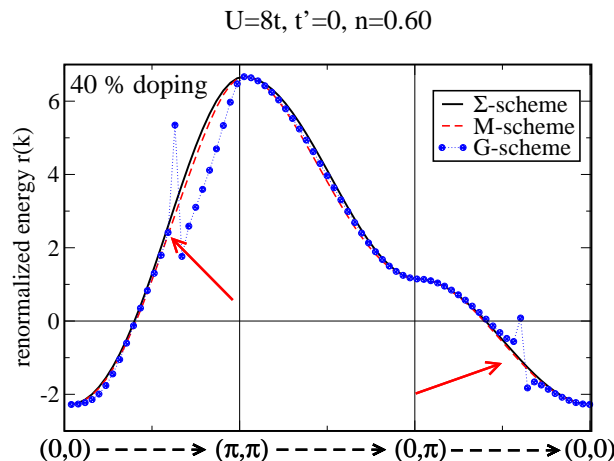


Figure 4.25: Renormalized energy  $r(k) = \varepsilon_k + \mu - \text{Re}\Sigma_k$  calculated with the three periodizing schemes:  $\Sigma$ ,  $M$  and  $G$ . The quantity is displayed along the path  $(0,0) \rightarrow (\pi,\pi) \rightarrow (0,\pi) \rightarrow (0,0)$  of the first quadrant of the BZ. The system is highly doped (40%), and it is in a FL state. The point of zeroes in  $r(k)$  correspond to the quasiparticle-poles in the lattice Green's function. Notice that, in the case of the  $G$ -scheme, also singular points appear in  $r(k)$  (indicated by the red arrows) corresponding to zeroes in the Green's function.

comparison to the  $\Sigma$ -scheme DOS. Notice the more detailed feature appearing at the Fermi energy  $\omega = 0$  in the plaquette calculation of these two curves. The  $\Sigma$ -scheme presents always some spurious states in the Mott-gap, and a less refined structure at the FS. However the weight of the spurious states is less in the plaquette calculation than in the link. We do expect the two methods  $\Sigma$  and  $M$  to converge to the same result for increasing  $N_c$ . But the  $M$ -scheme seems to be able to reproduce local quantities better for small cluster (at least in the insulating state and possibly in the metallic region that precedes the MT, as explained in Fig.4.17).

As we previously mentioned, the third scheme proposed, the  $G$ -scheme, produces results similar to the  $M$ -scheme in the low-doping region of the parameter space. In fact it is by construction exact in re-building the local cluster-quantity  $\text{Im}G_{11}(\omega_n)$ . This scheme, however, may have some inconvenient in describing  $k$ -dependent properties of the high-doped region, where the system is a simple FL. In Fig. 4.25 we show for a highly doped case (40% doping) the renormalized quasiparticle spectrum  $r(k) = \varepsilon_k + \mu - \text{Re}\Sigma_k$  along the path  $(0,0) \rightarrow (\pi,\pi) \rightarrow (0,\pi) \rightarrow (0,0)$  of the first quadrant of the BZ. The

quasiparticle poles in the Green's function  $G(k, \omega) = \frac{1}{\omega + r(k) + i\delta}$  (with  $\text{Im}\Sigma_k \rightarrow 0$ ) correspond to zeroes of  $r(k)$ , as expected from a FL viewpoint. In Fig. 4.25 we see that for all the three periodizing schemes there are two points where quasiparticles are formed, corresponding to the crossing of the FS with the path in  $k$ -space considered. In the  $G$ -scheme, however, we observe the appearance of points of *infinities* in  $r(k)$  (red arrows in Fig. 4.25), i.e. zeroes in the Green's functions. In spite this is a real possible property in a strongly interacting many-body system, as we will see in detail in the next chapter studying the approach to the Mott transition, in this case it is probably an artifact of the  $G$ -scheme, as the system is expected to be a simple FL for this value of doping. Therefore the  $G$ -scheme shows to introduce spurious zeroes in the Green's function, not interpretable as physical properties of the system.

#### 4.5 Reduced bath-parametrization for the Exact Diagonalization procedure

We want in this section to present an operative method for search out the solution with the ED-CDMDT method. In this procedure a most delicate point is represented by the minimization step that determines the best finite set of bath parameters  $(\varepsilon_k, V_{\mu k})$  describing the continuous hybridization function  $\Delta_{\mu\nu}(\omega)$ , born out of the self-consistent CDMFT-loop. The minimization searches in the  $(\varepsilon_k, V_{\mu k})$ -parameter landscape for the minimum of the distance function  $f = |\Delta(\hat{\omega}) - \Delta_{ns}(\hat{\omega})|/\omega$ , and re-inputs the values it finds into the CDMFT-loop. The solution is therefore determined by a compromise between optimal approximation of  $\Delta_{\mu\nu}(\omega)$ , given by a minimum of  $f$ , and fulfillment of the CDMFT-self-consistency. There is always the risk of finding and remaining trapped in a minimum of  $f$  which at some numerical degree of precision satisfies the CDMFT-equations but that is not physically meaningful. In order to drive the solutions towards physically interesting regions of the bath-parameters space, we have introduced a reduced bath-parametrization which allows to exploit the symmetries in the square lattice to gain a better physical insight of the Green's function properties we look for. Moreover using fewer parameters the work required by the minimization procedure is faster and the result simpler to interpret. The most general parametrization of the bath

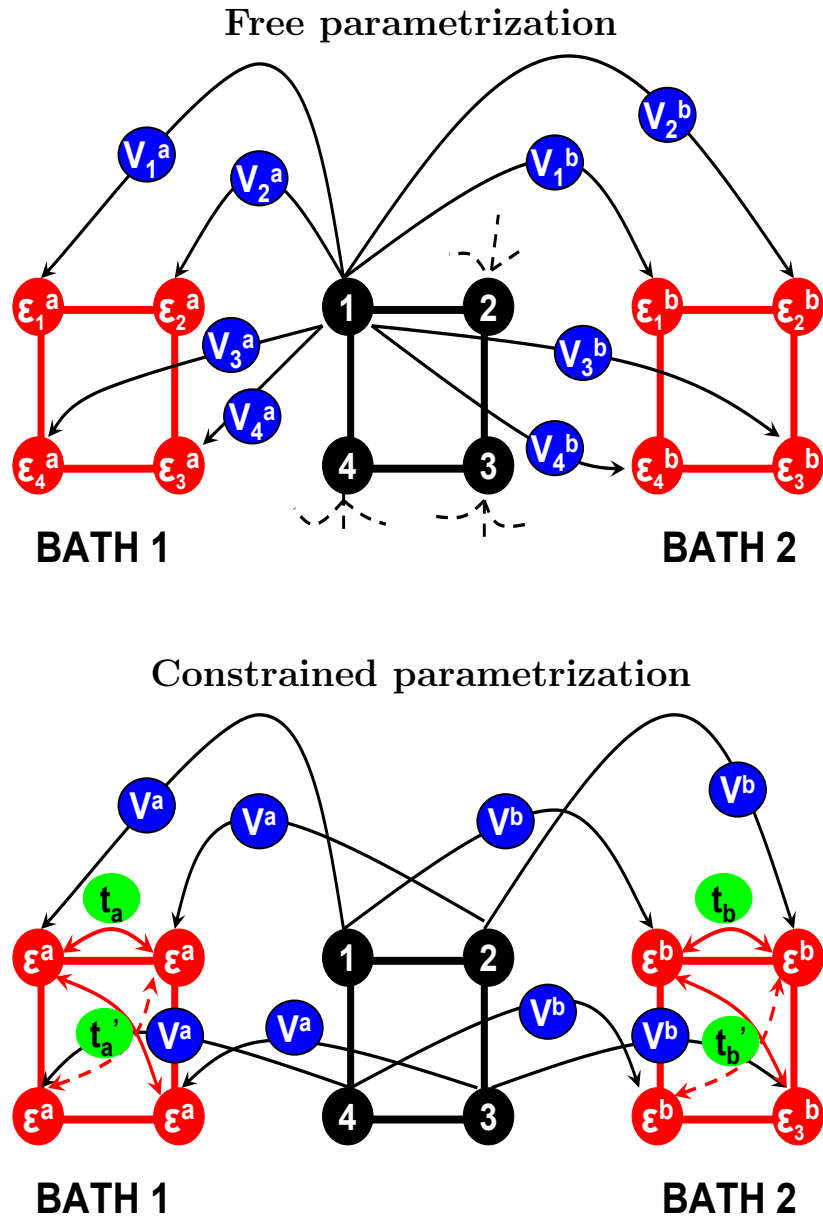


Figure 4.26: Schematic drawing of a free bath-parametrization (upper row) and the constrained bath-parametrization (lower row).

is given in the Hamiltonian by

$$\sum_k \sum_{\sigma} \varepsilon_{k\sigma} a_{k\sigma}^+ a_{k\sigma} + \sum_k \sum_{\mu\sigma} V_{k\mu\sigma} a_{k\sigma}^+ c_{\mu\sigma} + V_{k\mu\sigma}^* c_{\mu\sigma}^+ a_{k\sigma} \quad (4.14)$$

here as usual  $c_{\mu\sigma}$  is the destruction operator of an electron with spin  $\sigma$  on site  $\mu = 1 \dots 4$  of the cluster-impurity,  $a_{k\sigma}$  is the destruction operator of an electron in the site  $k = 1, \dots, N_b$  of the bath,  $\varepsilon_{k\sigma}$  are the level energies of the bath and  $V_{k\mu\sigma}$  the hybridizing couplings between cluster and bath. A sketch of this bath is shown in the top of Fig. (4.26), where, for convenience's sake, only the hybridization of the cluster-site  $\mu = 1$  with 8 bath sites (also arranged in two 2X2 plaquette for convenience's sake) is shown. An electron can jump from site  $\mu = 1$  to every site of the bath, which in general has an energy  $\varepsilon_k$  different from the other bath-sites, with a hopping parameter  $V_{\mu k}$  which is also different for different bath-site. In the lower row of Fig. (4.26) we show the constrained bath-parametrization. The bath-sites are grouped in 4-site plaquettes to mimic the original lattice structure parted by the plaquette-cluster (in the picture we show the two plaquette-bath on the left-hand side and right-hand side respectively). For each of this bath-plaquette we impose the same bath-energy  $\varepsilon_j$  ( $j = a, b$  for different sub-bath-plaquette), to respect a translational invariance inside the bath-plaquette, and we allow for hopping of electrons inside the bath-plaquette introducing a nearest neighbor hopping  $t_j$  ( $j = a, b$ ) and next-nearest neighbor hopping  $t'_j$  ( $j = a, b$ ). An electron in a cluster-site can hop to the corresponding bath-plaquette-site with hopping parameter  $V_j$  ( $j = a, b$ ), which is the same for all the cluster-site and it is only plaquette-dependent. The reduction in the number of parameters is clear. Considering the simple example displayed in Fig. (4.26), with  $N_c = 4$  and  $N_b = 8$ , a free bath-parametrization requires a search for  $2XN_cXN_b = 64$  hybridization parameters  $V_{k\mu}$  plus  $2XN_b = 16$  bath energies  $\varepsilon_{k\sigma}$ , giving a total of 80 parameters to optimize (the factor 2 is for the spin). In the case of the constrained parametrization, instead, we have 2 hybridizing  $V_j$ , one for each sub-plaquette-bath, 2 bath energies  $\varepsilon_j$ , 2 bath hopping terms  $t_j$  and 2  $t'_j$  ( $j = a, b$ ), in total 8 parameters only! It is now much easier to associate some physical property of the system to some specific set of parameters which can be turned on or off, according to the kind of solution sought. But this is not the only advantage: the bath-plaquette

constructed to be "copies" of the cluster-impurity do respect the square symmetry of the original lattice model, producing Weiss fields  $\mathcal{G}_o$  which automatically respect these symmetries. This property guarantess obtaining results physically meaningful and also helps in determining good starting seeds for a full free-parameters DMFT calculation. The risk with too many parameters is that one ends up with a solution which, although of a small distance and respecting (in the limits of numerical precision) the CDMFT-self-consistency condition, breaks the physical symmetries expected for the solution.

It is easily shown how the constrained parametrization is included in the most general expression (4.14). To this purpose it is convenient to introduce spinor notation in the example presented above with  $N_c = 4$  and  $N_b = 8$ :

$$\begin{aligned}\psi_{j\sigma} &= (c_{1\sigma}^j, \dots, c_{4\sigma}^j) \\ \phi_{j\sigma} &= (a_{1\sigma}^j, \dots, a_{4\sigma}^j)\end{aligned}\tag{4.15}$$

where  $j = a, b$  indicates the 2 sub-bath-plaquettes, and write the bath (formula 4.14):

$$\sum_{j=a,b} \phi_{j\sigma}^\dagger \mathbf{E}_{j\sigma} \phi_{j\sigma} + \phi_{j\sigma}^\dagger \mathbf{V}_{j\sigma} \psi_{j\sigma} + \psi_{j\sigma}^\dagger \mathbf{V}_{j\sigma}^\dagger \phi_{j\sigma}\tag{4.16}$$

where  $\mathbf{E}_j$  is a matrix containing the bath energies in the free parametrization (for which is diagonal) and also the bath-hopping in the constrained parametrization:

$$\mathbf{E}_{j\sigma} = \begin{pmatrix} \varepsilon_{1j\sigma} & 0 & 0 & 0 \\ 0 & \varepsilon_{2j\sigma} & 0 & 0 \\ 0 & 0 & \varepsilon_{3j\sigma} & 0 \\ 0 & 0 & 0 & \varepsilon_{4j\sigma} \end{pmatrix} \quad \text{free parameterization}$$

$$\mathbf{E}'_{j\sigma} = \begin{pmatrix} \varepsilon_{j\sigma} & t_j & t'_j & t_j \\ t_j & \varepsilon_{j\sigma} & t_j & t'_j \\ t'_j & t_j & \varepsilon_{j\sigma} & t_j \\ t_j & t'_j & t_j & \varepsilon_{j\sigma} \end{pmatrix} \quad \text{cons. parameterization}$$

while in general for the free parametrization the hybridizing hopping  $\mathbf{V}_j$  is

$$\mathbf{V}_{j\sigma} = \begin{pmatrix} V_{11}^j & V_{12}^j & V_{13}^j & V_{14}^j \\ V_{21}^j & V_{22}^j & V_{23}^j & V_{24}^j \\ V_{31}^j & V_{32}^j & V_{33}^j & V_{34}^j \\ V_{41}^j & V_{42}^j & V_{43}^j & V_{44}^j \end{pmatrix}$$

in the constrained it is simply diagonal

$$\mathbf{V}'_{j\sigma} = \begin{pmatrix} V_j & 0 & 0 & 0 \\ 0 & V_j & 0 & 0 \\ 0 & 0 & V_j & 0 \\ 0 & 0 & 0 & V_j \end{pmatrix}$$

So to express the constrained parametrization in terms of the free one it is enough to look for the congruence transformation  $\mathbf{S}$  ( $\mathbf{S}\mathbf{S}^T = \mathbf{1}$ ) which diagonalizes  $\mathbf{E}'_{j\sigma}$ :

$$\mathbf{E}_{j\sigma} = \mathbf{S}\mathbf{E}'_{j\sigma}\mathbf{S}^T = \begin{pmatrix} \varepsilon_{j\sigma} - t'_j & 0 & 0 & 0 \\ 0 & \varepsilon_{j\sigma} + t'_j & 0 & 0 \\ 0 & 0 & \varepsilon_{j\sigma} - \sqrt{t_j'^2 + 4t_j^2} & 0 \\ 0 & 0 & 0 & \varepsilon_{j\sigma} + \sqrt{t_j'^2 + 4t_j^2} \end{pmatrix} \quad (4.17)$$

and clearly  $\mathbf{V}_{j\sigma}$  is not diagonal anymore:

$$\mathbf{V}_{j\sigma} = \mathbf{V}'_{j\sigma}\mathbf{S}^T = \begin{pmatrix} 0 & -V_j/\sqrt{2} & 0 & V_j/\sqrt{2} \\ -V_j/\sqrt{2} & 0 & V_j/\sqrt{2} & 0 \\ -\Theta^+V_j/2\Lambda & t_bV_j/\Theta^+ & -\Theta^+V_j/2\Lambda & t_jV_j/\Theta^+ \\ -\Theta^-V_j/2\Lambda & t_jV_j/\Theta^- & -\Theta^-V_j/2\Lambda & t_jV_j/\Theta^- \end{pmatrix} \quad (4.18)$$

where we indicate  $\Lambda = \sqrt{t_j'^2 + 4t_j^2}$ ,  $\Theta^{+(-)} = \sqrt{4t_j^2 + t_j'(t_j' + (-)\Lambda)}$ . Notice that in the

case  $t'_j = 0$  the expressions 4.17 and 4.18 further simplify:

$$\mathbf{E}_{j\sigma} = \mathbf{S} \mathbf{E}'_{j\sigma} \mathbf{S}^T = \begin{pmatrix} \varepsilon_{j\sigma} & 0 & 0 & 0 \\ 0 & \varepsilon_{j\sigma} & 0 & 0 \\ 0 & 0 & \varepsilon_{j\sigma} - 2t_j & 0 \\ 0 & 0 & 0 & \varepsilon_{j\sigma} + 2t_j \end{pmatrix} \quad (4.19)$$

and

$$\mathbf{V}_{j\sigma} = \mathbf{V}'_{j\sigma} \mathbf{S}^T = \begin{pmatrix} 0 & -V_j/\sqrt{2} & 0 & V_j/\sqrt{2} \\ -V_j/\sqrt{2} & 0 & V_j/\sqrt{2} & 0 \\ -V_j/2 & V_j/2 & -V_j/2 & V_j/2 \\ -V_j/2 & V_j/2 & -V_j/2 & V_j/2 \end{pmatrix} \quad (4.20)$$

a degeneracy appears in the poles of each cluster bath, which are symmetrically coupled to sites 1-3 and 2-4 of the cluster-plaquette (first two row in the hybridizing matrix 4.20). This transformation also shows that the form (4.14) is indeed the most general we can adopt. A good operative procedure for obtaining results is to start using the more controllable constrained parametrization, and, starting from this solution and exploiting the relations above (4.18)(4.17), relax the parameters using the free parametrization. In this way we first get close to a region of the parameter-space of physical interest, and then we improve the result freeing all the degrees of freedom we can.

## Chapter 5

### Results in 2D

#### 5.1 Strong Coupling $U/t=16$

In this chapter we apply CDMFT to the study of the MT in two dimensions. Anticipating the cuprate material physics, we consider once again the two-dimensional Hubbard model on the square lattice:

$$H = - \sum_{i,j,\sigma} t_{ij} (c_{i\sigma}^\dagger c_{j\sigma} + h.c.) + U \sum_i n_{i\uparrow} n_{i\downarrow} - \mu \sum_i n_i$$

where  $c_{i\sigma}$  ( $c_{i\sigma}^\dagger$ ) are destruction (creation) operators for electrons of spin  $\sigma$ ,  $n_{i\sigma} = c_{i\sigma}^\dagger c_{i\sigma}$  is the number operator,  $U$  is the on-site repulsion and  $\mu$  the chemical potential which determines the electron density  $n = 1/N \sum_{i,\sigma} \langle n_{i\sigma} \rangle$  ( $N$  being the number of sites). The hopping amplitude  $t_{ij}$  is limited to nearest-neighbors  $t$  and to next-nearest-neighbors  $t'$ . We want to focus our attention on the "Mottness". In the half-filled insulating case and for intermediate values of the coupling  $U$ , a crossover takes place from a AF-band insulator to a AF-Mott insulator for increasing  $U$ . Our task is to study the doped AF-Mott state, so we choose an on-site repulsion  $U = 16t$  in order to be deep in the strongly correlated regime. For the sake of convenience we also confine the study to the hole-doped system ( $n < 1$ ) at different levels of frustration controlled by the value of  $t'/t$ . This is equivalent to the electron-doped system ( $n > 1$ ) after a particle-hole transformation which reverses the sign of  $t'$ . In particular we consider relatively small values of  $t'/t = \pm 0.3$  suitable to describe the cuprates and a large value  $t'/t = 0.9$ , which, despite having no direct correspondence with real materials, is able to completely destroy any long-ranged AF ordering. (see the right panel of Fig. 5.1, displaying the staggered magnetization  $m = 1/N \sum_i (-1)^i (n_{i\uparrow} - n_{i\downarrow})$  at half-filling as a function of  $t'/t$ ). The quantum impurity model chosen for this case consists of a

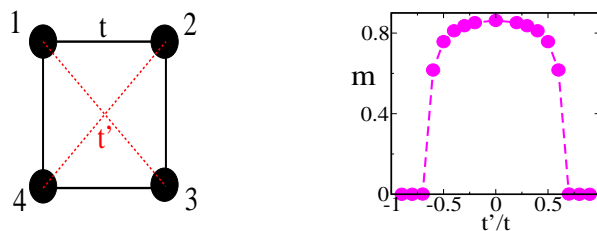


Figure 5.1: Left side: the CDMFT plaquette. Right side: staggered magnetization as a function of the next-nearest hopping  $t'$  at half-filling. The parameter  $t'$  controls the magnetic frustration in the system.

$2 \times 2$  plaquette (see Fig. 5.1), embedded in an effective medium described by a self-consistently determined Weiss function. We consider here a metallic phase which does not break any symmetry and follow its evolution as a function of doping. The choice of a plaquette-cluster is minimal in order to respect the lattice square-symmetry and it allows describing various broken symmetries, such as antiferromagnetism (AF) or  $d$ -wave superconductivity. With CDMFT on a plaquette we can describe the evolution of the electronic structure of the model in terms of just a few (three is the present case) functions of frequency which have a simple physical interpretation as parameterizing the lattice self energy, and which show a systematic evolution towards the Mott insulator (see Fig. 5.2 and discussion below). It can be considered as a dynamical generalization of the early slave boson mean field theory [36][43] which is able to treat both the coherent and the incoherent excitations (quasiparticle peak and Hubbard bands) on the same footing, capturing the short-range physics of singlet formation on bonds.

In order to perform an ED solution, the quantum impurity model is truncated to a finite number (in this case 8) bath levels, whose energies and hybridizations are self-consistently determined through the minimization procedure. As we explained in chapter 3, to implement the self-consistency condition, we need to introduce Matsubara frequencies and hence an effective inverse temperature  $\beta$  which we set to  $\beta = 128$  in units of the half bandwidth  $4t$ . At low  $\beta$  and relatively small  $U$  our results are qualitatively similar to those obtained solving the impurity by QMC (chapter 4.2). Details on the implementation of ED within CDMFT and a benchmark against the exact solution

of the Hubbard model in one dimension were presented in the previous chapter. As already stressed, ED method's main limitations are the small number of sites in the bath and the effective temperature, which induces a limited energy resolution [12, 19]. The small size of the cluster induces a finite  $k$  resolution : for the  $2 \times 2$  plaquette with the square symmetry we only have two independent directions in  $k$  space (along the diagonal and along the lattice axis).

### 5.1.1 Cluster quantities

We first analyze cluster quantities, postponing to the next subsection results in the momentum space. In the latter case in fact we will see that the periodizing method we use is important. Using the square symmetry, the CDMFT results for the plaquette are succinctly expressed in terms of three self-energies  $\Sigma_{11}$ ,  $\Sigma_{12}$ ,  $\Sigma_{13}$ , or alternatively in terms of the eigenvalues of the cluster self-energy matrix  $\Sigma_{ij}$ , which can be thought as the lattice self-energies in specific points of the momentum space, namely  $\Sigma_A$  in  $(0, \pi)$  and  $(\pi, 0)$ ,  $\Sigma_B$  in  $(\pi, \pi)$  and  $\Sigma_C$  in  $(0, 0)$  (Fig.5.3).

$$\begin{aligned}\Sigma_A &= \Sigma_{11} - \Sigma_{13} \\ \Sigma_B &= \Sigma_{11} - 2\Sigma_{12} + \Sigma_{13} \\ \Sigma_C &= \Sigma_{11} + 2\Sigma_{12} + \Sigma_{13}\end{aligned}\tag{5.1}$$

CDMFT causality requires that the imaginary part of all the self-energy eigenvalues is negative (i.e.  $\text{Im}\hat{\Sigma}$  is definitive negative). As shown in Fig. 5.2,  $\Sigma_A$ ,  $\Sigma_B$  and  $\Sigma_C$  exhibit a clear systematic behavior as the Mott transition is approached. This systematic tendency describes the approaching of the system to the Mott insulator. In particular we notice that, at the virtual temperature used in this study  $\beta^{-1}$ , the  $\text{Im}\Sigma_X \sim -\alpha\omega$  goes to zero for  $\omega \rightarrow 0$ , as expected in a regular FL. We keep here a conservative point of view, and assume at zeroth order approximation that the system is indeed a FL. As the transition is approached, we study how the quiparticles residua  $Z_X = (1 - \frac{\partial \text{Im}\Sigma_X}{\partial \omega})^{-1}$  ( $X = A, B, C$ ) behave in the 4 corner points of the momentum space that we have (Fig. 5.3). The result is shown in Fig. 5.4, where the 3 cases  $t' = \pm 0.3$ , and the strongly frustrated one  $t' = +0.9$  are displayed. In all of them the quasiparticle residuum  $Z_B$  corresponding to the point  $(\pi, \pi)$  in  $k$ -space goes in linearly to zero as the density

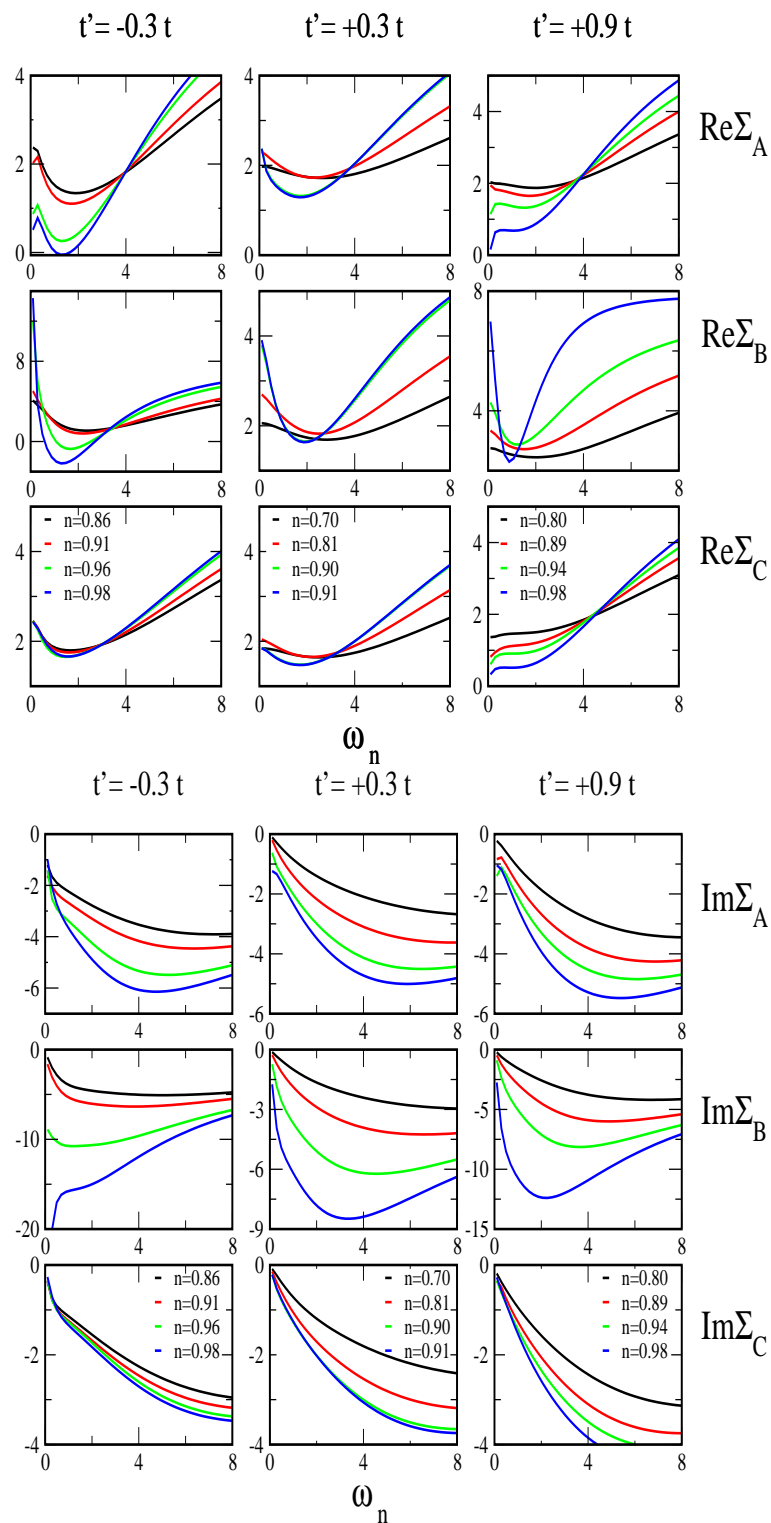


Figure 5.2: Real (top) and imaginary (bottom) parts of the eigenvalues of the cluster self-energies for  $t'/t = \pm 0.3, +0.9$ . Interaction  $U = 16t$ , the inverse virtual temperature  $\beta = 32/t$ .

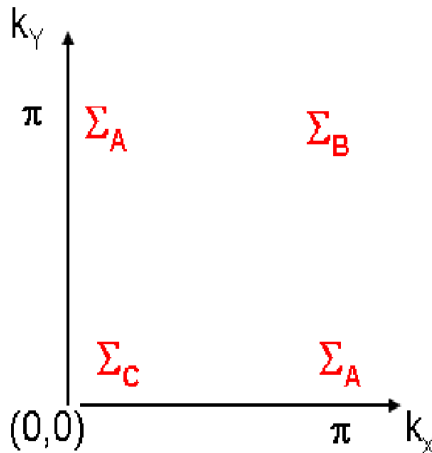


Figure 5.3: Eigenvalues of the cluster self-energy  $\Sigma_{\mu\nu}$ . They can be interpreted as the "corners" points in the first quadrant of the BZ

$n \rightarrow 1$ . This is reminiscent of previous results with DMFT [35], where at the Mott transition point the quasiparticles disappear because the residuum was going to zero. However in CDMFT, the residua in the other points  $A, C$  extrapolate to a finite value. This clearly shows that the Mott transition is not approached in the same way in the different regions of the BZ.

The real parts of the eigenvalues of the cluster self-energy (Fig.5.2) can be seen as renormalizing the bare chemical potential in the special corner points of the BZ (Fig.5.3:

$$\mu_{eff} = \mu - \text{Re}\Sigma_X \quad (5.2)$$

where  $X = A, B, C$ . The way this occurs is shown in Fig. 5.5, where we compare the renormalized chemical potential  $\mu_{eff}$  in the corner points B [  $k = (\pi, \pi)$ , black filled circles ] and C [  $k = (0, \pi)$ , open red circles ] with the bare band energy  $\varepsilon_k$  [ the minimum of the band in  $k = (0, 0)$  and the maximum of the band in  $k = (\pi, \pi)$  ]. For reference, we also plot the value of the band in  $(0, \pi)$  and the value of the bare chemical potential  $\mu$ . The graph displays how  $\mu_{eff}$  varies as a function of increasing bare chemical potential  $\mu$  (i.e. approaching the MT) for the two cases  $U = 16t$ ,  $t' = \pm 0.3t$ . In order for the

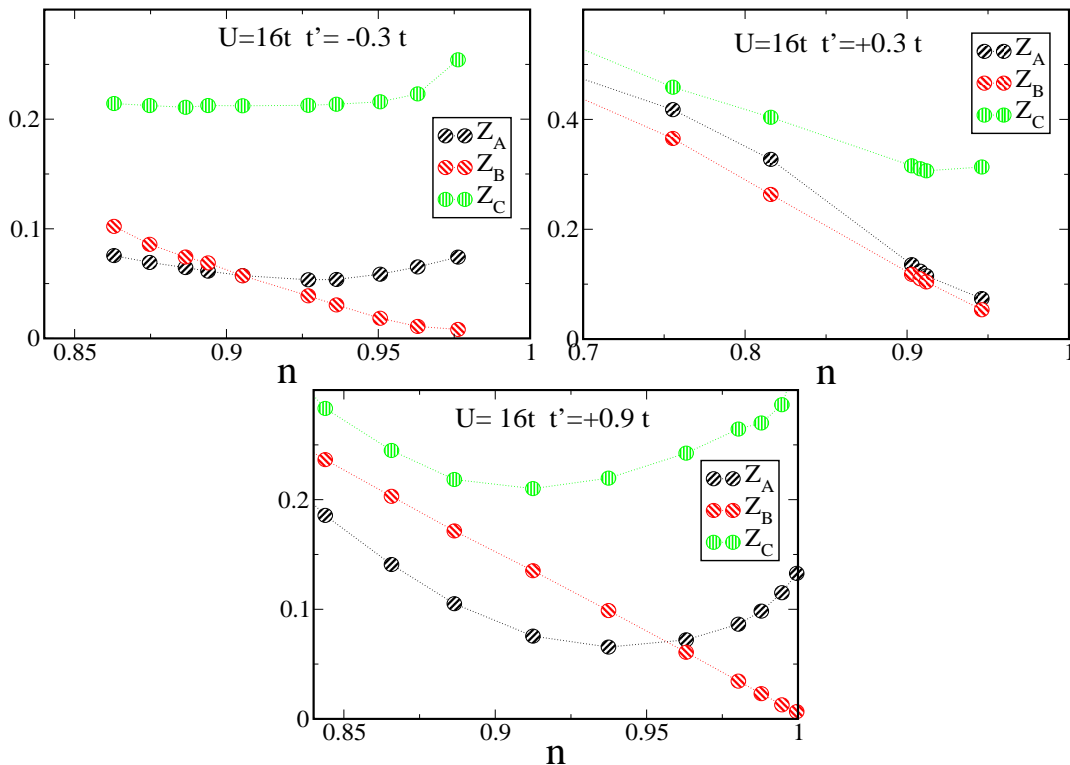


Figure 5.4: Cluster quasiparticle residua  $Z_X$  ( $X = A, B, C$ ) as a function of density  $n$ , for  $U = 16t$  and  $t' = \pm 0.3$  and  $t' = +0.9$ . Virtual temperature is  $\beta = 32/t$ .

FS to form, the value of the chemical potential has to lie inside the band, so that the equation  $\varepsilon_k - \mu_{eff} = 0$  can be satisfied and a pole is formed in the one particle Green's function, i.e. the chemical potential  $\mu$  has to meet the value of the band  $\varepsilon_k$  for some point  $k$  in the BZ. Now in all the three cases displayed something dramatic happens in correspondence of the B point  $k = (\pi, \pi)$ : the  $\mu_{eff}$  diverges from the value of the band in that point (black dashed line top of the band): this region in  $k$ -space is becoming insulating-like before all the others. In the cases  $U = 16t$ ,  $t' = -0.3t$  and  $U = 8t$ ,  $t' = 0.0$  it even escapes out of the bare band. When this happens in the  $k$ -point B there are no particle-states available at any energy. Though the effect is less pronounced, this is also true in the case  $U = 16t$ ,  $t' = +0.3t$ . In cases  $U = 16t$ ,  $t' = -0.3t$  and  $U = 8t$ ,  $t' = 0.0$ , even if less than in the B point,  $\mu_{eff}$  in the C  $k$ -point at  $(0, \pi)$  is also escaping its band value, becoming insulating-like. For  $U = 16t$ ,  $t' = +0.3$  instead we can observe that  $\mu_{eff}$  moves towards the band value (red dashed line), meeting it

in correspondence of the MT. From this picture we can infer that the FS will pass in  $(0, \pi)$  right at the MT. We will verify this observation in the next section. This result extends the previous DMFT conclusion that strong inelastic scattering is enhanced close to the MT and that the break-up of the metal is signed by the renormalized chemical potential  $\mu$  going out of the bare band [37]. In DMFT, however, the renormalized  $\mu$  is an uniform quantity in  $k$ -space. CDMFT, allowing for  $k$ -dependent self-energy, shows that the chemical potential  $\mu$  is renormalized at different rates in different points of the BZ, and that the MT may take place in an anisotropic fashion. In order to make some further steps, however, it is necessary to understand what happens to quasiparticles in correspondence of the FS, which lies between the 4 corner points A,B and C. For this it is necessary to periodize the cluster self-energy onto the  $k$ -space.

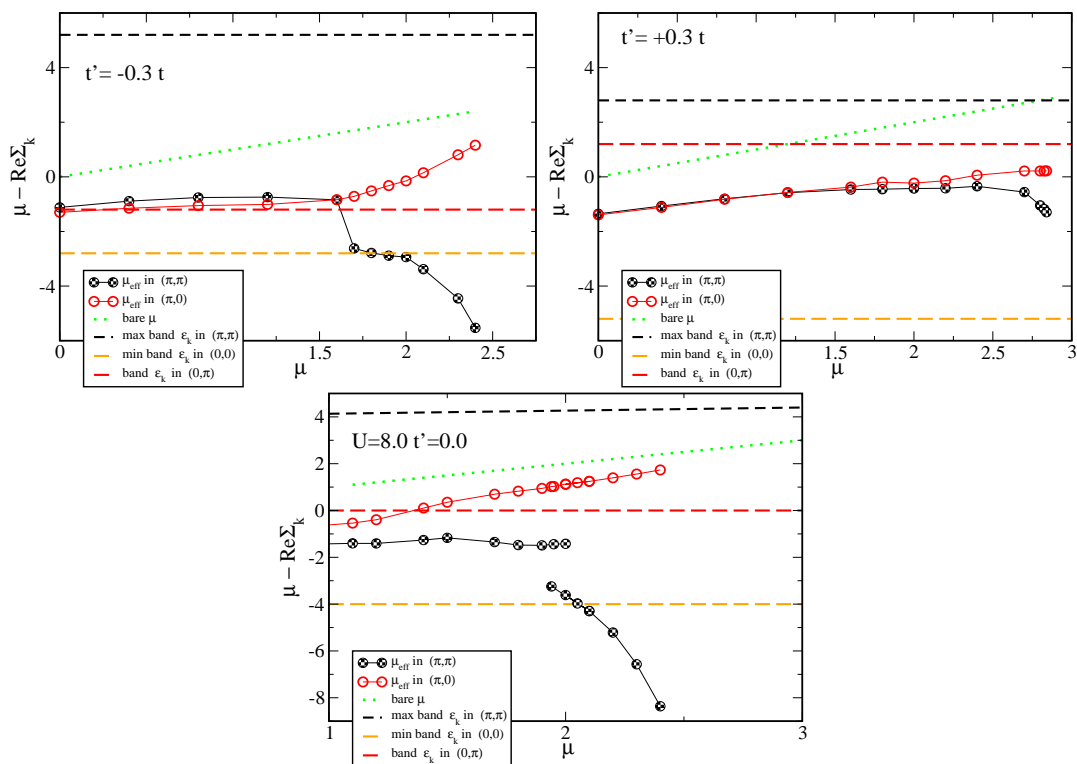


Figure 5.5: Renormalized chemical potential  $\mu_{eff} = \mu - \text{Re}\Sigma_k$  as a function of the bare chemical potential  $\mu$ . The maximum of the one particle spectrum  $\epsilon_k$  [ $k = (\pi, \pi)$ ], the minimum [ $k = (0, 0)$ ], and the its value in  $k = (0, \pi)$  are also displayed. A pole in the Green's function appears when  $\mu_{eff} \equiv \epsilon_k$ .

## 5.2 $\Sigma$ -scheme periodization: a conservative FL perspective

We first study the MT in our system by applying the  $\Sigma$ -scheme periodization, introduced in the previous chapter. This interpretation of the result is the more classical-FL-approach, as the self-energy is a simple linear combination of the cluster self-energies [55] and they cannot give rise to any singularity in the lattice Green's functions (if not already present in the cluster self-energies):

$$\Sigma_{\text{latt}}(k, \omega) = \Sigma_A S_A(k) + \Sigma_B S_B(k) + \Sigma_C S_C(k) \quad (5.3)$$

where the functions

$$\begin{aligned} S_A(k) &= (1 - \cos k_x \cos k_y)/2 \\ S_B(k) &= (1 - \cos k_x - \cos k_y + \cos k_x \cos k_y)/4 \\ S_C(k) &= (1 + \cos k_x + \cos k_y + \cos k_x \cos k_y)/4 \end{aligned} \quad (5.4)$$

are positive ( and notice that  $S_A(k) + S_B(k) + S_C(k) = 1$ ). At large doping, only  $\Sigma_{11}$  is appreciably different from zero, while  $\Sigma_{12}, \Sigma_{13} \simeq 0$ . The lattice self-energy  $\Sigma_{\text{latt}}(k, \omega)$  [from Eq. (5.3)] is therefore  $k$ -independent and single-site DMFT results are recovered. However the cluster self-energies increase sizably at low doping, making  $\Sigma_{\text{latt}}$  strongly  $k$ -dependent. So let us first look at the behavior of the FS as we get close to the MT. The zero frequency limit of the real part of  $\Sigma(k, \omega)$  determines the shape of the interacting FS, which we define as  $t_{\text{eff}}(k) = \mu$ , where  $t_{\text{eff}}(k) \equiv t(k) - \text{Re}\Sigma_{\text{latt}}(k, \omega = 0^+)$ ,  $t(k)$  being the Fourier transform of the hopping  $t_{ij}$  and the  $\omega = 0^+$  limit is extrapolated from the lowest Matsubara frequencies. The renormalization of the FS becomes appreciable close to the MT. The self-energy itself depends weakly on the sign of  $t'$ , and in particular it has the same sign for both positive and negative  $t'$ . However, given its large magnitude, when combined with  $t'$  of different signs, it produces interacting FS's of very different shape in the electron-doped and hole-doped case (dashed lines in Fig. 5.7). This can be understood in terms of the renormalized low energy hopping coefficients  $t_{\text{eff}} = t - \text{Re}\Sigma_{12}(\omega = 0^+)/2$  and  $t'_{\text{eff}} = t' - \text{Re}\Sigma_{13}(\omega = 0^+)/4$  presented in Fig. 5.6. Regardless the value of  $t'/t$ , correlations act to *increase* the value of  $t_{\text{eff}}$ . This physical effect, predicted by earlier slave-boson studies [36][43]

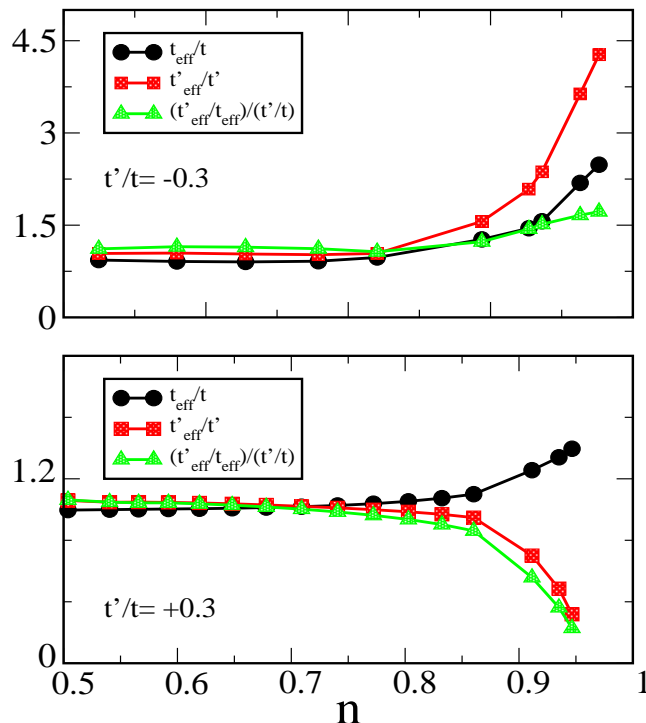


Figure 5.6: Renormalization of the hopping coefficients and of their ratio as a function of density for  $U = 16t$  and  $t'/t = \pm 0.3$ ,  $\beta = 32/t$ .

reduces the mass divergence characteristic of single-site DMFT where the effective mass scales inversely proportionally to the quasiparticle residue. The renormalization of  $t'$  depends instead on the sign of  $t'/t$ . This is an effect which is not present in slave-boson theories [36][43]. For  $t' = -0.3t$ ,  $|t'_{\text{eff}}|$  increases in such a way that the ratio  $(t'_{\text{eff}}/t_{\text{eff}})/(t'/t)$  weakly increases approaching the Mott insulator, thereby enhancing the hole-like curvature of the FS. On the other hand,  $t'_{\text{eff}}$  decreases for  $t' = +0.3t$ , giving rise to an almost nested FS as half-filling is approached. This is also clearly seen in Fig. 5.7, where the FS is shown on top of the spectral function (see below). In the hole-doped case we observe also a horizontal flattening of the FS close to  $(0, \pi)$  or  $(\pi, 0)$  approaching the MT. The shape of the FS is similar to what observed in ARPES [27], and thereby interpreted as resulting from a doping independent nesting vector.

Inelastic scattering strongly increases as the Mott insulator is approached [56, 37, 65]. In order to investigate the anisotropy of this quantity we study the imaginary part of the self-energy, plotted in Fig. 5.2. Using Eq. (5.3), we can evaluate the

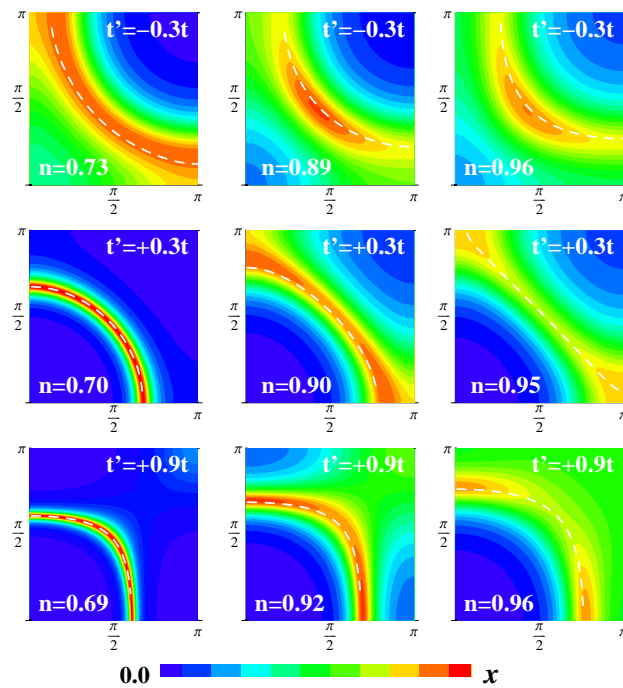


Figure 5.7:  $A(k, \omega = 0^+)$  in the first quadrant of the Brillouin zone. In the first row from the top  $t' = -0.3t$ , densities  $n = 0.73, 0.89, 0.96$ , color scale  $x = 0.28, 0.22, 0.12$ ; in the second row  $t' = +0.3t$ ,  $n = 0.70, 0.90, 0.95$ , color scale  $x = 0.82, 0.34, 0.27$ ; in the lowest row  $t' = +0.9t$ ,  $n = 0.69, 0.92, 0.96$ , color scale  $x = 0.90, 0.32, 0.22$ . The white dashed line is the FS given by  $t_{\text{eff}}(k) = \mu$ .

lifetime, or inverse scattering rate  $\tau_k^{-1} = -\text{Im}\Sigma(k, \omega = 0^+)$  (again extrapolating to zero the Matsubara values). Let us emphasize that our calculation is performed at a finite effective temperature. In a Fermi liquid this quantity would be small and vanish as  $T^2$  as the temperature goes to zero. Here we find a strong modulation of  $\tau_k^{-1}$  in the Brillouin zone that develops when the Mott point is approached. Our results, as well as the QMC-CDMFT of Ref. [55], may be interpreted in terms of a strongly anisotropic coherence scale, which decreases at low doping. When the scale becomes smaller than the energy resolution of our calculation we can not follow the decrease of  $\text{Im}\Sigma$  with decreasing frequency (as evidenced by the line for  $n = 0.98$  for  $t'/t = -0.3$  of Fig. 5.2). Therefore it not possible to decide between a scenario where the Fermi liquid picture breaks down or where the Fermi liquid coherence scale is smaller than our energy resolution.

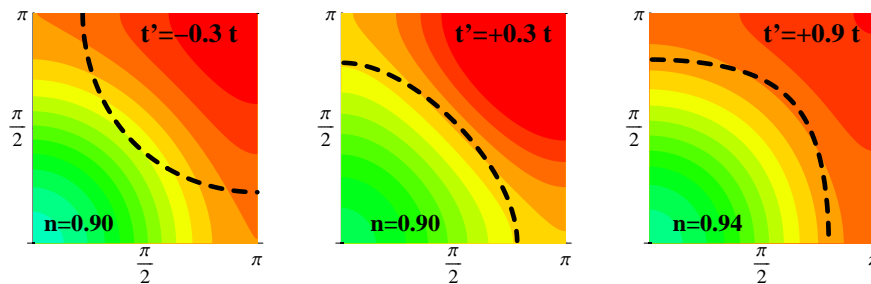


Figure 5.8:  $\tau_k^{-1}$  in the first quadrant of the BZ as calculated from Eq. 5.3. Red regions are high scattering, green low scattering. Color scale is relative. The dashed line is the renormalized FS given by  $t_{\text{eff}}(k) = \mu$ .

In Fig. 5.8 we show an intensity plot of  $\tau_k^{-1}$  for  $n = 0.9 - 0.94$  and the values of  $t'$  previously considered. We observe that approaching the MT the scattering rate is enhanced in the region around the  $(\pi, \pi)$  point of the momentum space, independently of the value of  $t'$ . This is also the point where the cluster-quasiparticle-residuum  $Z_B$  effectively goes to zero when approaching the MT. The FS (dashed line in Fig. 5.8) hits this region at different points, according to its hole-like or electron-like curvature. Hence the finite temperature lifetime is strongly modulated in momentum space. Extrapolating to zero temperature, quasiparticles disappear first in some regions of the momentum space and survive in others. In the hole-like case ( $t' = -0.3t$ ) the FS hits the large scattering region around  $(0, \pi)$  and  $(\pi, 0)$ , while for the electron-like cases ( $t' = +0.3, 0.9$ ) the crossing occurs close to  $(\pi/2, \pi/2)$ . Thus the combined effect of different scattering properties in the momentum space and the renormalization of the FS gives rise to the formation of a *cold* [*hot*] spot in  $(\pi/2, \pi/2)$  [ $(0, \pi), (\pi, 0)$ ] in the hole-like system. In the electron-doped system the position of hot and cold spots is inverted. The presence of hot/cold regions is reflected also by the spectral function  $A(k, \omega = 0^+) = -1/\pi \text{Im}G(k, 0^+)$ , shown in Fig. 5.7, which agrees with the qualitative behavior of experimental ARPES spectra [15][11]. These results have a direct experimental interpretation: in particular photoemission data should take into account the renormalization of the shape of the FS in order to extract the model Hamiltonian parameters. They also suggest a new viewpoint concerning the origin of the experimentally

observed asymmetry between electron and hole doped cuprates. We will explain this in the next chapter in more detail, where we will analyze the superconducting phase. Here we observe that in the hole-doped case the quasiparticles survive in the diagonal of the Brillouin zone, near  $(\pi/2, \pi/2)$ . This state, which has a fermionic spectrum with point zeroes can be connected to the quasiparticles of the d-wave superconducting state. The electron-doped case is completely different. On a technical level, it is harder to approach the MT closely, and a first-order phase transition may preempt a continuous approach to the insulating state. Furthermore, the FS is renormalized towards nesting, and the quasiparticles survive in a small region around  $(\pi, 0)$  and  $(0, \pi)$ . These quasiparticles cannot be easily deformed into the superconducting state as compared to the quasiparticles which live around  $(\pi/2, \pi/2)$ . These properties of the underlying normal state of the Hubbard model have striking resemblance to what is observed in the cuprates. The hole-doped materials have a superconducting region which appears almost immediately after doping the Mott insulator. This superconducting state evolves continuously into the pseudogap state which in turn evolves continuously from the Mott insulator. In the electron-doped case, the pseudogap region is small, and a much larger doping is needed to reach the superconducting phase.

Finally we emphasize that our results for large frustration  $t' = +0.9t$  (third panel in Fig. 5.8 and third row in Fig. 5.7, are always qualitatively similar to the weakly frustrated system with the same sign of  $t'$ . This clearly shows that, at the  $k$ -resolution considered in this study, the momentum-space differentiation does not depend on the AF ordering of the parent insulator, since it occurs also for a system in which AF is destroyed by frustration and the insulator is likely to have a more exotic form of long-range order. Moreover, since at high doping (or temperature) we find that non-local self-energies are negligible and single-site DMFT is not corrected by cluster DMFT, we expect similarly that there is an intermediate doping (or temperature) region where the results of the  $2 \times 2$  cluster will not be modified by increasing the cluster size. Our conclusion is that in this region there is  $k$ -space differentiation, which is independent of the value of  $t'$  and is therefore due to short-range correlations, captured within the plaquette, rather than to the specific order of the parent Mott insulator.

So, analyzing our CDMFT results under a  $\Sigma$ -scheme-periodization we can state that:

1. the FS is strongly renormalized by the interaction,
2. there is a breakdown of the FS and the appearance of *cold* and *hot* regions, whose precise location is the result of an interplay of the renormalization of the real and the imaginary parts of the self-energy,
3. the emergence of these hot/cold regions is a consequence of the proximity of the Mott transition and long-ranged AF correlation is not a necessary condition for its existence.

These are zeroth order results, whose general statement is independent of the periodizing scheme adopted to evaluate the momentum-space quantities. The point of view is conservative, in the sense that no particular anomaly in the FL is allowed by the  $\Sigma$ -scheme which has the FL hypothesis at its foundation.

### 5.3 Dependence of the Results on the periodizing-scheme

We want now to discuss how the results presented in the previous section, obtained in the framework of the  $\Sigma$ -scheme, depend on the periodizing scheme. Alternative periodizing schemes were presented in chapter 4.3 (formulas 4.4 and 4.6). We will show that the gross features are not in fact periodizing-scheme dependent, while the low-energy behavior indeed is. We focus here our attention on how the MT is approached. In Fig.5.9, we show that the phenomenon of momentum space differentiation plotting the spectral function  $A(k, \omega \rightarrow 0)$  in the first quadrant of the BZ for the 2 cases already considered  $t' = -0.3t, +0.3t$  (first, second rows), for the 3 different methods ( $\Sigma$ ,  $M$ ,  $G$ -schemes in the first, second and third columns respectively), and for a small value of doping where the effect is most evident (10% doping). We see a strong similarity in the shape of the *cold/hot* scattering regions. Moreover the effect of scattering differentiation is even enhanced in the case of the  $M$ -method and  $G$ -method, appearing to be a robust feature. If we further investigate the mechanism of interplay between the "bending"

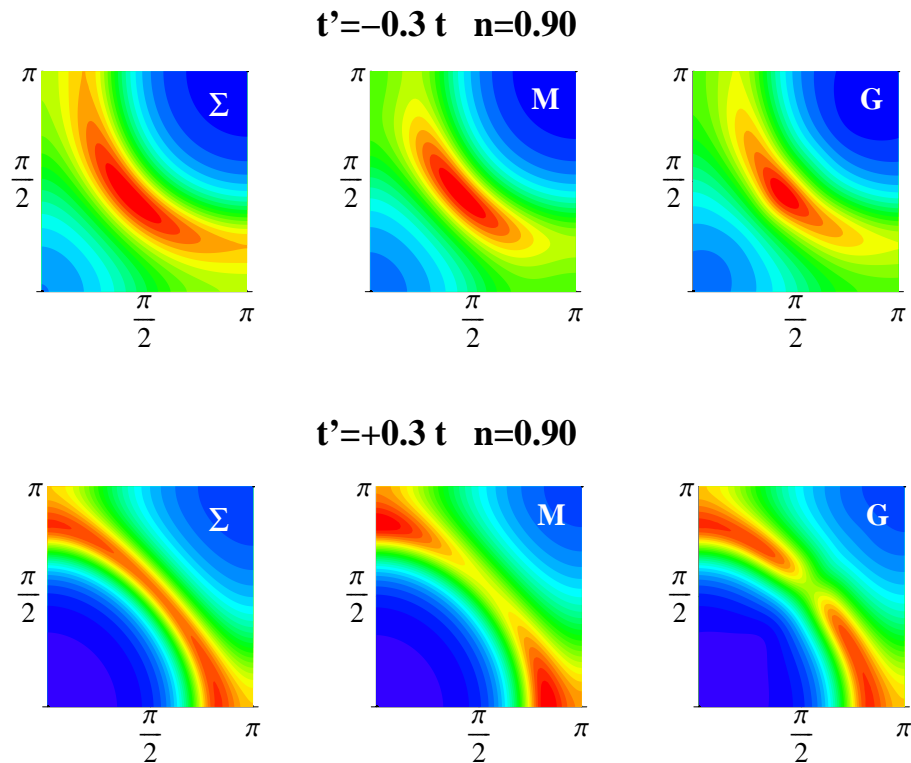


Figure 5.9: Spectral function at the Fermi level in the  $k$ -space. We present here the cases  $t' = -0.3t$  (upper row) and  $t' = +0.3t$  (lower row) at a density  $n = 0.90$ . The results from the three different periodizing schemes  $\Sigma$ ,  $M$  and  $G$  are presented.

of the FS in the hole/ $e^-$ -like system and the  $k$ -space-modulation of the scattering rate  $\tau_k = -\text{Im}\Sigma_k$  (Fig.5.10), we see that the shape of the modulation is method dependent, but that the  $(\pi, \pi)$  point is the highest-scattering driving the system into the MT remain un-altered. This gives, as was mentioned, a naive zeroth order picture on how the MI is approached and why the hot/cold spots appear as effect of the proximity to the MT. We show however that there are also fundamental differences, which start to appear while considering the frequency dependence of the Green's functions. For example in Fig. 5.11 (left hand side) we show the spectral function at  $\sim 10\%$  doping  $A(\omega, k)$  as a function of  $\omega$  along a path in the BZ  $(0, 0) \rightarrow (\pi, \pi) \rightarrow (\pi, \pi) \rightarrow (0, 0)$ , calculated with the  $\Sigma$ -method and for the two relevant cases  $t'/t = \pm 0.3$ . The  $\Sigma$ -scheme is "fitting" the results to a FL, producing a momentum-dependent self-energy which does not present any kind of singularity. In the case  $t'/t = -0.3$  (the upper graph), a quasiparticle peak

$$t' = -0.3t \quad n = 0.90$$

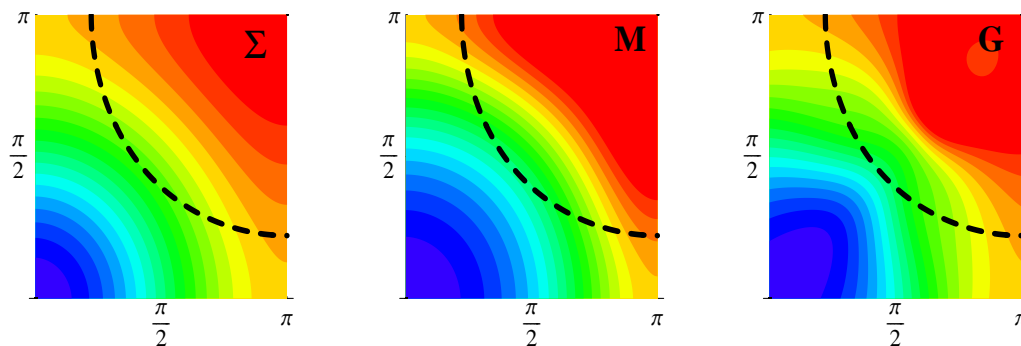


Figure 5.10:  $\tau_k^{-1}$  in the first quadrant of the BZ for the case  $t' = -0.3t$  and density  $n = 0.90$ . Results from the 3 periodizing-scheme  $\Sigma$ ,  $M$  and  $G$  are confronted. The color scale is relative.

disperses along the  $(0, 0) \rightarrow (\pi, \pi)$ , where a cold spot is formed at the Fermi level; on the contrary the peak is less dispersive passing through the region around  $(0, \pi)$ , where there is the hot spot. On the other hand, in the case  $t'/t = +0.3$  (lower graph in the left hand side) the quasiparticle peak is dispersing more in the vicinity of the region  $(0, \pi)$  and, while dispersing less, evaporates around  $(\pi/2, \pi/2)$ . The hot-cold spots are in this way switched. This is the FL viewpoint for the hot/cold spot formation as observed in ARPES experimental data [15][11], where a quasiparticle peak is detected in the spectral function  $A_k(\omega)$  in correspondence of the cold spot, while in the hot spot region  $A_k(\omega)$  present broad incoherent features. The effect of momentum-differentiation is however in this case quite weak. Looking at the same plots obtained using the  $M$ -scheme and the  $G$ -scheme, we observe a qualitatively similar behavior of the spectral function  $A(k, \omega)$ , as for example is shown in the right hand side of Fig. 5.11, where we display for the  $M$ -scheme (upper graph) and  $G$ -scheme (lower graph) for the case  $t' = -0.3t$ , to be confronted with the  $\Sigma$  scheme (upper graph, left hand side). However, a closer look in correspondence of the Fermi level (for example around the point  $(\pi/2, \pi/2)$ , as shown in detail in Fig. 5.12) shows that:

- the results of the  $M$ -scheme and the  $G$ -scheme are very close in spite the 2 methods

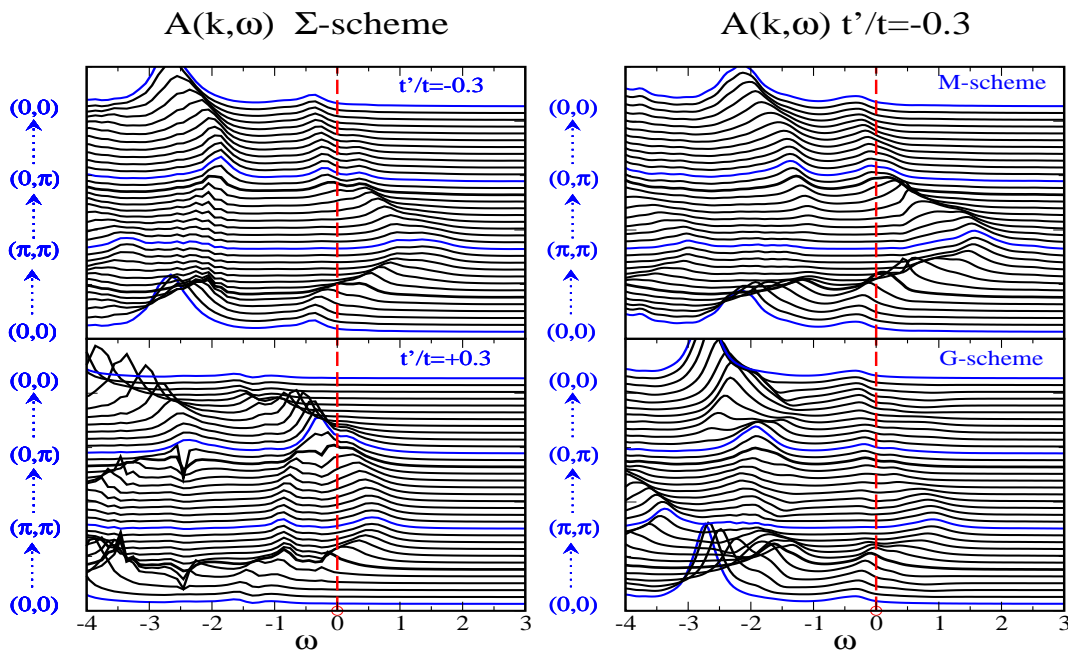


Figure 5.11:  $A(k, \omega)$  along the path  $(0, 0) \rightarrow (\pi, \pi) \rightarrow (0, \pi) \rightarrow (0, 0)$  in the first quadrant of the BZ. The density is  $n = 0.9$ . In the left hand side we present results obtained with the  $\Sigma$ -scheme periodization. The hole-like  $t'/t = -0.3$  case is on the upper graph, and electron-like  $t'/t = +0.3$  on the lower graph. On the right hand side we once again present the results for  $t'/t = -0.3$  case but obtained with the two other schemes:  $M$ -scheme periodization was used in the upper graph,  $G$ -scheme in the lower graph.

are a priori different (this was explained by Tudor Stanescu [66]).

- the low energy features, in particular the  $\omega \simeq 0$  corresponding to the Fermi level, are indeed quite different from the one obtained with the  $\Sigma$ -scheme (see detail Fig. 5.12).

In the  $M$  and  $G$ -scheme, and indeed around the cold region, the  $\Sigma$ -scheme quasiparticle peak appears now with a more complicated substructure, split in two other peaks. At the crossing of the FS in correspondence of the cold region the lower peak starts evaporating while the upper one (which is above the FS) increases. At the cold region, instead, we observe that the double pick feature with a depression in the middle creates a bigger difference in spectral weight in correspondence of the Fermi level at  $\omega = 0$ , and hence a more pronounced hot/cold spot modulation. This indicates a departure from a simply

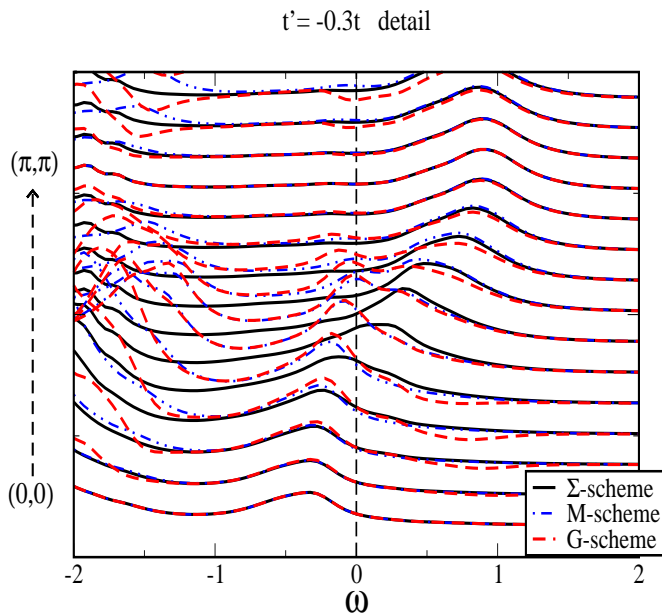


Figure 5.12: A detail of the spectral function  $A(k, \omega)$  as a function of  $\omega$  is presented along the path  $(0, 0) \rightarrow (\pi, \pi)$  in the first quadrant of the BZ. The 3 periodizing schemes  $\Sigma$ ,  $M$  and  $G$  are confronted in correspondence of the Fermi level at  $\omega = 0$ .

FL viewpoint given with the  $\Sigma$ -scheme.

In order to achieve a better understanding of these differences between schemes, let's continue to assume a FL state, and imagine that a good FL description of the system is valid in all methods. We can see if this hypothesis works or eventually breaks down. In the following we confront the  $\Sigma$ -method with the  $M$ -method, which, as we have seen, provides results very close to the  $G$ -method and it is more easy to hand from the theoretical viewpoint, as the  $k$ -dependent quantities we want to study can be directly linked to its cluster counterparts (as we show in the following). An indicator of the quasiparticle behavior is their residuum that can generally be extracted from the slope of the imaginary part of the self-energy on the Matsubara axis:

$$Z(k) = \lim_{\omega \rightarrow 0} \left( 1 - \frac{\partial \text{Im} \Sigma_k}{\partial \omega} \right)^{-1} \quad (5.5)$$

For convenience we link the  $k$ -dependent quantities to the corresponding cluster self-energies already used in the previous section:

$$Z_X = \lim_{\omega \rightarrow 0} \left( 1 - \frac{\partial \text{Im} \Sigma_X}{\partial \omega} \right)^{-1} \quad (5.6)$$

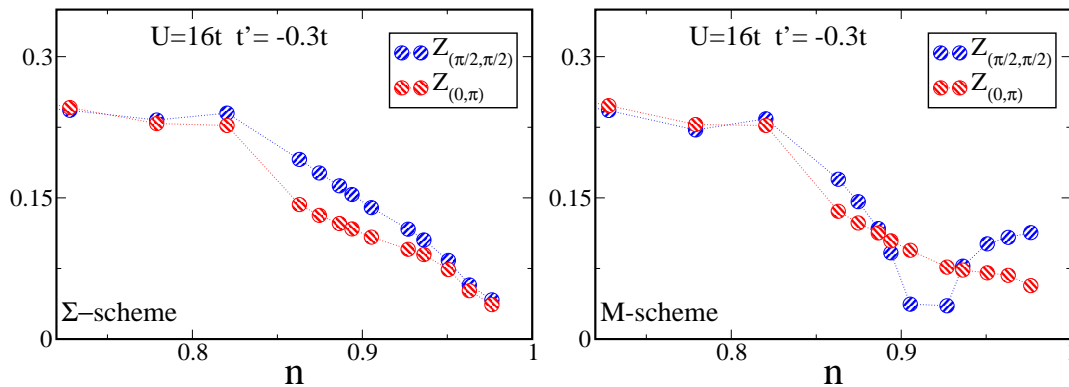


Figure 5.13: Quasiparticle residua in the *hot/cold* regions of the  $k$ -space. Left panel extracted from the cluster self-energies with the  $\Sigma$ -scheme, right panel from the cluster cumulant with the  $M$ -scheme. The virtual temperature  $\beta = 32/t$ .

where  $X = A, B, C$  are the three possible cluster-eigenvalues of the cluster-matrix. As we said, for the  $\Sigma$ -scheme and the  $M$ -scheme we can directly connect the lattice-residua to the cluster ones. In the  $\Sigma$ -method :

$$Z_{\text{latt}}(k, \omega) = [Z_A^{-1}(\omega)S_A(k) + Z_B^{-1}(\omega)S_B(k) + Z_C^{-1}(\omega)S_C(k)]^{-1} \quad (5.7)$$

In the  $M$ -method we can evaluate the cluster cumulant  $\hat{\mathbf{M}}_c$ :

$$\hat{\mathbf{M}}_c = [(\omega + \mu)\mathbf{1} - \hat{\Sigma}_c]^{-1} \quad (5.8)$$

and this is extracted onto the lattice:

$$M_{\text{latt}}(k, \omega) = M_A(\omega)S_A(k) + M_B(\omega)S_B(k) + M_C(\omega)S_C(k) \quad (5.9)$$

where, like with the  $\hat{\Sigma}$  cluster matrix, we have defined cluster cumulant eigenvalues.

We can equally express  $M_{\text{latt}}(k, \omega)$  directly in terms of the cluster self-energies:

$$M_{\text{latt}}^{-1}(k, \omega) = \left[ \frac{S_A(k)}{\omega + \mu - \Sigma_A} + \frac{S_B(k)}{\omega + \mu - \Sigma_B} + \frac{S_C(k)}{\omega + \mu - \Sigma_C} \right]^{-1} \quad (5.10)$$

It is then possible to extract the quasiparticle residua from the lattice self-energy:

$$\Sigma_{\text{latt}}(k, \omega) = (\omega + \mu) - M_{\text{latt}}(k, \omega)^{-1} \quad (5.11)$$

using the formula 5.5 and directly connecting it to the cluster-residua:

$$Z_{\text{latt}}(k, \omega) = M_k^2(\omega = 0) \left[ \frac{Z_A^{-1}S_A(k)}{(\mu - \Sigma_A)^2} + \frac{Z_B^{-1}S_B(k)}{(\mu - \Sigma_B)^2} + \frac{Z_C^{-1}S_C(k)}{(\mu - \Sigma_C)^2} \right]^{-1} \quad (5.12)$$

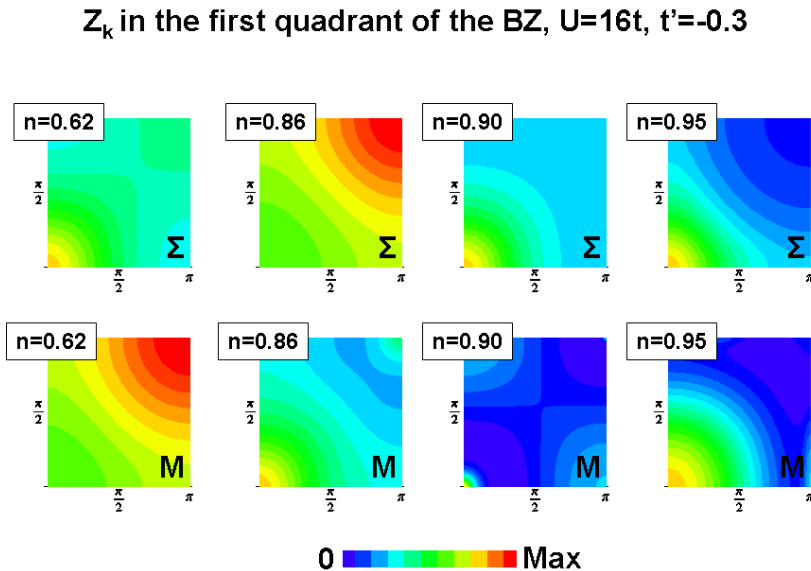


Figure 5.14: Quasiparticle residua in the  $k$ -space. The first row pictures are extracted from the cluster self-energy  $\Sigma$ , while the second row from the cumulant method  $M$ . The density of the system with  $U = 16t$  and  $t' = -0.3$  is:  $n = 0.62, 0.86, 0.90, 0.95$  from left to right, the inverse virtual temperature  $\beta = 32/t$ .

In Fig. 5.13 we show the  $Z$  extracted with the  $\Sigma$ -method on the left and the  $M$ -method on the right, evaluated in the  $k$ -points at the FS in correspondence of the cold (red circles) and hot (blue circles) regions. For convenience's sake we plot only the hole-like case  $U = 16t$  and  $t' = -0.3$ , but the qualitative result is the same for other values of the parameters. In fact we see that the FL-picture given by the  $\Sigma$ -scheme is well realized by the behavior of the  $Z$ 's, either in the hot and cold region, which can be seen to be proceeding roughly linearly to zero as the transition point is reached at density  $n = 1.0$ . The hot/cold spot modulation is here evident mainly around 15-10% doping in the different values of the  $Z$ s, higher for the low scattering cold spot. This is the extension of the old DMFT results, where a  $k$ -space modulation could not be described. The panel on the right hand side of Fig. 5.13 shows the same  $Z$ s extracted with the  $M$ -method, formula 5.9. Surprisingly, the behavior in this case is very different, despite the very similar results we observe in the hot/cold spot

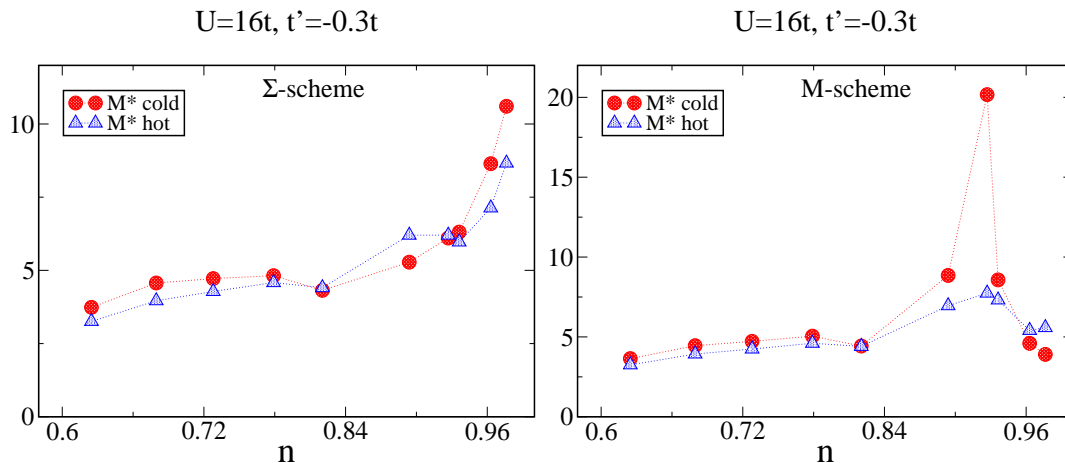


Figure 5.15: Quasiparticle renormalized mass in the *hot/cold* regions of the  $k$ -space. The  $\Sigma$ -scheme result is shown in the left-hand panel, the  $M$ -scheme result in the right-hand panel. The virtual temperature  $\beta = 32/t$ .

modulation (Fig.5.9). We once again stress that at high doping values ( $> 20\%$  doping), where the modulation in  $k$ -space is irrelevant, the methods give essentially the same values. Approaching the MT however (doping  $< 15\%$ ), in correspondence with the cold spot (right-hand panel, red circles), where the quasiparticle should be better defined and the spectral function  $A(k, \omega \rightarrow 0)$  presents a maximum, we see the  $Z$  collapsing to zero at around 10% doping, showing after this point a roughly constant value. The collapse of  $Z_k$  at 10% doping is driven by the lattice cumulant  $M_k$  in formula 5.12. This is in fact the quantity which goes to zero by tuning doping. According to formula 5.11, this implies that the lattice self-energy  $\Sigma_k(\omega_n = 0^+)$  is infinity exactly in that point, i.e. the lattice Green's function  $G_k(\omega_n = 0^+)$  is zero. The constant value of  $Z_k$  approaching the MT point results from the term  $Z_B (\mu - \text{Re}\Sigma_B)^2$  in formula 5.12, which remains finite despite  $Z_B \rightarrow 0$  [which is the quasiparticle-residuum contribution from the  $k$ -point  $(\pi, \pi)$ ] for  $n \rightarrow 1$ , as seen in Fig. 5.4. This is because the renormalized chemical potential  $\mu - \text{Re}\Sigma_B$  is rapidly increasing in absolute value, going out of the bare band as compared to the other points in the  $k$ -space, as we discussed in Fig. 5.5. The aforementioned collapse of the  $Z$ s in the  $M$ -scheme interpretation is extraordinary evident in Fig.5.14, where the full  $Z(k)$  are plotted in the first quadrant of the BZ for the  $\Sigma$ -scheme (upper row) and the  $M$ -scheme (lower row), for the case  $t' = -0.3t$ . As

usual we indicate with blue color the lower values of  $Z$  and with red color the highest values. Four values of doping (from left to right) 38, 24, 10, 5% are displayed. The highest doping panels (left hand side 38% and 24% doping ) do not display essential differences between the two methods. When however the MT is approached (third plot from the left) at 10% doping, we see that for the  $M$ -method the  $Z$  literally goes down to zero on a vast region of the  $k$ -space (as evident by the wide blue area that appears). In Fig. 5.15 we also display the renormalized quasiparticle mass  $m^*/m$ , obtained from

$$Z \frac{m^*}{m} = \frac{1}{1 + \frac{d\Sigma'(k,0)}{dk_{\perp}} / \frac{dE_k}{dk_{\perp}}}$$

where  $m^*$  and  $m$  are respectively the renormalized and the bare effective mass,  $k$  is along the Fermi surface and  $\frac{d}{dk_{\perp}}$  means the derivative perpendicular to the Fermi surface. The  $\Sigma$ -scheme result (left side of Fig. 5.15) once again displays the behavior expected at in a FL system which approaches a MT: the quasiparticle renormalized mass increases close to the phase-transition point (possibly diverging). This is in agreement with the previous single-site DMFT results. In the  $M$ -scheme instead (right side of Fig. 5.15) the mass divergence takes place in the cold region around 10% doping, where the self-energy  $\Sigma_k$  diverges and the Green's function is zero. After this critical point,  $m^*/m$  comes back to an approximately constant value which maintains until the MT point. In the hot region, the renormalized mass remains instead always approximately constant. In the  $M$ -scheme framework, this behavior hints at the existence of a transition around 10%, which is, instead, washed out by the FL-perspective given by the  $\Sigma$ -scheme. Such a phenomenon indicates that something dramatic may take place at 10%. This is worth to be investigated in the light of the very different physical interpretation that the  $M$ -scheme presents with respect to a FL  $\Sigma$ -scheme viewpoint.

#### 5.4 The $M$ -scheme perspective: an anomalous FL

How is the  $M$ -scheme periodization able to break down the simple FL description? As already mentioned, in the  $\Sigma$ -scheme the lattice self energy is a simple linear extrapolation (formula 5.3):

$$\Sigma_{\text{latt}}(k, \omega) = \Sigma_A S_A(k) + \Sigma_B S_B(k) + \Sigma_C S_C(k)$$

where the function  $S_X$  ( $X = A, B, C$ ) was given in formula 5.4. In the  $M$ -case instead the lattice self-energy is given by a highly non-linear relation

$$\Sigma(\mathbf{k}, \omega) = \omega + \mu - \left[ \frac{S_A(k)}{\omega + \mu - \Sigma_A} + \frac{S_B(k)}{\omega + \mu - \Sigma_B} + \frac{S_C(k)}{\omega + \mu - \Sigma_C} \right]^{-1}, \quad (5.13)$$

We find that at zero temperature the imaginary parts of the cluster self-energies go to zero at zero frequency (Fig. 5.2). For the following discussion we can therefore write the lattice Green's function as

$$G(\mathbf{k}, \omega) = \frac{1}{\omega - r(\mathbf{k}, \omega) - i\eta(\mathbf{k}, \omega)}, \quad (5.14)$$

where  $\eta(\mathbf{k}, \omega)$ ,  $\lim_{\omega \rightarrow 0} \eta = 0$  represents the imaginary part of the self-energy and  $r(\mathbf{k}, \omega) = \epsilon(\mathbf{k}) - \mu + \text{Re}\Sigma(\mathbf{k}, \omega)$  is the renormalized energy. Concerning the real part of the cluster self-energy, we distinguish two regimes. At large doping the diagonal cluster self-energies are dominated by the local component and Eq. (5.13) reduces in the first approximation to Eq. (5.3). In this regime the physics is almost local with small corrections due to short-range correlations. All the periodization schemes converge and the single-site DMFT represents a good first order approximation. In contrast, close to the Mott transition the short-range correlations become important and the off-diagonal components of the cluster self-energy become comparable with the local one. As a consequence, at zero frequency the denominators in Eq. (5.13) may acquire opposite signs generating a divergence in the lattice self-energy. This divergence of  $\Sigma(\mathbf{k}, \omega = 0)$ , or equivalently of  $r(\mathbf{k})$ , corresponds to a zero of the lattice Green's function. Here the main differences between the two schemes stands. The  $M$ -method allows for the appearances of lines of zeroes in the Green's function, a possibility not admitted with the  $\Sigma$ -scheme, and that is likely to be at the origin of the differences and anomalous  $Z$ s we found in the previous section. We now study this  $M$ -effect in a specific case.

#### 5.4.1 FS topology transition and Pseudogap regime

We present in this section results obtained with distance 3.21 between the continuous hybridization function from the impurity solver  $\Delta(i\omega)$  and  $\Delta_{nb}(i\omega)$ , parametrized by

the truncated bath:

$$\text{dist} = \sum_n^{Nw_{off}} \|\Delta(i\omega_n) - \Delta_{nb}(i\omega_n)\| \quad (5.15)$$

where  $Nw_{off}$  is a cut-off frequency chosen so that  $\omega_n \simeq 2t$ . This distance is designed to best describe the low-energy scale in the system, with the aim of grasping the behavior at 10% doping, more than the MT point. We present here the case  $U/t = 8.0$  and

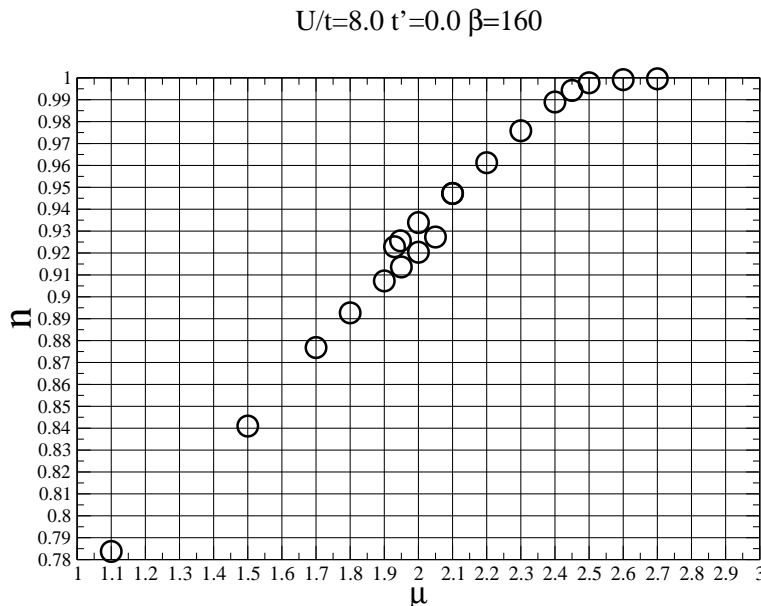


Figure 5.16: Density  $n$  vs. chemical potential  $\mu$

$t' = 0$ . With this value of the local interaction, relevant for cuprates superconductor materials, we were able to use a very low virtual temperature on the Matsubara axis. The inverse virtual temperature  $\beta$  in the data presented here is  $\beta = 160/t$  (energy units of half-band-width  $4t$ ). This allows us to better describe the low energy physics, capturing the small frequency behaviour of the Green's functions (displayed in Fig. 5.17 on the Matsubara axis, where no artificial spreading in the analytic continuation is required) and of the cluster self-energies  $\Sigma_{ij}$  (Fig. 5.18) and the eigenvalues of the cluster-self-energy  $\Sigma_X$  (Fig. 5.19). From  $\text{Im}\Sigma_{ij}$  in particular (Fig. 5.18) we can see that the extrapolation to a FL behaviour in the cluster quantities for  $\omega \rightarrow 0$ , extracted previously in the strong coupling case  $U = 16t$ , holds up to the low temperature reached in this case. In Fig. 5.20 we also present the eigenvalues of the cluster-self-energy on

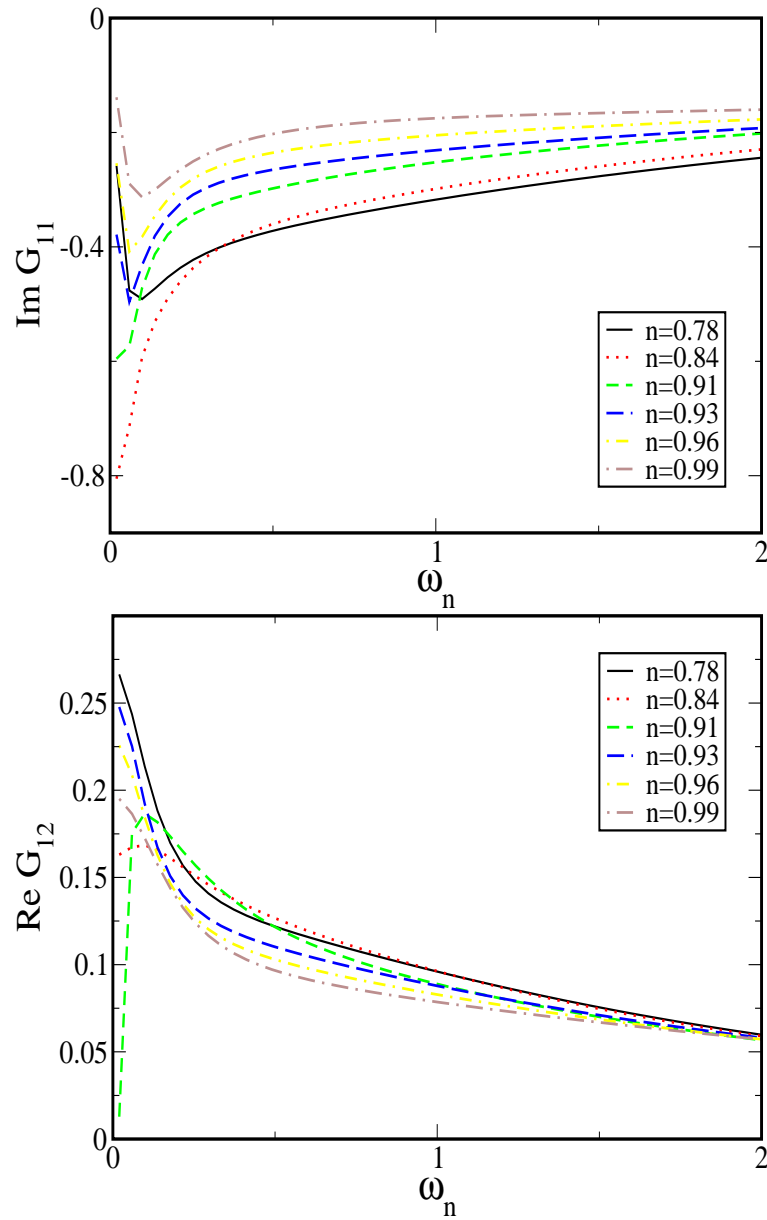


Figure 5.17: Imaginary part of the local Green's function  $\text{Im}G_{11}$  (top) and real part of the nearest neighbor Green's function  $\text{Re}G_{12}$  for  $U/t = 8.0$  and no frustration  $t' = 0$ .

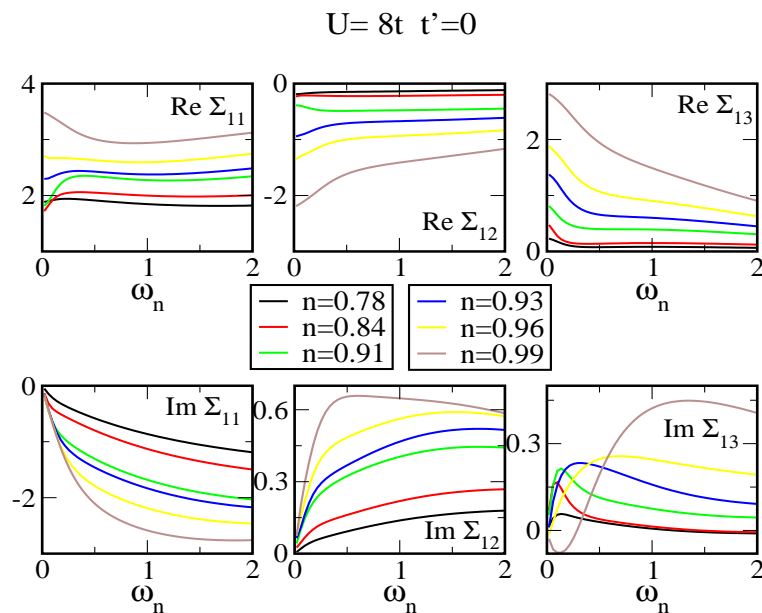


Figure 5.18: Cluster self-energies  $\Sigma_{\mu\nu}$  on the Matsubara axis for  $U/t = 8.0$ , no frustration  $t' = 0$  and inverse virtual temperature  $\beta = 160/t$ .

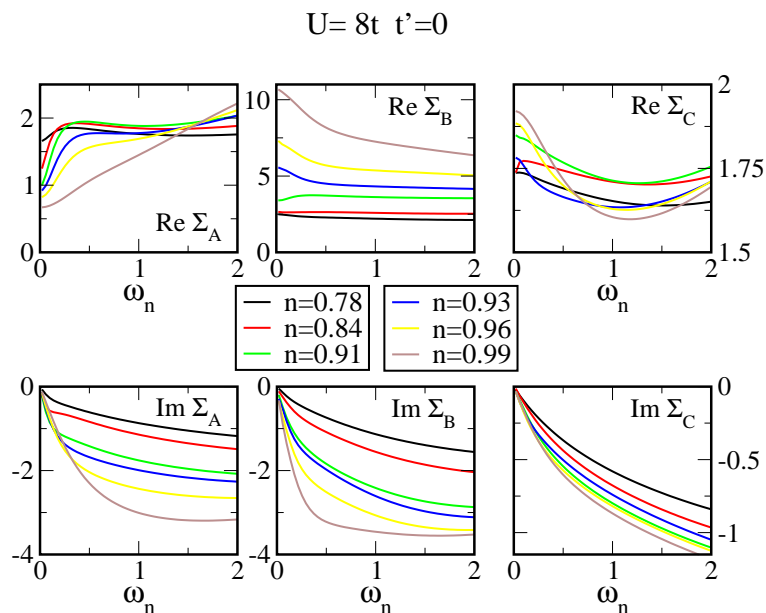


Figure 5.19: Eigenvalues of the Cluster self-energies  $\Sigma_A$ ,  $\Sigma_B$  and  $\Sigma_C$  on the Matsubara axis for  $U/t = 8.0$ , no frustration  $t' = 0$  and inverse virtual temperature  $\beta = 160/t$ .

$$U=8t, t'=0$$

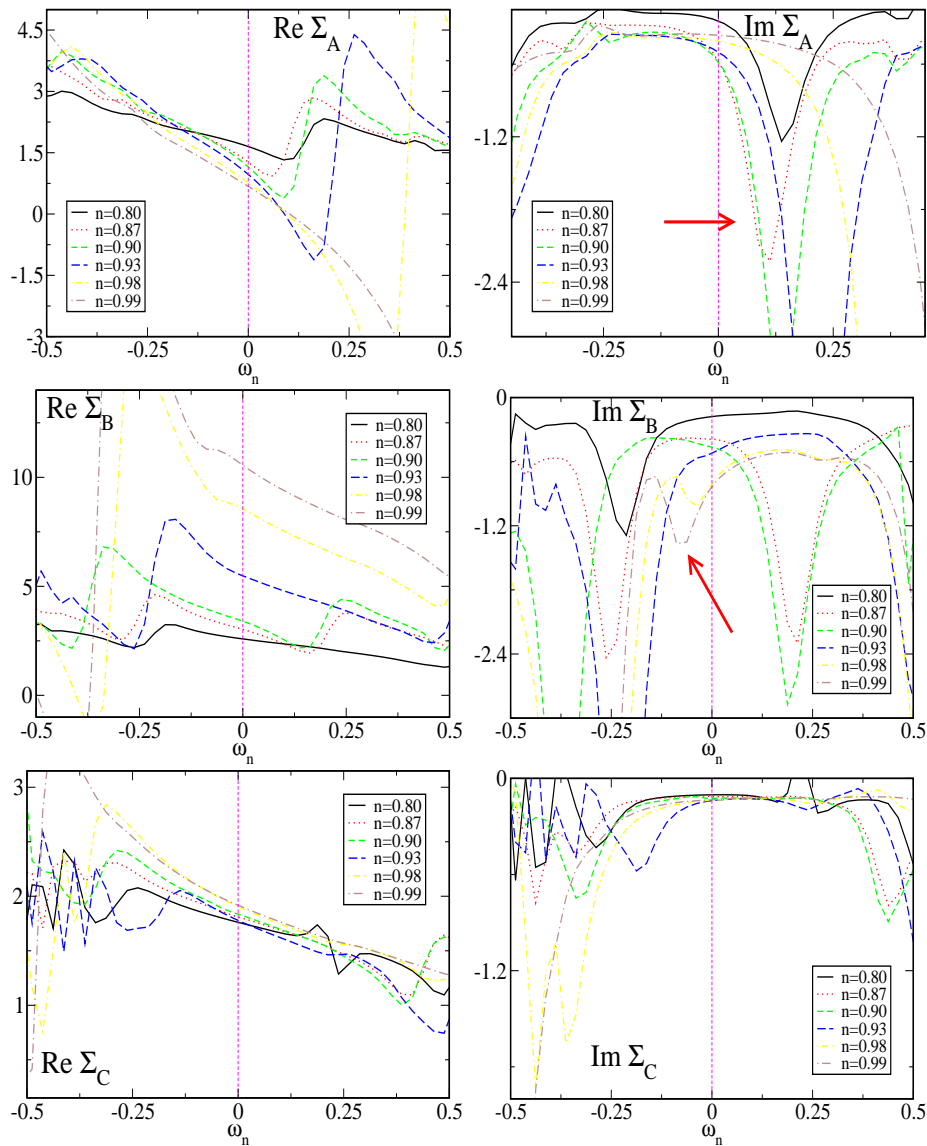


Figure 5.20: Eigenvalues of the Cluster self-energies  $\Sigma_A$ ,  $\Sigma_B$  and  $\Sigma_C$  on the real axis for  $U/t = 8.0$ , no frustration  $t' = 0$  and inverse virtual temperature  $\beta = 160/t$ .

the real axis, which, though less clean than those on the Matsubara axis, are easier to physically interpret in comparison to a FL system. In Fig. 5.16 we present first the density of particles in the system versus the chemical potential. We notice there are two lines of solutions which coexist in a small region around 10% doping, well before the MT. Both phases are in a metal state. At this level of energy resolution therefore, the CDMFT solution apparently detects a first-order phase transition between two states with no evident order parameter. It is difficult to be categorical on this point and on the nature of the transition, as it is difficult to reach this region accurately. The existence of two solutions may indeed be a fake effect of CDMFT which tries to describe the total behavior of the system with only 3 cluster-selfenergy parameters. A possibility of a second order phase transition, maybe even a quantum critical point (QCP) cannot be ruled out. Looking at the cluster quantities, it is not trivial to detect the appearance of the critical region. For example, the local propagator  $G_{11}(\omega_n)$  (in the top panel of Fig. 5.17 we show the imaginary part on the Matsubara axis) and the eigenvalue of the cluster-self-energies (Fig. 5.19) show a systematic and continuous behavior approaching the MT, as already described for the  $U = 16t$ ,  $t' = \pm 0.3$  case in section 5.1. An irregular behavior is observed in  $\text{Re}G_{12}$ , which decreases for decreasing doping up to 10%, where it has a sudden drop to zero. It then jumps back to a finite value for smaller doping, and increases until the Mott insulator is reached. A singular behavior, not observed in  $U = 16t$   $t' = \pm 0.3$  case of section 5.1 because of the too high virtual temperature  $\beta^{-1} = 32$ , is displayed also by the low energy part of the nearest next-neighbor cluster-self-energy  $\text{Im}\Sigma_{13}$  (Fig. 5.18). As a matter of facts  $\text{Im}\Sigma_{13}$  grows positive up to 10% doping with an increasing positive slope for  $\omega_n \rightarrow 0$  and after passing this critical point, it decreases, with the slope going to zero and eventually changing sign close to the MT. Notice that the energy-scale of this feature is small ( $\sim 0.1t$ ). This suggest a scenario in which approaching the critical doping (10%) the system has the tendency to break the FL (i.e.  $\text{Im}\Sigma_{13}$  does not go to zero for  $\omega_n \rightarrow 0$ ), and the way CDMFT describes this effect is by providing a region of coexistence of two FL "close to the breaking" point. This idea can also be supported by looking at the eigenvalues of the cluster self-energies on the real axis instead than on the Matsubara Fig. 5.20. In a

FL we expect the Real part to cross the  $\omega = 0$  point with a linear slope, the imaginary part has to be negative, in order to preserve causality, and have a local minimum at  $\omega = 0$ . We see that approaching the critical doping (10%), either from the overdoped and the underdoped side,  $-\text{Im}\Sigma_A$  has a maximum in the self-energy which moves close to  $\omega = 0$ , i.e. it moves toward breaking the FL (phenomenon indicated in Fig. 5.20 by a arrow, top-right panel). A similar effect (also indicated by a arrow, right panel in the second row) takes place in  $-\text{Im}\Sigma_B$  at the MT point. Therefore, the region around  $k = (0, \pi)[(\pi, 0)]$ , labeled A, drives the instability at 10% doping, which hints to a breaking of the simple FL picture (and the effect taking place in  $k = (0, \pi)[(\pi, 0)]$  strongly suggest the appearance of a pseudogap, as we will see in the following), while, as already pointed out in sections 5.1 and 5.2, the region around  $k = (\pi, \pi)$ , labeled B, drives the system into the Mott transition. The  $M$ -scheme scenario is exciting, proposing a critical 10% point which precedes the well-known Mott critical point at zero doping. The former is in some way connected to an instability appearing in the  $k = (0, \pi)[(\pi, 0)]$  A-region, but we cannot unfortunately access this point close enough with the present technique to make conclusive statements. We therefore concentrate our study on the over-doped region and at the small doped region around this critical area.

To illustrate this, we show in 5.21 how the renormalized energy,  $r(\mathbf{k}) = \varepsilon_k + \mu - \Sigma_{\varepsilon_k}$ , and the spectral function  $A(\mathbf{k}, \omega = 0) = -(1/\pi) \text{Im}G(\mathbf{k}, 0)$  evolve as a function of doping. For a better comparison, on the top of this figure we show again the density  $n$  vs chemical potential  $\mu$  plot, enlightening in a blue circle the region of co-existence around 10% doping, and the point where the quasiparticle residuum  $Z_k$  has the collapse to zero in the cold region. The lower part of the figure shows the first quadrant of the BZ for various values of doping. The blue lines represent poles in the Green's function for which  $r(\mathbf{k}) = 0$ , i.e. the FS. The green region is the  $k$ -space occupied by electrons for which  $r(\mathbf{k}) < 0$ , the yellow is the empty region,  $r(\mathbf{k}) > 0$ . Notice that already at  $\sim 17\%$  doping (right side), besides the FS (blue line) regions of infinite self-energy (red-line) appear. These correspond to zeroes in the Green's function, and are absent at high doping, as evidenced in the following picture 5.22, where a high value of doping ( $n = 0.78$ ) is displayed (left panel). At this point the line of zeros is far from the FS,

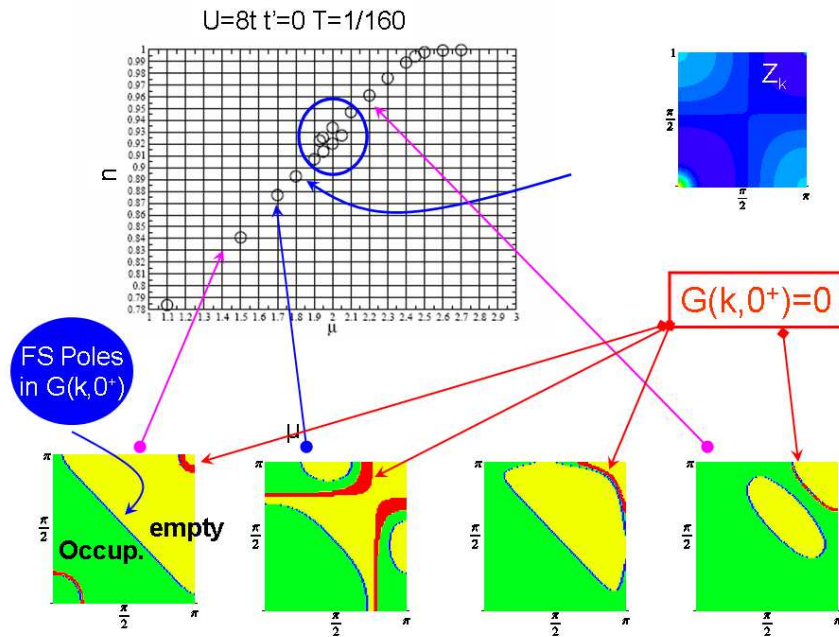


Figure 5.21: Renormalized energy,  $r(\mathbf{k})$ , (upper panels) and spectral function,  $A(\mathbf{k})$ , (lower panels) for the 2D Hubbard model with  $U = 8t$  and  $T = 0$ . The color code for the upper panels is: green ( $r < 0$ ), blue ( $r = 0$ ), yellow ( $r > 0$ ), red ( $r \rightarrow \infty$ ).

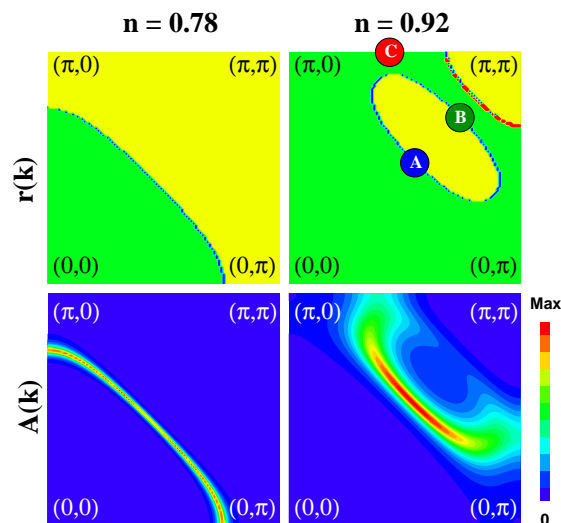


Figure 5.22: Renormalized energy,  $r(\mathbf{k})$ , (upper panels) and spectral function,  $A(\mathbf{k})$ , (lower panels) for the 2D Hubbard model with  $U = 8t$  and  $T = 0$ . The color code for the upper panels is: green ( $r < 0$ ), blue ( $r = 0$ ), yellow ( $r > 0$ ), red ( $r \rightarrow \infty$ ).

therefore it does not affect the physics of the system. However, approaching the 10% doping, the lines of zero approach the FS more and more until touching and breaking it. At this point we are in the critical region, which is not well described by our calculation. So it is difficult to state in detail how the FS modifies. The result of passing through this critical point however is the most left quadrant of Fig. 5.21, which shows a FS with a different topology: a pocket centered around  $(\frac{\pi}{2}, \frac{\pi}{2})$ . The critical point can be seen therefore like a topological phase transition of the FS, arising from the appearance of zeros in the Green's function. Although, as we said, we cannot describe well the critical point, we can get however insight on the nature of the phase resulting from this transition. In Fig. 5.22 we display the renormalized energy,  $r(\mathbf{k})$ , and the spectral function  $A(\mathbf{k}, \omega = 0) = -(1/\pi) \text{Im}G(\mathbf{k}, 0)$  for two values of doping outside the critical region. For  $n = 0.78$  (left panels) we have a large electron-type FS (blue line in the  $r(\mathbf{k})$  panel, a pole for the Green's function) separating the occupied region of the Brillouin zone (green), from the unoccupied region (yellow). The Fermi surface can also be traced in the  $A(\mathbf{k})$  panel as the maximum of the spectral function (red colors). This what is expected from the FL picture. On the other hand, for  $n = 0.92$ , after we passed through the critical point, a qualitatively different picture emerges in the topology of the FS. As we said, the FS (blue line) is now represented by a hole pocket and, in addition, we have a line of zeros of the Green's function (red line) close to the  $(\pi, \pi)$  region of the Brillouin zone. Furthermore, there is no one-to-one correspondence between the Fermi surface and the maximum of the spectral function. This behavior has two causes:

- the proximity of a zero line for the Green's function (the red one) suppresses the weight of the quasiparticle, so that in correspondence of the FS we do not observe a high spectral weight.
- for  $\mathbf{k}$ -points corresponding to  $r(\mathbf{k}) \neq 0$  the quasiparticles are pushed away from  $\omega = 0$  and a pseudogap opens at the Fermi level in the region close to the  $(0, \pi)$  and  $(\pi, 0)$  points.

Several works [51, 46] have established that a pseudogap is present in the cluster solution of DMFT. We show this explicitly in Fig. 5.23 by comparing the low frequency dependence of the spectral function in three different points of the Brillouin zone, marked by A, B and C in Fig. 5.22. Notice the suppression of the zero frequency peak at point B, due to the proximity to the blue line of zeroes of the Green's function and possibly not detected in ARPES experiments, and the frequency shift  $\delta = -0.05t$  of the peak at point C, which is the pseudogap effect. The  $M$ -approach provides a simple interpretation of this effect, as observed in photo-emission experiments, in terms of the emergence of infinite self-energy lines (i.e zeroes of the Green's function). In Fig. 5.25 we show along the usual path in the first quadrant of the BZ  $(0, 0) \rightarrow (\pi, \pi) \rightarrow (0, \pi) \rightarrow (0, 0)$  the spectral function as function of frequency  $\omega$ , the Fermi level is set at  $\omega = 0$ . In ARPES experiments the  $\omega > 0$  is not accessible, as it is in a theoretical calculation. In the first row we show a large energy scale ( $\omega_{max} \sim 8t$ ), while in the second row we have the same graphs in a more detailed energy scale ( $\omega_{max} \sim 2t$ ). At the density  $n = 0.88$  just before the critical region at 10% doping we can see that indeed the spectral functions crosses the Fermi level twice, once close to  $(\pi/2, \pi/2)$  and the second close to  $(0, \pi)$  with well defined quasiparticle peaks, even if around  $(0, \pi)$  the peak is "less dispersive" as observed in the previous section for the  $U = 16t$  results. For a density  $n = 0.95$  instead, there is still a quasiparticle-like peak in correspondence of the region around  $(0, \pi)$ , but this does not cross the Fermi level anymore, but rather remains tangent to it at negative energy equal to the  $\delta = -0.05t$  of peak C in  $(0, \pi)$  as compared to peak A in  $(\pi/2, \pi/2)$ . This is the real pseudogap, and the correspondence of this behavior observed in the ARPES experimental data of Fig. 5.24 (in particular at panels C1 going from  $(0, 0) \rightarrow (\pi, \pi)$  and C2 going from  $(0, 0) \rightarrow (0, \pi) \rightarrow (\pi, \pi)$ ) is quite impressive. We finally remark that this pseudogap is not the same feature we studied in [19], where the pseudogap observed was rather the higher energy feature we see in curve C of Fig. 5.23 at energy  $\sim 0.5t$  and labeled IR in Fig. 5.25, which is truly present around the hot point  $(0, \pi)$ , but, being at positive energies, does not appear in ARPES measure. It contributes instead as a depression in the integrated DOS close to the Fermi level.

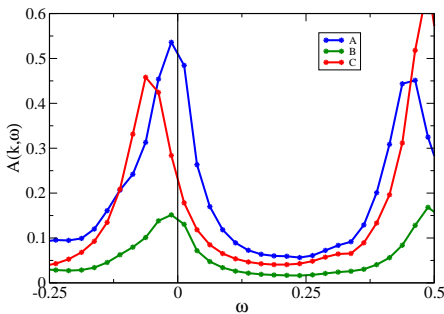


Figure 5.23: Frequency dependence of the spectral function for three points in the Brillouin zone marked by A, B, and C in Fig. 5.22.

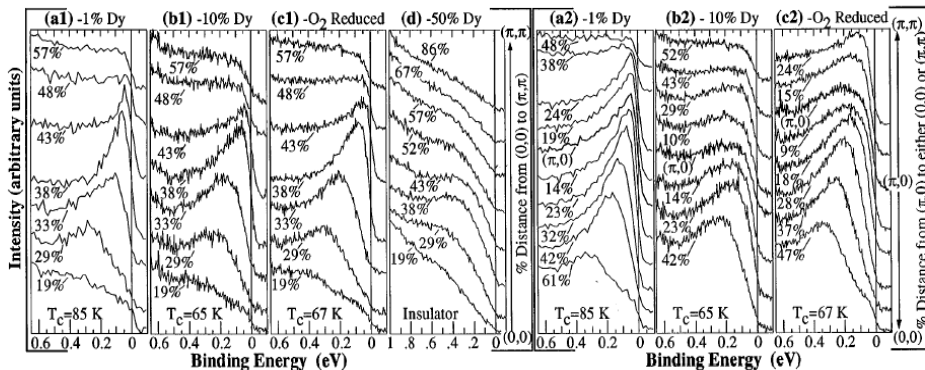


FIG. 1. ARPES spectra from  $\text{Bi}_2\text{Sr}_2\text{Ca}_{1-x_2}\text{Dy}_x\text{Cu}_2\text{O}_{8+\delta}$  single crystal thin films and deoxygenated  $\text{Bi}_2\text{Sr}_2\text{CaCu}_2\text{O}_{8+\delta}$  bulk crystals. The symmetry points identified correspond to those indicated in the two-dimensional Brillouin zone of Fig. 4.

Figure 5.24: Plot taken from D.S Marshall *et al.*, Phys. Rev. Lett 76, 4841 (1996).

Therefore the strong coupling  $M$ -CDMFT point of view suggests that the short-range correlation, which play a key role in the physics close to the Mott transition, can be naturally described by finite range cumulants  $M$  rather approximately in a cluster scheme, than the self-energy. Consequently, the lattice cumulant  $M_k$ , rather than the self-energy, is a smoothly varying function of  $k$  resulting in the appearance of surfaces of zeros of the Green's function for small values of doping. The existence of these lines is directly related to a change in the topology of the FS and the opening of a pseudogap in the spectral function at the Fermi energy. Remarkably, the lines of poles of the self energy appear first far from the Fermi surface. This is a strong coupling instability which has no weak coupling precursors on the Fermi surface. Our

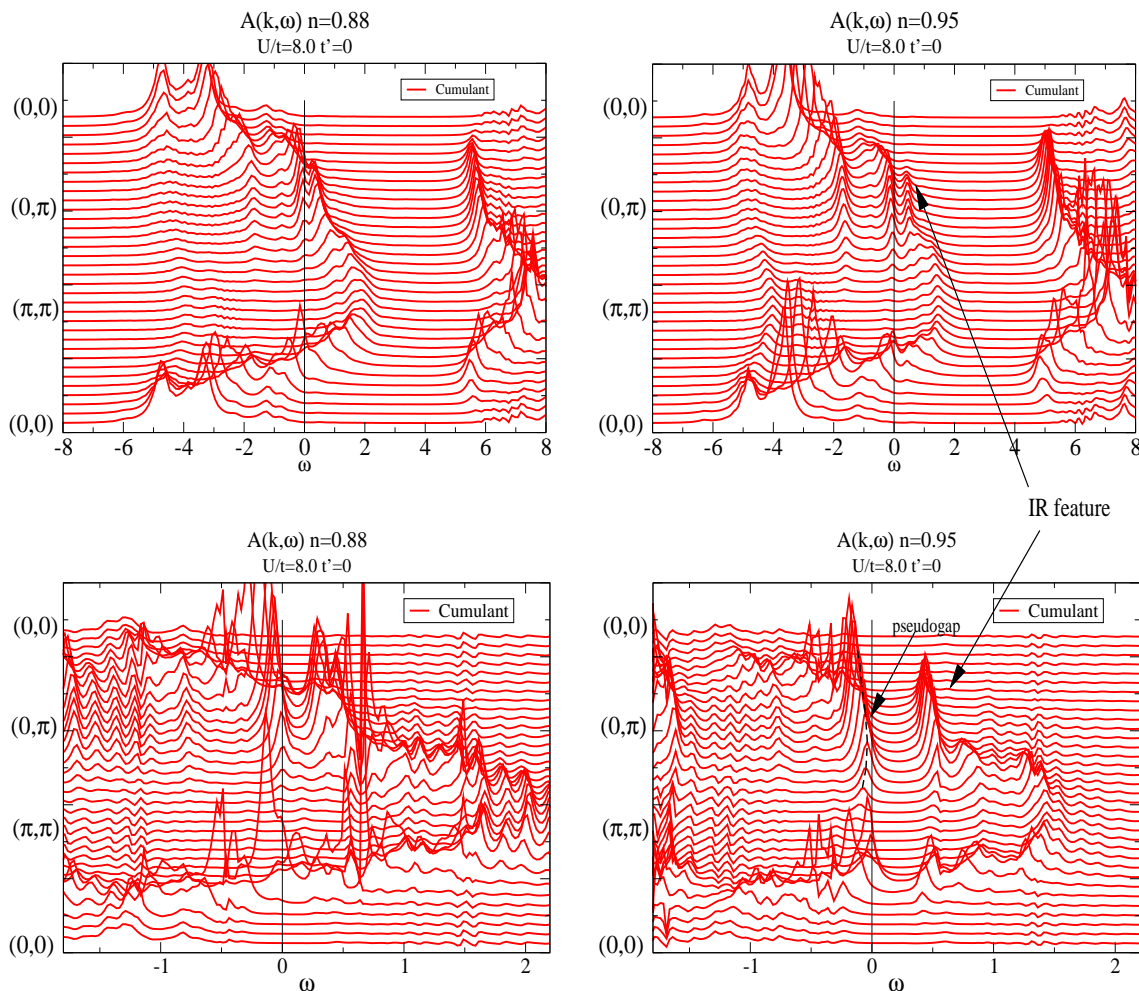


Figure 5.25: Spectral function  $A(k, \omega)$  along the path  $(0, 0) \rightarrow (\pi, \pi) \rightarrow (0, \pi) \rightarrow (0, 0)$  in the first quadrant of the Brillouin Zone. The red curves are calculated extracting onto the lattice the Cumulant  $M$  from the cluster./ In the left panel the density is  $n = 0.85$ , the state is at the left side of the coexistence region. In the right panel the density of the system is  $n = 0.95$ , the system is at the right of the coexistence region. The bottom panels are details at the Fermi level: notice that for  $n = 0.95$  in the region close to  $(0, \pi)$  the quasiparticle peak passes tangent, *but without touching* the Fermi level, it's the pseudogap!

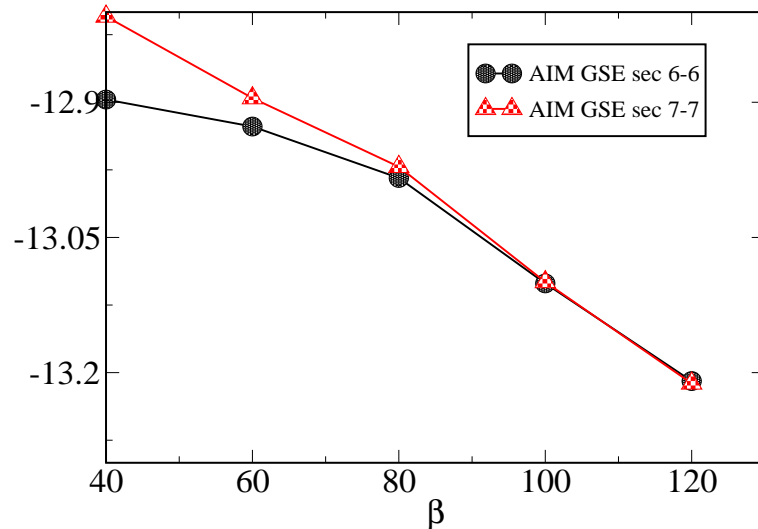


Figure 5.26: Ground state energy in two different but close particle-sectors,  $(n_{\uparrow}, n_{\downarrow}) = (6, 6)$  and  $(7, 7)$ , of the Anderson impurity model as a function of the inverse virtual temperature  $\beta$ . The system parameters are  $U = 12$ ,  $t' = 0$ , doping 10%.

results suggest an interesting scenario: if the evolution in Figure 5.22 from large to small doping is continuous (rather than the first order transition we observe with this CDMFT calculation), it has to go through a critical point where the topology of the Fermi surface (and perhaps that of the lines where the self energy is infinite) changes. This topological change and its possible connection to an underlying critical point at finite doping in the cuprate phase diagram deserves a deeper investigation with this techniques.

Finally, we can try to connect the technical difficulties in accessing the critical region (blue-circled area in the  $n$  vs  $\mu$  plot of Fig. 5.21) with the underlying physics. The impossibility of obtaining low virtual temperature  $\beta^{-1}$  results is an indication of the disappearance of a the CDMFT solutions. To obtain insight on how this takes place, we can start from a high temperature (low  $\beta$ ) result and gradually lower the temperature, until the last result is obtained. This was done in Fig. 5.26, where we display the ground-state energy of two different particle-sectors  $(n_{\uparrow}, n_{\downarrow}) = (6, 6)$  and  $(7, 7)$  as a function of the inverse virtual temperature  $\beta$ . At low  $\beta$ , the CDMFT-solution is determined in the sector with the lowest ground-state energy [i.e.  $(n_{\uparrow}, n_{\downarrow}) =$

(6, 6)]. However, as we approach the last temperature which produces a stable CDMFT-solution ( $\beta \sim 120$ ), the ground-state energy of the two close particle sectors  $(n_{\uparrow}, n_{\downarrow}) = (6, 6)$  and  $(7, 7)$  gets closer and closer, in the limit degenerate. This strongly indicates that a phase transition is taking place in this point as a function of temperature, and the high-temperature NS-solution disappear. We are not able to state if a different NS solution, maybe non-FL, will appear at lower temperatures, or if a NS has in fact totally disappeared. We will see in the next chapter that this critical point corresponds to the maximum in the dome of the high-temperature SC order-parameter. The possibility that the NS solution disappears replaced by the SC solution is mostly appealing, and promises a SC state which is the natural low-temperature continuation of an anomalous NS. This idea is in line with the findings on the momentum scattering differentiation, presented in section 5.1 and 5.2, the formation of hot/cold spots, whose position is inverted from hole to electron doped systems, with the topological change in the FS born out from a critical region that brings to the formation of the pseudogap around  $(0, \pi)$  and  $(\pi, 0)$  in the underdoped side. All these NS-properties seem well fit to a d-wave SC state for the hole-doped cuprates, as we will see in the next chapter.

## Chapter 6

### Superconductive Phase

In this chapter we investigate the superconductive phase (SC). In weakly correlated materials the superconducting state is well described in the frame work of the BCS theory [7]. In the strongly correlated systems however the description of this phenomenon is still one of the most challenging open problems in condensed matter physics. We will present the results we can achieve with CDMFT, which, as seen in the previous chapter, has been able to provide new insights in the non-trivial NS of the Hubbard Model in two dimension. In particular, we will try to clarify the link between the SC state and the peculiarity of the Mott transition, "the Mottness", and its relation with the NS properties. The idea that the  $H-T_C$  superconductive mechanism is related to the Mottness of the cuprates can be traced back to the Resonating Valence Bond (RVB) proposed by P.W. Anderson [1]. In this theory the insulating phase is a liquid of pre-formed Cooper pairs, ready to become a superconductor once doping is added into the system. Later slave boson studies [43] refined this idea, showing that the super-exchange interaction naturally selects a d-wave supeconductivity (dSC) and that gaped one-particle excitation survive in the NS above the critical temperature (the precursor of a pseudogap state). Further investigation with variational approaches [69] and more extensive numerical RVB approaches [2] have confirmed that many properties of cuprates can be qualitatively described with these methods in the framework of Hubbard-like models. We now extend the CDMFT-study to the SC state of the two dimensional Hubbard model, adopting once again the 2X2 plaquette as cluster-impurity. This is the minimal spatial arrangement required in order to describe the short range interaction between particles and the formation of a d-wave SC order parameter.

## 6.1 CDMFT equations for a d-wave superconducting state

In order to investigate the dSC phase within CDMFT we write an effective action containing a Weiss dynamical field  $\hat{\mathcal{G}}_o$  with both normal (particle-hole) and anomalous (particle-particle) components:

$$S_{\text{eff}} = \int_0^\beta d\tau d\tau' \Psi_c^\dagger(\tau) \left[ \hat{\mathcal{G}}_o^{-1} \right] \Psi_c(\tau') + U \sum_\mu \int_0^\beta d\tau n_{\mu\uparrow} n_{\mu\downarrow}.$$

Here, for the case of a  $2 \times 2$  plaquette, we indicate the Nambu spinor,

$$\Psi_c^\dagger \equiv (c_{1\uparrow}^\dagger, \dots, c_{4\uparrow}^\dagger, c_{1\downarrow}, \dots, c_{4\downarrow})$$

$\mu$  labels the degrees of freedom inside the cluster. Physically this action corresponds to a cluster embedded in a self-consistently determined bath with SC correlations. Given the effective action with a starting guess for the Weiss field  $\hat{\mathcal{G}}_o$ , we compute the cluster propagator  $\hat{G}_c$  and the cluster self energy  $\hat{\Sigma}_c = \hat{\mathcal{G}}_o^{-1} - \hat{G}_c^{-1}$ . Here,

$$\hat{G}_c(\tau, \tau') = \begin{pmatrix} \hat{G}_\uparrow(\tau, \tau') & \hat{F}(\tau, \tau') \\ \hat{F}^\dagger(\tau, \tau') & -\hat{G}_\downarrow(\tau', \tau) \end{pmatrix} \quad (6.1)$$

is a  $8 \times 8$  matrix for a  $2 \times 2$ -impurity-cluster,

$$G_{\mu\nu,\sigma} \equiv -T \langle c_{\mu\sigma}(\tau) c_{\nu\sigma}^\dagger(0) \rangle$$

and

$$F_{\mu\nu} \equiv -T \langle c_{\mu\downarrow}(\tau) c_{\nu\uparrow}(0) \rangle$$

are the normal and anomalous Green's functions respectively. Once again using the CDMFT self-consistency condition 3.8,

$$\hat{\mathcal{G}}_o(i\omega_n)^{-1} = \left[ \sum_K \hat{G}(K, i\omega_n) \right]^{-1} + \hat{\Sigma}_c(i\omega_n) \quad (6.2)$$

we recompute the Weiss field and iterate until convergence. The self-consistency condition is here expressed by a  $8 \times 8$  superlattice local Green's function (as there are the off-diagonal anomalous terms)

$$\hat{G}(K, i\omega_n) = \left[ i\omega_n + \mu - \hat{t}(K) - \hat{\Sigma}_c(i\omega_n) \right]^{-1}$$

with  $\hat{t}(K)$  the Fourier transform of the superlattice hopping matrix with appropriate sign flip between propagators for up and down spin and the sum over  $K$  is performed over the reduced Brillouin zone of the superlattice. To solve the cluster impurity problem represented by the effective action above, we use, as usual, an Anderson cluster-impurity Hamiltonian with a special superconductive bath:

$$\begin{aligned}
H_{\text{imp}} = & \sum_{\mu\nu\sigma} E_{\mu\nu\sigma} c_{\mu\sigma}^\dagger c_{\nu\sigma} + \sum_{m\sigma} \epsilon_{m\sigma}^\alpha a_{m\sigma}^\dagger a_{m\sigma}^\alpha \\
& + \sum_{m\mu\sigma} V_{m\mu\sigma}^\alpha a_{m\sigma}^\dagger (c_{\mu\sigma} + \text{h.c.}) + U \sum_{\mu} n_{\mu\uparrow} n_{\mu\downarrow} \\
& + \sum_{\alpha} \Delta^\alpha (a_{1\uparrow}^\alpha a_{2\downarrow}^\alpha - a_{2\uparrow}^\alpha a_{3\downarrow}^\alpha + a_{3\uparrow}^\alpha a_{4\downarrow}^\alpha - a_{4\uparrow}^\alpha a_{1\downarrow}^\alpha \\
& + a_{2\uparrow}^\alpha a_{1\downarrow}^\alpha - a_{3\uparrow}^\alpha a_{2\downarrow}^\alpha + a_{4\uparrow}^\alpha a_{3\downarrow}^\alpha - a_{1\uparrow}^\alpha a_{4\downarrow}^\alpha + \text{h.c.}).
\end{aligned}$$

Here  $\mu, \nu = 1, \dots, N_c$  label the sites in the cluster and  $E_{\mu\nu\sigma}$  represents the hopping and the chemical potential within the cluster. The energy levels in the bath are grouped into multiples of the cluster size ( $N_c = 4$ ) with the labels  $m = 1, \dots, N_c$  and  $\alpha = 1, 2$  such that we have 8 bath energy levels  $\epsilon_{m\sigma}^\alpha$  coupled to the cluster via the hybridization matrix  $V_{m\mu\sigma}^\alpha$ . Using lattice symmetries we take  $V_{m\mu\sigma}^\alpha \equiv V^\alpha \delta_{m\mu}$  and  $\epsilon_{m\sigma}^\alpha \equiv \epsilon^\alpha$ . This is similar to the reduced parametrization introduced in chapter 4.5, in order to target a first guess in the NS case. This time, however, we added particle-particle destruction and creation terms through the coupling  $\Delta^\alpha$ , which represents the amplitude of SC correlations in the bath. In this case no static mean-field order parameter acts directly on the cluster sites[41].  $\epsilon^\alpha$ ,  $V^\alpha$  and  $\Delta^\alpha$  are determined by imposing the self-consistency condition in Eq. 6.2 using a the usual conjugate gradient minimization algorithm with the distance function  $f$  introduced in chapter 3.4.1 that emphasizes the lowest frequencies of the Weiss field [12]. With the dSC order parameter defined as  $\psi_{ij} = \langle c_{i\downarrow} c_{j\uparrow} \rangle$  we consider  $d$ -wave singlet pairing ( $\psi = \psi_{12} = -\psi_{23} = \psi_{34} = -\psi_{41}$ ).

## 6.2 An anomalous superconductive state

We first observe that in our zero-temperature calculation the CDMFT-solution of the 2-dimensional Hubbard Model does support a  $d$ -wave superconducting state. The dSC order parameter  $\psi$  is shown in Fig. 6.1 as a function of the density  $n$  for  $t' = 0$  and

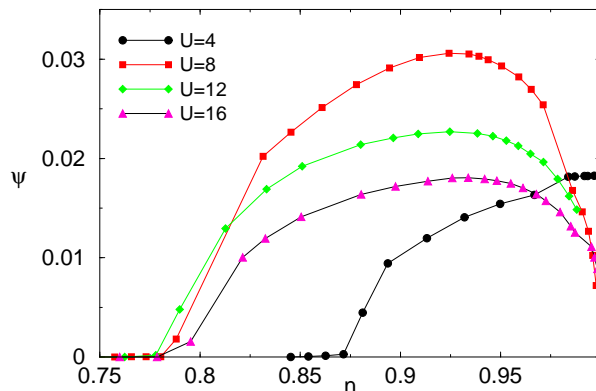


Figure 6.1: SC order parameter  $\psi = \langle c_\mu c_\nu \rangle$  as a function of filling  $n$  and onsite Coulomb repulsion  $U$ ,  $t' = 0$ .

different values of on-site Coulomb repulsion  $U$ . As  $U$  is increased to  $8t$  the order parameter acquires a maximum around  $\delta = 0.1$  (optimal doping) with a suppression above and below this doping. On the overdoped region, dSC disappears at a doping that is comparable with DCA and VCPT but smaller than the first case [31] and larger than the second [23].  $\psi$  shows a clearly different behavior for large and small interaction  $U$ , which can be ascribed to the proximity to a Mott-insulating state. For  $U = 4t$ ,  $\psi$  increases as  $n \rightarrow 1$ , in this case the half-filling insulating state is mostly an AF band-insulator. On the other hand, for  $U = 8t - 12t$ , the half-filled insulating state is a Mott-insulator even in the absence of AF. In this case, the superconducting state senses the proximity to the Mott state, and  $\psi$  goes to zero as the doping disappears because of the progressive localization of quasiparticles and hence, despite we observe stronger dSC Weiss field ( $\Delta$ ) in this region, there is a suppression of the dSC order parameter. This suppression is not seen for  $U = 4t$  because in that case it is the insulating gap that emerges from AF (Slater) correlations only at half-filling that kills dSC [20]. The maximum of the order parameter increases as  $U$  goes from  $4t$  to  $8t$  but then decreases as  $U$  changes to  $12t$  and then  $16t$ . This clearly signals that dSC is strongest at intermediate coupling and that at strong coupling the dSC order parameter scales as the magnetic exchange coupling  $J = 4t^2/U$ , as also found in early slave boson studies [43] and in other cluster approaches (like VCPT [23]). The value of optimal

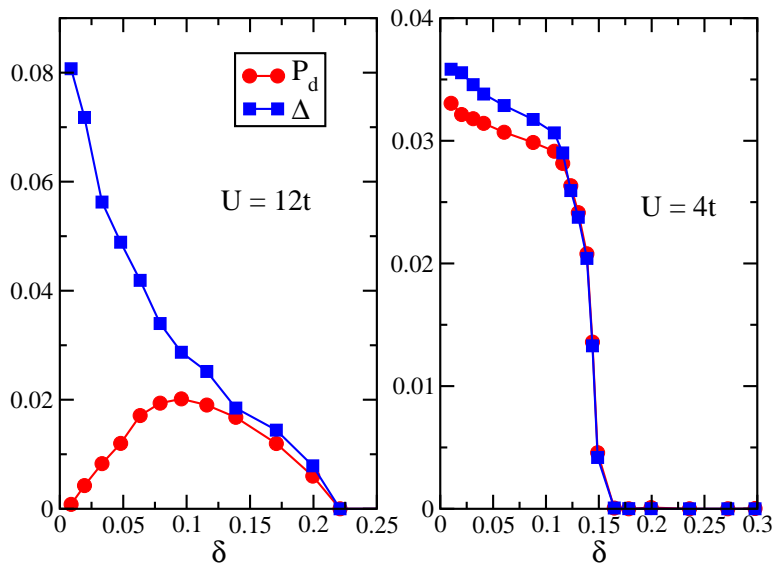


Figure 6.2:  $d$ -wave order parameter  $P_d = \langle c_\mu c_\nu \rangle$  and superconducting gap  $\Delta$  as a function of doping for weak-coupling  $U/t = 4$  (right) and strong-coupling  $U/t = 12$  (left).

doping is nearly independent of  $U$  in the intermediate to strong coupling regime.

### 6.2.1 Discrepancy between order parameter and anomalous gap

Another indication of the anomalous nature of the superconductivity in the strong correlated regime is given by the behavior of the anomalous gap  $\Delta$  (Fig. 6.2), which we computed from the density of states. The latter is obtained from the lattice Green's function which we can calculate with one of the three periodizing schemes ( $\Sigma, M$  or  $G$ -schemes).  $\Delta$  monotonically increases as  $n \rightarrow 1$ , even when the order parameter  $\psi$  is decreasing to zero (left panel of Fig.6.2 where the case  $U = 12t$  is displayed), in clear contrast with the prediction of BCS theory, where this two quantities are proportional, as instead takes place in the weak interacting regime (right panel of Fig.6.2 where the case  $U = 4t$  is displayed). This behavior is reminiscent of the cuprate superconductors, where the  $T = 0$  superconducting gap scales proportionally to the pseudogap as the

doping  $\delta \rightarrow 0$ , increasing instead of decreasing like the critical temperature  $T_C$ . It is also in accordance with experimental observation on the cuprates, e.g. thermal conductivity experiments [22]. These results in the strong coupling regime and the behavior of the maximum in the dome of the order parameter, which varies inversially proportional to  $U$ , support the super-exchange pairing hypothesis. This shows that the Hubbard Model presents underdoped and overdoped regions which reflect the properties of the corresponding phases in the cuprates. The magnitude of the gap at optimal doping is estimated to be around  $30meV$ , in good agreement with experimental estimates [22] for the cuprates, if we take a reasonable value for  $t$  of  $300meV$ .

### 6.2.2 Disappearance of the quasiparticle spectral weight at the MT

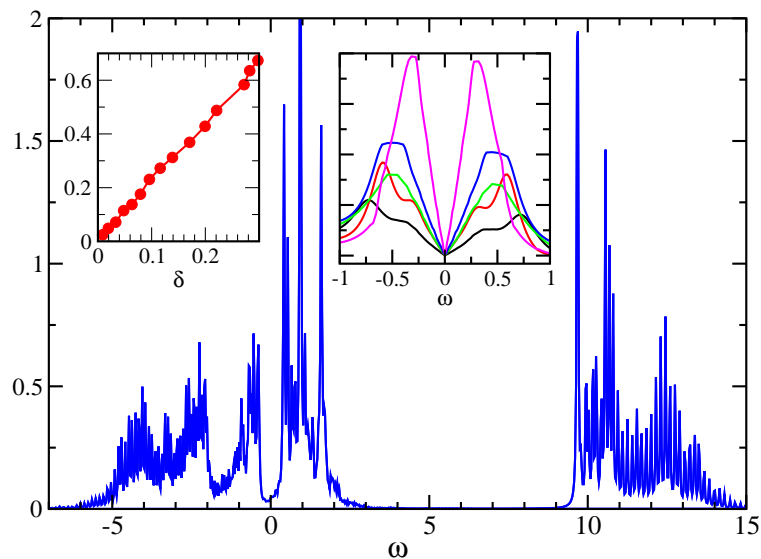


Figure 6.3: The local density of states  $\rho_0(\omega)$  in the superconducting phase for  $U/t = 12$ . Notice the presence of high and low energy features, and the strong particle-hole asymmetry. b) Integrated spectral weight of the low-energy feature as a function of doping. The vanishing of the low energy spectral weight signals the approach to the Mott insulator. c) Low energy spectral function vs energy. The large doping curves have a typical d-wave shape, and more involved structures appear for low-doping. Notice the similarity of the particle hole asymmetry with the experimental results of Ref. (16)

In order to better understand how the quasiparticles disappear in approaching the MT, bringing to the decreasing of the dSC order parameter, we can observe the local density of states  $\rho(\omega) = -1/\pi \text{Im}G_{loc}(\omega)$  ( $G_{loc}$  being the local Green's function), a quantity which can be measured accurately on the surface of a material by Scanning Tunneling Microscopy (STM). In proximity to the Mott insulator, most of the spectral weight lies in the high-energy Hubbard bands, but there is also a low-energy feature in correspondence of the Fermi level, taken as the reference zero-energy. In Fig.6.3, we plot  $\rho(\omega)$  from ED-CDMFT (the discretization inherent to the ED approach results in the spikes clearly visible in figure) for  $\delta \simeq 0.08$ . In Fig. 6.3-(b) we plot the integrated spectral weight of the low-energy feature as the doping is reduced to zero. Approaching half-filling, spectral weight is transferred from the low-energy feature to the Hubbard bands. The low-energy feature completely disappears as the Mott insulator is reached. The disappearance of mobile low-energy carriers, is an unequivocal feature of the approach to the Mott transition. This is ultimately the cause of the disappearance of superconductivity at the Mott boundary, rather than the vanishing of the attraction. In Fig. 6.4(c) we focus on the frequency dependence of the low-energy feature. A first evident observation is the asymmetry between positive and negative frequencies. Such an asymmetry has been first discussed by Anderson and Ong, who noticed it in the STM spectra, and ascribed it to the proximity to the Mott insulator[3]. On top of that, we identify a clear evolution from the underdoped to the overdoped physics. In all cases the low-energy spectrum is what we can expect for a d-wave superconductor, with zero weight only at  $\omega = 0$  and a linear behavior for small frequencies. As the doping is reduced  $\rho(\omega)$  develops a more complicated shape of the low-frequency profile of the spectrum, where the linear behavior is only limited to very low frequency, and a second feature appears at larger frequency. The behavior we have just described shares many similarities with what is observed in Bi2212 cuprate[30].

### 6.2.3 Nature of the pairing

We want now to get some insight in the pairing attraction, considering the frequency dependence of the anomalous self-energy in the d-wave channel  $S_d(\omega)$ . This quantity,

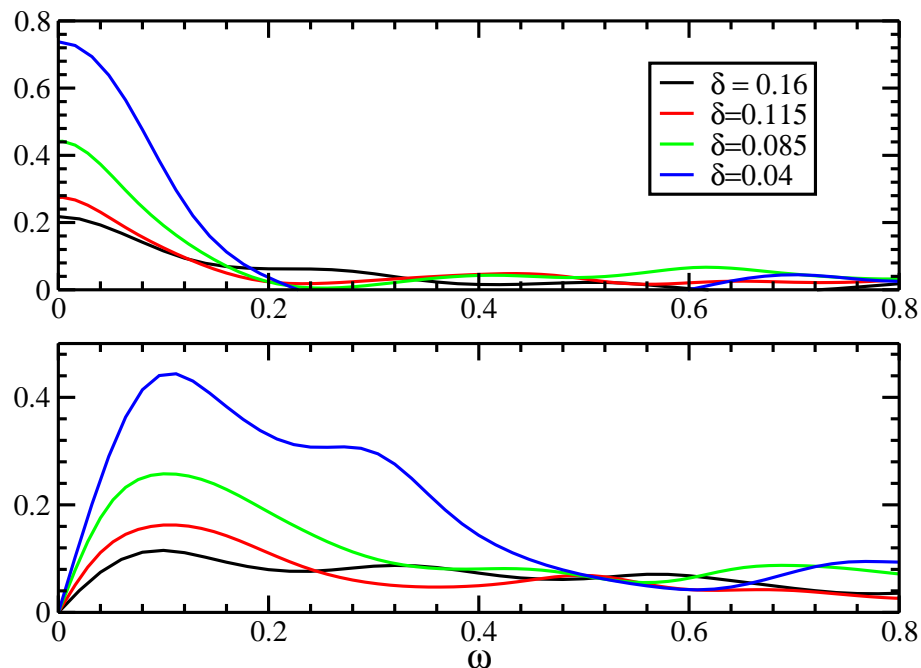


Figure 6.4: Real and imaginary part of the anomalous at low energy as a function of frequency for different doping levels. Notice that the scale over which the pairing is attractive is independent of doping. The real part of the self energy goes to a very small value beyond a scale of order  $J$  indicating that retardation plays a small role in this strongly correlated limit.

as well as any other dynamical observable, is directly obtained within ED-CDMFT, as opposed to many other approaches, where the dynamics is hardly accessible. In the classic Migdal-Eliashberg theory, the imaginary part of the anomalous self-energy is peaked at the frequencies of the phonons which mediate the pairing, while the real part changes sign around the same frequency, testifying that the attraction only lives up to the phonon energy scales, while high energies are dominated by Coulomb repulsion. In Fig. 6.4 we plot the evolution of this quantity with doping in our strong-coupling Hubbard model. Remarkably, we do not find sharp features, but rather a broad continuum which lives up to a scale of the order of the AFM superexchange coupling, indicating the magnetic origin of the pairing. Accordingly, the real part has less sharp behavior than in ordinary superconductors, but it is attractive up to a scale of order  $J$ , after which it is substantially zero, indicating a little role of retardation effects. Remarkably, the characteristic energy scale where the anomalous self-energy changes is

weakly doping-dependent.

### 6.2.4 The superconducting phase as "cure" for a ill normal state

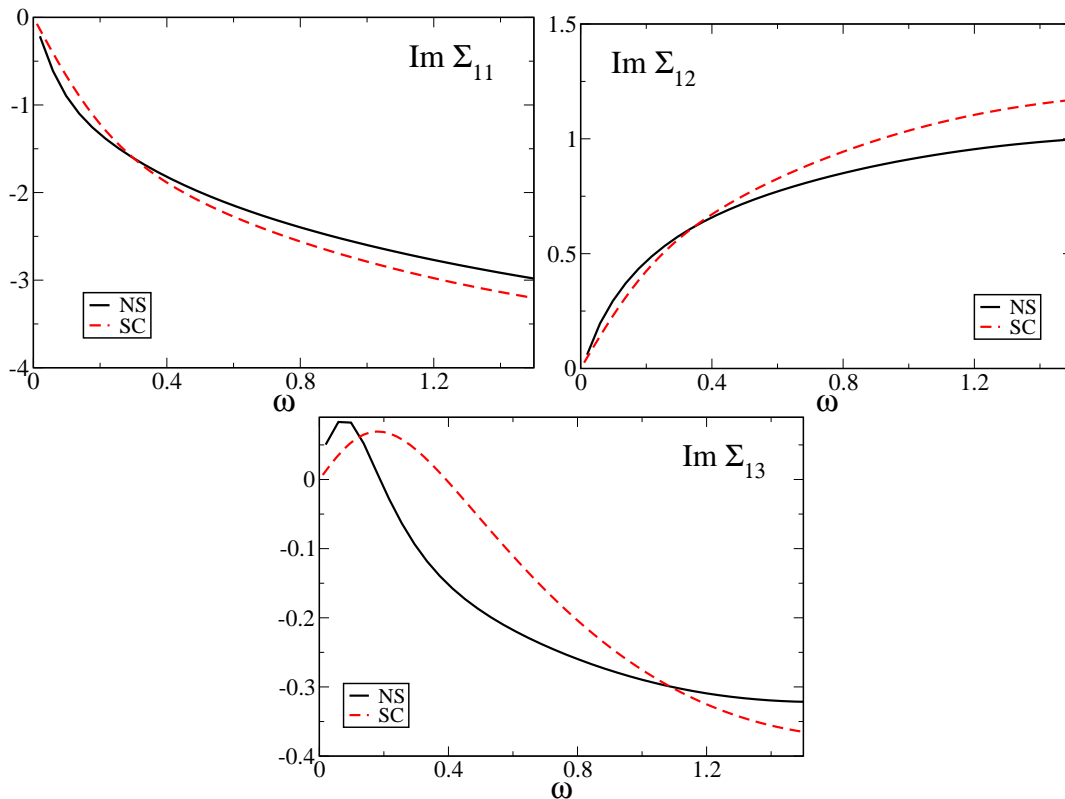


Figure 6.5: Imaginary parts of the normal-cluster components of the self-energy for  $U = 12t$ ,  $t' = 0$  and 10% doping. The normal state self-energies (black continuous line) are compared with the superconducting-state ones (red dashed line). Notice the enhanced FL-like behavior of the nearest-next-neighbor component  $\text{Im}\Sigma_{13} \rightarrow 0$  for  $\omega \rightarrow 0$  in the SC state.

It is useful to compare the dSC solutions with the corresponding NS ones. We have observed in the previous chapter that, approaching the MT, the NS quasiparticles present the formation of large scattering rates in some regions of the  $k$ -space, mainly around the  $(\pi, \pi)$  point in the first quadrant of the BZ (at least for the energy resolution used in this case,  $\beta^{-1} = 128$  in half-bandwidth units). This was at the origin of the momentum-space differentiation effect and the set up of an "anomalous" FL regime. Under the  $M$ -scheme viewpoint, the anomalies of this regime were enhanced with respect to the  $\Sigma$ -scheme viewpoint, displaying the formation of lines of zeroes of

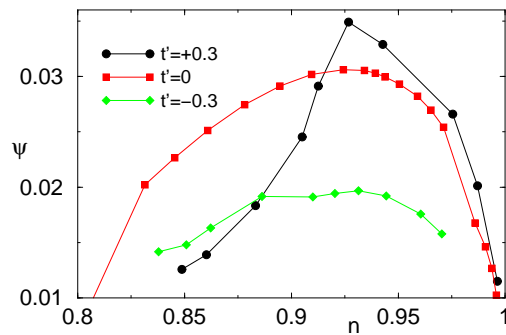


Figure 6.6: dSC order parameter as a function of  $n$  for various values of  $t'$  (frustration).

the one-particle Green's function in the  $k$ -space, accompanied by a radical change in the topology of the FS. The regime was nicely linked to the PG phase observed in experimental ARPES results. Zeroes in the Green's function are related to zeroes in the lattice-cumulant  $M$ , or in other words, to infinities of the lattice-self-energy  $\Sigma_k$ . Even if the relation of the lattice quantities with the cluster ones obtained as direct output of the CDMFT calculation is indeed  $\Sigma$ - $M$ - $G$ -scheme dependent, nevertheless we expect to observe an effect of the diverging behavior of  $\Sigma_k$  in certain points of the momentum mirrored in the cluster-self-energies. Rather than in the eigenvalues of the cluster-self-energy matrix, this is most evident in the cluster-self-energies, whose imaginary part we display in Fig. 6.5 for the intermediate coupling case  $U/t = 12$ ,  $t' = 0.0$  and 8% doping, and for a very low virtual temperature  $\beta^{-1} = 640$  (in half-bandwidth units). In spite at very low energies  $\omega \rightarrow 0$  all the cluster self-energies extrapolate to zero, the next-nearest-neighbor self-energy  $\Sigma_{13}$  present a very sharp low low energy feature, with a turning down very steep only at the last points of the Matsubara axis. This contributes to create in the  $k$ -space a strongly scattering quasiparticle with a small residuum  $Z$ , or, said in the  $M$ -language, to the formation of the self-energies-divergencies. We superimpose, for the same values of the Hubbard parameters, the normal-cluster-self-energies obtained from a SC solution. The effect of superconductivity is such as to "normalize" the cluster-self-energies, which are better behaved in terms of regular quasiparticles. The slopes of the  $\text{Im}\Sigma$  for  $\omega \rightarrow 0$  are going to zero more linearly, most evidently in the

next-nearest-neighbor case  $\text{Im}\Sigma_{13}$ . In other words it means that quasiparticles are better defined in the dSC phase than in its parent NS, in analogy with ARPES experiments on the cuprates [17]. This suggests that the origin of the dSC could be interpreted as the natural low-energy cure to an anomalous-FL NS.

As we did in the previous chapter for the NS, we now add a frustrating next-nearest neighbor (diagonal) hopping  $t' = \pm 0.3$  to the system. In Fig. 6.6 we plot the dSC order parameter  $\psi$  as a function of doping for various values of the  $t'$ . In the underdoped region,  $\psi$  grows with increasing  $t'$ , as it also was found in previous Dynamical Cluster Approximation (DCA) calculations[31]. This is un-expected if compared with experimental observation and band structure studies of the cuprates [24]. A possible explanation could be the proposal advanced in previous VCPT (Variational Cluster Perturbation Theory) studies [23, 49] suggesting that dSC may survive the onset of AF on the electron-doped side.

### 6.2.5 $k$ -dependent quantities

To try better clarifying this point, we need to extract the lattice quantities which can be directly connected to experimental observation, giving a physical interpretation to the results. As explained in chapter 4, this is achieved through a periodizing scheme, able to interpolate three cluster degree of freedoms (the cluster self-energies or the cluster cumulants) onto  $k$ -dependent quantities. In studying the NS in chapter 4, we adopted three of such schemes, the  $\Sigma$ ,  $M$  and  $G$ -schemes, which now we extend to the case of a superconductive state, where we have a non-zero pair-correlation function:

$$F(k, \tau) = -T \langle c_{k\uparrow} c_{-k\downarrow} \rangle \quad (6.3)$$

This is better described in the Nambu-spinor notation:

$$\Psi_k^\dagger = \left( c_{k\uparrow}^\dagger, c_{k\downarrow} \right)$$

and the matrix formulation of the one-particle Green's function:

$$\hat{G}(k, \tau) = -T \langle \Psi_k(\tau) \Psi_k^\dagger(0) \rangle$$

$$= \begin{pmatrix} G_{\uparrow}(k, \tau) & F(k, \tau) \\ F(k, \tau)^* & -G_{\uparrow}(-k, -\tau) \end{pmatrix} \quad (6.4)$$

The kinetic part of the Hamiltonian is simply re-written as:

$$\mathcal{H}_{kin} = -t \sum_{\langle ij \rangle} \Psi_i^{\dagger} \hat{\sigma}_3 \Psi_j \quad (6.5)$$

where  $\hat{\sigma}_3$  represents the Pauli matrix. A matrix self-energy is associated to the matrix Green's function:

$$\hat{G}^{-1}(k, \omega) = \omega \hat{1} + (\mu - \varepsilon_k) \hat{\sigma}_3 - \hat{\Sigma}_k(i\omega) \quad (6.6)$$

which contains normal  $\Sigma_k$  as well as anomalous  $\Sigma_k^A$  contributions:

$$\hat{\Sigma}_k(i\omega) = \begin{pmatrix} \Sigma_k(i\omega) & \Sigma_k^A(i\omega) \\ \Sigma_k^A(i\omega) & -\Sigma_k(i\omega)^* \end{pmatrix} \quad (6.7)$$

Naturally, this can be re-formulated in terms of the cumulant  $M_k$  :

$$\hat{G}^{-1}(k, \omega) = \hat{M}_k^{-1}(i\omega) + (\mu - \varepsilon_k) \hat{\sigma}_3 \quad (6.8)$$

which contains normal  $M_k$  as well as anomalous  $M_k^A$  contributions:

$$\hat{M}_k(i\omega) = \begin{pmatrix} M_k(i\omega) & M_k^A(i\omega) \\ M_k^A(i\omega) & -M_k(i\omega)^* \end{pmatrix} \quad (6.9)$$

Once again, in the  $\Sigma$ -scheme we periodize the cluster-self-energy, normal and anomalous:

$$\begin{aligned} \Sigma_k(\omega) &= \Sigma_{11}(\omega) + \Sigma_{12}(\omega) (\cos k_x + \cos k_y) + \Sigma_{13}(\omega) \cos k_x \cos k_y \\ \Sigma_k^A(\omega) &= \Sigma_{12}^A(\omega) (\cos k_x - \cos k_y) \end{aligned} \quad (6.10)$$

and in the  $M$ -scheme the cluster-cumulant :

$$\begin{aligned} M_k(\omega) &= M_{11}(\omega) + M_{12}(\omega) (\cos k_x + \cos k_y) + M_{13}(\omega) \cos k_x \cos k_y \\ M_k^A(\omega) &= M_{12}^A(\omega) (\cos k_x - \cos k_y) \end{aligned} \quad (6.11)$$

In the  $G$ -scheme we again periodize the super-lattice Green's function on the full lattice like in formula 4.6, but this time the superlattice Green's function is doubled in size

( $2N_c \times 2N_c$ ), considering the superconductive pairing correlations (formula 6.3) in the blocks out of diagonal, according to the super-cluster spinors  $\Psi_c$  notation introduced in formula 6.1:

$$\hat{G}(k, \omega) = \frac{1}{N_c} \sum_{\mu, \nu=1}^{N_c} e^{ik\mu} \left[ \hat{\mathbf{1}} \omega + \hat{t}_k^c - \hat{\Sigma} \right]_{\mu\nu}^{-1} e^{-ik\nu} \quad (6.12)$$

where  $\hat{G}(k, \omega)$  is  $2 \times 2$  Nambu's notation Green's function (6.4),  $\hat{\mathbf{1}}$  is the  $2N_c \times 2N_c$  identity matrix,

$$\hat{t}_k^c = \begin{pmatrix} \hat{t}_k & 0 \\ 0 & -\hat{t}_k \end{pmatrix}$$

$\hat{t}_k$  is the  $N_c \times N_c$  cluster-hopping matrix and  $\hat{\Sigma}$  the super-cluster self energy (6.2). We plot in Figs 6.7, 6.8 the spectral density  $A(k, \omega = 0^+)$  for a doping corresponding to the critical temperature and  $U = 12t$  in the first quadrant of the BZ for the two cases  $t' = -0.3t$  (relevant for cuprate materials Fig. 6.7), and  $t' = 0.0$  (Fig. 6.7) showing the 3 periodizing schemes (the  $\Sigma$ -scheme on the top row, the  $M$ -scheme in the middle row and the  $G$ -scheme in the bottom). In the first column we display  $A(k, \omega = 0^+)$  for the normal state (NS) corresponding to the same critical density. These plots are chosen to fix a reference scale for the color scale in the spectral density plots for the superconducting state (SC) in the second and third column, i.e. reading the plots horizontally the color scale is absolute and fixed by the NS plot. In the third column we extracted the quasiparticle spectrum underlying the SC by artificially zeroing the anomalous part of the self-energy in the SC solution (displayed in the second column).

In the case of  $t' = -0.3t$  all the three methods produce a consistent picture, where a dSC state is born out of a NS whose momentum-dependent scattering gives rise to the cold spots appearing in the  $(\frac{\pi}{2}, \frac{\pi}{2})$  region in the first quadrant of the BZ, the right place for the nodal gapless spectrum of a d-wave superconductor. In this sense we state the dSC state is a cure to an instability already evident in the NS and which originates the hot/cold spot modulation. The observation made in Fig. 6.5 that the dSC state rebuilds a more FL system, originating cluster self-energies whose  $\text{Im}\Sigma_{ij} \rightarrow 0$  more linearly (this above all in the nearest next-neighbor component) is here enforced by the third column graph (labeled  $SC = 0$ ), once again this is consistent in all the three

$$U = 12t, t' = -0.3t, n = 0.87$$

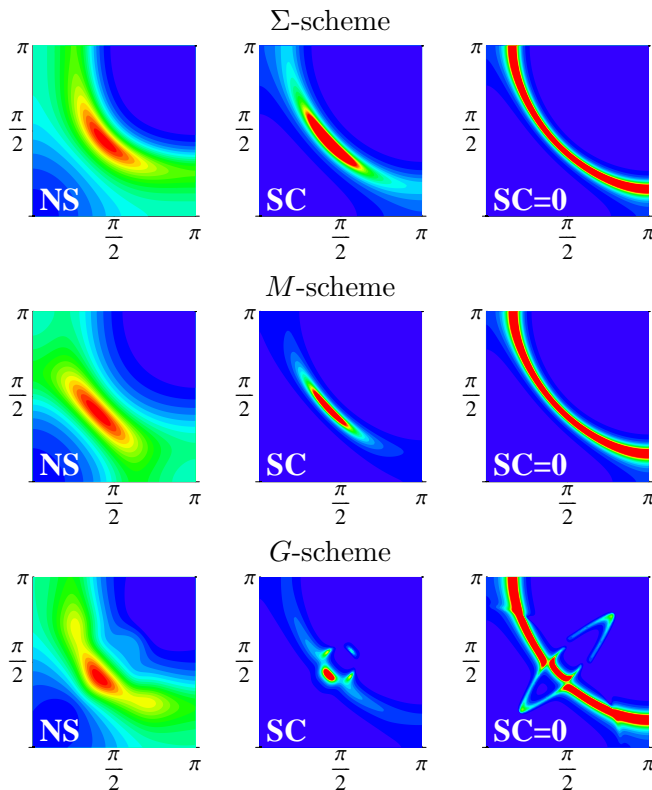


Figure 6.7: Spectral function  $A(k, \omega \rightarrow 0^+)$  for the case  $U = 12t$ ,  $t' = -0.3t$  and density  $n = 0.87$ . The result of the three periodizing schemes are displayed: the  $\Sigma$ -scheme in the first row, the  $M$ -scheme in the second, the  $G$ -scheme in the third. In the first column of each row the NS-result is presented, whose color scale is kept in the following SC (second column) and SC=0 (third column) plot. The SC is the superconducting state result, SC=0 is the normal quasiparticle spectrum in the SC state obtained zeroing the anomalous components from the SC result.

periodizing schemes. As mentioned above, this plot has been obtained by switching off superconductivity in the SC solution by simply putting to zero the anomalous components. It is evident how a full homogeneous FS is re-constructed equivalent in shape to the NS one (first column) but with a less  $k$ -dependent modulation in the spectral intensity, i.e. the one particle spectrum underlying the SC state is more regularly a FL than its corresponding NS. In Fig. 6.9 we show the spectral function  $A(k, \omega)$  displayed in the path  $(0, 0) \rightarrow (\pi, \pi) \rightarrow (0, \pi) \rightarrow (0, 0)$  of the first quadrant of the BZ as a function of the energy  $\omega$ , obtained in the SC system with the three periodizing schemes. As

$$U = 12t, t' = 0.0, n = 0.93$$

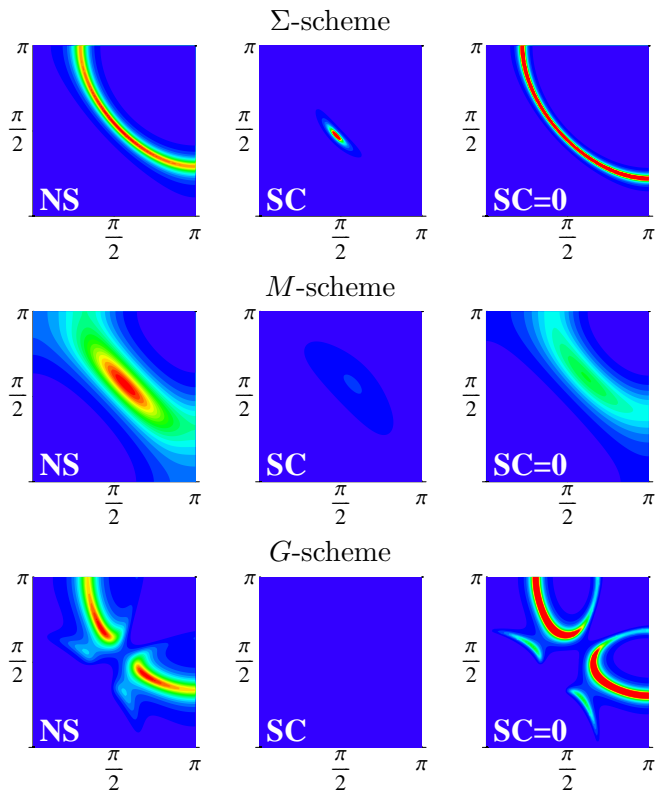


Figure 6.8: Spectral function  $A(k, \omega \rightarrow 0^+)$  for the case  $U = 12t$ ,  $t' = 0.0$  and density  $n = 0.93$ . The result of the three periodizing schemes are displayed: the  $\Sigma$ -scheme in the first row, the  $M$ -scheme in the second, the  $G$ -scheme in the third. In the first column of each row the NS-result is presented, whose color scale is kept in the following SC (second column) and SC=0 (third column) plot. The SC is the superconducting state result, SC=0 is the normal quasiparticle spectrum in the SC state obtained zeroing the anomalous components of the SC state.

observed in experimental ARPES data [15] [11], a FL quasiparticle peak is observed around the  $k = (\pi/2, \pi/2)$  nodal point, even more pronounced than in the NS, while a superconducting gap opens in the pseudogap region around  $k = (0, \pi)$  point, as required in a d-wave shaped SC gap. This enforces the idea that the dSC state is derived naturally from the pseudogap NS in the hole-doped case, and it represents the natural low-temperature elongation of the pseudogap instability at lower temperatures. The strong similarity of these graphs in all the 3 periodizing schemes considered supports the robustness of this result.

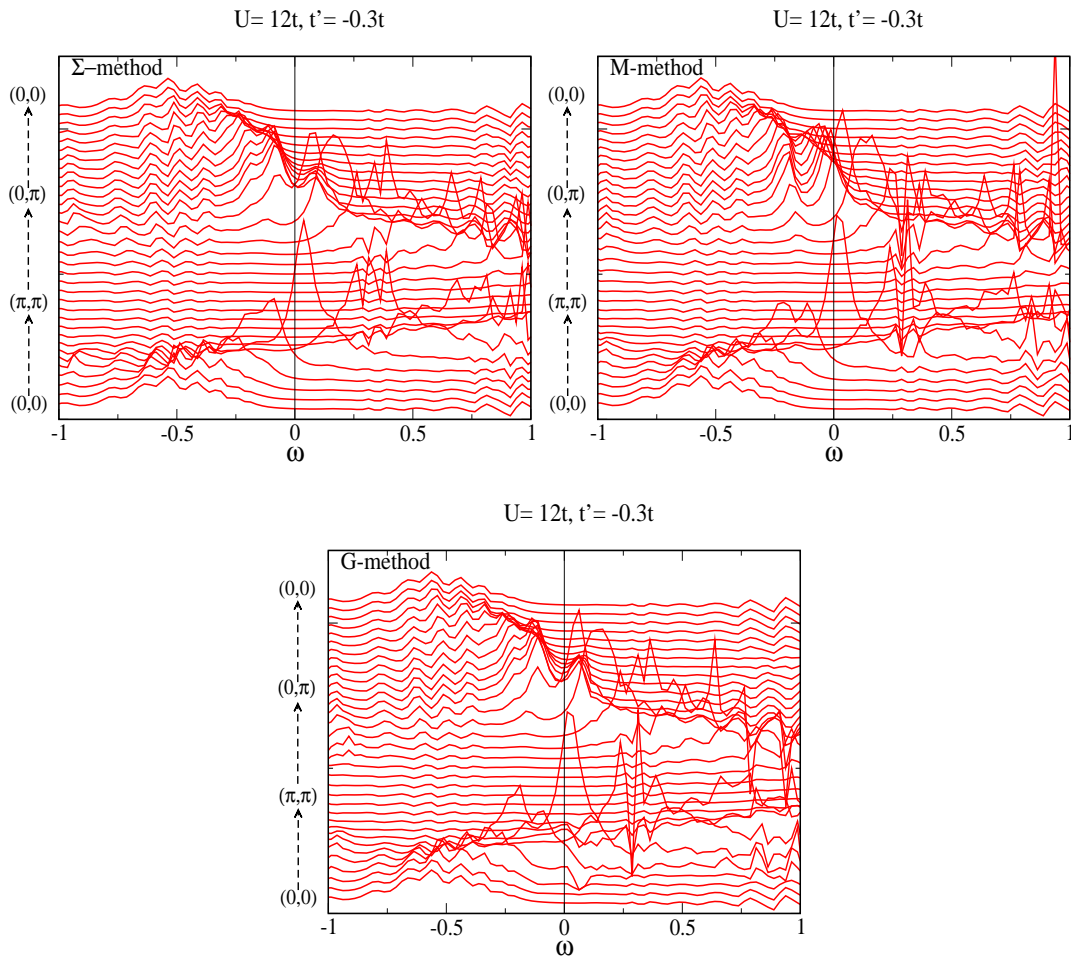


Figure 6.9: Spectral function  $A(k, \omega)$  along the path  $(0,0) \rightarrow (\pi, \pi) \rightarrow (0, \pi) \rightarrow (0,0)$  in the first quadrant of the Brillouin Zone obtained with the 3 periodizing schemes

We now show in Fig. 6.8 the case  $t' = 0$ . This is qualitatively different from the previous one, and the scenario more complex. In the NS already (first column) the three periodizing schemes give a non-uniform answer: in the  $\Sigma$ -scheme a weak modulation on the FS appears, with more spectral weight around  $(\frac{\pi}{2}, \frac{\pi}{2})$ , in the  $M$ -scheme the modulation is more enhanced with a clear cold spot forming around  $(\frac{\pi}{2}, \frac{\pi}{2})$  (but the total intensity, which is not explicitly shown in this graph, is very much reduced, being  $\frac{1}{5}$  of the one resulting from the  $\Sigma$  and  $G$ -schemes), in the  $G$ -scheme spectral weight disappears around  $(0, \pi)$  and  $(\pi, 0)$  regions of the first quadrant as well as around  $(\frac{\pi}{2}, \frac{\pi}{2})$ . More instabilities which (at least for the  $M$  and  $G$  schemes) push away spectral weight from  $(\frac{\pi}{2}, \frac{\pi}{2})$  seems to be taking place. Indeed, for the  $M$  and  $G$

schemes the  $t' = 0$  system is more connected to the electron-like-shaped FS, presenting (as seen in chapter 5) a dramatic change in the topology of the FS in correspondence of an hypothetical quantum critical point. The latter was instead washed away under a  $\Sigma$ -scheme viewpoint. We therefore see that in the  $\Sigma$ -scheme (first row Fig. 6.8) the scenario proposed is the same as in the case  $t' = -0.3t$ , where a d-wave SC was arising from a cold spot centered around the  $(\frac{\pi}{2}, \frac{\pi}{2})$  region. Switching off SC (third column labeled  $SC = 0$ ) re-builds a uniform FL-like FS. In the  $M$ -scheme (second row) the spectrum totally gaps in the SC state, and the nodal quasiparticle around the  $(\frac{\pi}{2}, \frac{\pi}{2})$  region disappears too. Restoring the NS from the SC (third column) partially re-insert spectral weight in  $(\frac{\pi}{2}, \frac{\pi}{2})$ , but strongly reduced as compared to the NS one. In this case the simple FL picture of the  $\Sigma$ -scheme is not recovered. We encounter some similarities in the  $G$ -scheme result (third row). Here, as was stated, already the NS is not a regular FL. Similar results for the electron-doped side were obtained from VCPT with AF and dSC coexisting as well as from CPT with no long range order when  $U$  is larger than  $6t$  [23, 21]. Here, according to this viewpoint, short-range AF correlations would be sufficient to suppress weight at  $(\frac{\pi}{2}, \frac{\pi}{2})$ . The SC (second column) state is once again, like in the  $M$ -scheme fully gaped. Restoring the normal state re-builds the NS FS, however spectral weight is not recovered in  $(\pi/2, \pi/2)$ . This, together with the behaviour observed in the  $M$ -scheme, may indicate that in these two schemes the instability responsible for the disappearance of weight in  $(\frac{\pi}{2}, \frac{\pi}{2})$  is a mechanism not directly connected with the dSC mechanism.

## Conclusions

In this thesis we have studied a strongly correlated electron model, the two dimensional Hubbard Model, which is considered to embody the essential physics of high temperature superconducting materials (chapter 1). Strongly interacting many-body systems are difficult to tackle because it is not possible to apply standard techniques like perturbation theory. In this work we have used an extension of Dynamical Mean Field Theory (DMFT) [35]. In the past decade, DMFT has proved a powerful tool to access strongly interacting many-body models. In spite of its successes however, DMFT is not able to accurately describe the physics of the cuprate materials as, being a local theory exact only in the infinite dimensional limit, misses the short ranged (i.e. momentum space dependent) spatial correlations, which experimentally showed to be an essential ingredient in the cuprate physics [15][11] (chapter 2). Moreover, DMFT by construction does not allow one to study phases with a definite spatial arrangement of the order parameter, like for example d-wave superconductivity. We have therefore:

- Developed an extension of DMFT, the Cellular Dynamical Mean Field Theory (CDMFT), which extends the single site character of DMFT to a cluster of sites, allowing for a first momentum space description of physical properties (chapter 3). The numerical technique used to solve an effective associate Anderson Impurity Model is the Lanczos algorithm, which allows to virtually access the zero temperature physics.
- Benchmarked the technique with exact known results in one dimension, with previous Quantum Montecarlo studies, set up the right implementation of the method and extracted physically interpretable results (chapter 4).
- Applied the method to the two-dimensional Hubbard Model, including the effect

of a next-nearest neighbor hopping. We studied the density-driven Mott metal-insulator (MT) transition in the hole-doped and electron-doped systems (chapter 5). Our findings can be summarized as follows:

1. Approaching the MT point the Fermi Surface (FS) is strongly renormalized by interaction, contrary to the common band-structure approach which fix the shape of the FS in the MT description.
2. In the region preceding the MT, we observe the phenomenon of momentum-space differentiation of scattering properties, as found in angle photo-emission experiments (ARPES) experiments [15][11]. In particular in the hole-doped systems a cold (low scattering) spot is formed around the point  $k = (\frac{\pi}{2}, \frac{\pi}{2})$  in the first quadrant of the Brillouin Zone (BZ), while high scattering regions (hot spots) develop around the points  $k = (0, \pi), (\pi, 0)$ . This state can be smoothly connected to a d-wave superconducting state (dSC), where a nodal quasiparticle survives in  $k = (\frac{\pi}{2}, \frac{\pi}{2})$ . In the electron-doped systems instead, the cold/hot spot position in the  $k$ -space is switched. This state cannot be easily connected with a d-wave SC.
3. Enforcing an artificially strong frustration into the system ( $t' = +0.9t$ ), we have shown that the phenomenon of momentum-space modulation is indeed associated with the proximity to the Mott transition rather than to long-ranged antiferromagnetic (AF) correlations of a insulating parent ordered state.
4. We have found hints of the presence of a quantum critical instability which precludes the formation of the phase with momentum-modulated properties (hot/cold spot formation). This quantum critical region is associated with the appearance of zeroes of the one particle Green's function in the momentum-space and with a dramatic change in topology of the FS. In this phase a depression of spectral weight forms in correspondence of the Fermi level in the hot regions of momentum space: this is the pseudogap phase observed also in ARPES experiments ([15][11]).

- finally applied CDMFT to study a dSC-state (chapter 6). We have found that at zero temperature the two-dimensional Hubbard model is capable of sustaining d-wave superconducting state, which present some anomalies compared with a standard Bardeen-Cooper-Shifferer (BCS) superconductor:
  1. the order parameter and the superconductive gap do not scale together, rather the superconductive gap increases with decreasing doping while the order parameter decreases to zero as the critical temperature  $T_C$ . This is in major contrast with the BCS predictions where these two quantities are proportional.
  2. The disappearance of SC is due to the disappearance of quasiparticles approaching the MT, rather than to weakening of the pairing interaction.
  3. The pairing mechanism originates from the magnetic super-exchange  $J \sim \frac{1}{U}$ , as shown by the maximum value of the order parameter that scales like  $J$  and by the frequency-dependence of the anomalous self-energy, which give insights into the range of the paring attraction (again of the order of  $J$  and roughly doping independent).

We finally conjecture that in the hole-doped system the d-wave nature of the superconducting state is naturally born out from its anomalous pseudogap normal state. We have shown that the momentum space modulated FS of the NS is uniformly restored in the normal-quasiparticle spectrum of the corresponding dSC state, which in this way "cures" the instability of the NS. In the electron-doped systems instead the scenario is more complicated, where other instabilities (like for example short ranged AF correlations) may play a role in determining a non d-wave SC gap, i.e. NS and dSC states may not be smoothly connected. Further investigations are in this case required.

## Appendix A

### The tJ Model

In Chapter 1 we presented a Hartree-Fock mean field treatment of the Hubbard Hamiltonian which is able to take into account the high-energy charge excitation. This is responsible for the splitting of the conduction band in an upper and lower part, separated by a gap of the order of the on-site repulsion  $U$ . We then showed that a Heisenberg Hamiltonian, introduced as the strong repulsion limit of the Hubbard model, is able to describe the low-energy collective spin-modes also deriving from the on-site repulsion but not encompassed into the mean-field approach. In this appendix we want now to extend the Heisenberg treatment to the doped case. The basic idea is to be able to describe the physics of few charge carriers immersed in an AF background, taking into account the forbidden double occupancy as well as the collective motion of the spin degrees of freedom. To this purpose, we define the interaction part of the Hamiltonian  $H_0$  and the kinetic part  $H_1$ , which we consider as the perturbing term. We seek for the effective Hamiltonian defined into the subspace  $\Xi$  of forbidden double occupation for  $H_0$ , corresponding to the zero eigenvalue. The difference with the previous section is that the states called  $\phi_0$ , which specify the positions of the electrons in the lattice, have now some holes corresponding to empty sites. Applying  $H_1$  to  $\phi_0$  creates a superposition of states which are not all double occupied. Said  $|\Psi_0\rangle \in \Xi$  a generic linear combination of  $|\phi_0\rangle$ , we have that  $H_1|\Psi_0\rangle$  has a non-zero component in  $\Xi$ . So, for convenience, let's decompose  $H_1|\Psi_0\rangle$  into two components in  $\Xi$  and in  $\Xi^\perp$ , introducing the projecting-operators onto these subspaces, respectively  $P_0$  e  $P_1 = 1 - P_0$ . Given then  $H = H_0 + \lambda H_1$  and  $|\Psi\rangle = |\Psi_0\rangle + \lambda|\Psi_1\rangle$ , where, without loss of generality,  $|\Psi_1\rangle \in \Xi^\perp$ , we write the eigenvalues equation  $H|\Psi\rangle = E|\Psi\rangle$ , and we have:

$$\lambda H_0|\Psi_1\rangle + \lambda H_1|\Psi_0\rangle + \lambda^2 H_1|\Psi_1\rangle = E(|\Psi_0\rangle + \lambda|\Psi_1\rangle). \quad (\text{A.1})$$

Let's multiply both terms by  $\langle \Psi_0 |$ . Noticing that the first term in the first side of the equation is zero, as  $H_0|\Psi_1\rangle \in \Xi^\perp$ , it is:

$$\lambda \langle \Psi_0 | H_1 | \Psi_0 \rangle + \lambda^2 \langle \Psi_0 | H_1 | \Psi_1 \rangle = E. \quad (\text{A.2})$$

If instead we multiply the (A.1) by  $\langle \Psi_0 | H_1 P_1$ , we have at the first order

$$\lambda \langle \Psi_0 | H_1 P_1 H_0 | \Psi_1 \rangle + \lambda \langle \Psi_0 | H_1 P_1 H_1 | \Psi_1 \rangle = E \langle \Psi_0 | H_1 P_1 | \Psi_0 \rangle,$$

and, as the second side is zero given  $P_1 H_1 | \Psi_0 \rangle \in \Xi^\perp$  (in fact  $H_0 P_1 H_1 | \Psi_0 \rangle = U P_1 H_1 | \Psi_0 \rangle$ , as  $P_1 H_1 | \Psi_0 \rangle$  is a linear combination of configurations with only one site double occupied), we obtain

$$\langle \Psi_0 | H_1 | \Psi_1 \rangle = -\frac{1}{U} \langle \Psi_0 | H_1 P_1 H_1 | \Psi_0 \rangle. \quad (\text{A.3})$$

We can plug the (A.3) into (A.2), and finally obtain :

$$\langle \Psi_0 | \lambda H_1 - \frac{\lambda^2}{U} H_1 P_1 H_1 | \Psi_0 \rangle = E.$$

The effective Hamiltonian we want, which is called  $tJ$ , is then:

$$H_{tJ} = P_0 (H_1 - \frac{1}{U} H_1 P_1 H_1) P_0$$

with the operators  $P_0$  limiting its action into the subspace  $\Xi$  only. Once again we can get a more representative expression by introducing spin operators. The action of the operators  $P_0$  e  $P_1$  can be described by redefining the creation and destruction operators. So given  $|\varphi\rangle$  a generic state in  $\Xi$ , we can write with good approximation:

$$c_{i\sigma}^+ |\varphi\rangle = P_0 |\varphi\rangle + P_1 |\varphi\rangle = [(1 - n_{i,-\sigma}) c_{i\sigma}^+ + n_{i,-\sigma} c_{i\sigma}^+] |\varphi\rangle.$$

Essentially the action of  $c_{i\sigma}^+$  on  $\Xi$  is described by  $(1 - n_{i,-\sigma}) c_{i\sigma}^+$ ; we can therefore create an electron with spin  $\sigma$  on the site  $i$  only if there is not already an electron of opposite spin. The term  $P_0 H_1 P_1 H_1 P_0$  can be written

$$t^2 \sum_{ij, \sigma\sigma'} (1 - n_{i,-\sigma}) c_{i\sigma}^+ c_{j\sigma} n_{j,-\sigma} n_{j,-\sigma'} c_{j\sigma'}^+ c_{i\sigma'} (1 - n_{i,-\sigma'}).$$

We want to consider the case for which the doping  $\delta \ll 1$ , so that at the first order in  $\delta$  we can disregard the three-site-hopping terms. As  $S^+ = c_\uparrow^+ c_\downarrow$  e  $S^- = c_\downarrow^+ c_\uparrow$ , after

some simple passage:

$$H_{tj} = -t \sum_{\langle ij \rangle, \sigma} P_0 [c_{i\sigma}^+ c_{j\sigma} + h.c.] P_0 + J \sum_{\langle ij \rangle} (\mathbf{S}_i \mathbf{S}_j - \frac{1}{4} n_i n_j).$$

This Hamiltonian differs from Heisenberg's only in the kinetic term, which appears because of doping. The second term describes the spin-spin interaction due to the virtual hopping of the electrons between occupied sites. Notice that in the half-filled case ( $\delta = 0$ ) the kinetic term disappears.

## Appendix B

### The Lanczos Algorithm

#### B.1 The Lanczos idea

We briefly overview the numerical principles underlying the numerical exact diagonalization method (Lanczos) that we used in this work to solve the AIM associated with the original non local problem. A complete and detailed explanation of this method, with its virtues and defects, can be found for example in [16]. The problem aims to find few eigenvalues and eigenvectors of a large matrix symmetric  $A$  which cannot be solved by direct methods. The simplest problem consist for example in finding the largest eigenvalue in absolute value, along with the corresponding eigenvector, and the simple algorithm able to achieve this goal is the power method:

$$\begin{aligned} y_{i+1} &= A x_i \\ x_{i+1} &= y_{i+1} / \| y_{i+1} \| \end{aligned} \tag{B.1}$$

If there exists only one eigenvalue of largest absolute value and the starting  $x_1$  it is not perpendicular to it,  $x_i$  converges to the desired eigenvector. Notice that the main calculation in the algorithm, the matrix multiplication  $A x_i$ , can be considered as a black box with  $x_i$  in input and  $A x_i$  in output. The procedure after  $k$  steps builds  $x_1 \dots x_k$  vectors which span the so called *Krylov subspace*  $\mathcal{K}_k(A, x_1) = \{ A x_1, \dots, A^{k-1} x_1 \}$ . In fact, rather than considering only  $x_k$ , a stronger procedure consist in seeking the best linear combination  $\sum_{i=1}^k \alpha_i x_i$  in the Krylov subspace, the *Ritz* vector, which best approximates the desired eigenvector. The corresponding approximation to the desired eigenvalue is the so called Ritz value and the procedure is called the Rayleigh-Ritz Method. In more precise terms, given the  $n \times n$  orthogonal matrix  $Q = (Q_k, Q_{n-k})$ , where with  $Q_k$  we indicate the  $k$  vector-columns (which in practice span the Krylov

subspace) and

$$T = Q^T A Q$$

Rayleigh-Ritz Method approximates the eigenvalues of  $A$  by the eigenvalues of  $T_k = Q_k^T A Q_k$ , the Ritz values, and, given the eigendecomposition of  $T_k = V \Lambda V^T$ , the corresponding eigenvectors approximations are the columns of  $Q_k V$ , the Ritz vectors. In using the Lanczos algorithm to compute  $Q_k$ ,  $T$  assumes the particular symmetric triangular form:

$$T = \left( \begin{array}{c|c} T_k & T_{ku}^T \\ \hline T_{ku} & T_u \end{array} \right) = \left( \begin{array}{cccc|cccc} \alpha_1 & \beta_1 & & & & & & \\ \beta_1 & \ddots & \ddots & & & & & \\ & \ddots & \ddots & \beta_{k-1} & & & & \\ & & & \beta_{k-1} & \alpha_k & \beta_k & & \\ \hline & & & & \beta_k & \alpha_{k+1} & \beta_{k+1} & \\ & & & & & \beta_{k+1} & \ddots & \ddots \\ & & & & & & \ddots & \ddots & \beta_{n-1} \\ & & & & & & & & \beta_{n-1} & \alpha_n \end{array} \right)$$

for which it is easy to compute eigenvalues and eigenvectors, and the Rayleigh-Ritz procedure simplifies. The following theorem, which we enunciate here without proof (for it we refer to [16]) elucidates the advantages:

Let  $T_k = V \Lambda V^T$  be the eigendecomposition of  $T_k$ , where  $V = [v_1 \dots v_k]$  is orthogonal and  $\Lambda = \text{diag}(\theta_1 \dots \theta_k)$ . Then

1. There are  $k$  eigenvalues  $\alpha_1, \dots, \alpha_k$  of  $A$  (not necessarily the largest  $k$ ) such that  $|\theta_i - \alpha_i| \leq \|T_{ku}\| = \beta_k$ , the single (possibly) nonzero entry in the upper right corner of  $T_{ku}$ .
2.  $\|A(Q_k v_i) - (Q_k v_i) \theta_i\| = \|T_{ku} v_i\| = \beta_k |v_i(k)|$  where  $v_i(k)$  is the  $k^{\text{th}}$  (bottom) entry of  $v_i$ . Thus, the difference between the Ritz value  $\theta_i$  and some eigenvalue  $\alpha$  of  $A$  is at most  $\beta_k |v_i(k)|$ , which may be much smaller than  $\beta_k$ . Moreover this

formula allow us to compute the residual  $\| A(Q_k v_i) - (Q_k v_i) \theta_i \|$  cheaply without multiplying any vector by  $Q_k$  or by  $A$ .

3. Without any further information on the spectrum of  $T_u$ , we cannot deduce any useful error bound on the Ritz vector  $Q_k v_i$ . However, if we know that the gap between  $\theta_i$  and any other eigenvalue of  $T_k$  or  $T_u$  is at least  $g$ , then we can bound the angle  $\varphi$  between  $Q_k v_i$  and a true eigenvector of  $A$  by

$$\frac{1}{2} \sin 2\varphi \leq \frac{\beta_k}{g}$$

In order to find the eigenvalues and the eigenstates of the symmetric matrix  $A$  the Lanczos procedure combines the Lanczos power method to construct the Krylov subspace and the Rayleigh-Ritz method: it first builds the orthogonal matrix  $Q_k = [q_1 \dots q_k]$  of Lanczos vectors and approximates the eigenvalues of  $A$  by the Ritz eigenvalues of the tridiagonal symmetric matrix  $T_k = Q_k^T A Q_k$ .

#### The Lanczos algorithm:

$$q_1 = b / \| b \|, \beta_0 = 0, q_0 = 0$$

for  $j = 1$  to  $k$

$$z = Aq_j$$

$$\alpha_j = q_j^T z$$

$$z = z - \alpha_j q_j - \beta_{j-1} q_{j-1}$$

$$\beta_j = \| z \|$$

if  $\beta_j = 0$  exit

$$q_{j+1} = z / \beta_j \text{ Compute eigenvalues, eigenvectors and error bounds of } T_j$$

end for

The algorithm is in principle able to provide the best  $k$  Ritz approximation to the eigenvalues and eigenvectors of  $A$ , though the largest eigenvalues converge much faster than the others. The starting vector should not however be nearly orthogonal to one of

the desired eigenvectors. If this is the case in fact, a difficulty arises in the procedure wherein the eigenvector orthogonal to  $q_1$  is missing in the solution. Choosing  $q_1$  at random can prevent this kind of problem and we can always rerun the Lanczos algorithm with a different random  $q_1$  to provide more "statistical" evidence that we did not miss any eigenvalues. Another difficulty arises if there are degenerate eigenvalues in the spectrum. In this case the Lanczos procedure is never able to obtain both eigenvalues, and one of them will be missing. Fortunately there are many applications where it is enough to determine the value of the eigenvalue without knowing its multiplicity. There are however procedure like the "Block" Lanczos that are able, at least to some extent, to tackle degenerate spectra and recover the multiplicity of the eigenvalues. We will return later on this method.

## B.2 The Lanczos algorithm in floating point arithmetic

We presented in the previous section an "ideal" Lanczos procedure which did not take into account the roundoff, unavoidable in any realistic calculation. At each Lanczos loop, the vector  $z$  is by construction orthogonal to  $q_1$  through  $q_{j-1}$ . Roundoff unfortunately destroys this orthogonality. However the algorithm does not become totally unpredictable: it can be shown (Paige's theorem [16]) that the  $q_k$  lose orthogonality because they acquire large components in the direction of the Ritz vectors  $y_{i,k} = Q_k v_i$  whose Ritz value  $\theta_i$  have already converged. This creates ghost copies of these Ritz vectors, i.e. instead of a  $T_k$  having one eigenvalue nearly equal to the desired value  $\lambda_i(A)$  it may have many eigenvalues nearly equal to  $\lambda_i(A)$ . This is not dramatic if the multiplicity of the eigenvalue it is not important in the problem studied, only the convergence of interior eigenvalues is further delayed. But if accurate multiplicities are important (as it is for example in calculating partition functions), then it is extremely important to keep the Lanczos vectors nearly orthogonal. One could for example use a Lanczos algorithm with full orthogonalization, imposing the  $z$  vector orthogonal to

each converged Ritz vector at each Lanczos step:

$$z = z - \alpha_j q_j - \beta_{j-1} q_{j-1} \quad \rightarrow \quad \begin{cases} z = z - \sum_{i=1}^{j-1} (z^T q_i) q_i \\ z = z - \alpha_j q_j - \beta_{j-1} q_{j-1} \end{cases} \quad (\text{B.2})$$

This implementation does cure the problem, however it is very expensive. One can easily check it costs  $O(k^2 n)$  flops instead of  $O(kn)$  and requires  $O(kn)$  space instead of  $O(n)$ : this may be a too high prize to pay. Fortunately there is a middle ground between no reorthogonalization and full reorthogonalization capable to get the best from both methods: the selective reorthogonalization.

### B.2.1 Selective reorthogonalization

Selective reorthogonalization exploits Paige's theorem which tells us that the ghost-Ritz-vector develop in the direction of the already converged Ritz vector. So we can simply monitor the error bound  $\beta_k |v_i(k)|$  at each step, and when it becomes small enough (less than the converging precision  $\epsilon$ ), the vector  $z$  in the inner loop of the Lanczos algorithm is orthogonalized against  $y_{i,k}$ :  $z = z - (y_{i,k}^T z) y_{i,k}$ :

#### The Lanczos algorithm with selective orthogonalization:

$$q_1 = b / \| b \|, \beta_0 = 0, q_0 = 0$$

for  $j = 1$  to  $k$

$$z = Aq_j$$

$$\alpha_j = q_j^T z$$

$$z = z - \alpha_j q_j - \beta_{j-1} q_{j-1}$$

*Selective orthogonalization against Ritz vectors:*

for all  $i \leq k$  such that  $\beta_k |v_i(k)| \leq \epsilon$

$$z = z - (y_{i,k}^T z) y_{i,k}$$

end for

$$\beta_j = \| z \|^2$$

if  $\beta_j = 0$  exit

$q_{j+1} = z/\beta_j$  Compute eigenvalues, eigenvectors and error bounds of  $T_j$

end for

## Bibliography

- [1] P. W. Anderson. *Science*, 235:1196, 1987.
- [2] P. W. Anderson, P. A. Lee, M. Randeria, T. M. Rice, N. Trivedi, and F. C. Zhang. *J. Phys. Condens. Matter*, 16:R755–R769, 2004.
- [3] P. W. Anderson and P. Ong. cond-mat/0405518.
- [4] Y. Ando and T. Murayama. *Phys. Rev. B*, 60:6991, 1999.
- [5] N.W. Ashcroft and N.D. Mermin. *Solid State Physics*. Saunders College Publishing, 1976.
- [6] Takagi et al. *J. of Appl.Phys. (Lett.)*, 26:L123, 1987.
- [7] J. Bardeen, L.N. Cooper, and J.R. Schrieffer. *Phys. Rev.*, 108(5):1175, 1957.
- [8] H. Bethe. *Zeitschrift für Physik*, 71:205, 1931. English translation by V. Frederick in: D.C. Mattis *The many-body problem*, World Scientific, (1993), pg 689.
- [9] C. J. Bolech, S. S. Kancharla, and G. Kotliar. *Phys. Rev. B*, 67:075110, 2003.
- [10] M. Caffarel and W. Krauth. *Phys. Rev. Lett*, 72:1545, 1994.
- [11] J. C. Campuzano, M. R Norman, and M. Randeria. *Physics of Superconductors II*. K. H. Bennemann and J. B. Ketterson, 2004. 167-273.
- [12] M. Capone, M. Civelli, S. S. Kancharla, C. Castellani, and G. Kotliar. *Phys. Rev. B*, 69:195105, 2004.
- [13] T.R. Chien, Z.Z. Wang, and N.P. Ong. *Phys. Rev. Lett.*, 67:2088, 1991.
- [14] P. Nozières D. Pines. *The Theory of Quantum Liquids*, volume I. W.A. Benjamin, Inc., New York, 1966.
- [15] A. Damascelli, Z. X. Shen, and Z. Hussain. *Rev. Mod. Phys.*, 75:473, 2003.
- [16] JW Demmel. *Applied Numerical Linear Algebra*. SIAM, Philadelphia, PA, 1997.
- [17] A. Kaminski et al. *Phys. Rev. Lett*, 84:1788, 2000.
- [18] A. Malinowski et al. cond-mat/0108360.
- [19] B. Kyung et al. cond-mat/0502565.
- [20] B. Kyung et al. *Phys. Rev. B*, 68:174502, 2003.
- [21] C. Dahnken et al. cond-mat/0504618.

- [22] D. G. Hawthorn et al. cond-mat/0502273.
- [23] D. Sénéchal et al. *Phys. Rev. Lett*, 94:156404, 2005.
- [24] E. Pavarini et al. *Phys. Rev. Lett*, 87:047003, 2001.
- [25] G. Biroli et al. *Phys. Rev. B*, 71:037102, 2005.
- [26] J. Mesot et al. *Phys. Rev. B*, 63:224516, 2001.
- [27] K. M. Shen et al. *Science*, 307:901, 2005.
- [28] K. Yamada et al. *Phys. Rev. B*, 40:4557, 1989.
- [29] N. Nücker et al. *Zeitschrift für Physik B*, 67:9, 1987.
- [30] S. H. Pan et al. *Nature*, 413:282, 2002.
- [31] Th. Maier et al. *Phys. Rev. Lett*, 85:1524, 2000.
- [32] G. Fano, F. Ortolani, and A. Parola. *Phys. Rev. B*, 46:1048, 1992.
- [33] L. Forro, D. Mandrus, C. Kendziora, L. Mihaly, and R. Reeder. *Phys. Rev. B*, 42:8704, 1990.
- [34] A. Georges and G. Kotliar. *Phys. Rev. B*, 45:6479–6483, 1992.
- [35] A. Georges, G. Kotliar, W. Krauth, and M. Rozenberg. *Rev. Mod. Phys.*, 68:13–125, 1996.
- [36] M. Grilli and G. Kotliar. *Phys. Rev. Lett*, 64:1170, 1990.
- [37] K. Haule, A. Rosch, J. Kroha, and P. Wölfle. *Phys. Rev. Lett*, 89:236402, 2002.
- [38] J. Hubbard. *Proc. Roy. Soc. London A*, 276:238, 1963.
- [39] M. S. Hybertsen, M. Schlüter, and N. E. Christensen. *Phys. Rev. B*, 39:9028, 1989.
- [40] J.E. Hyrsch and R.M. Fye. *Phys. Rev. Lett*, 56:2521, 1986.
- [41] D. Poilblanc et al. cond-mat/0202180 (2002).
- [42] Z. Konstantinovic, Z.Z. Li, and H. Raffy. *Phys. Rev. B*, 62:11989, 2000.
- [43] G. Kotliar and J. Liu. *Phys. Rev. B*, 38:R5142, 1988.
- [44] G. Kotliar, S.Y. Savrasov, G. Palsson, and G. Biroli. *Phys. Rev. Lett*, 87:186401, 2001.
- [45] G. Kotliar and D. Vollhardt. *Physics Today*, 57:53, 2004.
- [46] B. Kyung, S.S. Kancharla, D. Sénéchal, A.-M.S. Tremblay, M. Civelli, and G. Kotliar. 2005. cond-mat/0502565.
- [47] B. Kyung, G. Kotliar, and A. M. S. Tremblay. cond-mat/0601271.
- [48] C. Lanczos. *J. Res. Nat. Bur. Stand.*, 45:255, 1950.

- [49] A. I. Lichtenstein and M. I. Katsnelson. *Phys. Rev. B*, 62:R9283, 2000.
- [50] E.H. Lieb and F.Y. Wu. *Phys. Rev. Lett*, 20:1445, 1968.
- [51] T. Maier, M. Jarrel and T. Pruschke, and J. Keller. *Eur. Phys. J. B*, 13:613, 2000.
- [52] G.C. McIntosh and A.B. Kaiser. *Phys. Rev. B*, 54:12569, 1996.
- [53] W. Metzner and D. Vollhardt. *Phys. Rev. Lett*, 62:324, 1989.
- [54] S.D. Obertelli, J.R. Cooper, and J.L. Tallon. *Phys. Rev. B*, 46:14928, 1992.
- [55] O. Parcollet, G. Biroli, and G. Kotliar. *Phys. Rev. Lett*, 92:226402, 2004.
- [56] O. Parcollet and A. Georges. *Phys. Rev. B*, 59:5341, 1999.
- [57] A. Perali, M. Sindel, and G. Kotliar. *Eur. Phys. J. B*, 24:487, 2002.
- [58] D. Pini. Il modello di hubbard nella superconduttività ad alta temperatura. Master's thesis, Università degli studi di Milano, Facoltà di Scienze MM FF NN, 1989.
- [59] M.A. Quijada, D.B. Tanner, R.J. Kelley, and M. Onellion. *Physica C*, 235-240:1123, 1994.
- [60] M.J. Rozenberg, G. Moeller, and G. Kotliar. *Mod. Phys, Lett. B*, 8:535, 1994.
- [61] D. Senechal, P.-L. Lavertu, M.-A. Marois, and A.-M. S. Tremblay. cond-mat/0410162.
- [62] Q.M. Si, M.J. Rozenberg, G. Kotliar, and A.E Ruckenstein. *Phys. Rev. Lett*, 72:2761, 1994.
- [63] R.R.P. Singh. *Phys. Rev. B*, 39:9760, 1989.
- [64] T. D. Stanescu and G. Kotliar. cond-mat/0508302.
- [65] T. D. Stanescu and P. Phillips. *Phys. Rev. Lett*, 91:049901(E), 2003.
- [66] Tudor Stanescu. Private communication.
- [67] K. Takagi, B. Batlogg, H.L. Kao, J. Kwo, R.J. Cava, J.J. Krajewski, and W.F. Peck. *Phys. Rev. Lett*, 69:2975, 1992.
- [68] C.M. Varma and E. Abrahams. *Phys. Rev. Lett*, 86:4652, 2001.
- [69] F.C. Zhang, C. Gross, T.M. Rice, and H. Shiba. *Supercond. Sci. Tech.*, 1:36, 1998.
- [70] Y. Zhang, N.P. Ong, Z.A. Xu, K. Krishana, R. Gagnon, and L. Taillefer. *Phys. Rev. Lett*, 84:2219, 2000.

## Vita

### Marcello Civelli

#### Education

- 2006** Ph. D. in Physics, Rutgers, The State University of NJ, New Jersey, USA.
- 2000** Italian "Laurea" in Physics, Università degli Studi dell' Insubria, Como, Italy.

#### Positions

- 2003-2006** Graduate assistant, Department of Physics, Rutgers University.
- 2000-2003** Teaching assistant, Department of Physics, Rutgers University.

#### Publication List

- 2005** S. S. Kancharla, M. Civelli, M. Capone, B. Kyung, D. Sénéchal, G. Kotliar and A.-M.S. Tremblay, *Anomalous superconductivity in doped Mott insulators*, cond-mat/0508205.
- 2005** B. Kyung, S. S. Kancharla, D. Sénéchal, A. -M. S. Tremblay, M. Civelli and G. Kotliar, *Short-Range Correlation Induced Pseudogap in Doped Mott Insulators*, cond-mat/0502565.
- 2005** M. Civelli, M. Capone, S. S. Kancharla, O. Parcollet and G. Kotliar *Dynamical Breakup of the Fermi Surface in a doped Mott Insulator*, Phys. Rev. Lett. 95, 106402 (2005).
- 2004** M. Capone, M. Civelli, S.S. Kancharla, C. Castellani and G. Kotliar, *Cluster Dynamical Mean-Field Theory of the density-driven Mott transition in the one-dimensional Hubbard model*, Phys. Rev. B 69, 195105 (2004).